REMELTING OF ALUMINIUM BY CONTINUOUS SUBMERSION OF ROLLED SCRAP

Dr.ing. thesis

Snorre Farner
December, 2000

Reprinted September, 2001: Typing mistakes corrected, Eqs. (2.125) and (2.127) exchanged with Eq. (5.4) changed correspondingly.

Department of Materials Technology and Electrochemistry
Norwegian University of Science and Technology
IME-Rapport 2000:24

This thesis has been submitted to the Department of Materials Technology and Electrochemistry, Norwegian University of Science and Technology (NTNU), in partial fulfillment of the requirements for the doctoral degree Doktor ingeniør.

To my dear mother

Preface

While writing this book, I have tried to keep in mind that some will read it from front to back while most want to look up a certain topic. Apart from the table of contents and the abstract, I have provided a list of symbols at the beginning of the book, a keyword index at the end, and a large number of cross references throughout the book.

The introduction (Chapter 1) contains a motivation for the work, a literature review, and summary at the end. Chapter 2 present mathematical models and tools for treatment of the experimental results, which are given in Chapter 4. A description of the experiments is found in Chapter 3. The discussion (Chapter 5) is divided into sections considering the different aspects of the model and experimental results successively. Chapter 6 contains the conclusions as well as industrial implications and recommendations for further work. Parts of this work were presented at the TMS Annual Meeting in Nashville, Tennessee, USA, in March 2000 (Farner et al. 2000).

I wish to acknowledge the Research Council of Norway and Hydro Aluminium Holmestrand Rolling Mill (HRM) for the financial support of this work. HRM has provided the materials used in the experiments, offered help with metal analyses, and placed the remelting furnace with support at my disposal. The lacquered plates were provided by Hydro Aluminium AluCoat, and the launder experiments were performed at the Research Centre at Hydro Aluminium Sunndal. I am grateful for the technical support and assistance from all these plants.

I am indepted to my supervisor Professor Thorvald Abel Engh for his invaluable guidance and fruitful discussions, and not least for his great interest in my work.

I would also like to thank my second supervisor Dr. Frede Frisvold as well as my closest colleagues Harsharn Tathgar, Martin Syvertsen, Anne Kvithyld, and Jo Fenstad for their social and professional friendship.

The local workshop at the Department of Materials Technology and Electrochemistry, NTNU, is acknowledged for general help and for preparing the feeding apparatus, and the workshop at the Department of Machine Design and Materials Technology, NTNU, for putting together the water model. I am also thankful to all those around me at NTNU and SINTEF who have been of help here and there.

Finally, sincere thanks to my family and closest friends for being there for me as moods went up and down, and a special word of thank to my dear friend Jørgen Nyhus for mutual support during this work.

Trondheim, December 22, 2000

Snorre Farner

Contents

Preface **iii**

List of symbols **ix**

Abstract **xi**

1 Introduction **1**
1.1 Recycling of aluminium 1
1.1.1 Extraction of aluminium 2
1.1.2 Recycling of aluminium 2
1.1.3 The life cycle of aluminium 3
1.1.4 Common methods for remelting aluminium scrap 4
1.1.5 Holmestrand Rolling Mill 5
1.2 Oxidation and dross generation 6
1.2.1 Oxidation of aluminium 6
1.2.2 Dross generation 7
1.3 Floating and submersion of scrap 10
1.3.1 Floating of scrap 10
1.3.2 Submersion of light-gauge scrap 11
1.4 Heat transfer and moving boundaries 16
1.5 Shell formation upon immersion of cold objects 17
1.5.1 Shell formation 18
1.5.2 Interfacial heat-transfer coefficient 19
1.5.3 Heat-transfer coefficient and contact pressure 21
1.5.4 Shell temperature 22
1.6 Meniscus and gas entrainment 23
1.7 Introductory submersion experiments 24
1.7.1 Numerical simulations 24
1.7.2 Water-model experiments 24
1.7.3 Industrial melt experiments 28
1.7.4 Discussion 30
1.8 Summary and comments 32

2 Mathematical models for feeding of a plate into a melt 35
2.1 Continuous feeding of a plate into a melt . . . 35
2.2 The mathematical quantities . . . 36
2.3 General assumptions . . . 38
2.4 Model 1: Main model with shell formation . . . 39
2.4.1 Region A . . . 39
2.4.2 The shell . . . 40
2.4.3 Region B . . . 41
2.4.4 The wedge region . . . 42
2.4.5 Combined solution . . . 42
2.5 Model 2: One-dimensional model without shell . . . 44
2.6 Model 3: Model without gap between shell and plate . . . 46
2.7 Heating of the plate above the melt sufrace . . . 47
2.7.1 Heat radiation from the melt . . . 47
2.7.2 Heat conduction up through the plate . . . 50
2.8 The transient period . . . 52
2.9 Two-dimensional calculations . . . 56
2.9.1 A simple two-dimensional model . . . 56
2.9.2 The temperature difference between plate centre and surface 59
2.10 Criterion for shell formation . . . 60
2.11 Heat-transfer coefficient in thermal boundary layer . . . 61
2.11.1 Boundary-layer theory for molten metals . . . 61
2.11.2 The heat-transfer coefficient for feeding of plate into stagnant melt . . . 64
2.11.3 The heat-transfer coefficient for feeding of plate into horizontal melt flow . . . 65

3 Experimental 67
3.1 Experimental setup . . . 67
3.1.1 The feeding apparatus . . . 67
3.1.2 The furnace . . . 69
3.1.3 The launder . . . 69
3.2 Thermocouples . . . 71
3.3 Materials and experiment categories . . . 72
3.4 Measurement of melting point . . . 73
3.5 Experimental procedure . . . 75
3.6 Measurement of the temperature profile . . . 76
3.7 Analysis of the immersed plate . . . 77
3.7.1 The penetration depth . . . 77
3.7.2 Microscopy of cross section of plate . . . 78
3.8 Experimental uncertainties . . . 78
3.9 Fitting procedure . . . 80

4 Results **83**
4.1 Cross section of plate 83
4.2 Snap-off 86
4.3 Shell formation and meniscus 88
4.3.1 Shell formation 88
4.3.2 Shell start depth 91
4.3.3 The meniscus 92
4.4 Penetration depth 93
4.4.1 Quiescent-melt experiments 94
4.4.2 Launder experiments 96
4.4.3 No-lacquer experiments 99
4.4.4 Lacquer experiments 101
4.4.5 Summary 103
4.5 Vertical temperature profile in plate 104
4.6 Thicker plates 106

5 Discussion **109**
5.1 The validity of the model assumptions 109
5.1.1 Constant material properties 109
5.1.2 The effect of a melting range 110
5.1.3 Equal melting point for plate and melt 112
5.1.4 Constant heat-transfer coefficients 112
5.1.5 The sensible heat of the melt 113
5.1.6 The same liquid heat-transfer coefficient in all regions . . 114
5.1.7 Constant shell temperature 114
5.1.8 No heating of plate above melt surface 115
5.1.9 Steady state 115
5.1.10 Horizontal isotherms in plate 116
5.1.11 Constant wedge temperature 116
5.2 Melt flow and the liquid heat-transfer coefficient 116
5.2.1 Stagnant melt 117
5.2.2 Flowing melt 117
5.3 Meniscus and shell start depth 118
5.4 Shell formation 119
5.4.1 Criterion for shell formation 119
5.4.2 Shell thickness 121
5.5 The gap heat-transfer coefficient and lacquer 122
5.5.1 The gap heat-transfer coefficient 122
5.5.2 The effect of lacquer 122
5.6 Snap-off and uncertainties in penetration depth 123
5.7 Thick plates 124
5.8 The goodness of the main model 126

6 Conclusions and recommendations **131**
6.1 Model and experiments 131
6.2 Industrial implications 132
6.3 Recommendations for further work 133

A Apparatus drawings **135**
A.1 Water model 135
A.2 Feeding apparatus 137

B Material properties **139**
B.1 Physical properties of pure aluminium 139
B.1.1 Density 139
B.1.2 Specific heat 140
B.1.3 Viscosity 140
B.1.4 Thermal conductivity 142
B.2 Physical properties of aluminium alloys 142

C Mathematical details **145**
C.1 Approximate equation for the shell growth 145
C.2 The coefficients of the two-dimensional steady-state solution . . . 146
C.3 Inverse Laplace transformation 146

D Feeder control **151**

E Statistics of the experiments **155**
E.1 Weighted least-squares fit 155
E.2 Estimated error in the parameters 158
E.2.1 The covariance tensor 158
E.2.2 Nonparametric bootstrapping 158

F Experimental data **161**

References **169**

Index **175**

List of symbols

Normal dimensional quantities

Latin Symbols		Units	Dim.less
A	Area	m^2	
B	Plate width	m	
b	Plate thickness	m	1
c	Specific heat of solid	J/kg K	
c_l	Specific heat of liquid	J/kg K	
h	Melt level in launder	m	
Δh	Melt-level change past obstacle	m	
h	Heat-transfer coefficient	W/K m^2	
h_a	Heat-tr. coeff. between plate and air	W/K m^2	Nu_a
h_f	Heat-tr. coeff. of air film between plate and melt	W/K m^2	
h_g	Heat-tr. coeff. of gap between plate and shell	W/K m^2	Bi
h_l	Heat-tr. coeff. between melt and shell/plate	W/K m^2	Nu
h_t	Resultant (total) heat-transfer coefficient	W/K m^2	Nu
k	Thermal conductivity of solid	W/K m	
k_l	Thermal conductivity of liquid	W/K m	
L	Latent heat of melting	J/kg	Sf
M	Number of fitting parameters		
N	Number of measurements		
n	Number of sampled data sets in bootstrapping		
P	Penetration depth	m	Π
P_A	Penetration depth of Region A	m	Π_A
P_B	Penetration depth of Region B (and A)	m	Π_B
T	Temperature	K	θ
T_a	Ambient temperature and initial plate temperature	K	θ_a
T_l	Temperature of bulk melt	K	θ_l
T_m	Assumed melting point	K	1
T_p	Plate temperature	K	θ_p
t	Time	s	τ
V	Melt-flow velocity (in launder)	m/s	
v	Feeding velocity	m/s	Pe
x	Plate thickness co-ordinate, outward from centre	m	ξ

Latin Symbols (cont.)		Units	Dim.less
x_s	Shell thickness	m	ξ_s
y	Plate length co-ordinate, downward from melt surface	m	η
z	Plate width co-ordinate, along plate width	m	ζ
Greek Symbols		Units	Dim.less
α	Thermal diffusivity in solid ($k/\rho c$)	m^2/s	
α_l	Thermal diffusivity in liquid ($k_l/\rho_l c_l$)	m^2/s	
β	Expansion coefficient of solid ($\beta = -d\rho/\rho dT$)	K^{-1}	
δ_T	Thickness of the thermal boundary layer	m	
δ_v	Thickness of the viscous boundary layer	m	
δ_f	Shell start depth on plate front	m	
δ_b	Shell start depth on plate back	m	
μ	Coefficient of viscosity	kg/ms	
ν	Kinematic viscosity	m^2/s	
ν	Number of degrees of freedom		
ρ	Density of solid	kg/m^3	
ρ_l	Density of liquid	kg/m^3	
χ^2	Sum of squared residuals ("chi-square")		

Dimensionless quantities

Symbol	Description	Definition
Bi	Biot number (gap heat transfer/heat conduction)	$Bi = h_g b/k$
Nu	Nusselt number (melt heat transfer/heat conduction)	$Nu = h_l b/k$
Pe	Péclet number (heat convection to conduction)	$Pe = \rho c v b/k$
Sf	Inverse Stefan number (latent heat to sensible heat)	$Sf = \frac{L}{c_l(T_m - T_a)}$
Pr	Prandtl number (viscosity/thermal diffusivity)	$Pr = \nu/\alpha_l$
Re	Reynholds number	$Re = vL/\nu$
θ	Dimensionless temperature	$\theta = \frac{T - T_a}{T_m - T_a}$
τ	Dimensionless time	$\tau = \alpha t/b^2$
Π	Dimensionless penetration depth	$\Pi = P/b$
ξ	Dimensionless x co-ordinate	$\xi = x/b$
η	Dimensionless y co-ordinate	$\eta = y/b$
ζ	Dimensionless z co-ordinate	$\zeta = z/b$

Abstract

When remelting aluminium scrap, metal losses due to dross generation is a common problem. Reduction of these losses will give substantial economic and environmental benefits. Dross is generated when aluminium metal oxidizes and films of oxide envelope molten metal. When a cold metal object is immersed in a melt, the heat of the melt around this is transferred so rapidly into the object that a shell of melt often solidifies to the surface of the object. When scrap with low bulk density is charged to a melt, solidification of melt on the cold scrap prevents melt from entering the cavities in the bulk of the scrap, and the bulk density remains low. Thus the scrap tends to float on the melt surface. Submersion of this scrap is important to avoid oxidation and subsequent dross generation.

One solution to this is to roll scrap to a strip and feed it into the melt. This system has been examined by studying feeding of a continuous, thin aluminium plate into molten aluminium. Also, the effect of lacquer was considered, as well as feeding the plate into a launder with melt flowing along the surface of the plate.

An analytical, one-dimensional, steady-state model has been developed to describe the melting and the melting mechanisms. It is based on a shell solidifying on the plate surface and a gap introducing a thermal resistance $1/h_g$ between the shell and the plate. The thermal resistance $1/h_l$ of the boundary layer of the melt is included. Depending on these resistances, the initial temperature of the plate and the melt temperature, a shell will form, and the plate will penetrate a distance P into the melt before it melts away.

An experimental apparatus was designed and constructed to feed aluminium plate from a coil into a melt bath at a specified velocity. The plate could be withdrawn rapidly to "freeze" the situation like it was below the melt surface. The penetration depth P of the plate could be measured and shell formation observed.

More than 200 experiments were performed, and by comparing the penetration depth at different feeding velocities and melt temperatures to model predictions, the two heat-transfer coefficients h_l and h_g could be determined by curve fitting. They agree reasonably well with values found in the literature and calculated from boundary-layer theory. In a few experiments, the plate feeding was recorded on video tape, and the cross section of some plates was studied in a microscope. Feeding of somewhat thicker plates was also tried. This gave valuable background information for comparing the experiments to the model. We believe that snap-off of the plate due to low mechanical strength around the melting temperature may affect the measurement of the penetration depth of the plate.

Attempts were also made to measure the temperature in the plate by attaching thermocouples to its surface. The obtained temperature profiles in the plate were compared to the model predictions, but the method needs improvement.

A criterion for formation of a shell is formulated and tested against experimental observations. Qualitative agreement is achieved. Even if there is no shell formation, it seems that there will be an air film with thermal resistance $1/h_g$. This indicates that the melting rate will be independent of whether a shell is formed or not.

Two additional models with only one heat-transfer coefficient are also developed in order to challenge the main model. From this analysis it is found that the use of two heat-transfer coefficients is necessary to describe the system.

The model should be of direct interest when feeding rolled scrap into molten aluminium.

Improvement of the model can be attained by reconsidering the assumptions made, but then numerical methods must undoubtedly be applied. These new models should include the snap-off mechanism.

Chapter 1

Introduction

Recycling of aluminium is a growing industry due to the increasing environmental consciousness and the economical benefit of low energy consumption compared to primary production of aluminium. Aluminium has been used in a number of areas, for instance in the home, at work, in buildings, in cars, and in high-voltage cables, and its usage increases. When recycled, the scrap consists of very thin plates, as in beverage cans, and in thick extrusion profiles, as in window frames, it is painted, and it is attached to other metals. Thus, the challenges are many. In remelting of aluminium scrap, large amounts of aluminium are lost due to oxidation and dross formation. This is a major concern for the aluminium-recycling industry at present, in addition to increasing the melting rates of the scrap.

The present work seeks to provide a way to reduce the metal losses and enhance the rate of remelting aluminium scrap by continuous rolling and feeding of the scrap directly into molten aluminium.

This chapter contains: an introduction to recycling of aluminium (Section 1.1), a literature survey of subjects that are the basis for this thesis (Sections 1.2–1.6), and a presentation of introductory experiments (Section 1.7). A short summary with comments is provided in (Section 1.8).

1.1 Recycling of aluminium

Handbook of Chemistry and Physics (Lide 1997, p. 4-2) summarizes some historical facts about aluminium: Aluminium is the most frequently occurring metal in the earth's crust with about 8 %, not counting silicon (with 26 %) as a metal.

But it is not found in pure form. In 1761, de Morveau gave the name "alumine" to the base substance of alum, a white mineral salt which was used in medicine and cloth dyeing (aluminium potassium sulfate). In 1787, Lavoisier thought, althought somewhat wrongly, that this base was the oxide of a still undiscovered metal. The metal was in 1807 named "alumium" by Davy but changed to "aluminum" soon after and then to "aluminium" to conform with most other elements. But aluminium was not really known before Ørsted produced it in impure form in 1825 and Wohler isolated it in 1827. As a curiosity, the American Chemical Society officially decided in 1925 to write "aluminum", as is now correct in American English.

Aluminium has many important properties: low density, high corrosion resistance, high electrical and thermal conductivity, high machinability and formability, and if alloyed properly, also high strength compared to the weight. Its relatively low melting point of 660°C makes it less energy-consuming and easier to remelt than steel, for example.

1.1.1 Extraction of aluminium

Due to aluminium's favourable properties, it was a small revolution when aluminium for the first time could be produced in an efficient way from aluminium oxide by electrolysis in 1886, and production and use of aluminium grew quickly. The process is called the Hall-Héroult process after the American Hall and the Frenchman Héroult, who discovered it independently. Today, aluminium oxide is mainly produced from the mineral bauxite by the Bayer process, and the method used for producing aluminium from aluminium oxide is still the Hall-Héroult process (Ekström and Claesson 1983; Lide 1997). The pure aluminium (about 99.5 %) produced in this process is called *primary aluminium*.

The environmental problems with primary production of aluminium from hydroelectric power may be relatively small, but the process demands much electric energy, about 19 000 kWh/tonne of aluminium (Øye et al. 1999), and deposition of the by-products is an increasing problem. Gases from the smelting process, especially fluorides, was an environmental problem, but is now coped with by cleaning the exhaust gases.

1.1.2 Recycling of aluminium

Remelting of aluminium demands only 5 % of the energy consumed in primary production (Ekström and Claesson 1983), even when including collection and transportation etc. (Øye et al. 1999). In addition, the energy can be provided in lower-grade form such as heat. It is also a much simpler process than primary

production. Furthermore, the supply of aluminium scrap is increasing rapidly just as the production did a small century earlier. Investment in recycling of aluminium has become both necessary and technologically and economically beneficial. And even though *recycled aluminium* is sometimes called *secondary aluminium*, this should not imply any subordination to primary aluminium.

However, the aluminium-recycling industry does also have to stand up against several problems: The relative price between scrap and product is quite unstable, making it difficult to make long-term economic plans. Another problem involves separation of the returned aluminium scrap according to alloy. Mixing different alloys means generally a degrading of the metal. Much effort is therefore put into scrap-separation procedures and development of new alloys that are based on alloy mixes but still give material properties comparable to the old, well-known alloys. Another problem and challenge is the extensive losses of aluminium due to dross generation in the current recycling processes. The losses may amount to up to 10 % of the input scrap, which is several times more than the losses in the primary production of aluminium (see Section 1.2.2). Nevertheless, aluminium is both environmentally and economically suited for recycling, and an increasing effort is therefore made to solve these problems.

1.1.3 The life cycle of aluminium

Figure 1.1 illustrates the life cycle of aluminium from extraction to waste. Disregarding oxidation losses, the only limit to how many times aluminium can be recycled, is the ability and will in each step of the cycle to keep different alloys apart or to refine or separate mixed alloys.

Aluminium is cast and formed into a product in some way. Depending on the product, it becomes scrap after a short time, as for aluminium beverage cans, or after a long time, as for parts of buildings (30 years and more) or cars (about 15 years in Norway and 6 years in Japan, for instance). More and more aluminium is brought to scrap dealers who sell it more or less separated to recycling companies. Due to the limitations of current technology, the rest is lost. The recycling companies perform necessary pretreatment, such as further separation, delacquering, and preheating, before it is remelted, refined, cast, post-treated to give its expected material properties, and finally formed into a product and sold. The cycle is closed.

Of course this is a simplification of the process, for some scrap will inevitably go directly back to the market as second-hand products, and some aluminium will be lost along the way around the cycle, especially in remelting due to oxidation and dross formation, as will be discussed in Section 1.2.

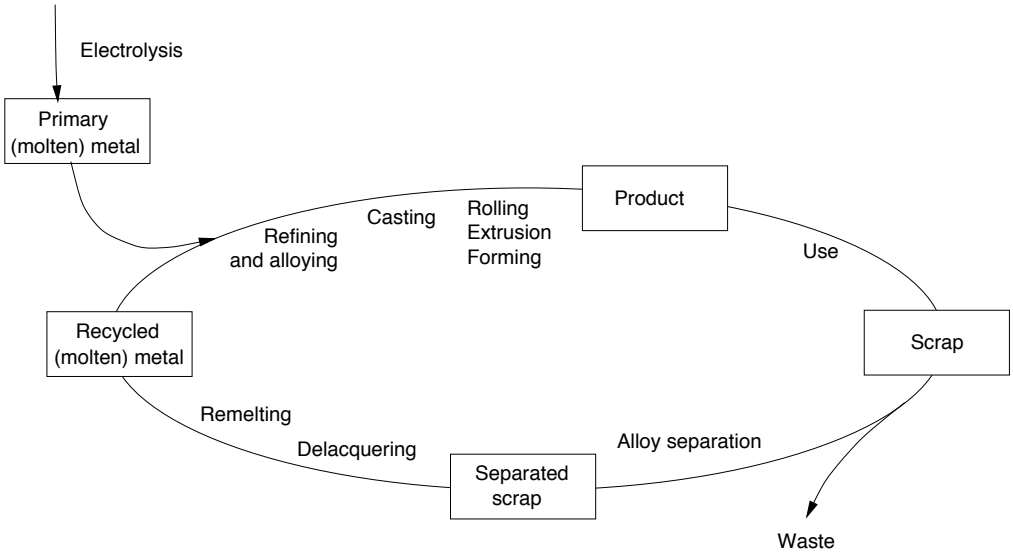

Figure 1.1: The life cycle of aluminium

1.1.4 Common methods for remelting aluminium scrap

In remelting of aluminium scrap in an industrial setting, a number of different principles are in use (Peterson 1995): the dry-hearth furnace, the flotation furnace, the induction furnace, the wet-hearth furnace, the rotary-barrel furnace, and the plasma furnace.

In the *dry-hearth furnace* cold scrap is charged into an empty furnace, often through a lid on the top (round-top melter), and then heated by direct flame impingement and radiation from the walls. A variant involves charging the scrap above the main hearth and letting it move downwards level by level while it is preheated by the exhaust gas from the main hearth (tower melter). The dry-hearth furnace is suitable for thick scrap with small surface area compared to volume, but unsuitable for *light-gauge scrap*, i.e. small-fraction scrap with large surface-to-volume ratio such as swarf, thin plates, foils, and *UBC* (Used Beverage Containers). This is a *batch* furnace since it is filled and then tapped entirely.

The *flotation furnace* has a conically shaped chamber, which widens upwards so that the combustion air decelerates on its way up. This is believed to be suitable for light-gauge scrap, which tumbles around in the chamber until it melts and then collapses to a droplet which falls down into a melt.

The *induction furnace* consists of a circular crucible with electrically conducting coils around it. An alternating current is set up in the coil and induces electromagnetic forces in the metal inside the crucible. In molten metal, the

forces produce recirculating melt flows in the large scale and power dissipation, i.e. heating, in the microscopic scale. In solid metal, movement is impossible, so we only get power dissipation. A treatment on the use of electromagnetism in the aluminium industry is provided by Meyer (1992). The induction furnace produces little oxidation and has a high melting rate, but needs electric power and has a low capacity (up to five tonnes). Contaminants tend to be entrained and entrapped due to the movement of the melt, so the scrap should be quite clean.

The *wet-hearth furnace* is called so because the hearth always contains a large pool of molten metal. It is normally heated by gas or oil burners and has a separate chamber or well for charging of scrap. The scrap is often submerged rapidly by means of vortexing, stirring, or feeding to avoid oxidation while floating on the melt surface (see Section 1.3). The wet-hearth furnace can either be run in a continuous or a semi-continuous way. In the *continuous* process, melt is charged and tapped continuously, while in the *semi-continuous* process, scrap is charged and melted until the furnace is full. Then a portion of the melt is tapped while the remaining melt is left for the next cycle. A disadvantage with rapid submersion is that water entrapped in cavities in the scrap may cause violent and lethal explosions since the entrapped water expands by over a thousand times as it evaporates and displaces large volumes of melt in a very short time. Thorough drying and preheating reduces the risk substantially.

Another principle is used in the *rotary-barrel* and the *plasma furnaces*. The rotary-barrel furnace is heated by gas or oil burners, and scrap is mixed with salt by rotating the furnace about its axis. Its main drawback is the large salt content in the by-product dross. The plasma furnace needs no salt and is heated by a plasma torch, i.e. heating by a gas that is ionized by an electric arc. Especially the plasma furnace has currently found its greatest use in dross processing.

1.1.5 Holmestrand Rolling Mill

Hydro Aluminium Holmestrand Rolling Mill (HRM), situated by the Oslo Fjord in Norway, is the first and currently the only company in Norway whose production is based on consumer scrap. They have two furnaces, one dry-hearth and one wet-hearth furnace, and both are heated by gas burners. The wet-hearth furnace is semi-continuous and has three separate chambers, as shown in Figure 1.2a. The main furnace consists of two chambers containing most of the melt. One is meant for heating (the main heating chamber, MHC) and the other for charging (the closed-well chamber, CWC), but also this has gas burners. The melt may flow between the chambers through holes in the wall

below the melt surface. The third chamber is called the *vortex chamber* (see Figure 1.2b) because a flow vortex is set up in the chamber as melt is forced tangentially into it with an electromagnetic pump from the MHC and let run out into the CWC. Its details are documented in a patent (Katyal et al. 1994). In addition to acting as a pump, the vortex chamber is meant to increase mass and heat transfer between the melt and scrap when scrap is charged directly into this chamber. We will return to the vortex chamber in Section 1.7.

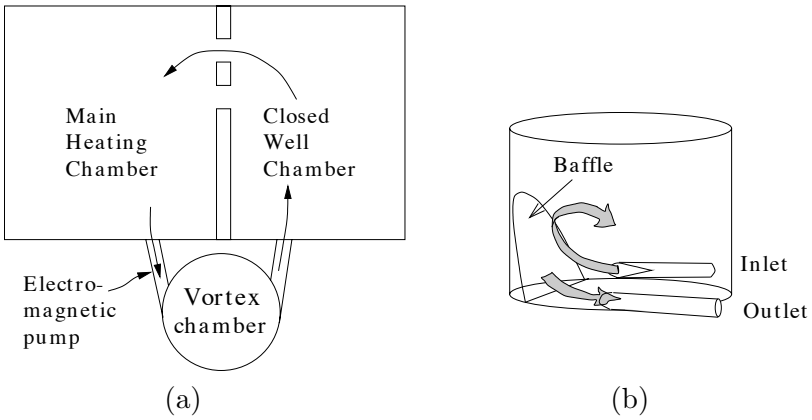

Figure 1.2: (a) Sketch of the wet-hearth furnace at HRM with (b) a sketch of the vortex chamber

1.2 Oxidation and dross generation

1.2.1 Oxidation of aluminium

Aluminium oxidizes to Al_2O_3 at once in contact with oxygen even at extremely low partial pressures of oxygen. But at room temperature, the oxide layer has a maximum thickness of only 2–3 nm, which is reached within a day (Wefers 1981). This is the case because the oxide layer itself prevents oxygen from diffusing further into the metal. This anti-corrosion property makes aluminium a very applicable material.

However, while thermal diffusion is the governing mechanism for oxidation at low temperatures, other mechanisms owing to recrystallization gradually take over above about 450°C. Thus, at high temperatures, the corrosion resistance is weakened, and the oxygen layer grows to a tenfold of the thickness at room temperature (Wefers 1981).

One of the most important alloy elements of aluminium is magnesium. But magnesium oxide (MgO) does not form a self-pretective layer, and magnesium is

thus oxidized more easily than aluminium. Moreover, the presence of magnesium in aluminium enhances oxidation at high temperatures significantly, and the oxidation rate starts to increase at lower temperatures (Wefers 1981).

On *molten* aluminium, the initially formed aluminium-oxide layer recrystallizes after an incubation time, resulting in stresses between the molecules of the layer. This gives cracks revealing fresh metal, which is oxidized immediately. Again, other alloy elements will change the oxidation rate, and as for the solid, presence of magnesium increases the oxidation rate substantially (Cochran et al. 1977; Frisvold and Engh 1997). Due to the movement of the melt under the oxide film, we get more cracking of the film and subsequently enhanced oxidation of the metal below. Additionally, as the chemical reactions become more rapid and temperature-driven convection in the melt increases with increasing temperature, oxidation will increase further at higher temperatures.

There are ways to protect the melt from oxidation. Cochran et al. (1977) have made an extensive survey of oxidation of aluminium-magnesium melts with different atmospheres. Although the gas protection is outside the scope of this, it is worth noting that they found carbon-dioxide contents of 65 % to slow down the oxidation process considerably.

1.2.2 Dross generation

Referring to the 1996 edition of Webster's Encyclopedic Unabridged Dictionary of the English Language, *dross* is defined as "a waste product taken off molten metal during smelting, essentially metallic in character".

In the process of remelting aluminium scrap, dross might as well consist of remains of paint, lacquer, and other combustibles, and possibly also entrapped gases in addition to metal oxide and large amounts of unoxidized metal. Bouquerel (1986) found that typically 70–90 % of the dross was metallic aluminium, and Sagen (1996a) reports that dross from HRM has been shown to contain up to 90 % metallic aluminium. Sagen also points out that the dross had different characteristics in the upper and the lower layer of the dross. The terms *dry* and *wet* dross are used to distinguish dross containing much oxide and little metallic aluminium (often found in the upper part of the dross layer on the melt) from dross with large contents of metal (the lower part of the dross) (Manfredi et al. 1997; Sagen 1996a). The boundary between dross and melt may be difficult to define exactly due to this gradual change from dry dross on the top to pure metallic melt below. After cooling, the dry dross is dark and granular while the wet dross is light grey and compact (Manfredi et al. 1997).

Metal losses due to dross generation can be defined as the weight difference

between the metal charged into the furnace and the metal poured out of it. As most of the dross is metallic and more than half of the mass of the oxide is aluminium, the mass of dross skimmed off is close to the metal loss.

Dross generation constitutes a great problem for the industry remelting aluminium as it represents metal losses that can exceed 10 % for some material types (Smith 1986; Fox and Nilmani 1993; Saavedra 1993; Katyal 1995; Roth and Beevis 1995; Sagen 1996b).

It should be noted that most measurements of metal losses are performed on industrial furnaces in more or less normal operation. The charging, skimming, and dross-cooling practice may vary a lot, as may the experimental conditions. Although these factors are important for the metal losses (Manfredi et al. 1997), they are often not documented well in the literature, possibly because of confidentiality considerations.

The amount of oxide on the surface of the charged scrap during melting is insignificant in comparison with the level of metal loss experienced. This can be illustrated by a simple estimate with an oxide layer of 20 nm (for example of an Al-0.8 % Mg alloy after one hour at 580°C; Wefers 1981) on both sides of an aluminium plate. Even if the plate is very thin, say 0.1 mm, the oxide fraction would still make only 0.06 % of the whole plate.

Nevertheless, the oxide formation is important for the dross formation owing to the film-like nature of the oxide. Hald (1995) has studied dross in the microscope and revealed that the oxide layers lie as films enclosing metal in droplets less than a millimetre large. Røhmen (1996) melted down about 0.8 mm thin plates of the AA3105 alloy in argon atmosphere and held them molten for four hours. After slow cooling, still in argon atmosphere, the oxide layers were found more or less intact although much of the metal had run out and filled the container. This is in accordance with laboratory experiments with *swarf*, i.e. thin, small pieces such as shavings and filings, where oxide films were found to remain intact in the melt even after several hours if there was no stirring (Smith 1986). Furthermore, the laboratory experiments showed that the thicker the oxide layer, the stronger the entrapment of molten metal. For example, dross formation was shown to increase greatly due to anodization, which gives an oxide skin 2–3 orders of magnitude thicker than the normal oxide film in room temperature.

Obviously, some of the greatest dross problems are connected to remelting of the light-gauge scrap because this has a large surface-to-volume ratio. Furthermore, since the pieces of this scrap are small, even thin layers of oxide may be able to entrap metal due to surface-tension effects. As the size of the pieces increases, gravity forces eventually exceed surface forces so that the entrapped metal drops

may coalesce. Remelting experiments performed by Rossel (1990) show that the melting loss increased significantly with decreasing thickness, from less than 1 % for 0.2 m thick pieces to 5–18 % for pieces a thousand times thinner, depending on temperature and alloy composition.

Stirring is the subject of Section 1.3.2, but some comments on dross generation due to stirring should be included here. The result of stirring may well be stirring up the melt surface and thereby exposing unoxidized metal to the atmosphere. For instance, Hald (1995) experienced losses of 2–3 % when melting aluminium without stirring and the double amount when he stirred the melt by gas purging with argon or nitrogen, independently of the gas type. The same was the experience when a vortex chamber with an electromagnetic pump was installed in the furnace at HRM (see Section 1.7). The melting rate and dross generation was observed before and after the installation. The charging practice was not changed. An increased melting rate was achieved, but dross generation also increased (Sagen 1996b). The fact that metal recovery from the dross also increased indicates that the stirring probably mixed the oxide films into the melt so that the boundary between dross and metal became more diffuse.

However, stirring may also contribute to breaking the oxide films, resulting in coalescence of entrapped drops of molten metal. Furthermore, it seems to be a common opinion that submersion of scrap by stirring gives less oxidation and thereby reduced dross generation (Fox and Nilmani 1993; Katyal 1995; Saavedra 1993).

It may be discussed whether some dross should be retained on top of the melt to protect the melt against further oxidation. As a matter of fact, a shiny, drossless melt surface may reflect away much of the heat radiation from the walls of the furnace, so a layer of dross is probably desirable. However, a thick dross layer will inhibit heat conduction. The dross layer may also prevent the scrap from penetrating the melt surface. Once it penetrates, dross may stick to the scrap and probably reduce the heat transfer between the melt and the scrap. Furthermore, submersion of the dross may well result in further entrapment of metallic aluminium.

Another challenge is that consumer scrap often is contaminated with paint, lacquer, remains of oil, et cetera. It is agreed upon that dross generation is enhanced by such contaminants. For example, Hald (1995) got 2–3 % dross when charging clean, unpainted scrap, and 12–13 % dross when charging clean but painted scrap. Fox and Nilmani (1993) argue that contaminants enhance the effect of the oxide skin so that metal is prevented from coalescing as it melts and that reaction of contaminants below the melt surface may cause percolation of melt into the dross layer. They suggest using a dry-hearth furnace for contaminated

scrap although this makes parts of the scrap melt down in the atmosphere with the result of increased surface oxidation. Another opinion is that contaminated scrap should be submerged quickly to reduce metal loss (Neff 1993b). In any case, cleaning and delacquering the scrap is possibly the best way to reduce dross formation when remelting contaminated scrap.

Another way to reduce dross formation is to use salt fluxes. This serves three purposes: It provides a protective cover over the molten aluminium, releases metal from oxide entrapment, and retains the oxide in the dross layer (Øye et al. 1999). However, the resulting contents of salt fluxes in the dross are harmful to the environment upon deposition. Also, salts may give salt inclusions in the aluminium.

Of course, it is possible to recover metallic aluminium from dross after it is skimmed off the melt. This can be carried out in two stages. Just after skimming, the dross is hot and can be pressed or centrifuged to strain out the metallic aluminium from the dross. After the dross is cold, metal can be recovered by remelting and using salt fluxes to release the metal from the dross, or with the use of a plasma furnace (Drouet et al. 1994). If the dross is not cooled quickly, the oxidation will proceed after skimming, and there will be less metallic aluminium to recover in the second stage. Naturally, it is of greater economic benefit to the remelter to reduce dross generation during melting than to recover the metal from the dross afterwards, even though recovery directly after skimming can be quite efficient as well.

To sum up, the basic cause for dross generation is oxidation (due to its film-like nature). Apart from the undesirable use of salt fluxes, the most efficient way to reduce oxidation seems to be rapid submersion of the scrap.

1.3 Floating and submersion of scrap

1.3.1 Floating of scrap

It is a common experience that light-gauge scrap floats on the surface of the melt even though solid aluminium is about 15 % more dense than molten aluminium (Fox and Nilmani 1993). Individual pieces of such scrap may not be able to break through the surface tension (Areaux and Behnke 1992) or the oxide skin of the melt. The thicker the dross layer, the larger pieces will float.

Large piles of loose swarf, for example, still tend to float although a part of the pile is below the melt surface. This is because the cavities in the bulk of the scrap give a reduced *bulk density*. The bulk density of two types of shredded scrap that is remelted at HRM was measured to the order of 400 $\mathrm{kg/m^3}$, only

15 % of solid aluminium (Farner 1997).

Now, if the light-gauge scrap were immersed in water, the cavities would rapidly be filled with water, and the scrap would sink. But the scrap is cold compared to the melting point of the molten metal, so once there is contact, the heat transfer from the melt to the scrap will be very high and cause the melt to solidify. This will be treated in Section 1.5. The result is that the melt solidifies and stops itself from penetrating into the bulk of the pile of swarf. Thus the pile floats.

In a gas- or oil-fired furnace, the heat is mainly transferred to the melt by radiation, either directly from the burning gas or from the wall, which has been heated by the flame (Neff 1986). Thus, scrap floating on the surface of the melt is heated while being exposed to the oxidizing atmosphere. This leads to high oxidation rates and dross generation.

Furthermore, heat transfer by direct contact with the melt is superior to that of radiation at these temperatures. This may be concluded from the experience that scrap on a platform inside the furnace needs long time to melt down. Floating thus results in a lower melting rate.

To attain an increased heat-transfer rate and decreased oxidation of the light-gauge scrap, rapid submersion is important. In the next section we will review methods for submerging this scrap.

1.3.2 Submersion of light-gauge scrap

Many ways to submerge scrap have been proposed. To our knowledge, they all belong to one of the following groups:

- stirring the melt mechanically or by electromagnetism,
- pushing or feeding into the melt,
- shooting or dropping into the melt, or
- compacting the scrap before charging.

Figure 1.3 shows one example from each group.

1.3.2.1 Stirring

Stirring of the melt has at least two advantages: it enhances heat transfer in the melt, and it may break down the oxide films. On the other hand, as we saw in

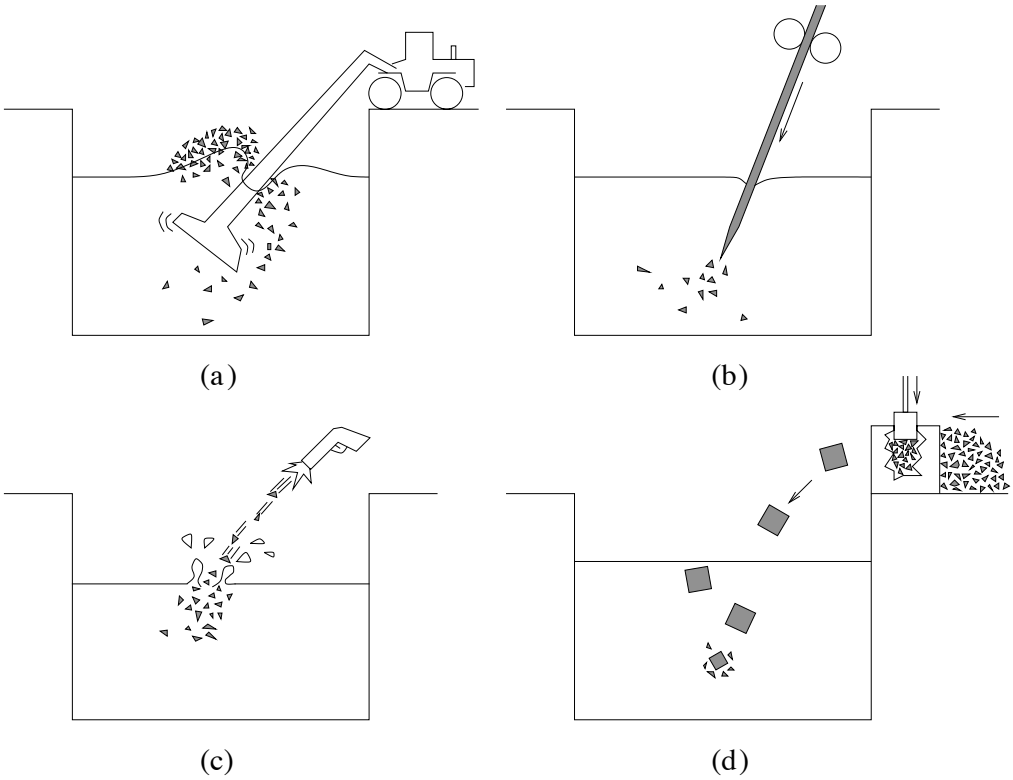

Figure 1.3: Various submersion techniques: (a) stirring, (b) feeding, (c) shooting, and (d) compacting

Section 1.2.2, stirring may also cause mixing of oxide films and contaminants into the bulk melt. Another drawback is that stirring tends to increase the oxidation rate as new metallic aluminium melt is exposed to the oxidizing atmosphere due to movements in the melt surface.

The main objective here is stirring used to submerge scrap with low bulk density, i.e. light-gauge scrap. Stirring may be achieved with a skimming rake, for instance, but efficient submersion is better accomplished by pumping the melt, or by stirring with an impeller or electromagnetism (Neff 1993a).

There are many ways to pump metal, but in general, it is carried out either by some mechanical system, often a centrifugal pump, or by use of electromagnetism (Neff 1993a). The mechanical system is simple but is subject to considerable wear. The electromagnetic system, on the other hand, is more complicated and requires a heavier investment, but it has no mechanical parts. The force on the melt is generated by inducing an electrical current in the melt and then combining it with a perpendicular magnetic field.

The metal can be pumped from one chamber into another chamber, for instance through a charging well where obstacles deflect the melt flow to create vertical flows. The descending flow pulls down light-gauge scrap. One such system with electromagnetic pumping and a charging well is described by Katyal (1995) and in a patent (Katyal et al. 1994). This is the system used at HRM, and submersion experiments with this installation are presented in Section 1.7.

Similar descending flows can be achieved by some kind of impeller immersed in the melt. It is often called *vortexing* because the rotation of the impeller sets up a vortex-like flow where the melt surface slopes down towards the centre with converging melt flow below it. It is considered efficient for submersion of scrap and widely used (Fox and Nilmani 1993). To submerge scrap without entraining air and dross, the rotation should not be too fast (below about 150 rpm; Neff 1993a). Neff further recommends to pump the melt past the impeller.

1.3.2.2 Pushing/feeding

A skimming rake or similar tools can be used to push light-gauge scrap down, but the scrap will probably resurface unless it is held down until it has melted. If it resurfaces, it brings along liquid aluminium to the surface, and increased oxidation may well be the result. A *puddling* device (mechanical mixer) attached to a lift truck, for example, could be used to simplify the submersion work. Another suggestion is to put the scrap into a cage and submerge this, but the cage will be subject to considerable wear and little by little dissolve in the melt. Furthermore, these methods involve batchwise charging while a continuous method is easier to automate and thus more efficient.

Dump charging involves piling up light-gauge scrap in a superheated melt pool so that the bottom of the pile is well submersed by the weight above the melt surface. This method can be automated by charging the scrap at a steady rate to create a stationary pile that sinks continuously (see also Section 1.7). A problem is that the scrap pieces on top of the pile tend to run down and make the pile wide. This inhibits efficient weight gathering over a small pile base, resulting in less efficient submersion. A powerful heat input will be necessary to increase the melting rate and thereby reduce the time that the scrap is in contact with oxygen above the melt surface. Pumping hot molten metal from a separate chamber is a better method than having gas burners in the charging chamber.

Wire injection is a method that is used in adding low-density alloy additions to a melt. The problem of floating is also common when adding aluminium to steel, and a wire-feeding method was proposed by Tanaka (1977). This was then studied in academic depth by Mucciardi (1980) and put into industrial application (Gourtsoyannis and Mucciardi 1982). Mucciardi's work gives an

empirical expression relating the depth that the aluminium wire penetrates into the molten steel before it melts, to the wire diameter, feeding velocity, and melt *superheat*, i.e. the melt temperature in excess of the melting point of the melt. However, application of this method for feeding of scrap requires that the scrap is formed as a wire.

Areaux and Behnke (1992) report success with a couple of feeding mechanisms based on feeding scrap through a pipe whose end is submersed in the melt. The feeding mechanism is either a roll feeder (Areauz and Dudley 1987) which compacts the scrap to a strip and forces it into the melt (see also Figure 1.4b), or an *auger* (screwing) mechanism that screws the shredded scrap through a tube into the melt (Areaux 1989). Both submersion mechanisms gave reduced metal loss compared to a puddler system.

1.3.2.3 Shooting/dropping

Again we can learn from the steelmakers. In their search to submerge aluminium in molten steel (aluminium being 40 % as dense as steel melt), dropping and throwing of aluminium lumps into the steel bath have been used. Dropping of alloy additions has been studied for different density ratios by Guthrie et al. (1975) by means of wooden spheres dropped into water and compared with mathematical calculations. With the low density ratio of aluminium to molten steel, they found that aluminium in general resurfaces before it melts.

Tanoue et al. (1973) have developed a technique for *shooting* bullets of aluminium into the steel bath in order to achieve deep penetration and thus melting below the melt surface. In their paper, they provide theoretical considerations and experimental data and inform that the system was in commercial use at the time the paper was published.

Mucciardi (1980) also studied bullet shooting. He concludes that bullet shooting seems less promising than wire feeding because of practical and economical advantages with the production of wire compared to bullets and the purchase and handling of the respective charging equipment.

In theory, light-gauge scrap could be compacted to bullets and shot into the aluminium melt. The relative density difference for this system is much smaller than for aluminium in steel melt, so the aluminium bullet will stay immersed longer. On the other hand, the temperature differences are also much smaller, so the bullet will need more time to melt down. Additionally, it must be considered that oxidation of the aluminium melt is likely to occur when the bullet penetrates the melt surface and the melt is splashed around.

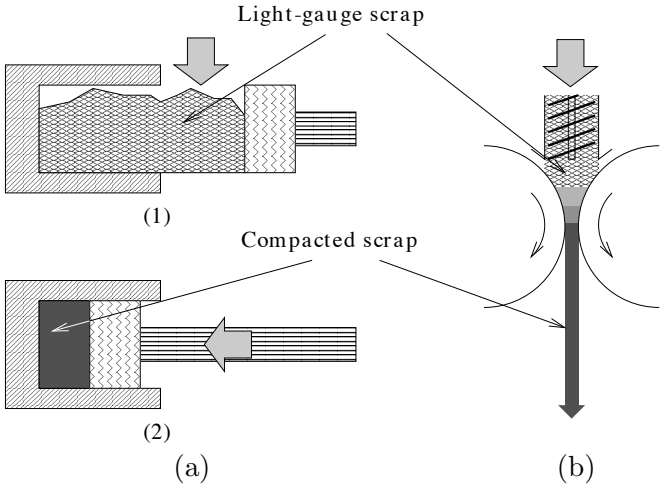

Figure 1.4: Compaction techniques: (a) single-bolt compaction and (b) continuous-strip compaction

1.3.2.4 Compacting

Submersion may also be attained by merely compressing light-gauge scrap to compact briquettes which are dumped into the melt. A problem is, however, to get sufficient compression, so that the resulting bulk density is above the density of molten aluminium. According to Pietsch (1993) there are two methods: single-bolt compaction and continuous-strip compaction, as illustrated in Figure 1.4.

Pietsch argues that the single-bolt method, although being widely applied, has a number of disadvantages, especially that a high compaction degree requires much force and some time to dwell in order to relax the elastic forces that will increase the volume of the bolt once the pressure is released. Since it is a batch process, the machine must be large and very powerful to compress large quanta of scrap in a short time. At HRM, it is observed that compacted bolts of fine swarf float on the melt surface. This indicates that it is difficult to compact light-gauge scrap to sufficiently high bulk density.

Tests (Pietsch 1993) have shown that processed aluminium swarf can be force-fed through a roller press to a continuous strip. The swarf consisted of turnings, borings, and chips of different qualities. The rolls were one metre large and from the figures in the paper, they gave an uneven surface with a pattern of semi-spheres (see Figure 1.5), probably in order to achieve a higher compression rate. The advantage with this process is firstly that it is continuous, although the strip was cut to handable lengths for later charging, but Pietsch also claims that it has a high capacity and that the strips always were denser than $2\,300\,\mathrm{kg/m^3}$

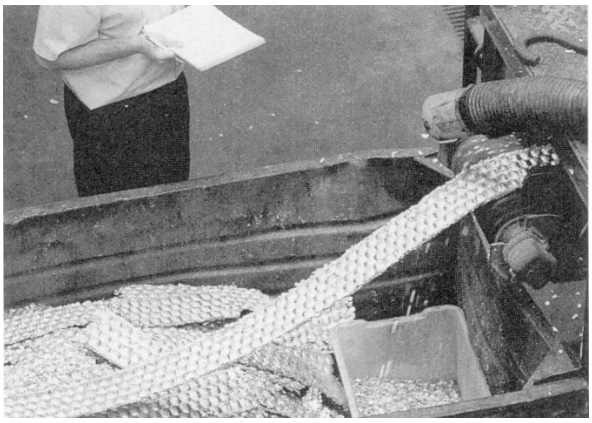

Figure 1.5: Strips made using compression rollers (Pietsch 1993)

and easily attained $2\,550\,\mathrm{kg/m^3}$. Another advantage is that swarf with highly entangled pieces need not be separated before compression. No literature following up this system has been found, and the system is no longer in use at the plant mentioned by Pietsch (Koppern Equipment Inc. in Pittsburgh, USA).

1.4 Heat transfer and moving boundaries

Before proceeding, we will shortly mention the governing equations and set the historical background for heat transfer.

Starting around 1830, study of solidification and melting was limited to analytical models. The problems studied were simple one-dimensional one-phase problems with constant thermal properties and simple boundary and initial conditions until far into the 20th century. With the computer and later the explosive evolution of computer capacity, more and more complex, multi-dimensional, multi-phase, multi-equation problems with complex geometries and even convection could be solved. However, the analytical modelling of the early times still serves as a cornerstone of this disipline and is important in verification of numerical models (Hu and Argyropoulos 1996).

Crank (1984) divides solidification and melting problems into two categories: *free-boundary problems*, where the system is in a steady state, and the *moving-boundary problems*, or *Stefan problems*, where the system changes with time. The former term is easily confused with free-surface problems, so it is common to recognize all solidification and melting problems as moving-boundary problems, whether the boundary moves or not.

In this thesis, analytical models of a specific steady-state moving-boundary problem will be considered. The mathematics will be based on Fourier's Law of

Conduction and Newton's Law of Cooling.

Heat conduction through a solid is given by *Fourier's Law of Conduction*, which relates the heat conduction q in a material with the thermal conductivity k to the temperature gradient at this point:

$$\vec{q} = -k\nabla T \qquad \text{or} \qquad q_x = -k\frac{\partial T}{\partial x}. \tag{1.1}$$

When the heat-transfer mechanisms through an area are complex or information about the heat transfer is not known, this information may be expressed empirically by the heat-transfer coefficient h. *Newton's Law of Cooling* relates the heat transfer q through the area to the temperature difference ΔT across the area:

$$q = h\Delta T. \tag{1.2}$$

We will use heat-transfer coefficients for the heat flow across a thermal boundary layer between the bulk melt and a solid surface, h_l, and over the gap between two solids, h_g.

When there is solidification or melting, i.e. change of state, the heat of fusion L enters the boundary conditions in some way. For instance, if $x < x_s(t)$ is solid and $x > x_s(t)$ liquid, and the interface $x_s(t)$ is at the melting point, then

$$q_s + \rho L\frac{dx_s}{dt} = q_l \qquad \text{at } x = x_s(t), \tag{1.3}$$

where q_s and q_l are the heat transfer towards positive x at the solid and liquid side of the boundary at $x_s(t)$, respectively (Carslaw and Jaeger 1959, Ch. XI).

1.5 Shell formation upon immersion of cold objects

When a cold object is submerged into a warm liquid, heat is quickly extracted from the liquid around the object and transferred into the object. Depending on whether or not this heat-transfer rate is larger than that from the bulk melt to the object, either solidification or melting will occur (Guthrie and Gourtsoyannis 1971). When solidification occurs, we refer to a *shell* solidifying to the object. Shell formation is usually the case when immersing a cold solid metal into a molten metal, for instance adding scrap or alloying elements to melts.

Addition of alloying elements can be divided into two classes (Engh 1992, Sec. 8.1): alloying elements that have a melting point below or equal that of the melt (Class I) and alloying elements with melting point above the melt temperature

(Class II). The latter class requires dissolution by diffusion or exothermal reactions that produce heat for melting. We will not consider these aspects here.

For Class I additions, melting is the dominant dissolution mechanism. Much of the literature considers low-density addition of alloying elements to steel. Furthermore, it is mainly concerned with time-dependent systems, i.e. systems in which an object is immersed and its course in time is studied. Systems involving continuous feeding seem less frequently studied.

1.5.1 Shell formation

Guthrie and Gourtsoyannis (1971) calculated the dissolution time of a Class I cold sphere immersed in a quiescent melt bath. Shell growth was considered and the melting rate was calculated numerically. The heat-transfer coefficient h from the bulk melt to the sphere (see Section 1.4) was calculated by a Nusselt-number relation, which is an expression relating h to the flow conditions and material properties of a given system. They compared the calculations to a few experiments carried out by immersing an iron hemispheres in molten iron. The experiments showed higher melting rates than predicted, and this was assumed to be a result of higher heat-transfer rate due to natural convection outside the hemisphere surface as well as high convective heat transfer immediately after immersion due to rather violent initial reactions causing gas evolution. The effect of preheating (initial sphere temperature in excess of room temperature) and superheat (melt temperature in excess of the melting point) was treated theoretically. Increasing either would lead to reduced melting time, but in particular, *decreasing* the superheat would give disproportionately low melting rates due to decreased natural convection as well.

They followed up with a study of addition of spheres with relatively low density and low melting point to a steel melt (Gourtsoyannis et al. 1974). In this case the addition melts more or less completely before the shell disappears. Furthermore, they combined this with a theoretical and experimental study of the movement of the sphere after it is dropped into the melt. They found that immersion times were much shorter than the melting time and explain this in terms of shell formation.

A numerical treatment of the shell formation and the melting of cold sponge iron spheres that are immersed in an iron melt is presented by Ehrich et al. (1978). These calculations are followed up with experiments and further calculations in a subsequent paper (Ehrich et al. 1979). Also in these papers, the heat-transfer coefficient was calculated by use of a Nusselt-number relation.

Taniguchi et al. (1983) made a similar study of the melting rate of aluminium

spheres in molten aluminium alloys. Differently from the previous authors, they curve-fitted the computer calculations to the measurement data and found that a heat-transfer coefficient of $25\,000\,\mathrm{W/m^2K}$ gave the best fit. Nusselt-number relations gave somewhat higher values (up to 1.5 times for the highest melt temperature used). Stirring the melt by argon gas purging gave significantly higher h and thus higher melting rates.

Zhang and Oeters (1999) have used a different approach for estimating the melting time for addition of large numbers of small spheres of different size to a melt. They used Nusselt-number relations and an overall heat balance for each sphere to find an expression for the maximum radius a sphere can have in order to melt down within a given time. By introducing a size distribution for the spheres, they obtained a melting-distribution function, which gives the fraction of the added material that is melted after a certain time.

Mucciardi (1980) seems to be the first author to study a continuous-feeding system such as feeding of an aluminium rod into a steel melt. This system could be expected to be a steady-state version of the melting of spheres as discussed above. A steel shell was formed just below the melt surface, and the aluminium rod melted inside the shell. A distance further down, the shell melted away and the molten aluminium was released into the steel melt, accompanied by a rapid heat generation due to the heat of mixing of molten aluminium and steel. Much of the shell thus melted away, but started to grow again due to the continued supply of cold aluminium, and the process repeated itself. However, at sufficiently high feeding velocities, the aluminium and heat release was stabilized, and the system became virtually stationary.

It is interesting to notice that Mucciardi (1980, p. 249) tried to reduce shell formation by painting aluminium cylinders with latex paint before immersion. The result was less shell formation, but also lower melting rates. He suggested that formation of a gaseous film increased the heat-transfer resistance. Furthermore, the shell was thicker in the upper part of the cylinder. This was explained by gas bubbles that formed in the lower region of the cylinder and rose to the upper region where they increased the thermal resistance. This leads us to the introduction of an interfacial heat-transfer coefficient.

1.5.2 Interfacial heat-transfer coefficient

We have seen that many studies of alloy addition to a melt do not consider a thermal resistance between the shell and the addition, although such a resistance always is present between two adjacent solids. The only heat-transfer coefficient used is that of the melt boundary layer between the shell and the bulk melt.

But in 1977, Guthrie (1977) reported the existence of a thermal resistance corresponding to an air-filled gap of thickness about 5–15 μm or a heat-transfer coefficient of 3–8000 $\mathrm{W/m^2K}$ between the shell and the added sphere, inhibiting heat transfer from the shell to the sphere. This interfacial thermal resistance is included in the calculations of Argyropoulos and Guthrie (1979) although no value is given. Mucciardi (1980, p. 138) studied immersion of aluminium cylinders in lead melt as a low-temperature analogy to steel melt. He needed an interfacial thermal resistance corresponding to a heat-transfer coefficient of $h_g = 5300\,\mathrm{W/m^2K}$ (where g means *gap*) to fill the discrepancy between experimental and predicted heating curves. For an aluminium cylinder immersed in a steel bath, this interfacial resistance was not observed, except maybe immediately after immersion. Mucciardi believed that this was due to expansion of the cylinder upon heating and the fact that there was no solid-to-solid interface once the cylinder started to melt.

This interfacial heat-transfer coefficient seems neglected by many authors. A reason may be that many of the situations studied involve exothermal reactions that dominate the heat transfer in this interfacial region, or the immersed object starts to melt early so that the gap disappears long before the shell melts down.

However, Røhmen (1995) and Røhmen et al. (1995) have studied the immersion of spherical additions to liquids and obtained heat-transfer coefficients by curve-fitting the calculated time dependence of the sphere radius to that measured. For aluminium spheres in aluminium melt, he reported a value of $h_g = 4000\,\mathrm{W/m^2K}$ for the interfacial gap between the shell and the sphere. Røhmen also performed ice-shell experiments by cooling aluminium spheres in liquid nitrogen and immersing them in water, but he realized that the thermal resistance between the ice shell and the sphere was more than ten times higher, probably because the water expands when it solidifies while metals contract. The ice shell thus expands away from the sphere, leaving a larger gap, in contrast to the metal shell. contracting on the expanding sphere.

Similarly, Goudie and Argyropoulos (1995) performed a number of experiments with a variety of cylindrical addition metals and several different melts. By curve fitting they obtained h_g for most of the combinations, and all of these lie between 1000 and 5000 $\mathrm{W/m^2K}$, with aluminium in aluminium melt at about 2500 $\mathrm{W/m^2K}$. Furthermore, they found a correlation between h_g and the ratio of the thermal expansion coefficients of the addition to that of the melt: The trend was that the heat-transfer coefficient increased with this ratio, i.e. h_g increased with the force pressing the cylinder towards the shell. This is in accordance with Røhmen's observation.

1.5.3 Heat-transfer coefficient and contact pressure

We have seen that few authors who have investigated the melting of additions, have considered the interfacial gap between the shell and the immersed addition, and even fewer have made an estimation of the thermal resistance of the gap.

Nonetheless, the thermal resistance between a solidifying melt and a cold mould has been studied at least since the late 1950's when Adams (1958) introduced a heat-transfer coefficient, which we continue to call h_g in the following. There is a large number of authors that have performed measurements and made calculation of the heat-transfer rate or coefficient and/or the size of the interfacial gap, including the time dependence of these quantities, between various solidifying metals in, on, or around a metallic mould. The reported values of h_g vary substantially, from 200 to 10 000 $\mathrm{W/m^2K}$ (for instance Reynolds 1964; Sun 1970; Prates and Biloni 1972; Robertson and Fascetta 1977; Garcia and Prates 1978; Ho and Pehlke 1985; Nishida et al. 1986; Lau et al. 1998; Griffiths 1999; Loulou et al. 1999).

It is interesting to note that Reynolds (1964) states that when a molten metal solidifies and shrinks around a cylindrical metal core, the thermal resistance is less than when it solidifies and shrinks away from the surrounding wall of a mould.

Kim and Lee (1997) have studied the effect of contraction and expansion simultaneously by casting aluminium alloys in a torus-shaped steel mould where the melt is in contact with both an inner and an outer wall. They found that the *inner* heat-transfer coefficient increased while the *outer* decreased as the melt solidified and the temperature decreased. This was attributed to the increased contact pressure at the inner mould wall and the opposite at the outer wall. The *contact pressure* is the pressure with which the solids are pressed against each other.

Apart from providing a large number of references to papers about the heat-transfer coefficient, Griffiths (1999) has examined the effect of the pressure on the contact zone by three different casting tubes with refractory walls as illustrated in Figure 1.6. The metal was cooled from the water-cooled copper surface, the *chill*, at the end of the tube. The melt (an Al-Si alloy) could thus be cooled from below, from the side, and from the top, that is, with different pressure against the chill surface. The heat-transfer coefficient h_g was highest for the bottom-cooled, intermediate for the side-cooled, and lowest for the top-cooled setup. The conclusion was again that increased contact pressure gives increased heat-transfer coefficient h_g.

The fact that h_g varies a great deal from author to author may be a result of

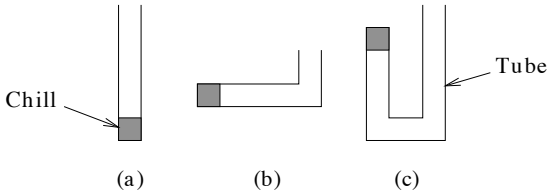

Figure 1.6: Downward (a), sideways (b), and upward (c) solidification in different tubes with a chill at the end (Griffiths 1999)

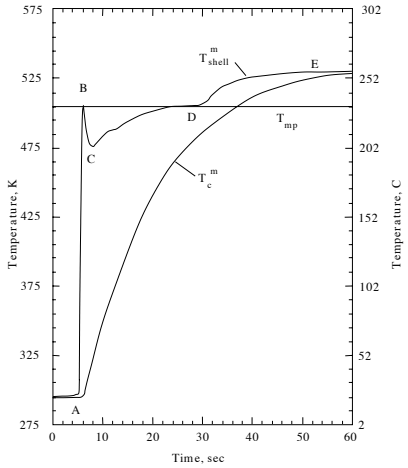

Figure 1.7: The temperature of the shell and the centre of an aluminium cylinder immersed in molten tin at 25°C superheat (Goudie and Argyropoulos 1995).

varying contact pressure caused by variations in the density of the metal or the height and radius of the mould, for example.

1.5.4 Shell temperature

The only study that was found in which the *shell temperature* was measured, is the one by Goudie and Argyropoulos (1995). In their paper about immersion of cylinders in a molten metal, they present curves with the temperature development in the shell and the cylinder for aluminium immersed in tin with melting point at 232°C. As shown in Figure 1.7, they observed that, at about 25°C superheat, the temperature in the shell quickly dropped about 30°C below the melting point (B–C) and thereafter returned slowly towards the melting point (C–D). Then the shell melts away and the temperature approaches the melt temperature (D–E).

1.6 Meniscus and gas entrainment

When a drop of liquid is placed on a solid surface, the liquid surface will intersect the solid surface at a certain *contact angle* ϑ as shown in Figure 1.8a and b (White 1994). If the contact angle $\vartheta < 90°$, the liquid is said to *wet* the solid, and it does not wet it if $\vartheta > 90°$.

The same occurs when the solid is partly immersed in a bath of liquid, as illustrated in Figure 1.9a. A *meniscus* is formed, either downwards as in the nonwetting case in the figure or upwards as can be observed for water in a glass. But if the partly immersed solid is moved up or down, the contact angle will change, as shown in Figure 1.9b and c, and we call it the *dynamic* contact angle ϑ_d in contrast to the *static* contact angle ϑ (Perry 1966). If the solid is pushed down, $\vartheta_d > \vartheta$ and vice versa. Thus, if it is pulled up sufficiently fast, $\vartheta < 90°$, and the liquid will seem to wet the solid as in Figure 1.9c.

The dynamic contact angle was investigated by Perry (1966, Ch. III) for continuous feeding of a solid (a magnetic recording tape) perpendicularly into water-based liquids with a viscosity range of more than two decades. The surface tension was varied somewhat by addition of small amounts of Aerosol 70. All the liquids wetted the tape to some degree, so the meniscus rose up from the liquid when the tape was at rest. Perry observed that at increasing feeding velocities, the dynamic contact angle increased, and the contact point between the liquid and the moving tape moved downwards. Eventually, at feeding velocity v_f, $\vartheta \approx 180°$, and an increasingly long, thin *air film* was established along the tape below the liquid surface. Instability of this film further down resulted in entrainment of air into the liquid and development of bubbles. The critical feeding velocity v_f was found to decrease with increasing viscosity and decreasing surface tension.

Perry (1966) also studied liquid jets plunging into a liquid bath and used the same model for both phenomena, assuming that the static contact angle was 0° since a liquid is considered to wet itself. He found the film thickness to be of the order of 10 μm.

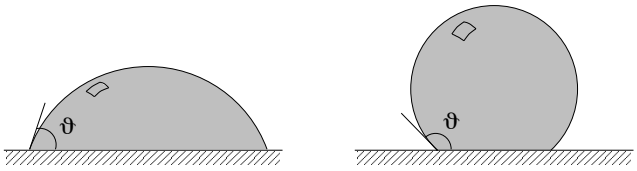

Figure 1.8: Illustration of a droplet wetting (a) a solid surface and not wetting it (b). ϑ is the wetting or contact angle.

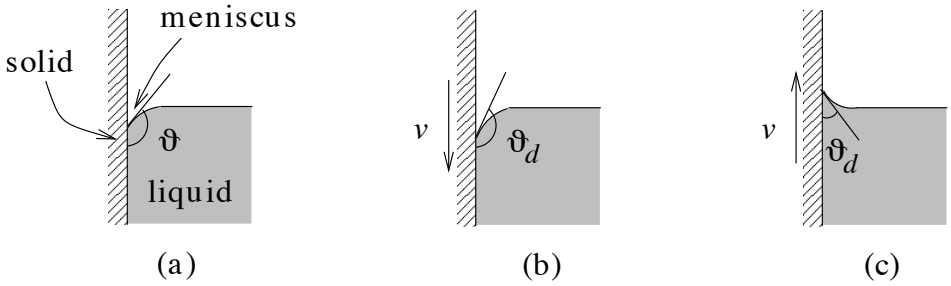

Figure 1.9: Formation of a meniscus for a liquid in nonwetting contact with a solid surface (a) where ϑ is the static contact angle. (b) and (c) show the formation of a dynamic meniscus with dynamic contact angle $\vartheta_d \neq \vartheta$ when the solid moves vertically.

1.7 Introductory submersion experiments

As mentioned, the aim of the present work has been to reduce losses of aluminium due to dross generation upon remelting of aluminium scrap and to increase the melting rate. Based on the knowledge achieved through the above review about dross generation and submersion, and because the vortex chamber was newly installed at HRM, it was initially decided to study submersion of scrap in the vortex chamber by means of a water model and industrial experiments as well as by numerical simulations. This section is a summary of this study.

It should be mentioned that this angle of approach was later abandoned in favour of the melting of plate strips, which constitute the main part of this thesis (see Section 1.8). However, the experience from the work with the vortex chamber was part of the development work and is therefore included.

1.7.1 Numerical simulations

It was attempted to simulate the flow in the vortex chamber by means of Fluent, a commercial computer-simulation program for heat and mass flow. The flow in the vortex chamber is three dimensional because the axial symmetry is broken by in- and outlets and by an obstacle, a *baffle*, installed to deflect the inlet flow and enhance the vertical mixing in the melt. Furthermore, we have a free surface, which, together with the recirculating flow, makes the problem very complex. In fact, a convergent solution was not obtained.

1.7.2 Water-model experiments

Flow experiments with aluminium are expensive, and it is very difficult, if not impossible, to obtain quantitative information about the melt flow due to the high temperature and the opaque nature of aluminium. However, water has a

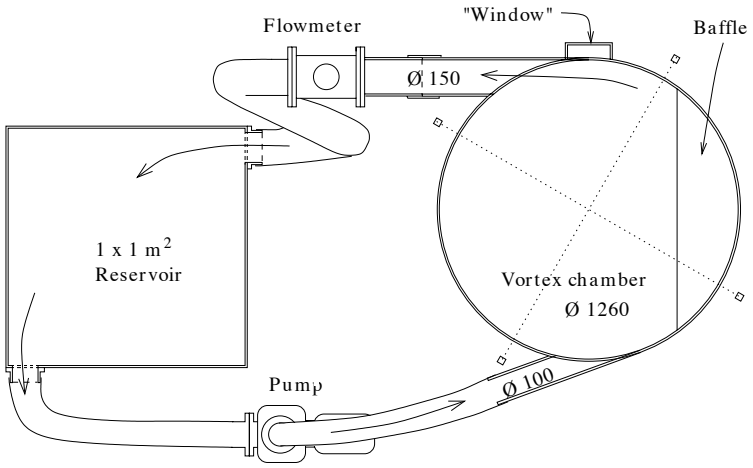

Figure 1.10: Setup of water model of vortex chamber

comparable viscosity and is frequently used to provide qualitative and quantitative information about the flow in aluminium melts. It is also much easier and less expensive to make changes to a plexiglass model than to the actual furnace (see Neff 1986).

However, it should also be noted that a water model cannot simulate the temperature effects of molten aluminium, partly because of substantially differing thermal conductance, and partly because the temperature dependence of the density is qualitatively different. Also solidification and melting phenomena can hardly be simulated.

1.7.2.1 Experimental setup

The setup of the water model is shown in Figure 1.10. The model of the vortex chamber itself was constructed from an existing plexiglass cylinder with 1.26 m diameter. This is 90 % of the diameter of the actual vortex chamber at HRM, so the whole model is scaled down correspondingly. The baffle is modelled by a sloping plate which can be taken out of the model. Three inlets at different heights were installed to make possible the study of a high inlet and a low outlet. However, only the lower one was used. Photographs and videofilms were taken through a *window* on the wall of the plexiglass tank. The window is a transparent pocket filled with water and placed on the outside of a curved plexiglass wall in order to minimize refraction of light. Detailed drawings of the model are found in Appendix A.1.

Apart from the vortex-chamber model itself, the apparatus consists of a cubic reservoir tank of plexiglass from which water is pumped with an electric water

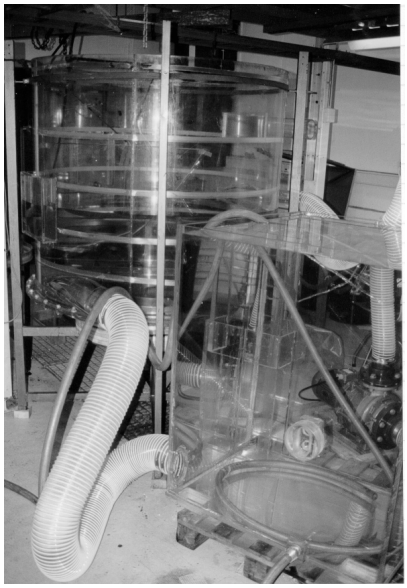

Figure 1.11: Photograph of the water model of the vortex chamber. The cubic container in the front is the reservoir while the vortex chamber is in the background. The flowmeter was not installed when the picture was taken.

pump (EDUR-Pumpenfabrik, Germany, Model NUBL700 M170) into the vortex chamber. The pump velocity was controlled by a frequency converter, and the maximum flow rate against a three-metre water column is 2.5 m^3/min or 5.3 m/s water velocity through the 10 cm inlet into the vortex chamber. The water then flows back into the reservoir through a turbine flowmeter (Zenner WPI-I Woltmann) which has less than 0.1 bar pressure loss and was calibrated to about $\pm 2\,\%$ accuracy. The flowmeter was connected via a PVC tube to the end of the outlet pipe. This provided a straight pipe before the flowmeter of about three times the diameter of the pipe, as required to get correct readings. A mosquito net was attached across the outlet opening in order to prevent that particles go into the flowmeter turbine. Figure 1.11 shows a photograph of the water model.

1.7.2.2 Submersion experiments and results

With the water model just presented, it was possible to change a number of parameters such as the baffle geometry, inlet height, flow velocity, and liquid level in the tank. Additionally, small particles of various density and size could be added in order to study the submersion efficiency for various sets of parameters.

Preliminary experiments were performed with addition of a handful of small, cylindrical plastic *beads*, about 5 mm in diameter and height, and with density

about 85 % of that of water. They were dropped from the same height, about 50 cm above the water surface, at two places: in the centre and 10 cm from the wall over the baffle (whether present or not). The addition experiments were recorded on video tape and the time for *most* of the beads to get submerged (*the submersion time*), was taken. The particles did not resurface once they were submerged. This criterium was used consequently by the same observer, but an uncertainty of plus/minus a couple of seconds should be considered, especially for the longest submersion times. Furthermore, in this preliminary experiment, each set of parameters was used only once.

The water level was fixed to a level about 62 cm above the bottom plate, i.e. just above the top of the baffle. The flow rate was changed between 1.0, 1.3, and 1.7 m^3/min, which corresponds to 2.6–4.4 tonnes of aluminium melt per minute. Also, the experiments were performed with and without the baffle plate.

The results are shown in Table 1.1. Despite the large uncertainties, we can see that an increased flow rate decreased the submersion time, i.e. increased the submersion *rate*. The presence of the baffle reduced the submersion time to about the half. The submersion was more efficient at the wall than in the centre, and the beads were first pulled out towards the wall before they were submerged, especially at low flow rates. By increasing the flow rate, the submersion in the centre increased. The mechanism submerging the floating beads seemed to be turbulent mixing in the surface. The baffle created violent waves at high flow rate as the inlet flow was deflected up to the surface and carried beads with it as it plunged down into the bulk liquid again.

One would thus expect that the violent mixing in the melt surface due to the baffle would create increased dross formation in the corresponding molten-aluminium system.

Table 1.1: The time (in seconds) to submerge beads dropped at the wall over the baffle and at the centre with and without a baffle

Submersion time [s]				
Flow rate [m^3/min]		1.0	1.3	1.7
Baffle	At wall	2	1	0
	Centre	6	3	1
No baffle	At wall	9	3	1
	Centre	12	6	4

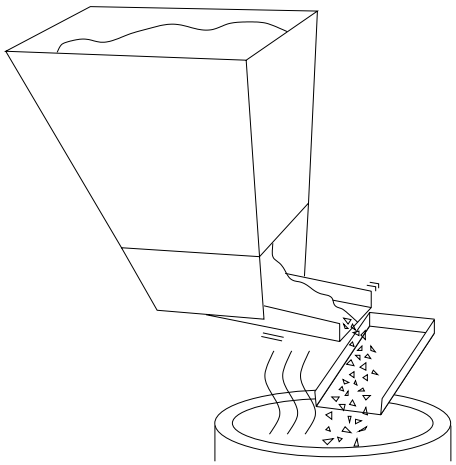

Figure 1.12: Temporary industrial setup for changing of swarf into the actual vortex chamber

1.7.3 Industrial melt experiments

In order to validate the water-model results, an industrial experiment was performed at HRM (see Section 1.1.5) where swarf was sprinkle-charged into a revolving bath of molten aluminium in the vortex chamber (Farner 1998).

1.7.3.1 Experimental setup and procedure

Two types of aluminium swarf (AA3105 alloy) were used in the experiment: milling swarf (about 1 mm thick, 1–2 cm long pieces) and sawing swarf (about 0.1 mm thick, but many centimetres long pieces). The density of the swarf was estimated to be of the order of 500 kg/m^3, and it was charged into a funnel-shaped container, which took about 1.5–2 tonnes of swarf. A vibration feeder (Skako as, Denmark) was attached under the container, and the vibration intensity could be adjusted to vary the feeding rate of swarf. The swarf was thus shaken out and sprinkled into the melt. The feeding apparatus was lifted up over the vortex chamber with a lift truck and had to be taken down to be refilled. The setup is shown in Figure 1.12.

Three cycles of charging and tapping of the furnace took place during the 10-hour experiment. A total of 10 large ingots of four tonnes each, a couple at a time, were charged into the main furnace (MHC; see Section 1.1.5) during the experiment to ensure high productivity. The ingots were preheated for one to two hours on the platform inside the furnace before they were pushed into the bath.

During each cycle, about 20 tonnes of swarf (about 40 %) and ingots (60 %)

were charged. The container was taken down and refilled with swarf between each run, and a total of 18 runs were performed. Even though the ingots were partly melted away when they were pushed into the bath, a subsequent drop in temperature was observed, and three runs had to be discarded due to this. The mean charging rate for each run was calculated by dividing the weight of swarf by the time it took to empty the container.

The temperature was logged continuously in the vortex chamber and in the MHC during the experiments, and the gas consumption was read from a flowmeter about four times an hour. It was concluded that the gas consumption was fairly constant. The electromagnetic pump was operated at full power. No attempts were made to measure the flow rate, but the pump characteristics from the supplier indicate a flow rate between 6 and 10 tonnes of molten aluminium per minute (about 2.5–4 m^3/min).

1.7.3.2 Submersion results

Before an experimental run was started, there was no swarf left on the melt surface, but shortly after starting sprinkle-feeding, a pile of swarf started to build up on the melt surface. Soon, a lid of swarf covered the melt surface except a couple of square decimetres where the melt flow was turned up to the surface by the baffle. This is sketched in Figure 1.13a. The vibration intensity was maximized without overloading the vortex chamber. The melt level was judged to barely cover the baffle while the deflected flow went about a decimetre above this. See the photograph in Figure 1.13b.

The pile was observed continuously during the experiment, and two melting mechanisms were proposed: Firstly, the pile was sinking slowly into the melt, indicating melting from below. The fact that the pile floated, was attributed to *shell formation* (see Section 1.5): The melt starts to flow in between the swarf pieces, but heat is extracted from the melt to heat the swarf, and the melt solidifies to a shell along the bottom of the pile. The shell temporarily inhibits the melt from flowing further into the cavities of the pile of swarf, and the bulk density remains small. The heat transfer between the individual pieces is low due to their minimal contact area. The bulk thus remains cold, and when a part of the shell melts away, new melt enters and solidifies as it touches the relatively cold pieces of swarf inside. Thus, the pile melts gradually from below and sinks slowly into the melt.

The second melting mechanism was due to the baffle. The deflected flow continuously tore off and submerged small pieces of swarf from the lid while swarf kept flowing down from the pile and maintained the lid.

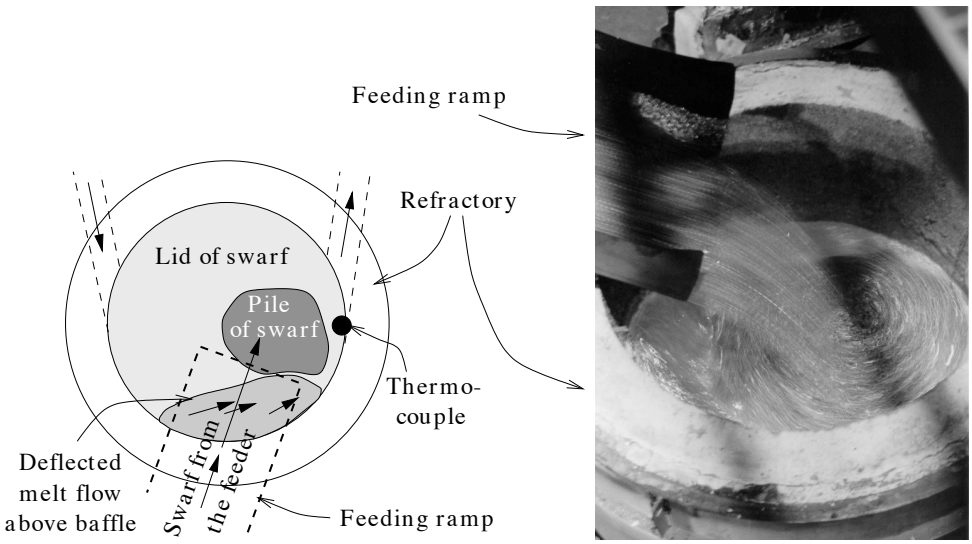

Figure 1.13: The vortex chamber during melting: (a) sketch from the top, and (b) photograph with swarf flowing down the feeding ramp.

Based on the temperature variation, it was possible to relate the average charging rate for each run with the corresponding temperature decrease. This is summarized for the 15 successful runs in Figure 1.14. For the same charging rate, the temperature obviously fell more rapidly in the vortex chamber than in the main bath of molten aluminium, as expected because the cold swarf was added in the vortex chamber. Higher charging rates gave larger temperature decrease. The curve fits intercept the line of no temperature change at about 3 or 4 tonnes/h, indicating that this is the melting capacity of the vortex chamber.

During the 10-hour experiment and charging of about 26 tonnes of swarf and about 40 tonnes of ingots, the dross generation was negligible compared to normal operation. Unfortunately, no quantitative data were obtained. The absence of dross generation should partly be attributed to the fact that the swarf was not lacquered and that large ingots create very little dross. However, the charging method itself was also believed to reduce the dross generation.

1.7.4 Discussion

The preliminary water-model experiments were inexpensive and fairly simple to perform compared to the experiments in the industrial vortex chamber. The difference in material properties between the water and molten-aluminium systems can partly be compensated by dimensional analysis (see f.ex. White 1994, Ch. 5). All physical parameters such as viscosity and chamber diameter, for instance,

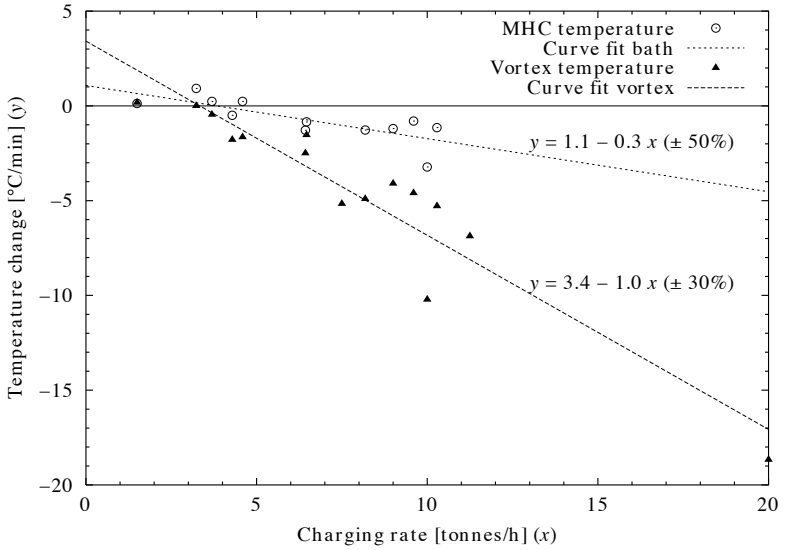

Figure 1.14: Temperature change in the vortex chamber and in the MHC during a single run due to charging of swarf

can be grouped to form new quantities, mostly as dimensionless numbers. As long as these numbers are equal in the two systems, the systems are directly comparable.

The basic dimensionless group for liquid flow is the Reynolds number, $Re = vD/\nu$, where v is the typical flow velocity, for example at the inlet, D is the diameter of the inlet tube, and ν is the kinematic viscosity. For water at 10°C, $\nu \approx 1.3 \times 10^{-6}\mathrm{m/s^2}$ (varying substantially with temperature; Lide 1997, p. 6-3), and for aluminium at 700°C it is about $0.5 \times 10^{-6}\mathrm{m/s^2}$ (Brandes and Brook 1992, p. 14-7). For equal dimensions and flow velocities, Re for water is thus less than a half of that for molten aluminium. We could compensate for this by increasing the diameter of the water model or the flow velocity by about 2.5 times, heavily depending on the water temperature.

However, since $Re \sim 5 \times 10^5$, the flow is highly turbulent. Then flow patterns change little with Re. Instead, we can concentrate on another dimensionless number, the Froude number $Fr = v^2/gh$, where g is the gravitional acceleration, and h is the depth of the liquid. This is an important number for free-surface flow. It is independent of material, so a real-size water model should give the same surface effects if we neglect differences in surface tension and effects due to surface oxide.

As mentioned, the experimental dimensions were scaled down 10 % in order to use the already available cylinder, but the value of the Froude number is retained if the flow rate is reduced by about 5 %. The flow rates used in the

water-model experiments were much lower than those assumed for the actual vortex chamber (estimated from the pump characteristics). However, the waves due to the deflected flow were more violent in the water-model. This suggests that the actual flow rate is lower than the characteristics of the electromagnetic pump indicate.

Now, although the water flow in the plexiglass tank did show a qualitative resemblance with the melt flow at HRM and thus gave valuable information about the flow patterns in the vortex chamber, the submersion mechanisms were very different in the two cases. In the water model, we found that the individual beads were pulled down by surface mixing. In the melt system, the swarf formed clusters that eventually formed a floating lid that covered the melt surface and slowly melted from the bottom while the deflected melt flow tore loose and submerged swarf from the lid.

The shell formation is not present in a water system unless the pieces added to the water are frozen far below 0°C. And even then the relevance of such experiments would be small because the thermal conductivity, for instance, is much larger for liquid aluminium than that of water. Although dimensional analysis makes us able to compare water flow with melt flow, problems occur when we have to adjust several dimensionless groups at the same time. The Prandtl number involves the viscosity and the thermal conductivity. It is a material-specific number that is several orders of magnitude greater for water than for molten aluminium. This indicates that water is inappropriate to simulate heat-transport and solidification and melting phenomena in aluminium melts.

Thus, the most important conclusions of these experiments are that:

- the water model can be used to simulate submersion of particles in a melt as well as provide estimates for the time it takes to submerge the particle and whether they will resurface, and
- the water model cannot be used to simulate melting and solidification behaviour of a metal.

1.8 Summary and comments

In the introductory sections, we have seen that the problem of reducing dross generation is complex. It is important to prevent oxidation of the scrap to avoid entrapment of metallic aluminium in oxide films. Rapid submersion seems to be the most efficient way to achieve this. The search for a way to reduce dross generation was initiated by attempting to study submersion by stirring

the melt. The introductory experiments demonstrated the limitations of using water models to simulate a system where melting and solidification occur.

Interest was thus directed towards the melting mechanisms of aluminium scrap when immersed in molten aluminium. The work was restricted to studying the simplified system where an aluminium plate is fed at steady state into the melt.

This concept can be applied directly in an industrial process by rolling scrap to a strip and feeding it directly into the melt. The melt may be stirred, for instance in a vortex chamber, to enhance heat transfer, and the scrap may be preheated and delacquered continuously at some stage in the process. The benefits are rapid submersion of light-gauge scrap and probably also a simplified and more efficient melting operation.

Chapter 2 contains a mathematical study of the simplified system while melting experiments with aluminium are described in Chapter 3. The results are presented in Chapter 4 and discussed in Chapter 5. The conclusions follow in Chapter 6.

Chapter 2

Mathematical models for feeding of a plate into a melt

We have seen that rapid melting of scrap is inhibited by several mechanisms when it is charged directly into a melt. Apart from floating, the melting rate is decreased by oxide and gas films, and possibly also by melt solidifying on the added object.

The physics of adding randomly shaped scrap pieces into a melt is very complicated. To be able to examine such systems, we have resorted in studying continuous feeding of a thin metal plate into the melt. Mathematical models attempting to describe this simplified system are developed in this chapter.

But before starting to model, it is very important to remember that "there is no statistical universe of models from which the parameters are drawn. There is just one model, the correct one, and a statistical universe of data sets that are drawn from it!" (Press et al. 1992, Sec. 15.1). Thus, the data sets obtained by measurements are realizations offered by Mother Nature while we, by means of our model, try to describe nature and predict her behaviour.

2.1 Continuous feeding of a plate into a melt

A metal plate ideally extending infinitely far upwards is fed vertically into a molten-metal bath at a steady velocity v as shown in Figure 2.1. After a transient period, the system reaches a steady state. At the *penetration point*, i.e. where the plate penetrates the melt surface, the surface curves down and forms a *meniscus*. From this area and below, heat flows from the melt into the cold plate. If the

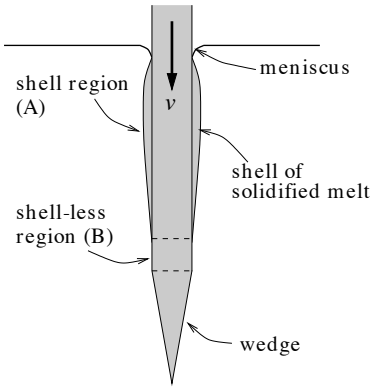

Figure 2.1: Continuous feeding of a metal plate into its own melt

supply of heat from the melt is lower than the heat flow into the plate, the melt closest to the plate solidifies and forms a *shell* on the plate. This is normally the case, but a criterion will be presented in Section 2.10. As the plate moves downwards into the melt, the temperature in the plate increases, and the shell grows until the heat flows into and out of the shell balance each other. From this point on, the shell melts back and finally vanishes. Heat now flows directly from the melt into the plate, and after a distance the plate reaches its melting point and starts to melt. This final region is modelled as a *wedge*.

2.2 The mathematical quantities

Figure 2.2 shows the co-ordinates, dimensions, and some other quantities representative of all models presented. The heat-balance equations and boundary conditions will be presented for each model. Dimensionless quantities will, in general, be used for simplicity and for generality. All quantities are summarized in a separate *List of symbols* at the beginning of this thesis.

The co-ordinate system has its origin in the centre of the thickness of the plate, on a level with the melt surface. The y axis points downwards while the x axis points horizontally out of the plate. The plate has width B (into the paper) and thickness $b \ll B$. It continues infinitely upwards but penetrates a finite distance P (*the penetration depth*) down into the melt. The shell region ends at P_{A} and the shell-less region at P_{B}. The temperature of the ambient air is T_a, which is also the temperature of the plate far above the melt. T_l is the temperature of the melt far from the plate, i.e. in the *bulk melt*. T_m is the melting point of the melt and the plate as we will assume that both are of the same alloy. The melting range will be discussed later. $T_p = T_p(y)$ and $T_s = T_s(y)$ denote the temperature of the plate and the shell, respectively, as functions of y.

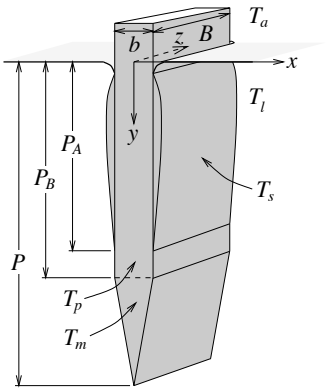

Figure 2.2: Three-dimensional sketch of the plate that is fed into the melt with dimensions and temperatures

Four different dimensionless numbers will be used: Bi, Nu, Pe, and Sf. The *Biot number*, defined as

$$Bi = \frac{h_g b}{k}, \tag{2.1}$$

is the ratio of heat transfer through the gap between the shell and the plate to the heat conduction across the plate thickness. b is the thickness of the plate while k is its thermal conductivity. The heat-transfer coefficient h is defined by Newton's Law of Cooling, $q = h\Delta T$ (see Section 1.4). The Biot number is in effect a dimensionless version of the heat-transfer coefficient h_g. A Biot number much less than unity means that the dominating heat-transfer barrier is the gap and not the plate.

The complex heat-transfer nature of liquid-flow boundary layers can also be described in terms of a heat-transfer coefficient, here denoted h_l (l for liquid). The corresponding dimensionless number is usually the *Nusselt number*, defined as

$$Nu = \frac{h_l b}{k}, \tag{2.2}$$

which may be understood as a ratio of the heat transfer through the boundary layer between the bulk melt and the plate to the heat conduction across the plate thickness. The Nusselt number for the boundary layer between the air above the melt and the plate will be denoted $Nu_a = h_a b/k$. If the Nusselt number is much less than unity, the boundary layer is the important heat-transfer resistance.

The dimensionless version of the feeding velocity v is the *Péclet number*:

$$Pe = \frac{\rho c v b}{k}, \tag{2.3}$$

where ρ is the density of the solid plate and c its specific heat. The Péclet number is here the ratio of heat transport with the moving plate to heat conduction

across it. For a value of one, the heat transferred due to the motion of the plate is comparable to the heat conducted across it.

The last dimensionless number is the ratio between sensible and latent heat, called the *Stefan number* after Josef Stefan, who worked with free- and moving-boundary problems already at the end of the 19th century. For convenience, we will use the *inverse* Stefan number, defined here as

$$Sf = \frac{L}{c\,(T_m - T_a)}. \tag{2.4}$$

This inverse Stefan number is the ratio between the latent heat L of melting and the sensible heat of heating the plate from the ambient temperature T_a to the melting point T_m.

In addition, dimensionless co-ordinates are introduced: $\xi = x/b$, $\eta = y/b$, and $\zeta = z/b$, the dimensionless penetration depth $\Pi = P/b$, and the dimensionless temperature $\theta = (T - T_a)/(T_m - T_a)$. The melting point thus becomes $\theta_m = 1$ and the ambient temperature $\theta_a = 0$.

2.3 General assumptions

In order to derive models that can be treated analytically, a few basic assumptions have been made. Additional assumptions will be introduced when necessary.

1. The material properties are constant,
2. there is a well-defined melting point T_m, i.e. liquidus and solidus curves coincide,
3. the plate and the melt are of the same material and thus have the same melting point T_m,
4. the heat-transfer coefficients (h_g and h_l) are constant along the plate,
5. h_l from the bulk melt also accounts for the sensible heat released from the melt before solidification,
6. the liquid heat-transfer coefficient (h_l) from the melt is the same whether the heat flows to the shell or directly to the plate,
7. the shell is considered to be “thin” and to have a constant temperature equal to its melting point T_m,

8. the temperature in the plate at the penetration point ($y = 0$) is constant and equal to T_a, and

9. a steady state is reached except in the transient model.

2.4 Model 1: Main model with shell formation

The main model is a one-dimensional steady-state model consisting of three regions and a shell as shown in Figure 2.3. Four connected heat equations can be established: one equation for each of the two *Regions A and B* of the plate, one for the *shell* formed outside Region A, and the last for the *wedge*. In addition to the assumptions of Sections 2.3, two more assumptions are necessary:

10. The thickness of the plate is so small that the isotherms inside the plate can be assumed to be horizontal, and

11. the plate ends in a wedge with constant temperature equal to the melting point.

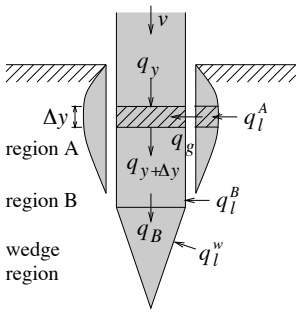

Figure 2.3: The heat flow in a cross section of the plate according to Model 1

2.4.1 Region A

In Region A of the plate, the heat balance of a horizontal cross section of thickness Δy of the plate (see Figure 2.3) is governed by vertical conductive and convective heat flow along the plate,

$$q_y = -k\frac{\partial T_p}{\partial y}(y) + \rho c v T_p(y) \tag{2.5}$$

and heat transfer from the shell through a thin *gap* with heat-transfer resistance inversely proportional to h_g. The heat flow over the gap is expressed by Newton's Law of Cooling:

$$q_g = h_g(T_m - T_p(y)), \qquad 0 \le y < P_{\mathrm{A}}. \tag{2.6}$$

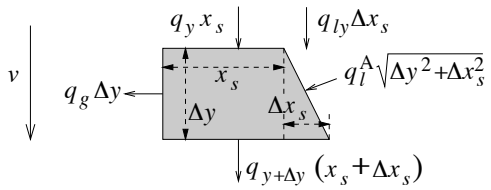

Figure 2.4: The heat balance of a section of the solidified shell.

While the plate temperature T_p depends on y, the shell temperature is constant and at the melting point T_m. P_{A} is the penetration depth of Region A.

The resulting heat balance for the cross section is thus

$$-\Delta\left(-kb\frac{dT_p}{dy}+\rho cvbT_p\right)+2h_g(T_m-T_p)\Delta y=0. \tag{2.7}$$

Divide this by Δy, let Δy approach zero, and introduce dimensionless quantities (see Section 2.2), and we obtain the temperature profile along the plate, with primes denoting differentiation with respect to η:

$$\theta_p''-Pe\,\theta_p'-2Bi\,(\theta_p-1)=0, \qquad 0\le\eta<\Pi_{\mathrm{A}}. \tag{2.8}$$

The general solution is

$$\theta_p^{\mathrm{A}}(\eta)=1+Ae^{\lambda_1\eta}+Be^{-\lambda_2\eta}, \qquad 0\le\eta<\Pi_{\mathrm{A}}, \tag{2.9}$$

where

$$\begin{aligned}\lambda_1&=\tfrac{1}{2}Pe\left(\sqrt{1+\tfrac{8Bi}{Pe^2}}+1\right),\\ \lambda_2&=\tfrac{1}{2}Pe\left(\sqrt{1+\tfrac{8Bi}{Pe^2}}-1\right).\end{aligned} \tag{2.10}$$

The constants A and B will be determined from boundary conditions. The superscript A in Equation (2.9) means Region A and is included to avoid confusion.

2.4.2 The shell

The heat balance for a cross section of the shell is reduced to a one-dimensional problem of the shell thickness due to Assumption 7 of constant shell temperature. Figure 2.4 gives an overview of the heat-flux terms that must balance each other:

$$q_l^{\mathrm{A}}=h_l\,(T_l-T_m), \tag{2.11}$$
$$q_g=h_g\,(T_m-T_p), \tag{2.12}$$
$$q_y=\rho cvT_m, \tag{2.13}$$
$$q_{ly}=\rho cvT_m+\rho vL. \tag{2.14}$$

Thermal conductivities do not enter the expressions because the shell temperature is taken to be constant and equal to the melting point. The specific heat of liquid and solid aluminium differs insignificantly (less than two percent), so only c is used in Equation (2.14). Furthermore, we consequently use the *solid* density ρ in the heat balances since expansion and shrinkage due to melting and solidification do not affect the heat balance, only the convection in the liquid. Due to Assumption 5 that the sensible heat of the melt can be accounted for by the heat-transfer coefficient, T_l does not occur in q_{ly}. The heat balance becomes

$$q_{ly}\Delta x_s + q_y x_s - q_{y+\Delta y}(x_s + \Delta x_s) + q_l^{\mathrm{A}}\sqrt{\Delta x_s^2 + \Delta y^2} - q_g \Delta y = 0,$$

or, after dividing by Δy and letting it approach zero:

$$\rho v L \frac{dx_s}{dy} + q_l^{\mathrm{A}}\sqrt{1 + \left(\frac{dx_s}{dy}\right)^2} - q_g = 0. \tag{2.15}$$

The square root appears because the outer surface of the shell curves and thereby slightly increases the surface area through which the heat flows from the melt.

Equation (2.15) is easily solved with respect to dx_s/dy, and the sign of the resulting square root is chosen such that $q_g = q_l^{\mathrm{A}}$ when $dx_s/dy = 0$. We rewrite it in dimensionless quantities:

$$\frac{d\xi_s}{d\eta} = \frac{Bi\,(1-\theta_p)}{Pe\,Sf}\left(\frac{1 - \sqrt{1 + \left[1 - \left(\frac{Nu\,(\theta_l - 1)}{Pe\,Sf}\right)^2\right]\left[\left(\frac{Nu\,(\theta_l-1)}{Bi\,(1-\theta_p)}\right)^2 - 1\right]}}{1 - \left(\frac{Nu\,(\theta_l-1)}{Pe\,Sf}\right)^2}\right). \tag{2.16}$$

If no approximations are introduced, this equation must be solved by numerical integration. A convenient and accurate approximation is presented in Appendix C.1.

Notice that $q_g = q_l^{\mathrm{A}}$ is identical to $Bi\,(1-\theta_p) = Nu\,(\theta_l - 1)$ and that $\xi_s(\eta) = 0$ defines the length Π_{A} of Region A.

2.4.3 Region B

There is no shell in Region B, so heat flows directly from the bulk melt to the plate with the thermal boundary layer as the only thermal resistance:

$$q_l^{\mathrm{B}} = h_l(T_l - T_p(y)), \qquad P_{\mathrm{A}} \le y < P_{\mathrm{B}}, \tag{2.17}$$

where h_l is the heat-transfer coefficient through the boundary layer of the liquid metal, and T_l is the temperature in the bulk melt. P_B is the penetration depth of Region B. With dimensionless quantities we get

$$\theta_p'' - Pe\,\theta_p' - 2Nu\,(\theta_p - \theta_l) = 0, \qquad \Pi_\mathrm{A} \le \eta < \Pi_\mathrm{B}. \tag{2.18}$$

This equation is very similar to Equation (2.8) except that now the temperature θ_l of the melt enters, and Nu replaces Bi. The general solution is thus

$$\theta_p^\mathrm{B}(\eta) = \theta_l + A' e^{\lambda_1' \eta} + B' e^{-\lambda_2' \eta}, \qquad \Pi_\mathrm{A} \le \eta < \Pi_\mathrm{B}, \tag{2.19}$$

where

$$\begin{aligned} \lambda_1' &= \tfrac{1}{2} Pe \left(\sqrt{1 + \tfrac{8Nu}{Pe^2}} + 1 \right), \\ \lambda_2' &= \tfrac{1}{2} Pe \left(\sqrt{1 + \tfrac{8Nu}{Pe^2}} - 1 \right). \end{aligned} \tag{2.20}$$

The constants A' and B' are to be determined by the boundary conditions.

2.4.4 The wedge region

Finally, the heat flowing into the wedge from the melt must balance the latent heat of melting of the plate material transported into the wedge region and the heat conduction $q_\mathrm{B} = -k\,dT_p/dy$ between Region B and the wedge. As a consequence of a constant wedge temperature, there are no heat gradients in the wedge, and in principle we cannot allow any heat conduction through the wedge or out of it. We therefore set $q_\mathrm{B} = 0$, and obtain the steady-state heat balance for the wedge:

$$q_l^w \sqrt{1 + \left(\frac{2(P - P_\mathrm{B})}{b} \right)^2} = \rho v L, \tag{2.21}$$

where $P - P_\mathrm{B}$ is the vertical length of the wedge (see Figure 2.2) and $q_l^w = h_l(T_l - T_m)$. Solving for $P - P_\mathrm{B}$ and applying dimensionless quantities, we get

$$\Pi - \Pi_\mathrm{B} = \frac{1}{2} \sqrt{\left(\frac{Pe\,Sf}{Nu(\theta_l - 1)} \right)^2 - 1}. \tag{2.22}$$

2.4.5 Combined solution

We now have four unknown constants A, B, A', and B' in Equation (2.9) and (2.19), and two lengths Π_A and Π_B which must be determined.

The dimensionless penetration depth Π_A of the shell is determined by integrating Equation (2.16) numerically and finding the solution of $\xi_s = 0$ for $\eta > 0$ or using the approximation presented in Appendix C.1. Notice that if $d\xi_s/d\eta \leq 0$ at $\eta = 0$, there is no shell growth and $\Pi_\mathrm{A} = 0$.

The remaining constants are determined with the aid of five boundary conditions. Four of them demand continuous temperature and derivative of the temperature between the regions A and B and the wedge:

$$\theta_p^\mathrm{A}(\eta) = 0 \qquad \eta = 0, \tag{2.23}$$
$$\theta_p^\mathrm{A}(\eta) = \theta_p^\mathrm{B}(\eta) \qquad \eta = \Pi_\mathrm{A}, \tag{2.24}$$
$$\theta_p^{\mathrm{A}\prime}(\eta) = \theta_p^{\mathrm{B}\prime}(\eta) \qquad \eta = \Pi_\mathrm{A}, \tag{2.25}$$
$$\theta_p^\mathrm{B}(\eta) = 1 \qquad \eta = \Pi_\mathrm{B}, \tag{2.26}$$
$$\theta_p^{\mathrm{B}\prime}(\eta) = 0 \qquad \eta = \Pi_\mathrm{B}. \tag{2.27}$$

The constants A' and B' may be eliminated by starting with boundary conditions (2.26) and (2.27) to give

$$A' = -\frac{\lambda_2'}{\lambda_1' + \lambda_2'} (\theta_l - 1)\, e^{-\lambda_1' \Pi_\mathrm{B}}, \tag{2.28}$$
$$B' = -\frac{\lambda_1'}{\lambda_1' + \lambda_2'} (\theta_l - 1)\, e^{\lambda_2' \Pi_\mathrm{B}}. \tag{2.29}$$

and the temperature profile in Region B ($\Pi_\mathrm{A} \leq \eta < \Pi_\mathrm{B}$) is thus

$$\boxed{\theta_p^\mathrm{B}(\eta) = \theta_l - \frac{\theta_l - 1}{\lambda_1' + \lambda_2'} \left(\lambda_2' e^{-\lambda_1'(\Pi_\mathrm{B} - \eta)} + \lambda_1' e^{\lambda_2'(\Pi_\mathrm{B} - \eta)} \right).} \tag{2.30}$$

Boundary condition (2.23) then gives

$$B = -(A + 1), \tag{2.31}$$

and A is obtained from boundary condition (2.24):

$$A = \frac{\left(\theta_l - 1 + e^{-\lambda_2 \Pi_\mathrm{A}} \right) - \dfrac{\theta_l - 1}{\lambda_1' + \lambda_2'} \left(\lambda_2' e^{-\lambda_1'(\Pi_\mathrm{B} - \Pi_\mathrm{A})} + \lambda_1' e^{\lambda_2'(\Pi_\mathrm{B} - \Pi_\mathrm{A})} \right)}{e^{\lambda_1 \Pi_\mathrm{A}} - e^{-\lambda_2 \Pi_\mathrm{A}}}. \tag{2.32}$$

The temperature profile in Region A ($0 \leq \eta < \Pi_\mathrm{A}$) becomes

$$\boxed{\theta_p^\mathrm{A}(\eta) = A \left(e^{\lambda_1 \eta} - e^{-\lambda_2 \eta} \right) + 1 - e^{-\lambda_2 \eta}.} \tag{2.33}$$

It is worth noticing that if $8Bi \ll Pe^2$, then $\lambda_1 \approx Pe$ and $\lambda_2 \approx 2Bi/Pe$, which is small. The same is the case in Region B: When $8Nu \ll Pe^2$, $\lambda_1' \approx Pe$ while $\lambda_2' \approx 2Nu/Pe$.

Application of the remaining boundary condition (2.25) gives an implicit solution for Π_B:

$$e^{\lambda_2'(\Pi_\mathrm{B}-\Pi_\mathrm{A})}\left(1+\frac{\Lambda}{\lambda_2'}\right) = e^{-\lambda_1'(\Pi_\mathrm{B}-\Pi_\mathrm{A})}\left(1-\frac{\Lambda}{\lambda_1'}\right) + \frac{\Lambda}{\Lambda'}\Theta + \frac{\lambda_2}{\Lambda'}\frac{e^{-\lambda_2\Pi_\mathrm{A}}}{\theta_l - 1}, \quad (2.34)$$

where

$$\Lambda = \frac{\lambda_1 e^{\lambda_1\Pi_\mathrm{A}} + \lambda_2 e^{-\lambda_2\Pi_\mathrm{A}}}{e^{\lambda_1\Pi_\mathrm{A}} - e^{-\lambda_2\Pi_\mathrm{A}}},$$
$$\Lambda' = \frac{\lambda_1'\lambda_2'}{\lambda_1' + \lambda_2'},$$
$$\Theta = \frac{\theta_l - 1 + e^{-\lambda_2\Pi_\mathrm{A}}}{\theta_l - 1}.$$

A convenient way to find Π_B is to solve for the Π_B on the left-hand side and to iterate the resulting equation:

$$\Pi_\mathrm{B}^{i+1} = \Pi_\mathrm{A} + \frac{1}{\lambda_2'}\ln\left[\frac{\frac{\Lambda}{\Lambda'}\Theta + \frac{\lambda_2}{\Lambda'}\frac{e^{-\lambda_2\Pi_\mathrm{A}}}{\theta_l - 1} + e^{-\lambda_1'(\Pi_\mathrm{B}^i-\Pi_\mathrm{A})}\left(1-\frac{\Lambda}{\lambda_1'}\right)}{1+\frac{\Lambda}{\lambda_2'}}\right]. \quad (2.35)$$

With $\Pi_\mathrm{B}^0 = \Pi_\mathrm{A}$ as start value, rapid convergence is achieved.

A summary of the calculation of the penetration depth is presented together with the fitting procedure in Section 3.9

2.5 Model 2: One-dimensional model without shell

A second model is derived for the case that no shell is formed, based on a single heat-transfer coefficient from the melt to the plate, as shown in Figure 2.5. The model is equivalent to Model 1 when the shell formation is absent except for the boundary condition at the melt surface. We keep the notation from Model 1 and merely skip Region A.

We need the two additional assumptions which were necessary for Model 1 (Assumptions 10 and 11 at the start of Section 2.4), but Assumptions 5, 6, and 7 in Section 2.3 are no longer necessary, and Assumption 3 can be relaxed to assuming that the melt is not allowed to solidify.

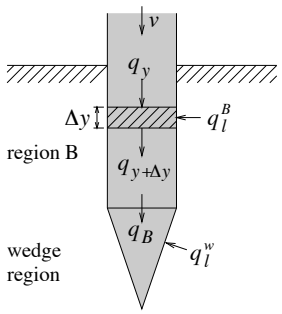

Figure 2.5: The heat flow in a cross section of the plate according to Model 2

The governing equation is taken directly from Model 1:

$$\theta_p'' - Pe\,\theta_p' - 2Nu\,(\theta_p - \theta_l) = 0, \qquad 0 \le \eta < \Pi_\mathrm{B} \tag{2.36}$$

with general solution

$$\theta_p(\eta) = \theta_l + Ae^{\lambda_1\eta} + Be^{-\lambda_2\eta}, \qquad 0 \le \eta < \Pi_\mathrm{B}, \tag{2.37}$$

where λ_1 and λ_2 are the same as the primed versions in Equation (2.20). The boundary conditions are similar:

$$\theta_p(\eta) = 0 \qquad \eta = 0, \tag{2.38}$$
$$\theta_p(\eta) = 1 \qquad \eta = \Pi_\mathrm{B}, \tag{2.39}$$
$$\theta_p'(\eta) = 0 \qquad \eta = \Pi_\mathrm{B}. \tag{2.40}$$

Boundary condition (2.38) gives $B = -(A+\theta_l)$, and a combination with boundary condition (2.39) gives

$$A = \frac{1 + \theta_l e^{-\lambda_2\Pi_\mathrm{B}}}{e^{\lambda_1\Pi_\mathrm{B}} - e^{-\lambda_2\Pi_\mathrm{B}}}, \tag{2.41}$$

$$B = -\frac{1 + \theta_l e^{\lambda_1\Pi_\mathrm{B}}}{e^{\lambda_1\Pi_\mathrm{B}} - e^{-\lambda_2\Pi_\mathrm{B}}}. \tag{2.42}$$

Now, Π_B is given implicitly by utilizing boundary condition (2.40), just as in Model 1. However, implicit functions are cumbersome to use. Noticing that $e^{-\lambda_2\Pi_\mathrm{B}} \ll e^{\lambda_1\Pi_\mathrm{B}}$, we find that $A \ll B$. We can thus simplify the solution by setting $A = 0$. This makes $\theta_p'(\Pi_\mathrm{B}) = \theta_l\lambda_2 e^{-\lambda_2\Pi_\mathrm{B}}$, which is a small number, thus implying that the last boundary condition is almost satisfied. The simplified

solution is then (when simply $B = \theta_l$)

$$\theta_p(\eta) = \theta_l \left(1 - e^{-\lambda_2 \eta}\right), \tag{2.43}$$

where

$$\lambda_2 = \frac{1}{2} Pe \left(\sqrt{1 + \frac{8Nu}{Pe^2}} - 1\right). \tag{2.44}$$

Boundary condition (2.39) now gives an expression for Π_{B}:

$$\Pi_{\mathrm{B}} = \frac{1}{\lambda_2} \ln \frac{1}{\theta_l - 1}. \tag{2.45}$$

This is combined with Equation (2.22), and we obtain an expression for the total penetration depth when the shell is absent:

$$\Pi = \frac{1}{\lambda_2} \ln \left(\frac{1}{\theta_l - 1}\right) + \frac{1}{2} \sqrt{\left(\frac{Pe\, Sf}{Nu(\theta_l - 1)}\right)^2 - 1}. \tag{2.46}$$

2.6 Model 3: Model without gap between shell and plate

A third model neglects the thermal resistance in the gap in Model 1 between the shell and the plate. This is not accomplished merely by setting Bi to infinity, because we cannot assume that the shell stays near the melting point. Only the interface between the shell and the melt is at the melting point while the temperature inside the plate increases as the plate slides down in the melt. A complete study of this probably demands a non-analytic two-dimensional model. However, we can derive a relation between the penetration depth P and the total heat-transfer coefficient h_l from the melt to the shell by a simple heat balance, as illustrated in Figure 2.6:

$$\Delta H_{\mathrm{out}} B b v \Delta t = 2 q_l B P \Delta t + \Delta H_{\mathrm{in}} B b v \Delta t, \tag{2.47}$$

where ΔH is the enthalpy per unit volume of the plate, $\Delta H_{\mathrm{in}} = \rho c T_a$, $\Delta H_{\mathrm{out}} = \rho c T_m + \rho L$, and $q_l = h_l(T_l - T_m)$. The plate width B and the arbitrary time interval Δt cancel in all terms. This results in a relation for P:

$$P = \frac{\rho v b \Big(c(T_m - T_a) + L\Big)}{2 h_l (T_l - T_m)} \tag{2.48}$$

or

$$\Pi = \frac{Pe(1 + Sf)}{2Nu(\theta_l - 1)} \tag{2.49}$$

in dimensionless quantities.

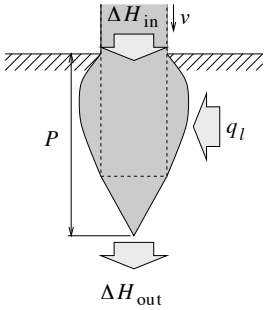

Figure 2.6: The heat balance of a continuously fed plate according to Model 3

2.7 Heating of the plate above the melt sufrace

Till now we have concentrated on the part of the plate that is below the melt surface. But also the part above the melt surface may be heated by the melt. Two mechanisms will be treated in the following: radiation from the melt and conduction up through the plate.

2.7.1 Heat radiation from the melt

All bodies radiate energy to some degree, partly reflecting incident radiation and partly emitting radiation due to atomic movement. And they absorb the part of the incident radiation that is not reflected (or transmitted). When a body and its surface have the same temperature, the incident energy must be equal to the emanating energy, so absorption must be equal to emission (Kirchhoff's Law; Bird et al. 1960, Ch. 14). The ability of a material surface to absorb, emit, and reflect radiation is expressed by the *absorptivity* a, *emissivity* e, and *reflectivity* r, all being fractions of the total incident radiation. We thus have $a = e$ and $r + a = r + e = 1$. They depend on the temperature of the surface, the wavelength of the radiation, and the angle of incidence as well as the surface material and condition. A black body is a fictive body which absorbs all incident radiation ($a = 1$) and thus does not reflect at all ($r = 0$).

We will now make an estimate for how much the radiation from the melt affects the temperature of the plate before it enters the melt. For simplicity, we shall not consider the dependence of wavelength, but instead use the *total* absorptivity, emissivity, and reflectivity. For a start we will assume that both the plate and the melt are black bodies and that the surface of the melt bath is a square with sides 50 cm and the plate a rectangle with width 10 cm and height 30 cm penetrating at the centre of the square, as shown in Figure 2.7a.

Now, the Stefan-Boltzmann Law states that the emitted energy from a black

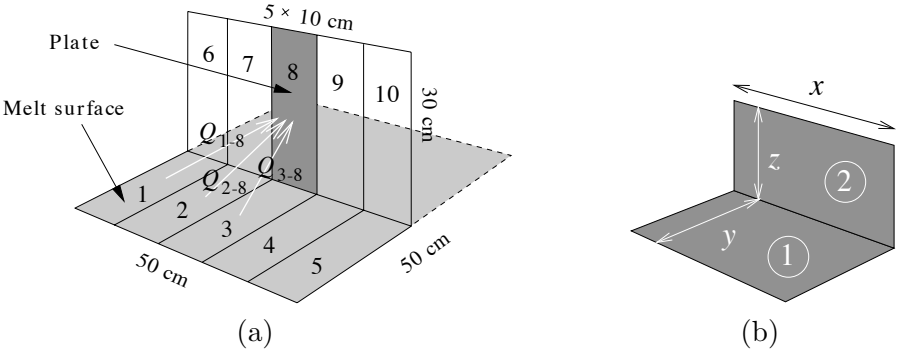

Figure 2.7: (a) Rectangle simplification of the plate being fed into the melt, and (b) two perpendicular rectangles between which the radiation view factor F_{12} is given by Bird et al. 1960, Fig. 14.4-3

body (for which reflection is zero and thus $e = 1$) is

$$q_b = \sigma T^4, \tag{2.50}$$

where the index b refers to black body, and $\sigma = 56.7 \times 10^{-9}\,\mathrm{W/m^2K^4}$ is the Stefan-Boltzmann Constant. Absolute temperature must be used. The dependence of the angle ϕ of incidence is expressed by Lambert's Law (Bird et al. 1960):

$$q_b(\phi) = \frac{q_b}{\pi}\cos\phi. \tag{2.51}$$

Imagine two arbitrarily shaped objects 1 and 2 with temperatures T_1 and T_2, and that energy is radiated between infinitesimal areas dA_1 and dA_2 on the two objects at incidence angles ϕ_1 and ϕ_2, respectively. Following the derivation by *Bird, Stewart, and Lightfoot* (1960, Sec. 14.4) the net radiation from object 1 to object 2 is then

$$Q_{12} = \frac{\sigma}{\pi}(T_1^4 - T_2^4)\int_{A_2}\int_{A_1}\frac{\cos\phi_1\cos\phi_2}{r_{12}}dA_1dA_2, \tag{2.52}$$

where r_{12} is the distance between the two infinitesimal areas. This result is conventionally written

$$Q_{12} = A_1F_{12}\sigma(T_1^4 - T_2^4) \tag{2.53}$$

where F_{12} is called a *view factor*. The integral is not trivial to calculate, but fortunately it is graphed in Bird et al. (1960, Fig. 14.4-3) for the radiation between two perpendicular rectangles as illustrated in Figure 2.7b. The view factor is listed in Table 2.1 together with the net heat radiation Q_{12} for $y = 30\,\mathrm{cm}$, $z = 25\,\mathrm{cm}$ (about the distance from the melt surface to the heat shield), and four interesting values of x.

Table 2.1: The viewfactor F_{12} and net heat radiation Q_{12} from 1 to 2 in Figure 2.7b for $y = 30\,\text{cm}$, $z = 25\,\text{cm}$, and four values of x. $T_1 = 25°\text{C}$ and $T_2 = 750°\text{C}$. The given values of Q_{12} correspond to the heat radiation Q_n between n adjacent rectangles in on the melt surface in Figure 2.7a and the corresponding rectangles in the plate plane.

x [cm]	10	20	30	50
F_{12}	0.14	0.19	0.23	0.26
Q_{12} [W]	220 (Q_1)	590 (Q_2)	1070 (Q_3)	2020 (Q_5)

We return to Figure 2.7a and notice the division of the melt surface into equally sized rectangles, and the same with the plane parallel to the plate. To calculate the net heat radiation to the plate from the half of the melt that "sees" the plate, we need to know the heat radiation between each of the rectangles in the melt to the plate. We will denote this by Q_{i-j} for the net heat radiation from rectangle i to j, and Q_n from n adjacent rectangles on the melt to the corresponding n rectangles in the plate plane. Q_n is listed in Table 2.1 for $n = 1$, 2, 3, and 5. The notation $Q_{ij..-kl..}$ is used between several arbitrary rectangles, i.e. Q_{12-678} means the heat radiation from rectangles 1 and 2 to rectangles 6, 7, and 8.

We want to calculate the net radiation from the melt to the plate, so we need $Q_{12345-8}$. First,

$$Q_{3-8} = Q_1. \tag{2.54}$$

To find Q_{2-8}, we note that $Q_{23-8} = Q_{23-7}$ for symmetry reasons, so that $Q_{23-78} = Q_{23-7} + Q_{23-8} = 2Q_{23-8}$ and thus $Q_{23-8} = \frac{1}{2}Q_{23-78} = \frac{1}{2}Q_2$. This gives

$$Q_{2-8} = Q_{23-8} - Q_{3-8} = \tfrac{1}{2}Q_2 - Q_1. \tag{2.55}$$

Similarly, we get

$$Q_{1-8} = \tfrac{1}{2}Q_3 - Q_2 + \tfrac{1}{2}Q_1. \tag{2.56}$$

Then, with these elements established, we see that the net black-body heat radiation from the melt to the plate is

$$\begin{aligned} Q_{b,m-p} &= 2Q_{1-8} + 2Q_{2-8} + Q_{3-8} \\ &= Q_3 - Q_2. \end{aligned} \tag{2.57}$$

Using the values in Table 2.1, $Q_2 = 590\,\text{W}$ and $Q_3 = 1070\,\text{W}$, each side of the 30 cm long plate is heated by $Q_{b,m-p} = 480\,\text{W}$, still assuming black bodies.

For aluminium, the emissivity perpendicular to the surface is measured to be about 0.038 at 100°C and 0.064 at 500°C (Brandes and Brook 1992, p. 17-10). The absorptivity of the plate at about 25°C should therefore be less, say $a_p = 0.035$. The melt, however, is heavily oxidized and will have much higher emissivity. We use data given for aluminium oxidized above 600°C which range

from 0.11 at 200°C to 0.19 at 600°C (Brandes and Brook 1992, p. 17-11). Extrapolation gives $e_m = 0.22$ at 750°C as an approximate number. The emitted energy from the melt is thus only 22 % of that of a black body, and all but 3.5 % of the incident radiation is reflected off the plate. Of course, we get some reflection between the melt, the heat shield on top of the crucible, the crucible wall, and the plate, but due to the very low absorptivity of the plate, most of this should be absorbed by the other surfaces. An estimate for the radiative heat transfer from the melt to the plate is thus $Q_{m-p} = e_m a_p Q_{b,m-p} = 3.7\,\mathrm{W}$.

At the lowest feeding velocity $v = 6.4\,\mathrm{cm/s}$, the plate moves past the 30 cm of radiation during $t = 4.7$ seconds. The plate is heated from both sides, so the temperature of the plate should increase

$$\Delta T = \frac{2Q_{m-p}t}{\rho c b A} = 0.8\,\mathrm{K} \tag{2.58}$$

before it penetrates the melt surface.[1] This number increases with increasing melt temperature, but decreases when the feeding velocity or the thickness of the plate is increased. The heating of the plate due to heat radiation can thus be ignored in the present work.

2.7.2 Heat conduction up through the plate

Heat is conducted very well in aluminium, and at least for low feeding velocities, heat conduction up through the plate from the immersed part of the plate may be important.

Figure 2.8 shows Region A of the plate as well as a portion of the plate above the melt, which we will call *Region C*. The temperature profile is exaggerated in the figure. We assume that the conditions above the melt hardly are affected by Region B and the wedge down in the melt. The govering heat equations are derived in the same way as Equation (2.8), and we get

$$\begin{aligned} &\theta_p'' - Pe\,\theta_p' - 2Nu_a\theta_p = 0, && \eta < 0, \\ &\theta_p'' - Pe\,\theta_p' - 2Bi\,(\theta_p - 1) = 0, && \eta > 0. \end{aligned} \tag{2.59}$$

The boundary conditions are

$$\theta_p^{\mathrm{C}}(\eta) = 0 \qquad \eta \to -\infty, \tag{2.60}$$

$$\theta_p^{\mathrm{A}}(\eta) = 0 \qquad \eta \to +\infty, \tag{2.61}$$

$$\theta_p^{\mathrm{A}}(\eta) = \theta_p^{\mathrm{C}}(\eta) \qquad \eta = 0, \tag{2.62}$$

$$\theta_p^{\mathrm{A}\prime}(\eta) = \theta_p^{\mathrm{C}\prime}(\eta) \qquad \eta = 0. \tag{2.63}$$

[1] We have used values for ρ and c from Table B.1, $b = 0.5\,\mathrm{mm}$, and $A = A_8 = 0.03\,\mathrm{m}^2$.

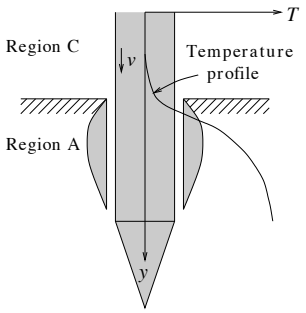

Figure 2.8: Heat conduction up through the plate above the melt surface

Boundary conditions (2.60) and (2.61) require that terms with exponential functions that go to infinity are removed, giving the following solution:

$$\theta_p^{\mathrm{C}} = Ce^{\lambda_{\mathrm{C}}\eta} \qquad \eta < 0, \tag{2.64}$$

$$\theta_p^{\mathrm{A}} = 1 + Be^{-\lambda_{\mathrm{A}}\eta} \qquad \eta > 0, \tag{2.65}$$

where

$$\begin{aligned} \lambda_{\mathrm{C}} &= \tfrac{1}{2}Pe\left(\sqrt{1+\tfrac{8Nu_a}{Pe^2}}+1\right). \\ \lambda_{\mathrm{A}} &= \tfrac{1}{2}Pe\left(\sqrt{1+\tfrac{8Bi}{Pe^2}}-1\right). \end{aligned} \tag{2.66}$$

Boundary condition (2.62) gives $C = 1+B$, and boundary condition (2.63) gives $B = -\lambda_{\mathrm{C}}/(\lambda_{\mathrm{A}} + \lambda_{\mathrm{C}})$. The temperature is thus

$$\theta_p = \begin{cases} \dfrac{\lambda_{\mathrm{A}}}{\lambda_{\mathrm{A}} + \lambda_{\mathrm{C}}} e^{\lambda_{\mathrm{C}}\eta} & \text{for } \eta < 0, \\ 1 - \dfrac{\lambda_{\mathrm{C}}}{\lambda_{\mathrm{A}} + \lambda_{\mathrm{C}}} e^{-\lambda_{\mathrm{A}}\eta} & \text{for } \eta > 0. \end{cases} \tag{2.67}$$

The temperature in the plate at the penetration point $\eta = 0$ is

$$\theta_p(0) = \frac{\lambda_{\mathrm{A}}}{\lambda_{\mathrm{A}} + \lambda_{\mathrm{C}}}. \tag{2.68}$$

If we take the heat-transfer coeffient h_a to be zero, i.e. assuming no cooling from the air, we can calculate the maximum heating of the plate above the plate due to heat conduction. Thus $Nu_a = 0$ and $\lambda_{\mathrm{C}} = Pe$. The plate temperature at the penetration point is thus

$$\theta_p(0) = \frac{\sqrt{1+\frac{8Bi}{Pe^2}}-1}{\sqrt{1+\frac{8Bi}{Pe^2}}+1}, \qquad Nu_a = 0. \tag{2.69}$$

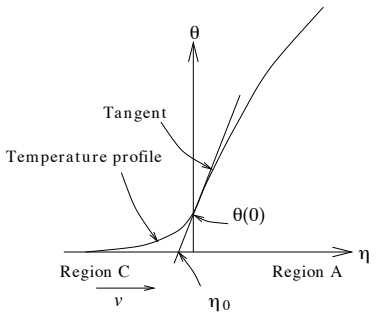

Figure 2.9: Temperature profile in the plate around the penetration point.

At low feeding velocity $Pe = 0.5$ and with $Bi = 0.01$, we get $\theta_p(0) \approx 0.07$, or $T_p(0) \approx 70°\mathrm{C}$. This corresponds to a preheating of 45°C, which is not negligible.

The increase in the penetration temperature can also be interpreted as a shift of the profile a distance $|\eta_0|$ upwards (see Figure 2.9). The tangent to the temperature profile at $\eta = 0$ is given by $\theta_p(0) + \theta_p'(0)\eta$, which intersects the η axis at η_0. From Equation (2.67), we get $\eta_0 = -1/\lambda_\mathrm{C}$, or $-1/Pe$ for $Nu_a = 0$. The shift is thus inversely proportional to the feeding velocity. For $Pe = 0.5$, we get $|\eta_0| = 2$, which is about one millimeter for $b = 0.5\,\mathrm{mm}$.

2.8 The transient period

In the real case, we get a transient period before a steady state can be achieved. The time it takes to stabilize the system is important to know when comparing the experiments to the steady-state model. Only the one-dimensional case will be considered.

Before the plate is set to move into the melt, it has room temperature T_a. It slides into the melt, and after a second or two the end starts to melt. A lower limit for the time before a steady state is attained, is $\Delta t = P/v$, the time it takes for the plate to move from the melt surface down to its steady-state penetration depth P at feeding velocity v.

To estimate the transient period and to obtain an upper bound for this period, we study the case where the plate is initially cold and immersed a distance P_A into the melt, as shown in Figure 2.10. In this estimate, we neglect the wedge region, which is drawn with a dashed line in the figure. The plate moves at a constant velocity v into the melt, and the boundary conditions are $T_p(y{=}0) = T_a$ at the melt surface and $T_p(y{=}P_\mathrm{A}) = T_m$ at the end of the plate. The temperature in the plate will increase due to the heat transfer $q_g = h_g(T_m - T_p)$ from the shell at the melting point T_m. The time-dependent heat balance over a length

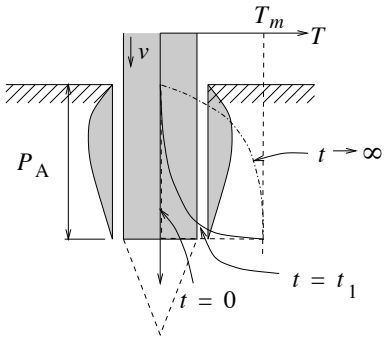

Figure 2.10: The temperature profile in the plate during the transient period from initial condition ($t = 0$) until steady state is attained (strictly, as $t \to \infty$)

Δy is

$$q_y b\Delta t - q_{y+\Delta y} b\Delta t + 2q_g \Delta y \Delta t = \rho c(T(y, t + \Delta t) - T(y, t))b\Delta y. \tag{2.70}$$

After dividing by Δt and Δy, letting both vanish, and then introducing dimensionless co-ordinates, we get

$$\theta'' - Pe\theta' - 2Bi(\theta - 1) = \dot{\theta}, \tag{2.71}$$

where $\theta = \theta_p(\eta, \tau)$ is the dimensionless plate temperature, prime means differentiation with respect to η and $\dot{\theta}$ with respect to $\tau = \alpha t/b^2$.

The system is similar to that of Carslaw and Jaeger (1959, Sec. XV–15.2), but the different initial condition makes the approach different, however similar. We start with the Laplace transformation, which is defined by

$$\tilde{f}(s) = \mathcal{L}\left(f(\tau)\right) = \int_0^\infty f(\tau)e^{-s\tau}\, d\tau, \tag{2.72}$$

where s is the transformed time variable. We set $\tilde{\theta} = \mathcal{L}(\theta)$, and get $\mathcal{L}(1) = 1/s$ and the derivatives

$$\mathcal{L}(\dot{\theta}) = s\tilde{\theta}(\eta, s) - \theta(\eta, \tau = 0) = s\tilde{\theta}(\eta, s), \tag{2.73}$$

$$\mathcal{L}(\theta') = \tilde{\theta}'(\eta, s), \tag{2.74}$$

$$\mathcal{L}(\theta'') = \tilde{\theta}''(\eta, s). \tag{2.75}$$

The transformed equation is thus

$$\tilde{\theta}'' - Pe\tilde{\theta}' - (2Bi + s)\left(\tilde{\theta} - \frac{2Bi}{s(2Bi + s)}\right) = 0 \tag{2.76}$$

with general solution

$$\tilde{\theta}(\eta, s) = Ae^{\lambda_1^s} + Be^{-\lambda_2^s} + \frac{2Bi}{s(2Bi+s)}\,, \tag{2.77}$$

where

$$\begin{aligned} \lambda_1^s &= \sqrt{Pe^2/4 + 2Bi + s} + Pe/2, \\ \lambda_2^s &= \sqrt{Pe^2/4 + 2Bi + s} - Pe/2. \end{aligned} \tag{2.78}$$

Laplace-transformation of the boundary conditions gives

$$\theta(0,\tau) = 0 \quad \Leftrightarrow \quad \tilde{\theta}(0,s) = 0, \tag{2.79}$$

$$\theta(\Pi_\mathrm{A},\tau) = 1 \quad \Leftrightarrow \quad \tilde{\theta}(\Pi_\mathrm{A},s) = 1/s, \tag{2.80}$$

where $\Pi_\mathrm{A} = P_\mathrm{A}/b$. By using the relation $\sinh x = \frac{1}{2}(e^x - e^{-x})$ and Equations (2.78), the Laplace-transformed solution becomes

$$\begin{aligned} \tilde{\theta}(\eta, s) = \frac{2Bi}{s(2Bi+s)} &+ \frac{e^{-\frac{1}{2}Pe\,(\Pi_\mathrm{A}-\eta)}\,\sinh[\eta\sqrt{Pe^2/4+2Bi+s}]}{(2Bi+s)\,\sinh[\Pi_\mathrm{A}\sqrt{Pe^2/4+2Bi+s}]} \\ &- \frac{2Bi\,e^{\frac{1}{2}Pe\,\eta}\,\sinh[(\Pi_\mathrm{A}-\eta)\sqrt{Pe^2/4+2Bi+s}]}{s(2Bi+s)\,\sinh[\Pi_\mathrm{A}\sqrt{Pe^2/4+2Bi+s}]} \end{aligned} \tag{2.81}$$

The *inverse* Laplace transformation is

$$\theta = \frac{1}{2\pi i}\int_{\gamma-i\infty}^{\gamma+i\infty} \tilde{\theta}(\eta, s)e^{s\tau}\,ds, \tag{2.82}$$

where the value of γ is unimportant as long as it is positive and to the right of the rightmost pole of $\tilde{\theta}$ in the complex s plane. The details of this calculation are given in Appendix C.3, and the result can be written as a sum of two terms:

$$\theta(\eta,\tau) = \theta_1(\eta) + \theta_2(\eta,\tau). \tag{2.83}$$

The first term is the steady-state solution, which remains when the time dependence has faded out:

$$\theta_1(\eta) = 1 - \frac{\sinh[(\Pi_\mathrm{A}-\eta)\sqrt{Pe^2/4+2Bi}]}{\sinh[\Pi_\mathrm{A}\sqrt{Pe^2/4+2Bi}]}\,e^{\frac{1}{2}Pe\,\eta}, \tag{2.84}$$

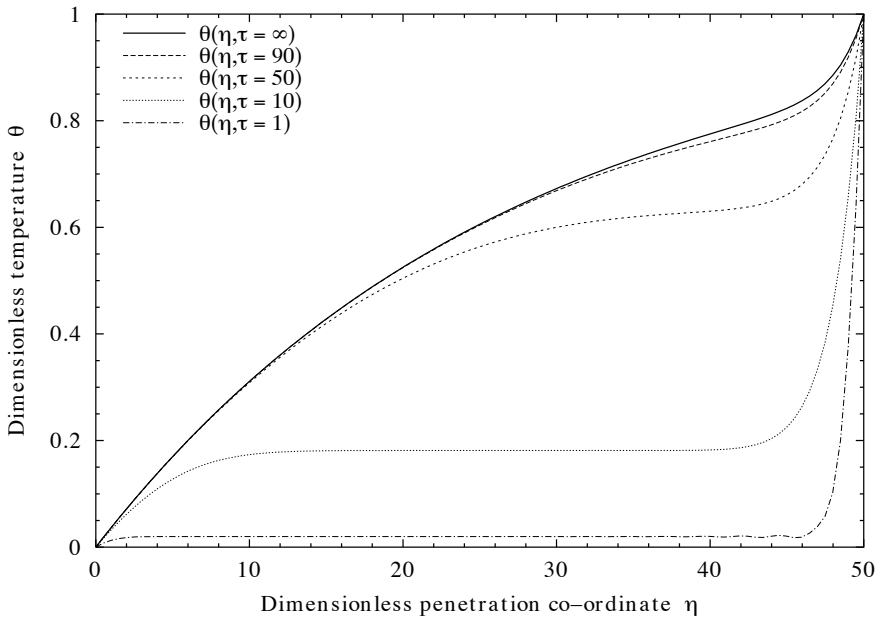

Figure 2.11: The transient temperature profile of an initially cold plate in a warm medium that at time $\tau = 0$ starts to move along its length with dimensionless velocity $Pe = 0.5$ with the temperatures $\theta(0) = 0$ and $\theta(50) = 1$ fixed and with heat transfer $Bi(1-\theta)$ to its surfaces, $Bi = 0.01$

while the second term reveals the transient behaviour of the system:

$$\theta_2(\eta,\tau) = \frac{2\pi}{\Pi_A^2}\sum_{k=1}^{\infty}\sin\frac{k\pi\eta}{\Pi_A}\,e^{-\left[\frac{k^2\pi^2}{\Pi_A^2}+\frac{Pe^2}{4}+2Bi\right]\tau}\times \\ \times\left[\frac{(-1)^k\,k\,e^{-\frac{1}{2}Pe(\Pi_A-\eta)}}{\frac{k^2\pi^2}{\Pi_A^2}+\frac{Pe^2}{4}}-\frac{2Bi\,k\,e^{\frac{1}{2}Pe\,\eta}}{\left(\frac{k^2\pi^2}{\Pi_A^2}+\frac{Pe^2}{4}\right)\left(\frac{k^2\pi^2}{\Pi_A^2}+\frac{Pe^2}{4}+2Bi\right)}\right]. \tag{2.85}$$

Figure 2.11 shows the transient temperature profile of the system for a series of times τ. The ultimate steady-state profile is shown as an extra thick line. The result will be used in Chapter 5 to discuss the steady state assumption as well as in explaining deviations for thick plates. Nonetheless, it is interesting to see that a steady state is attained already for $\tau = 100$, or about 0.3 seconds for a 0.5 mm thick aluminium plate fed at about 7 cm/s. This is faster than the time it takes for the plate to penetrate its penetration depth.

2.9 Two-dimensional calculations

When the thickness of the plate increases so that the isotherms no longer can be considered as horizontal, the system becomes two-dimensional and difficult if not impossible to solve analytically. Nevertheless, by isolating a part of the system, it can still be studied analytically to obtain knowledge about its deviations from the one-dimensional system. In this section, we will derive a model for the temperature profile across the plate in Region A.

2.9.1 A simple two-dimensional model

Figure 2.12 shows the heat transport in a section of Region A of the plate. The heat balance is governed by horizontal and vertical heat conduction and vertical heat convection due to the movement of the plate, here separated in horizontal and vertical terms:

$$q_x = -k\frac{\partial T_p}{\partial x}, \tag{2.86}$$

$$q_y = -k\frac{\partial T_p}{\partial y} + \rho cv T_p(x, y). \tag{2.87}$$

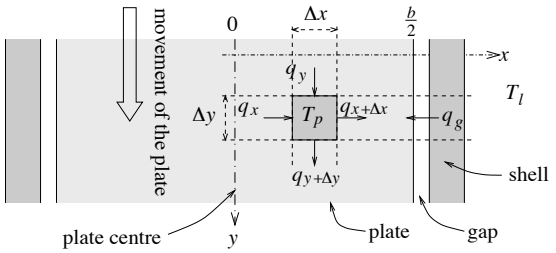

Figure 2.12: Section of the plate with two-dimensional heat balances

The two-dimensional heat balance becomes

$$(q_y - q_{y+\Delta y})\,\Delta x + (q_x - q_{x+\Delta x})\,\Delta y = 0, \tag{2.88}$$

and after dividing by Δx and Δy and letting these approach zero, we get the heat equation

$$k\frac{\partial^2 T_p}{\partial x^2} + k\frac{\partial^2 T_p}{\partial y^2} - \rho cv\frac{\partial T_p}{\partial y} = 0, \tag{2.89}$$

where the two first terms are the heat conduction in both directions and the third term is the heat convection along the plate.

To obtain a set of boundary conditions, it is necessary to make the following assumption in addition to those stated in Section 2.3:

12. The shell and the plate continues infinitely far downwards.

This assumption makes it possible to solve Equation (2.89) analytically, and it gives us a good estimate for the temperature variation across the plate thickness. However, we cannot use the result to calculate the penetration depth as we can with the one-dimensional models. The boundary conditions become

$$T_p(x,y) = T_a \qquad \text{for } y = 0 \tag{2.90}$$

$$T_p(x,y) \to T_m \qquad \text{as } y \to \infty \tag{2.91}$$

$$\frac{\partial T_p}{\partial x}(x,y) = 0 \qquad \text{for } x = 0 \tag{2.92}$$

$$\frac{\partial T_p}{\partial x}(x,y) = \frac{h_g}{k}\left(T_m - T_p(x,y)\right) \qquad \text{for } x = \frac{b}{2}. \tag{2.93}$$

The first boundary condition is due to Assumption 8 while the second one is a consequence of Assumption 12. The third takes care of the symmetry of the temperature at the centre of the plate. The heat transfer from the shell, $q_g = h_g\left(T_m - T_p(\frac{b}{2}, y)\right)$, is no longer a part of the system equation but combines with $k\partial T_p/\partial x = q_g$ to make the fourth boundary condition.

In dimensionless co-ordinates, we get

$$\frac{\partial^2 \theta_p}{\partial \xi^2} + \frac{\partial^2 \theta_p}{\partial \eta^2} - Pe\frac{\partial \theta_p}{\partial \eta} = 0, \tag{2.94}$$

and the boundary conditions become

$$\theta_p(\xi,\eta) = 0 \qquad \text{for } \eta = 0 \tag{2.95}$$

$$\theta_p(\xi,\eta) \to 1 \qquad \text{as } \eta \to \infty \tag{2.96}$$

$$\frac{\partial \theta_p}{\partial \xi}(\xi,\eta) = 0 \qquad \text{for } \xi = 0 \tag{2.97}$$

$$\frac{\partial \theta_p}{\partial \xi}(\xi,\eta) = Bi\left(1 - \theta_p(\xi,\eta)\right) \qquad \text{for } \xi = \tfrac{1}{2}. \tag{2.98}$$

Now, assume that

$$\theta_i(\xi,\eta) = u_i(\eta)\cos\alpha_i\xi \tag{2.99}$$

is a solution a Equation (2.94). We have already removed the corresponding sine term because of the symmetry condition (2.97). Substitute Equation (2.99) into Equation (2.94) and find

$$u_i'' - Pe\,u_i' - \alpha_i^2 u_i = 0 \tag{2.100}$$

where primes denotes differentiation with respect to η. The general solution to this equation is $u_i(\eta) = A_i e^{\lambda_i' \eta} + C_i e^{-\lambda_i \eta}$ where A_i must be zero to give a finite solution when $\eta \to \infty$. We thus get

$$u_i(\eta) = C_i e^{-\lambda_i \eta} \tag{2.101}$$

with

$$\lambda_i = \frac{Pe}{2}\left(\sqrt{1 + \frac{4\alpha_i}{Pe^2}} - 1\right). \tag{2.102}$$

The general solution to Equation (2.94) is thus the sum of all θ_i for $i = 1, 2, \ldots$ plus a constant C_0 which is also a solution of the steady-state equation:

$$\theta_p(\xi, \eta) = C_0 - \sum_{i=0}^{\infty} C_i e^{-\lambda_i \eta} \cos \alpha_i \xi. \tag{2.103}$$

Applying boundary condition (2.96), we find that $C_0 = 1$. Boundary condition (2.98) gives

$$\sum_i C_i e^{-\lambda_i \eta}\left(\alpha_i \sin\frac{\alpha_i}{2} - Bi \cos\frac{\alpha_i}{2}\right) = 0,$$

or

$$\alpha_i \sin\frac{\alpha_i}{2} = Bi \cos\frac{\alpha_i}{2}, \tag{2.104}$$

which must be solved numerically to find α_i. After some mathematical manipulations (see Appendix C.2), boundary condition (2.95) gives

$$C_i = \frac{4 \sin\frac{\alpha_i}{2}}{\alpha_i + \sin \alpha_i} \tag{2.105}$$

The temperature in the plate is thus given by

$$\boxed{\theta_p(\xi, \eta) = 1 - 4\sum_{i=1}^{\infty} e^{-\lambda_i \eta} \frac{\sin\frac{\alpha_i}{2} \cos \alpha_i \xi}{\alpha_i + \sin \alpha_i},} \tag{2.106}$$

where α_i and λ_i are given by

$$\alpha_i \sin\frac{\alpha_i}{2} = Bi \cos\frac{\alpha_i}{2} \qquad \text{and} \qquad \lambda_i = \frac{Pe}{2}\left(\sqrt{1 + \frac{4\alpha_i}{Pe^2}} - 1\right).$$

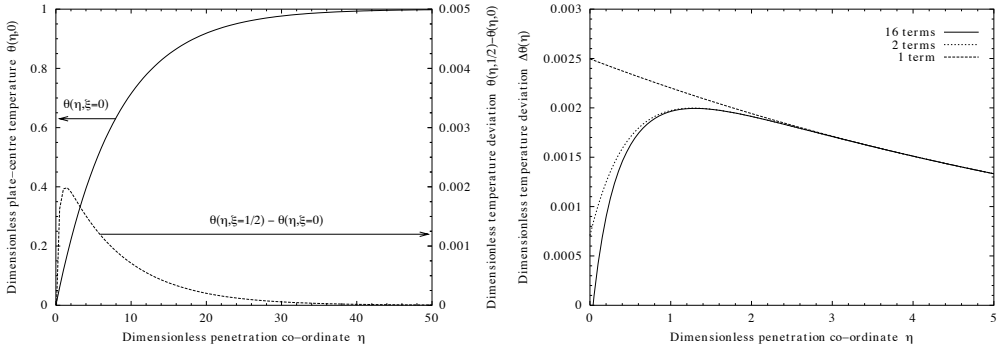

(a) (b)

Figure 2.13: (a) The temperature profile (solid line) and the deviation between the centre and surface temperatures, and (b) the significance of the first and second term in the sum in Equation (2.107)

2.9.2 The temperature difference between plate centre and surface

The deviation between the temperature in the centre of the plate and at the surface is simply

$$\Delta\theta(\eta) = \theta_p(\eta, \tfrac{1}{2}) - \theta_p(\eta, 0) = 4\sum_{i=0}^{\infty} \frac{\sin\frac{\alpha_i}{2}}{\alpha_i + \sin\alpha_i}\left(1 - \cos\frac{\alpha_i}{2}\right) e^{-\lambda_i \eta}. \qquad (2.107)$$

Its variation with the penetration co-ordinate η is shown by a dashed line in Figure 2.13a for a plate with thickness 0.5 mm, $Pe = 1.0$ and $Bi = 0.01$. The scale is to the right in the plot. The centre temperature is plotted in the same plot with a solid line. The deviation curve is also drawn in Figure 2.13b for small η together with two curves showing that the first two terms are sufficient to quantify the temperature profile along the thickness of the plate except at very small η. The maximum deviation for given Bi and Pe can thus be obtained with only two terms, in which case we can calculate the approximate position of the maximum:

$$\eta_{\max} = \frac{1}{\lambda_2 - \lambda_1} \ln\left[\frac{\lambda_2\left(-\sin\frac{\alpha_2}{2}\right)\left(\alpha_1 + \sin\frac{\alpha_1}{2}\right)\left(1 - \cos\frac{\alpha_2}{2}\right)}{\lambda_1 \sin\frac{\alpha_1}{2}\left(\alpha_2 + \sin\frac{\alpha_2}{2}\right)\left(1 - \cos\frac{\alpha_1}{2}\right)}\right]. \qquad (2.108)$$

Table 2.2 lists λ_i and α_i as well as $\eta_{\max}$ and $\Delta\theta(\eta_{\max})$ for a few sets of Bi and Pe. For a plate thickness of $b = 0.5$ mm, Pe corresponds to feeding velocities of about 8 and 24 cm/s. This will be used in discussing the assumption of horizontal isotherms in Section 5.1.10 and in the analysis of thick plates in Section 5.7.

Table 2.2: Values of α_i, λ_i, $\eta_{\max}$, and $\Delta\theta(\eta_{\max})$ for two different feeding velocities v and $3v$ and plate thicknesses b, $3b$, and $5b$ (thus the variations in Bi and Pe)

Bi	α_1	α_2	Pe	λ_1	λ_2	$\eta_{\max}$	$\Delta\theta(\eta_{\max})$
0.01 (b)	0.14130	6.2864	0.5 (v)	0.201	2.27	0.9	0.002
			1.5 ($3v$)	0.0889	1.867	1.4	0.002
0.03 ($3b$)	0.24434	6.2927	1.5 (v)	0.1482	1.868	1.2	0.006
			4.5 ($3v$)	0.0537	1.120	2.4	0.006
0.05 ($5b$)	0.31492	6.2991	2.5 (v)	0.1202	1.554	1.4	0.009
			7.5 ($3v$)	0.0418	0.762	3.4	0.010

2.10 Criterion for shell formation

The heat drawn into the plate upon immersion is taken from the immediately surrounding melt, which in turn is supplied with heat from the bulk melt through the boundary layer. If the heat supply from the bulk melt is less than the heat drawn into the plate, the melt immediately surrounding the plate solidifies, and a shell is formed. Once the shell is established, shell growth requires that the heat flow q_l from the bulk melt must be less than the heat flow q_g over the gap into the plate. The heat-transfer resistances past the boundary layer and past the gap are denoted by the heat-transfer coefficients h_l and h_g, respectively. Mathematically, the criterion for shell formation thus becomes

$$h_l(T_l - T_m) < h_g(T_m - T_a) \tag{2.109}$$

where T_a is the ambient temperature and thus the initial temperature of the plate. After a slight rearrangement, the dimensionless form is

$$\boxed{\theta_l - 1 < \frac{Bi}{Nu}} \qquad \text{gives shell formation.} \tag{2.110}$$

This is obtained directly from Equation (2.16) by setting the initial shell growth $d\xi_s/d\eta$ at $\eta = 0$ greater than zero.

We can thus inhibit shell formation by increasing either the dimensionless superheat, the heat transfer from the melt, or the gap resistance between the shell and the plate. The latter does not seem to be a good idea as it probably increases the melting time as well. Increasing the heat transfer from the melt is an option as it can be attained by stirring. The dimensionless superheat can be increased by increasing the melt temperature, but also by pre-heating the plate.

2.11 Heat-transfer coefficient in thermal boundary layer

As the plate slides into the melt, melt is dragged along with the plate surface, as shown in Figure 2.14. We will use the boundary-layer approximation to describe the heat transfer from the melt to the plate or the shell. This approach allows us to find values for the melt heat-transfer coefficient h_l for a stagnant bath as well as for melt flow past the plate. We will not consider natural convection.

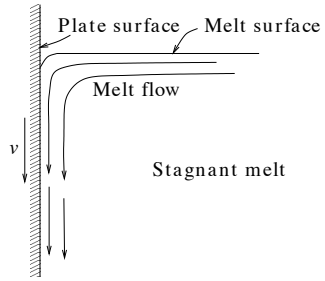

Figure 2.14: The flow of melt due to the movement of the plate

2.11.1 Boundary-layer theory for molten metals

When a fluid flows past a flat plate, heat and momentum are exchanged between the fluid and the plate. Boundary-layer theory considers the fluid outside a distance $\delta(x) \propto \sqrt{x}$ from the plate, to be independent of the presence of the plate. The layer between the plate and the outer fluid is the *boundary layer*. In general, heat and momentum are transported be different mechanisms, so it is natural to distinguish between a viscous boundary layer with thickness $\delta_v \sim \sqrt{\nu x/v}$, and a thermal one with thickness $\delta_T \sim \sqrt{\alpha_l x/v}$. As indicated by the dependence on x, the thickness varies along the plate as shown in Figure 2.15. Across the thermal boundary layer, the temperature changes from the plate temperature to the temperature of the bulk fluid, and similarly for the viscous boundary layer. The temperature and velocity profiles across their respective boundary layers are also shown in the figure for a distance x_0 from the start of the plate. A more detailed discussion of the boundary-layer theory can be found in Schlichting's book (1979), for instance.

When a fluid has a large viscosity, momentum is easily transferred, the velocity gradients become small, and the boundary layer is thick. The same is the case for the thermal diffusivity $\alpha_l = k_l/\rho_l c_l$, which is relatively high for fluids that conduct heat well and have low heat capacity such as metals. The *Prandtl number* is the ratio of the kinematic viscosity ν and the thermal diffusivity:

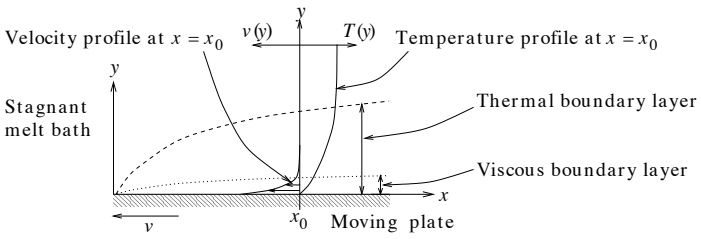

Figure 2.15: The velocity and temperature profiles close to a plate which moves to the left through a stagnant melt bath. The broken lines mark the thickness of the boundary layers.

$Pr = \nu/\alpha_l$. For fluids with $Pr \sim 1$, like gases, the thermal boundary layer will be of similar thickness as the viscous boundary layer. If $Pr \gg 1$, as is the case for "normal" liquids, especially oils, the thermal boundary layer will be insignificant compared to the viscous boundary layer. For metals, however, we have $Pr \ll 1$, as implied in Figure 2.15, and the melt is at rest in most of the thermal boundary layer.

Aluminium has $\alpha_l = 34 \times 10^{-6}\,\mathrm{m}^2/\mathrm{s}$ and $\nu = 0.50 \times 10^{-6}\,\mathrm{m}^2/\mathrm{s}$ (see Table B.1), so Pr becomes 0.015. We can thus disregard the viscous boundary layer and assume that the melt velocity is zero throughout the thermal boundary layer.

For laminar flow, the heat equation in a co-ordinate system following the plate at negative velocity v along the x-axis, as shown in Figure 2.15, is

$$\rho_l c_l \left(v_x \frac{\partial T}{\partial x} + v_y \frac{\partial T}{\partial y} \right) + \rho_l c_l v \frac{\partial T}{\partial x} = k_l \left(\frac{\partial^2 T}{\partial x^2} + \frac{\partial^2 T}{\partial y^2} \right), \tag{2.111}$$

where v_x and v_y are the melt-velocity components, and the last term on the right-hand side enters due to the motion of the co-ordinate system. The flow is laminar when $Re = vx/\nu < 10^5$ (Schlichting 1979, Sec. II.c).

Now, $v_x = 0$ because the viscous boundary layer is disregarded, and $v_y = 0$ as a consequence of the continuity constraint ($\nabla \cdot \vec{v} = 0$). Furthermore, the temperature inside the thermal boundary layer changes much more rapidly perpedicular to the plate than along it, so we can also neglect $\partial^2 T/\partial y^2$ compared to $\partial^2 T/\partial x^2$.

This leaves only two terms:

$$v \frac{\partial T}{\partial x} = \alpha_l \frac{\partial^2 T}{\partial y^2}. \tag{2.112}$$

We use the similarity transformation

$$\phi = y \sqrt{\frac{v}{4\alpha_l x}}, \tag{2.113}$$

and rewrite Equation (2.112) to

$$T''(\phi) + 2\phi T'(\phi) = 0, \tag{2.114}$$

where primes denote differentiation with respect to ϕ. $T'(\phi) = Ce^{-\phi^2}$ is a solution of Equation (2.114), C being independent of ϕ. In normal co-ordinates, the horizontal temperature change is

$$\frac{\partial T}{\partial y} = Ce^{-\phi^2}\frac{\partial \phi}{\partial y} = Ce^{-vy^2/4\alpha_l x}\sqrt{\frac{v}{4\alpha_l x}}. \tag{2.115}$$

We notice that the temperature slope and thereby the heat flow is infinite at $x = 0$, the first contact point between the plate and the melt, where the boundary-layer thickness is zero.

To obtain the temperature profile in the thermal boundary layer, Equation (2.115) must be integrated across the boundary layer:

$$T_l - T_m = \int_0^\infty \frac{\partial T}{\partial y}\, dy = C\int_0^\infty e^{-\phi^2} d\phi = C\sqrt{\frac{\pi}{4}}, \tag{2.116}$$

where the error function $\mathrm{erf}(x)$ with relations $\mathrm{erf}(x) = 2\pi^{\frac{1}{2}}\int_0^x e^{-x^2}dx$ and $\mathrm{erf}(x \to \infty) \to 1$ has been used.

To calculate the *local* heat-transfer coefficient $h(x)$ at position x along the plate, we use its definition:

$$q_y|_{y=0} = k\left.\frac{\partial T}{\partial y}\right|_{y=0} = h(x)\,(T_l - T_m)\,. \tag{2.117}$$

Now, apply Equations (2.115) and (2.116) to this and rearrange to get

$$h(x) = \sqrt{\frac{k_l^2 v}{\pi \alpha_l x}}. \tag{2.118}$$

For a plate of length L, Equation (2.118) gives the mean heat-transfer coefficient

$$\boxed{\bar{h} = \frac{1}{L}\int_0^L h(x)\, dx = \sqrt{\frac{4k_l^2 v}{\pi \alpha_l L}}.} \tag{2.119}$$

Using dimensionless quantities, we obtain the well-known Nusselt relation for the mean heat transfer across a laminar boundary layer set up by a flat plate moving through a molten metal:

$$Nu = \sqrt{\frac{4}{\pi} Pr\, Re}, \tag{2.120}$$

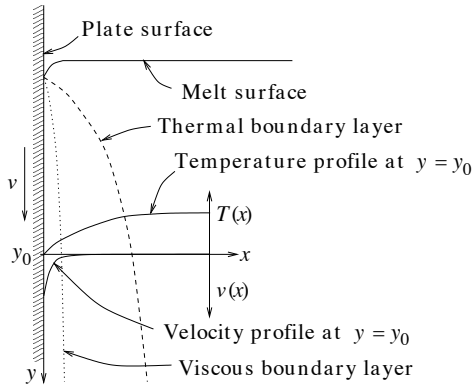

Figure 2.16: The boundary-layer solution applied to a plate penetrating into the melt

where $Nu = hL/k_l$, $Re = vL/\nu$ is the *Reynolds number*, and $Pr = \nu/\alpha_l$ is the Prandtl number discussed earlier in this section.

2.11.2 The heat-transfer coefficient for feeding of plate into stagnant melt

Due to the movement of the plate in the melt, there will be a boundary layer between the plate and the bulk melt. Szekely and Themelis (1971, p. 61) shows the application of the boundary-layer approximation to the air flow around a jet of melt from a bottom nozzle in a ladle, a very similar system.

In the present system, melt is drawn down from the melt surface with the plate as illustrated in Figure 2.14. Hot melt flows from the bulk melt via the melt surface and meets the cold plate. We can expect that the thermal boundary layer is very thin here, giving a very high heat transfer, and that it grows thicker down along the plate. We apply the boundary-layer solution to our plate-feeding problem as a first order approximation, as illustrated in Figure 2.16. Note that the co-ordinates x and y are exchanged.

To obtain an estimate for h_l, we assume that the temperature is close to the melting point in all three regions of the plate. This is normally true as Region B is short and Region A and the wedge region are assumed to be at the melting point. From Equation (2.119) we thus get

$$\boxed{h_l = \sqrt{\frac{4k_l^2 v}{\pi \alpha_l P}}.} \tag{2.121}$$

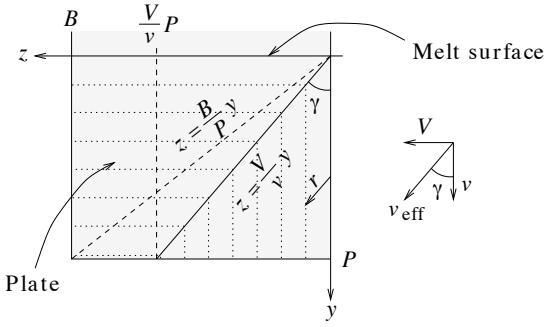

Figure 2.17: Illustration of the plate surface below the melt surface and how the boundary-layer theory can be used with both a feeding velocity v and a melt-flow velocity V. The *solid, sloping line* is the resulting flow direction while the *broken line* is the diagonal of the plate. The heat-transfer coefficient is constant along the *dotted lines*.

2.11.3 The heat-transfer coefficient for feeding of plate into horizontal melt flow

If the plate is at rest and the melt flows horizonally past the plate surface with velocity V, we have a boundary-layer system for which we can use the results from the boundary-layer theory with no further assumptions. However, the plate moves at velocity v into the melt, so we have a boundary layer set up by the movement of the plate as well.

Figure 2.17 illustrates how the two flow directions combine to a superimposed boundary-layer system. It illustrates the surface of the penetrating plate with a diagram with flow velocities to the right. P is the penetration depth of the plate, B is the width of the plate, and z is the co-ordinate going horizontally along the width of the plate. v_{eff} is the effective velocity calculated by Pythagoras' Law: $v_{\text{eff}} = \sqrt{v^2 + V^2}$, and the melt flows in the direction of $\vec{v}_{\text{eff}}$. The local heat-transfer coefficient $h(z, y)$ is assumed only to depend on the distance r in parallel with $\vec{v}_{\text{eff}}$ from the edge of the plate or the melt surface. It is thus given by

$$h(z,y) = \sqrt{\frac{k_l^2 v_{\text{eff}}}{\pi \alpha_l r(z,y)}}, \tag{2.122}$$

where

$$r(z,y) = \begin{cases} z\dfrac{v_{\text{eff}}}{V} & \text{for } z \leq \dfrac{V}{v}y, \\ y\dfrac{v_{\text{eff}}}{v} & \text{for } z \geq \dfrac{V}{v}y. \end{cases} \tag{2.123}$$

The order of integration should be chosen carefully since the resultant flow direction seldom coincides with the diagonal of the submerged plate. For small

melt-flow velocities V, or more correctly, when the resultant velocity is steeper downwards than the diagonal (or $V/v < B/P$), as is the case in the figure, then it is simplest to integrate with respect to z first:

$$\begin{aligned} h(y) = & \frac{1}{B}\int_0^B h(z,y)\,dz \\ = & \frac{1}{B}\int_0^{\frac{V}{v}y}\sqrt{\frac{k_l^2 V}{\pi\alpha_l z}}dz + \frac{1}{B}\int_{\frac{V}{v}y}^{B}\sqrt{\frac{k_l^2 v}{\pi\alpha_l y}}dz \\ = & \sqrt{\frac{k_l^2 v}{\pi\alpha_l B}}\left(\frac{V}{v}\sqrt{\frac{y}{B}}+\sqrt{\frac{B}{y}}\right), \end{aligned} \tag{2.124}$$

The mean heat-transfer coefficient for $V/v < B/P$ is now obtained by integrating $h(y)$ with respect to y:

$$\begin{aligned} h_l = & \frac{1}{P}\int_0^P h(y)\,dy \\ = & \sqrt{\frac{4k_l^2 v}{\pi\alpha_l P}}\left(1+\frac{VP}{3vB}\right) \qquad \text{for } \frac{V}{v} < \frac{B}{P}. \end{aligned} \tag{2.125}$$

Similarly, for large melt-flow velocities ($V/v > B/P$), we get

$$h(z) = \sqrt{\frac{k_l^2 V}{\pi\alpha_l P}}\left(\frac{v}{V}\sqrt{\frac{z}{P}}+\sqrt{\frac{P}{z}}\right), \tag{2.126}$$

and

$$h_l = \sqrt{\frac{4k_l^2 V}{\pi\alpha_l B}}\left(1+\frac{vB}{3VP}\right) \qquad \text{for } \frac{V}{v} > \frac{B}{P}. \tag{2.127}$$

We easily verify that the two expressions for h_l are identical for $V/v = B/P$.

Chapter 3

Experimental

In parallel with the development of the mathematical models, effort was put into designing experiments simple enough to allow comparison with the mathematical models. Through the experiments, important mechanisms in the melting process could be found and checked. This chapter tells how the experiments were prepared and performed. The results of the experiments are presented in the next chapter.

3.1 Experimental setup

Figure 3.1 shows a photography of the feeding apparatus used for the experiments. A feeding device with a coil of aluminium plate is placed on a crucible containing molten aluminium or on a launder with flowing melt. There is a feeding and straightening mechanism that leads the plate into the melt below at a given velocity. On operator command, the feeder is quickly reversed and efficiently withdraws the plate out of the melt. The part of the plate that has been immersed in the melt, is cooled in air and can be analyzed later.

3.1.1 The feeding apparatus

The feeding apparatus is shown schematically in Figure 3.2a, and technical drawings are provided in Appendix A.2. It consists of a holder for a coil of aluminium plate and a feeding mechanism through which the plate is fed. The feeding mechanism in particular is sketched in Figure 3.2b. The four rolls were made of a PVC cylinder to minimize their inertia and situated in a case using ball bearings. The upper pair of rolls is the feeding rolls, and the lower pair straightens out

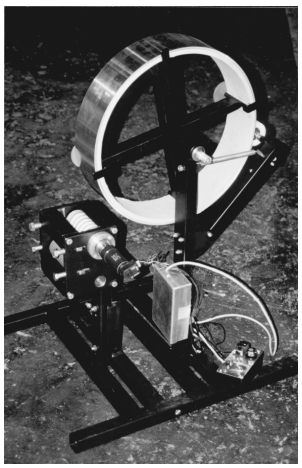

Figure 3.1: Photography of the experimental apparatus

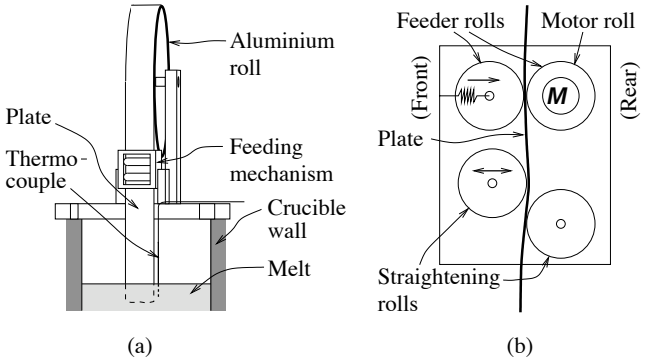

Figure 3.2: Sketches of the feeding apparatus (a) and the feeding mechanism (b)

the plate and steers it vertically into the melt. This is carried out by adjusting the horizontal position of the upper of these two rolls.

One of the feeding rolls was covered with band for tennis rackets to increase the friction to the plate. This roll is driven by a Faulhaber motor (3564 K048B-K312) with encoder (HEDS 5500 A14) and servo amplifier (BLD 5606 SE4P-K1008) for speed control, and a gearhead (38/2S 36:1-K372) to achieve a feeding-velocity range from about 1 to 65 cm/s. The response time of the amplifier was optimized so that it could reverse the speed of the plate as quickly as possible. At feeding velocities around 10 cm/s, the plate could be reversed and attain full speed of about 65 cm/s in the opposite direction after only 2–300 ms.

The motor is controlled by a ± 5 V analog signal, and a simple electric circuit was developed for control and for easy and immediate withdrawal of the plate. This control circuit as well as a calibration curve for the feeding velocity are presented in Appendix D.

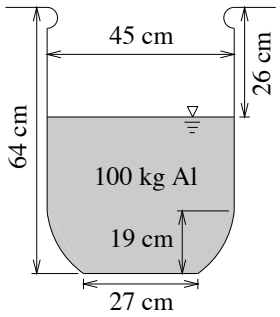

Figure 3.3: The crucible with dimensions

The apparatus was placed on two layers of aluminium plates separated by bricks to prevent heat radiation from heating the apparatus and the aluminium coil. The space in front of the feeding apparatus was open so that the melt could be easily skimmed. However, except during skimming, this hole was kept closed by an aluminium plate with only a small hole of about $12\times4\,\mathrm{cm}^2$ for the plate to enter the melt. When it was open, the heat radiation was reduced as much as possible with a temporary aluminium plate further up. The small hole was closed between each feeding run.

A Campbell 21X data logger connected to a computer was used to record the feeding-velocity voltage and the temperatures at short time intervals (mainly 10 measurements per second). The data were continuously transferred to the computer and plotted on the screen as well as saved for later analysis.

3.1.2 The furnace

During all experiments with a stagnant melt, a Naber Liquitherm K80 tilting furnace with a 35 kW power supply was employed. Its crucible, an 80 litre Naber TPC 287 ladle, is sketched in Figure 3.3. It is resistance-heated, and except for the bottom, it is cylindrical with 45 cm diameter and depth of 64 cm. All experiments were performed with about 100 kg of aluminium melt, melted down from a number of plates of the specified alloy. The melt surface was normally located about 60 cm below the feeding mechanism, but before the experiments with AA3105 alloy the feeding mechanism was lowered 5 cm because these rolls were thicker and would not fit between the roller and the feeding mechanism in the original setup.

3.1.3 The launder

At the Research Centre at Hydro Aluminium a.s. Sunndal, a closed-loop launder is connected to a reverberatory aluminium furnace. The launder leads melt from

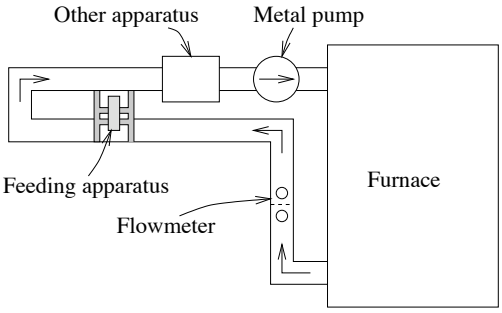

Figure 3.4: Schematic view of the closed-loop launder with the feeding apparatus

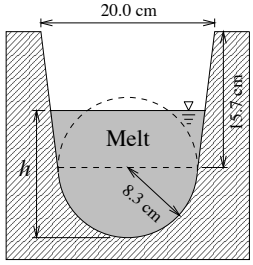

Figure 3.5: The cross section of the launder

the furnace through a device for measuring the velocity of the melt flow, and ends in the furnace again after a metal pump, as shown in Figure 3.4. The feeding apparatus was placed just downstream from the flowmeter, and further down there was another research apparatus before the metal pump. This other apparatus should not interfere with the feeding apparatus, but it is mentioned for completeness.

The flow velocity is continuously estimated by measuring the melt level with a laser beam on each side of an obstacle in the canal with a circular hole. The flow velocity was calculated with the following formula:

$$V = \frac{\pi D^2}{4A}\sqrt{g\Delta h} \tag{3.1}$$

where D is the diameter of the obstacle hole (59 mm the first day, and 77 mm the second), g is the gravitational constant (9.8 m/s^2), and Δh is the difference between the melt level before and after the obstacle. The cross section of the launder is drawn in Figure 3.5, and the cross-sectional area A of the melt in the launder after the obstacle is given by the melt level h: $A(h) = 0.108h^2 + 0.148h - 0.0022$ with h in metres and A in square metres. The measurement of the melt level h was calibrated within ± 1 cm although the relative melt level Δh had an uncertainty of only 1 mm. The flow velocity of the melt varied during the experiments, as shown in Figure 3.6.

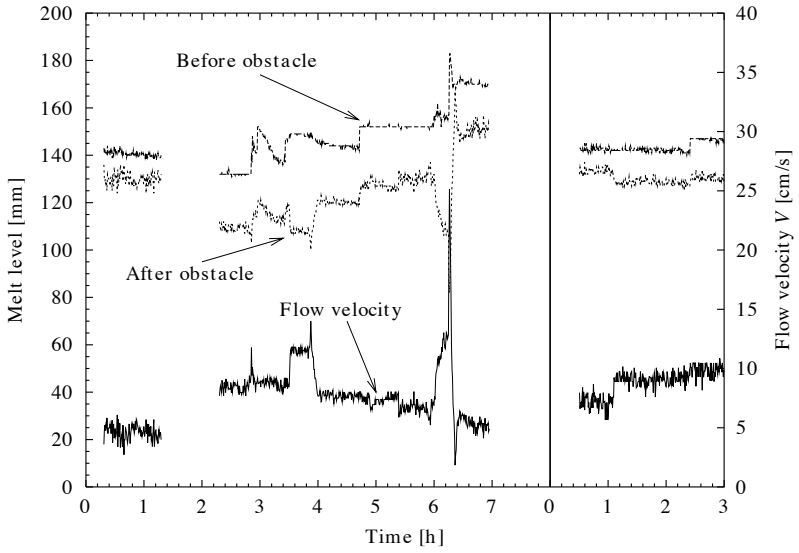

Figure 3.6: The melt level h (upper two curves) and the melt flow velocity (V) during the melt-flow experiments. The vertical line separates the first and second day.

The feeding apparatus was placed on the launder so that the melt flow would pass *along* the surface of the plate. The apparatus was thoroughly shielded from the heat radiation by an aluminium plate, a layer of stone wool, a brick in each corner, and a steel plate. It was necessary to have an additional layer of stone wool over the base of the feeding apparatus to keep the temperature of the aluminium coil low. The distance between the melt and the bottom of the feeding mechanism was about 42 cm varying up to ± 2 cm mainly due to the variations in the melt velocity.

3.2 Thermocouples

Two K-type thermocouples were employed to measure the temperature of the melt in the crucible. A quite slow and inexpensive one (701T-12-72 from Teck Instruments, Norway) was situated close to the crucible wall and used merely to control the temperature of the melt. The other, a more expensive one, was hung from the feeding apparatus and entered the melt a couple of centimetres away from the edge of the penetrating plate, as shown in Figure 3.2. Its body was protected from the melt by a ceramic tube while the end was only covered by a layer of a alumina cement (Fiberfrax QF180 from The Carborundum Company Ltd.) to avoid a slow thermal response. It was calibrated within ± 1.5°C accuracy, and its readings are the ones used for the melt temperature. The distance between the thermocouple and the plate as well as the depth of the thermocouple

(about 5 cm) could vary a little, but probably not significantly.

K-type thermocouple wires were used for quick-response measurements of the temperature change in solidifying melt (see Section 3.4) and in the plate during feeding (see Section 3.6). The wire (K1-0.2-GL) is inexpensive and available by the metre from Teck Instruments. Each of its two conductors is 0.2 mm thick, and they are wound in fibre glass. The thermocouple wires were cut from the same roll, from which one was calibrated. The uncertainty is less than ±3°C. The calibration should be valid for the whole roll.

3.3 Materials and experiment categories

We divide most of the experiments into the four groups listed in Table 3.1. In addition, a number of preliminary experiments were performed in order to examine the effect of thicker plates and to obtain experimental data for the temperature profile in the plate. They are also listed in the table. The composition of the alloys as well as their physical properties are tabulated in Appendix B.2.

Table 3.1: Overview of the experiment groups

Experiment group	Plate alloy	Melt alloy	Plate thickness	Lacquer thickness
Quiescent-melt exp.	AA1050	AA1050	0.54 mm	–
Launder exp.	AA1050	AA6060	0.54 mm	–
No-lacquer exp.	AA3105	AA3105	0.48 mm	–
Lacquer exp.	AA3105	AA3105	0.48 mm	5–6 μm
Thick plates	AA1050	AA1050	1.50 mm	–
Temp. profile	AA1050	AA1050	0.54 mm	–
Centre temp.	AA1050	AA1050	2×0.54 mm	–

The *quiescent-melt experiments* are the main group of experiments, which were performed with a quiescent melt of a commercially pure aluminium alloy called AA1050 (99.5 % pure Al). This is the largest group of experiments and was carried out to test the validity of the mathematical model.

The same type of plate was used for the *launder experiments*, in which the melt flowed past the plate surface, parallel to the plate. The melt was of the AA6060 alloy. This is the only case where the alloy of the melt was not the same as the alloy of the plate. These experiments were performed in an attempt to change the boundary-layer heat-transfer coefficient h_l.

The last two groups of experiments were performed with plates with and with-

out lacquer, called the *lacquer* and the *no-lacquer* experiments. A chemically simple coating was not available on the AA1050 alloy, so the common rolling alloy AA3105 was employed instead. The melt alloy was also changed. These experiments allowed us to study the effect of changing the gap heat-transfer coefficient h_g. They were all performed in a quiescent melt but should not be confused with the quiescent-melt experiments.

The plate material was made of recycled aluminium by Hydro Aluminium Holmestrand Rolling Mill a.s. It was rolled to a thickness of about 0.5 mm (see Table 3.1), cut to a width of 10.0 cm, and delivered in coils of many metres length. The AA1050 coils were not cleaned in any special manner apart from the rough cleaning in the production. Remains of oil could be seen at some places. The *inner* side of the coiled plate seemed to be cleaner than the *outer* side. This difference is probably due to the fact that the inner side of the plate always faces down during production, and oil will more easily fall off the plate on this side than on the other.

One coil was cleaned with ethanol to see whether the oil had any important effect, but no difference could be detected within the experimental uncertainties, maybe because ethanol is not a sufficiently efficient solvent for these oils.

The AA3105 coils, however, were cleaned at Hydro Aluminium AluCoat by an anodization process (*eloxal*) that gives a clean surface with a thickened oxide layer as a base for painting. A difference between the inner and outer side was neither expected nor found. Some of these coils were lacquered with a 5–6 μm thick layer of a polyester lacquer, a clear and chemically fairly simple coating. Further information about the lacquer was not obtainable from the producer, but may be given in Dr. ing. thesis of Anne Kvithyld at the Department of Materials Technology and Electrochemistry at NTNU, which will be published in 2002.

3.4 Measurement of melting point

Attempts were made to measure the melting temperature T_m of the melt by slowly letting melt solidify in a small ladle with a thin thermocouple wire (see Section 3.2) in it. The temperature was continuously monitored using the data logger, as shown in Figure 3.7 for AA1050 to the left and AA3105 to the right.

During the rather flat period (A) in the figure, the ladle with the thermocouple was kept in the melt. At B, the ladle was removed from the melt and the melt started to cool. The temperature decrease stopped abruptly at C, and also in E and H, as solidification started and latent heat was released. Around

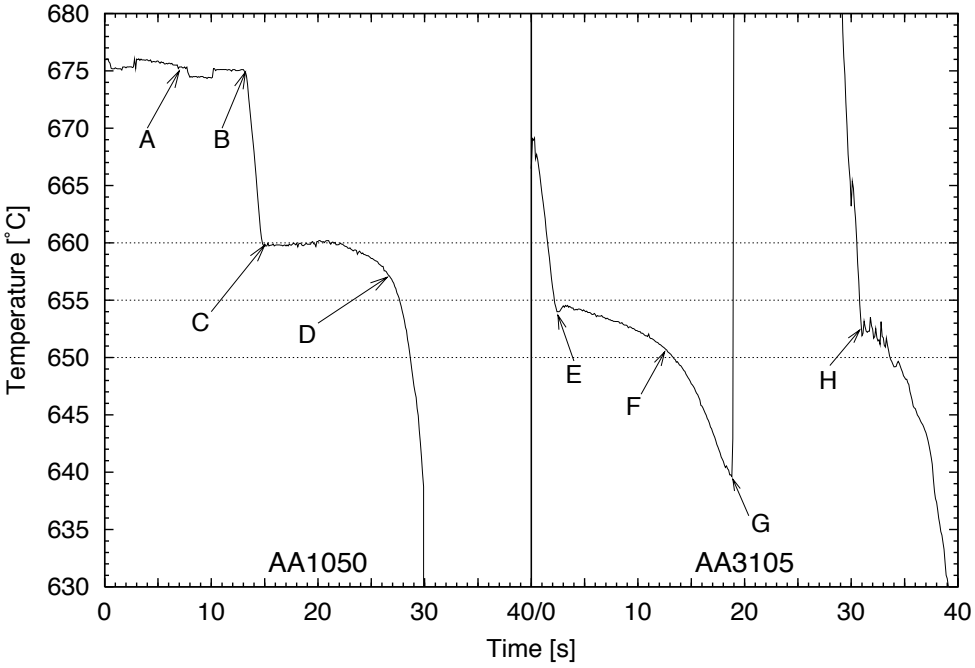

Figure 3.7: The temperature change of a melt in a small ladle during the measurement of the melting temperatures of alloys AA1050 and AA3105 by slow cooling in air

D and F and somewhere after H, the solid fraction was close to 100 % and the temperature started to decrease again. The ladle was re-immersed in the melt at G. Obviously, solidification occurred at a higher temperature in the experiments with AA1050 than with AA3105.

We can fairly well locate the liquidus of the alloys at the point where the temperature temporarily ceases to fall (see Table 3.2). The solidus is, however, difficult to place from these experiments.

Dons et al. (1999) have developed a model called Alstruc for predicting the solidification path and some physical properties of aluminium alloys alloyed with Cu, Fe, Mg, Mn, and Si. The model was tuned by control experiments on seven different aluminium alloys, among them AA1050. They claim that the accuracy is the same as the reproducibility of the control experiments for alloys not too far from the alloys used for the final tuning of the model. The same is the case for the temperature at which 90 % of the melt is solidified. Furthermore, the temperature at which a high fraction of the liquid is solidified is very sensitive to the solidification rate.

With the aid of a computerized version of the Alstruc model, the solidification process was simulated for the compositions of the three alloys AA1050, AA3105,

and AA6060. The simulated liquidus temperature and the temperature at which 50 % of the metal is solidified are shown in Table 3.2 together with the liquidus temperatures obtained from our own measurements. The predicted physical properties are shown in Appendix B.2.

Table 3.2: Melting ranges calculated with the Alstruc model (Dons et al. 1999) and the measured liquidus temperature

	Experimental	Calculated	
Alloy	liquidus	Liquidus	50 % solid
AA1050	660°C	659°C	657°C
AA3105	654°C	653°C	648°C
AA6060	—	655°C	651°C

Notice that the liquidus temperatures found by the present experiments are comparable to the calculated ones. Furthermore, the experiments show that we need not worry about undercooling. This is probably because the solid plate acts as nucleation sites for the first solidification.

In order to utilize the plate-melting model, we need a well-defined melting point. In the shell we have both solidification and melting, and in the plate we have melting. We thus choose to use the temperature at a solid fraction of 50 % as a compromise. For the launder experiments, we use the average of the half-solid temperature of both alloys, i.e. 654°C. This is discussed in Section 5.1.2.

3.5 Experimental procedure

A large number of penetration experiments were performed. The bulk melt temperature T_l was measured by the melt thermocouple that was closest to the plate. Before each measurement run, the melt temperature was held constant within a degree Celsius. No significant change in the temperature was observed during each individual run. In fact, a small temperature drop came just after withdrawal of the plate. Temperatures in the range from below 700 to above 800°C were used. Mostly, only four feeding velocities v were used: 6.4, 9.6, 12.8, and 16.0 cm/s.

The measurement runs were divided into series usually of eight runs, with two runs at each of the four feeding velocities. The temperature tended to sink a little (less than a degree) between each run, but seldom more than five degrees within each series. The heat loss was compensated somewhat by increasing the heat input during the series, but complete control over the temperature was not attained.

Before each run, the oxide skin was skimmed off the melt surface (about a minute before), and the end edge of the plate was pushed past the rolls so that it was even with the bottom of the feeding mechanism. The feeding motor was started at a given velocity v, and the plate was fed for at least 15 seconds including the distance down to the melt. This would mean at least 6–11 seconds immersion time, depending on the feeding velocity. The feeding was finished by instantly reversing the motor at full speed (about 65 cm/s) so that the plate was quickly withdrawn out of the melt, hopefully retaining the length and shape as it had during the feeding. After cooling in air, the end of the plate was cut off for later analysis. In a few experiments, we also video-filmed the plate to be able to study the feeding and withdrawal in slow motion.

Three runs were also performed with thicker plates (AA1050, 1.50 mm thick) of 90 cm length. They were cut from plates that otherwise were melted to establish the melt.

3.6 Measurement of the temperature profile

Two attempts were made to measure the temperature profile in the plate. In both cases, thermocouple wires (see Section 3.2) were point-welded to the surface of a plate of AA1050 alloy. If we assume that the system is in a steady state, the temperature in a single point following the plate is easily transformed to a temperature profile for the whole length of the plate at an instant by multiplying the time by the feeding velocity.

The first attempt to measure the temperature profile was performed by attaching up to three of these thin thermocouple wires 5 cm vertically apart to the surface of a 1.6 metre long plate such that the upper thermocouple was allowed to penetrate about 6 cm into the melt. The thermocouples were placed in different horizontal positions and on both sides of the plate so that the lower thermocouples should not interfere with the heat flow to the thermocouples further up the plate. The plates were fed into the plate in the normal way, except that the feeding time was limited by the plate length, of course. The feeding velocity was 9.6 cm/s for all single plates.

Many problems were encountered during the experiments: The plate bent and did not go vertically into the melt, the thermocouple wire broke near the welding point, and the wires fastened in the feeding mechanism or somewhere else. The experiment had to be interrupted. The problems either made a run fail or, if it was detected before penetration, it was stopped and redone although the temperature of the plate had already increased a little due to the heat radiation. Furthermore, we quickly realized that we probably measured the temperature of

the shell or the melt rather than the plate temperature.

In order to avoid direct contact between the thermocouples and the melt, improvement was attained by putting two plates against each other, inner surface to inner surface. The thermocouples were attached in the same way to one of the plates in the small space between the plates. The two plates were fixed to each other by taping the edges together. Edge effects are neglected in any case. Once they are immersed, the melt pressure should keep them together. This worked well. Plates of 200 cm length were used, and about 124 cm of the length could be fed into the melt. The upper thermocouple was attached so that it was well immersed before the plate was yanked out of the melt. The vertical distance between the thermocouples was similar to that of the single-plate experiments, as was the horizontal placing.

The fact that the double plates gave double thickness as well, is taken as an advantage as this gives an opportunity to study thicker plates. However, the air gap between the two plates may give problems and lead to some lack of symmetry.

3.7 Analysis of the immersed plate

3.7.1 The penetration depth

Figure 3.8 shows a sketch of a typical end of a plate that has been immersed in melt and yanked up. Whether or not a shell had formed, there was always a shell on the edges of the plate, as illustrated in the figure. The top of this *edge shell* is assumed to be the point where the melt surface had been just prior to withdrawal of the plate. The height was not always exactly the same on both sides, so the melt surface was assumed to follow the line that could be drawn perpendicularly across the plate surface from the heighest edge shell. The length of the plate below this line is measured at $m = 5$ equidistant places along the

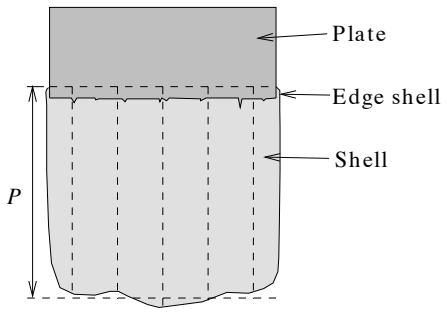

Figure 3.8: Sketch of a typical immersed plate with shell

width of the plate. The outer measurements are taken 1 cm off the edges to avoid measuring edge effects. The average penetration depth becomes

$$\bar{P} = \sum_{i=1}^{m} \frac{P_i}{m}, \tag{3.2}$$

and an *estimate* for the (population) standard deviation σ_P can then be calculated:

$$s_P = \sqrt{\sum_{i=1}^{m} \frac{\left(P_i - \bar{P}\right)^2}{N-1}}. \tag{3.3}$$

Note, however, that the five measurements of P are not independent due to heat conduction along the width of the plate. s_P is thus an *underestimate* of σ_P.

3.7.2 Microscopy of cross section of plate

Four plates with shell were cut along their length in order to study the cross section and compare it to the model. The cross-sectional surface was polished and anodized, and pictures were taken in polarized light through an optical microscope. This treatment made it easy to see the grains and thereby distinguish the shell from the plate and analyze the solidification mechanism. The cross sections were also studied in an optical microscope before anodization in order to compare the concentration of iron in the shell and the plate.

3.8 Experimental uncertainties

All the quantities that are used in the mathematical model have physical meaning and are subject to uncertainties. They may be divided into three groups:

1. the material properties, k, c, ρ, L, T_m, etc.,
2. the measured quantities, T_l, T_a, v, V, and P, and
3. the fitting parameters, h_l and h_g.

Mathematically, the first two groups contain independent variables while the variables in the last group are dependent. Experimentally, P is the dependent variable, and its uncertainty is discussed in Section 5.6.

The *material properties* are mostly obtained from the literature, sometimes given with uncertainty estimates or at least with a significant number of digits, and

sometimes without or even with too many significant digits. Often they vary somewhat from source to source (see Appendix B.2).

The quantities also vary with the alloy. The literature indicates that the most important variations between alloys comparable to those used in this work, are in the thermal conductivity k and the melting interval, and thus T_m (defined in Section 3.4). We therefore use alloy-dependent values for these two properties and assume that the other properties are equal to those of pure aluminium.

Furthermore, the material properties are assumed to be average values over a temperature interval of more than 600°C. These deviations are more or less constant for all the measurements and will thus give systematic errors that are less important for the discussions in this work. The effect of the variation in the material properties is discussed in Section 5.1.1.

The *measured quantities* are quantities that tell the state of the system and can be controlled to some degree or at least be observed continuously. The systematic error in the melt temperatures T_l was discussed in Section 3.2, and except for this, the uncertainty should not be more than ±2°C.

The ambient temperature T_a could, however, vary more because the aluminium coil was above the melt and was heated somewhat in spite of the heat shield. The coil temperature was checked frequently by touch, and it stayed cold (at most about 30°C a few times) except during the launder experiments. In this case, heat shielding was not completely successfull, so the coil was replaced and the apparatus taken down and cooled with pressurized air when the coil became unpleasantly warm (above 50°C).

During the experiments, the feeding velocity v was set by a potentiometer which was calibrated beforehand and showed about ±5 % uncertainty.

Finally, the uncertainty in the flow velocity can be calculated from

$$\frac{\Delta V}{V} = \sqrt{\left(\frac{\partial V}{\partial A}\frac{\Delta A}{V}\right)^2 + \left(\frac{\partial V}{\partial(\Delta h)}\frac{\Delta(\Delta h)}{V}\right)^2} = \sqrt{\left(\frac{\Delta A}{A}\right)^2 + \left(\frac{\Delta(\Delta h)}{2\Delta h}\right)^2}, \quad (3.4)$$

where V is given by Equation (3.1). From Section 3.1.3, we have that the uncertainties in h and Δh are $\Delta(h) \approx 1\,\text{cm}$ and $\Delta(\Delta h) \approx 1\,\text{mm}$, respectively, and from Figure 3.6, we see that $h \sim 12\,\text{cm}$ and that Δh varies from 10 to 20 mm. Do not confuse the uncertainty h, denoted $\Delta(h)$, with the difference in melt level before and after the obstacle, which is denoted Δh. Using Equation (3.1) and the relation $\Delta A = (dA/dh)\Delta(h)$, we get about 10 % uncertainty in the melt-flow velocity.

The uncertainty in the *fitting parameters* are calculated together with the parameters in Section 4.4.

3.9 Fitting procedure

The procedure for calculating the penetration depth $\Pi = P/b$ is as follows when the input parameters θ_l and Pe and the fitting parameters Bi and Nu are given:

1. Obtain Π_A by calculating the positive solution $\eta = \Pi_\mathrm{A}$ of $\xi_s(\eta) = 0$ by numerical integration of Equation (2.16) or from the approximate Equation (C.2) in Appendix C.

2. Iterate Equation (2.35) to find Π_B.

3. Π is then obtained from Equation (2.22).

This procedure cannot be expressed as an analytical function although we will denote it by $\Pi(\theta_l, Pe; Bi, Nu)$ for simplicity in the following.

To find the best fit of the model to the measurement data, we will apply the *weighted least-squares method* presented in Appendix E.1. The method requires independent and identically distributed observations, but although it is natural to assume that they are independent, a look at the measurement data shows that the estimated standard deviation s_Π increases with the penetration depth Π, thus they are not identically distributed. Assuming that σ_Π is proportional to Π, we can obtain an identical distribution by transforming Π to $y = \ln \Pi$ which gives $\sigma_y = \sigma_\Pi/\Pi = \text{constant}$ (Box et al. 1978, Sec. 7.8).

The function to be minimized, χ^2, is expressed by Equation (E.1) and becomes

$$\chi^2(Bi, Nu) = \sum_{i=1}^{N} \left[\frac{\ln \Pi_i - \ln \Pi(\theta_{l,i}, Pe_i; Bi, Nu)}{s_{\Pi,i}/\Pi(\theta_{l,i}, Pe_i; Bi, Nu)} \right]^2 . \tag{3.5}$$

The minimum is found by iterating Equation (E.13), which becomes

$$Bi_\mathrm{next} = Bi_\mathrm{prev} + \sum_{l=1}^{M} C'_{1l}\beta_l, \tag{3.6}$$

$$Nu_\mathrm{next} = Nu_\mathrm{prev} + \sum_{l=1}^{M} C'_{2l}\beta_l, \tag{3.7}$$

with $a_1 = Bi$ and $a_2 = Nu$. $\overrightarrow{\overrightarrow{C}}'$ is obtained from Equations (E.12) and $\vec{\beta}$ from Equation (E.3). $\overrightarrow{\overrightarrow{C}}'$ depends on λ, which is adjusted during the iteration to attain fast convergence, as described below Equation (E.13) in Appendix E.1.

It is also important to know the uncertainties of these parameters. Remember that s_Π was considered to be an underestimate (Section 3.7.1) of the population standard deviation σ_Π of the penetration depth. In Appendix E.2.1, the standard deviation was calculated by using the *covariance tensor* $\overrightarrow{\overrightarrow{C}}$, which is equal to $\overrightarrow{\overrightarrow{C}}'$ for $\lambda = 0$. However, since s_Π is an underestimate, then χ^2, which is a sum of terms inversely proportional to s_Π^2, becomes higher than expected and thus affects $\overrightarrow{\overrightarrow{C}}$. We therefore use *nonparametric bootstrapping* instead (see Appendix E.2.2) to estimate the standard deviation of the parameters.

Chapter 4

Results

A total of 239 experimental runs have been performed. Almost all divide into the four groups defined in Section 3.3: the quiescent-melt and launder experiments with AA1050 alloy, and the no-lacquer and lacquer experiments with AA3105 alloy. The first two sections of this chapter contain qualitative observations while the next two are quantitative studies. The last two sections present the results from the special experiments with thicker plates and plates with thermocouples.

4.1 Cross section of plate

In the model, we presumed that the plate can be divided into three regions, Region A with a shell on the surface, Region B where the shell has vanished, and the wedge region in which the plate melts down (see Section 2.1). Figures 4.1a–d show magnified cross sections of four plates of both alloys AA1050 and AA3105. These particular plates were chosen merely because their penetration depths are comparable and close to the model prediction at the prevailing experimental conditions. They also show the variation of behaviour of the immersed plates, a variation which is difficult to incorporate into a mathematical model. Note that the very large gap between the shell and the plate in the figures is due to the preparation of the plates for microscopy. The lower shell of plate *c* is probably more representable. Furthermore, the shell was found to stick to the plate at its lower end, indicating that the gap has disappeared or at least become very small.

The cross sections in Figure 4.1 show that it is difficult to determine the borders between the three regions that constitute the model. In Region A, the shell growth differs much from the model in some cases. The shell may be completely missing, as in plate *d*, or it may have grown differently on the two sides, as

Figure 4.1: Magnified cross sections of the grain structure of four plates with framed details in later figures. The plate numbers refer to particular experimental runs, which are listed in Appendix F.

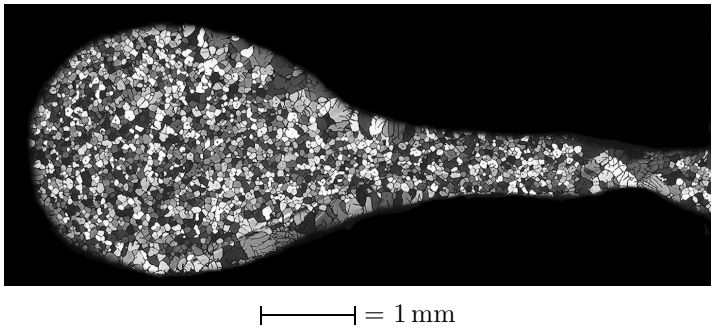

Figure 4.2: Cross section of the droplike end of the plate in optical microscopy, plate 990525-05, AA1050

all but plate *c* show. The shell ends in different positions on the two sides on these plates, and the starting point is different on plate *a*. The upper border of Region B is thus difficult to distinguish from Region A.

Nor does the wedge region always look as presumed in the model. Plate *b* and *d* end in a *droplet* of solidified melt. That of plate *b* is magnified in Figure 4.2. The fine grains in the droplet indicate that it has solidified in air after withdrawal. The end of plate *c* seems to have been snapped off during withdrawal of the plate. Plate *a* is maybe the plate whose end is closest to a wedge except for the small droplet at the end.

The grain structure in the plate and the shell is shown in Figures 4.3 and 4.4 for AA1050 and AA3105, respectively. The plate itself consists of fine grains while the shell is made of large dendritic grains, which indicates rapid solidification. The outer part of the shell has finer grains, as is especially clear in Figure 4.3 (see Section 5.4.2).

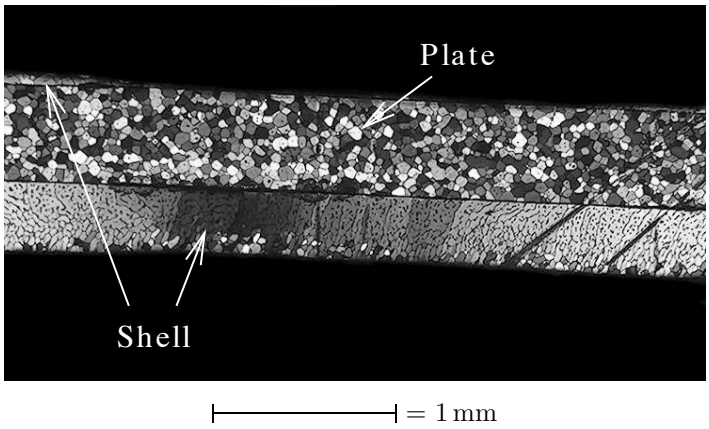

Figure 4.3: Grain structure cross section of plate 990521-06, AA1050 alloy

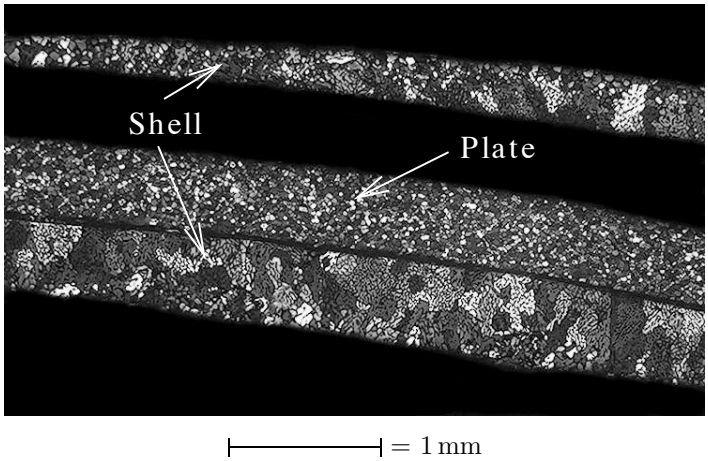

Figure 4.4: Grain structure of cross section of plate 991129-10, AA3105 alloy

The plates in Figure 4.1 were also studied in an optical microscope prior to the anodization. It may be mentioned that in the AA1050 plates and shell, iron could be detected in the grain boundaries. The same was true for the AA3105 alloy although the iron in the plate tended to gather in round particles instead. The concentration was approximately the same in the plate and the shell, and we know that the iron concentration was the same in the plate and the bulk melt. The shell can therefore be assumed to be of the same composition as the melt.

4.2 Snap-off

Video recordings of the feeding (at 6.4 cm/s) and withdrawal were made for four plates, 990521-03–06. Unfortunately, it was difficult to get a good viewing angle due to the heat radiation and the crucible walls. Nevertheless, the withdrawal sequence for plate 990521-04 is shown in Figure 4.6 at 24 pictures per second. This plate was withdrawn a little slower (about 40 cm/s) than normal in order to get finer time resolution. A description of what you see is provided in Figure 4.5. Picture 1 shows the plate while it moves into the melt. Two similar but not so clear pictures are omitted before the withdrawal has just started in Picture 2. In Picture 3, the top of the shell becomes visible. The melt surface seems to be raised a little at this point. In some cases, parts of the shell was observed to have bent down or even fallen off. This is probably what is seen to the left in Picture 3 and more clearly in Picture 4. The top of the shell disappears out of view (hidden by the ladle wall) in Picture 6. The end of the plate is torn off between Pictures 7 and 8 and falls back into the melt while the plate continues upwards.

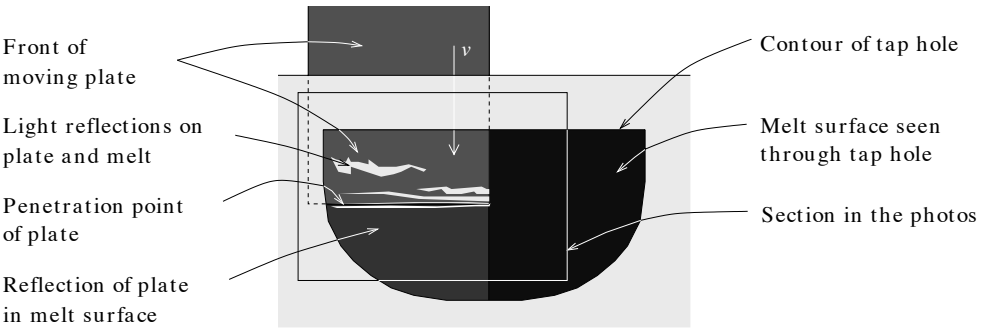

Figure 4.5: Sketch of the tap hole through which the sequence of pictures in Figure 4.6 are taken. The plate moves at first downwards as the arrow indicates, then is yanked up in the opposite direction.

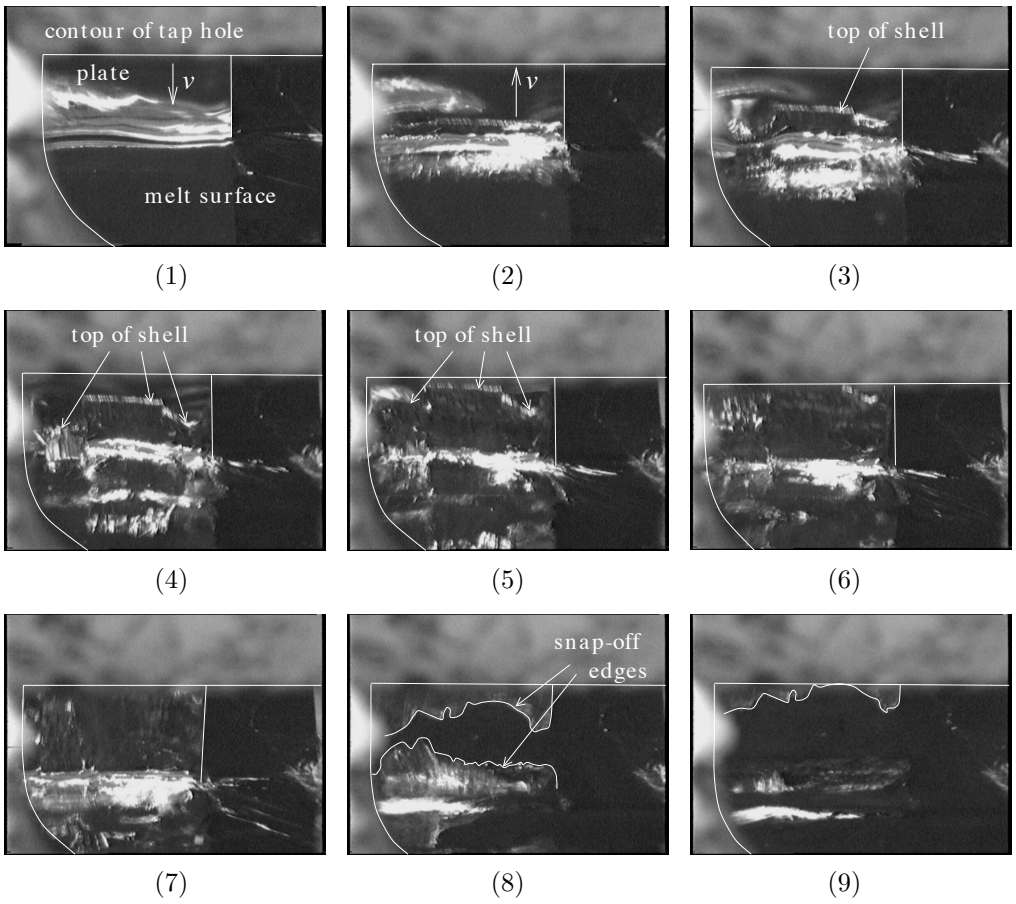

Figure 4.6: Sequence of video recording at 24 pictures per second showing withdrawal of plate 990521-04 (see Figure 4.5 for a description of what you see). The plate is moving downwards in Picture 1. Two very similar pictures are omitted before the withdrawal has just started in Picture 2. Pictures 2–5 show the top of the shell as it rises, and from Pictures 7 to 8 the end of the plate is torn off, and falls back into the melt while the plate continues upwards.

In many cases it was also observed that the lower part, sometimes as much as 2/3 of the immersed part, was soft and dangled a few seconds just after the plate was yanked out of the melt, seemingly in a state between solid and molten. On a few occations, a part of the dangling part fell off right after withdrawal, and in other cases, the bottom of the dangling part was thrown up in a bend at withdrawal and attached to the surface a little further up on the plate.

4.3 Shell formation and meniscus

4.3.1 Shell formation

Although many plates are completely covered with a shell on both sides, only a few have no shell on any side, and in most cases the coverage is partly and differ between the two sides of the plate. We can value approximately the percentage of the width of a single side of the plate that is covered with shell, and from this the shell extent can be divided into the following three categories: *little shell* (less than 10 %), *some shell* (10 to 50 %), and *much shell* (more than 50 %). The tables in Appendix F lists the shell extent according to these criteria together with the other experimental data for all the plates.

Figure 4.7 shows one plate covered with shell and one without a shell, and the two sides of a partly covered plate is shown in Figure 4.8. It is seen that the areas with shell run *along* the plate, not across. The shell in the latter figure covers the plate in opposite spots on the two sides, thus being *complementary* and in sum cover the area of one side of the plate. A small tendency to complementarity can be seen in the experiments, but it is not very prominent.

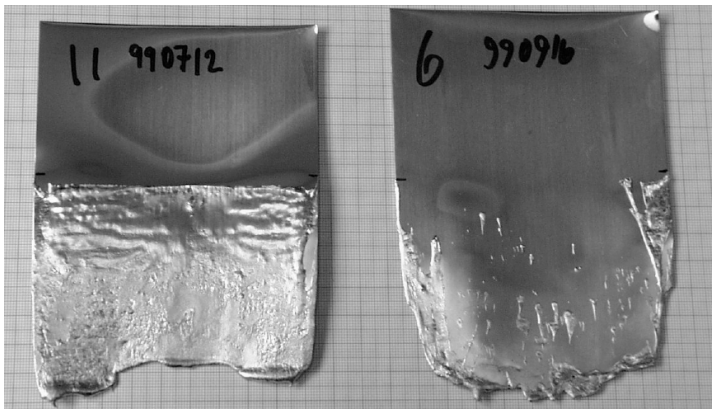

(a) (b)

Figure 4.7: Photography of (a) a typical immersed plate with shell and (b) one without

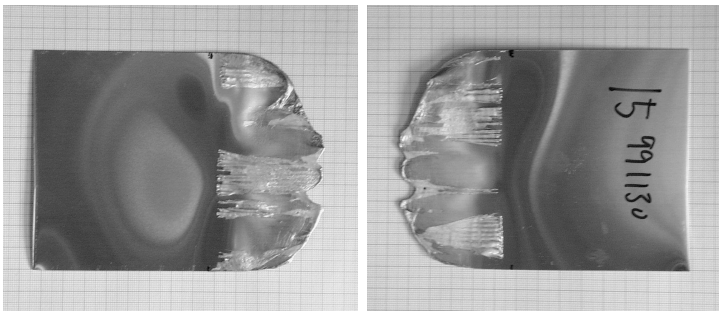

(back) (front)

Figure 4.8: Photographies of both side of plate 991130-15 illustrating *complementary shell formation* on the two sides of the plate

It should be mentioned that the lower part of the plate surface often had changed to grey, indicating that the oxide layer had grown thicker during the immersion. On the AA3105 plates, which contains manganese, the oxide had a golden tinge probably caused by manganese oxide.

Section 2.10 presented a criterion for shell formation. It is thus interesting to be able to decide whether or not shell formation has occurred on each plate. To achieve this, we have attempted to categorize the plates according to the certainty that a shell was formed or not, using the terms defined above:

- ● *Shell:* much shell on one side and much or some shell on the other,
- ⊙ *Shell on one side:* much shell on one side and little shell on the other,
- ▽ *Maybe no shell:* some shell on both sides, and
- × *No shell:* little shell on one side and little or some shell on the other.

Figures 4.9 to 4.11 arrange the plates according to the feeding velocity v (in chronological order) and the dimensionless superheat $\theta_l - 1$ (which is zero at the melting point). Four different symbols place each measurement in appropriate category. None of the thick plates or the plates with thermocouples are included due to the difference in thickness or that we expect the external thermocouples to have affected the shell formation. The lacquer experiments are also not included as shell formation was completely absent in these experiments.

There is a tendency that there is less shell formation and that the shell is thinner at high temperatures. Spot tests indicate that the shell thickness varies from less than 0.1 mm to more than the thickness of the plate (~ 0.5 mm). Furthermore, there seems to be no significant correlation between shell formation and feeding velocity.

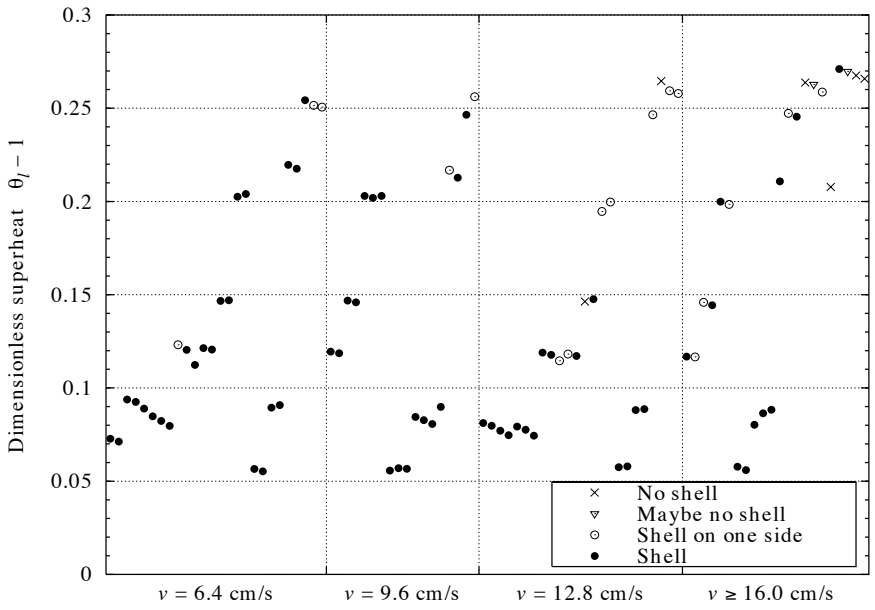

Figure 4.9: Shell formation versus superheat and feeding velocity for the *quiescent-melt* experiments. The five plates with thermocouples are not included.

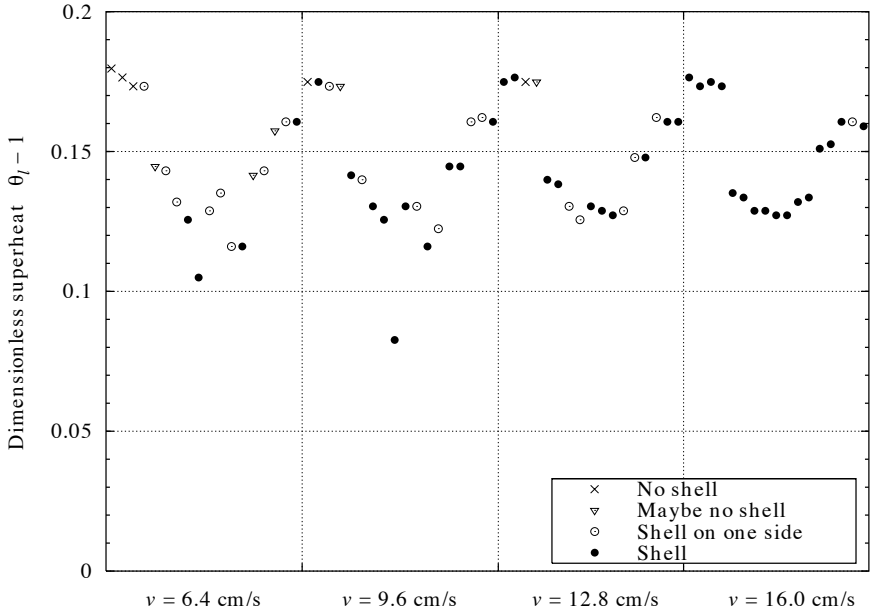

Figure 4.10: Shell formation versus superheat and feeding velocity for the *launder* experiments

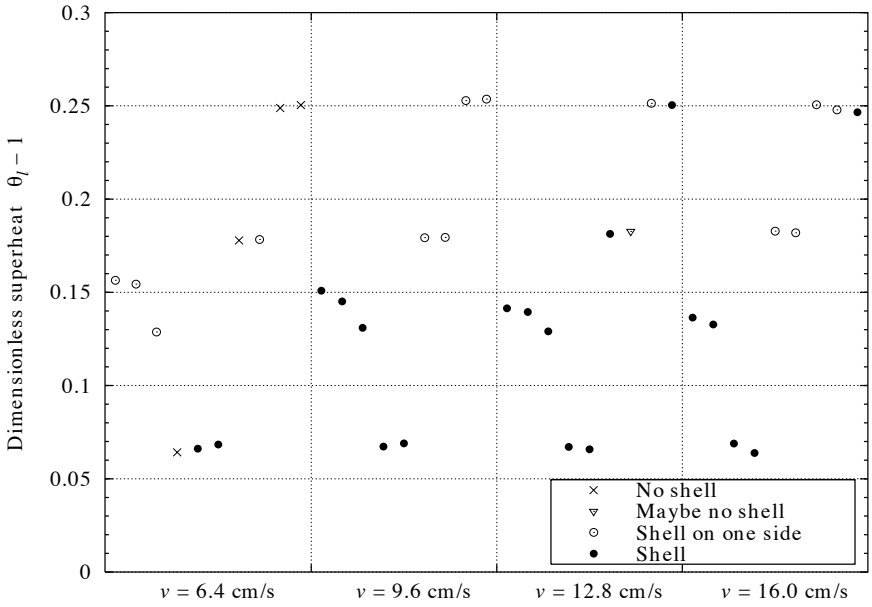

Figure 4.11: Shell formation versus superheat and feeding velocity for the *no-lacquer* experiments

4.3.2 Shell start depth

With the exception of the lacquered plates, there is a shell on both edges of all plates. The edge shell starts a few millimetres further up on the plates than the surface shell. Unfortunately this is difficult to see in Figure 4.7, but a sketch of the edge shell can be found in Figure 3.8 on page 77. The start of the edge shell is therefore marked by a short pen stroke on the plate. Table 4.1 shows averaged *shell start depth* δ, i.e. the depth at which the surface shell starts below the start of the edge shell. The shell start depth was measured from a line drawn perpendicularly across the plate from the top of the highest edge shell. The top edge of the main shell was often quite uneven, so δ was measured a few places and averaged. As δ often differs between the two sides of the plate, a mean shell start depth is used if possible.

The overall mean start depth is 4.6 mm, and a simple curve fit of the shell start depth δ to the feeding velocity v gives no significant correlation. A curve fit of δ to the melt temperature T_l can be obtained as shown in Figure 4.12, but the vast scattering of the data suggests that the correlation has little significance.

Table 4.1: Average shell start depth δ for each experiment group at the four feeding velocities v. N is the number of plates for each δ, of which N_s plates provided at least one shell start depth.

v	Quiescent melt			Launder			No lacquer			Lacquer	
[cm/s]	N	N_s	δ [mm]	N	N_s	δ [mm]	N	N_s	δ [mm]	N	N_s
6.4	26	26	4.8	18	17	4.8	10	7	4.4	15	0
9.6	23	18	5.0	18	18	4.3	9	9	4.0	6	0
12.8	24	24	4.9	17	17	4.1	9	9	4.2	6	0
16.0	17	16	4.9	17	17	4.4	9	9	4.5	4	0

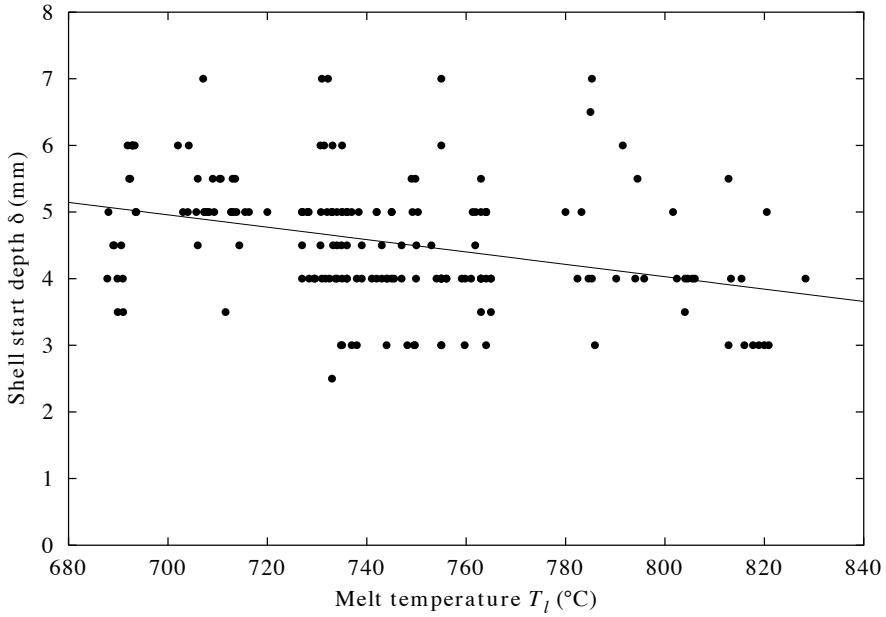

Figure 4.12: Shell start depth versus melt temperature for all groups of experiments. The curve fit is $\delta = aT_l + b$ where $a = -9.3 \times 10^{-3} \pm 20\,\%$ and $b = 11.5 \pm 12\,\%$.

4.3.3 The meniscus

Although it was difficult to get a good viewing angle for the video recordings, it can be seen in Figure 4.13 that the melt surface curves downwards and forms a *meniscus* close to the plate surface. The melt surface did not seem to curve significantly on the edges of the plate. The meniscus was not attempted measured due to the great practical difficulty, but it was visually estimated to about 5 mm depth. It was thus also difficult to detect any variation in the meniscus depth due to change in the feeding velocity. However, during withdrawal of the plate, it was clearly seen that the the meniscus was inversed, i.e. the melt surface curved upwards.

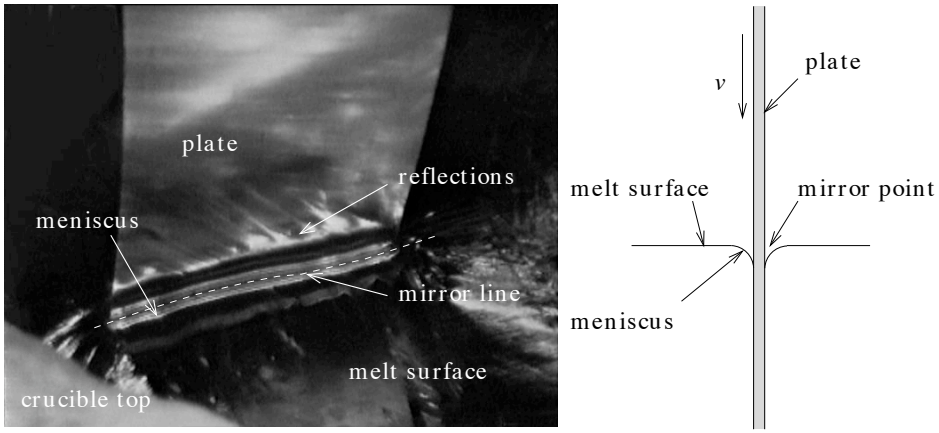

Figure 4.13: Plate sliding continuously down into melt. The melt surface is pulled down, and a meniscus is formed close to the plate. Reflections between plate and melt surface meet in the mirror line.

It is also interesting to notice that the oxide skin was not observed to move during the feeding, except at the very first contact between the plate and the melt surface. Thus, the movement of the plate did not give rise to submersion of the existing oxide layer from the melt surface.

The oxide-film thickness on the melt surface may vary a little with melt temperature and the time between skimming and measurement, so a few runs were performed without skimming for comparison. The penetration depth of these runs lined up well with the other ones. This is taken as an indication that the oxide-skin thickness does not contribute significantly to the results.

4.4 Penetration depth

The penetration depth P and its standard deviation s_P are determined by measurements as described in Section 3.7.1. The main model (Section 2.4) is then fitted to these data by the weighted least-squares method presented in Section 3.9. Although the parameters are found from this method, bootstrapping (Appendix E.2.2) is used to obtain the parameters and uncertainties in these. All fitting is performed by using $T_a = 25°\text{C}$ and T_m equal to the temperature at which the alloy consists of equal fractions of solid and liquid metal, as discussed in Section 3.4. The physical properties of the alloys in question are listed in Section B.2. Section 4.4.5 gives a summary of the heat-transfer coefficients that are obtained during the following.

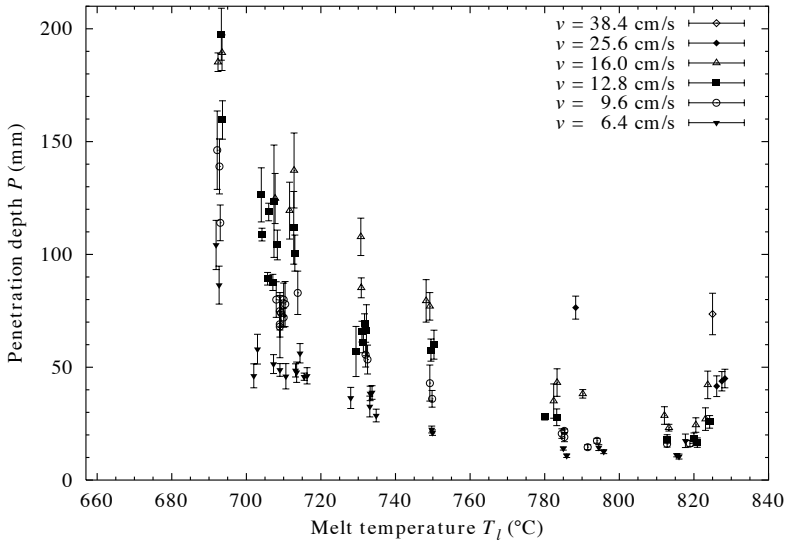

Figure 4.14: Penetration depth versus melt temperature for the *quiescent-melt experiments* (AA1050). Errorbars show the estimated standard deviation in each measurement.

4.4.1 Quiescent-melt experiments

The quiescent-melt experiments are the experiments where an AA1050 plate was immersed into a quiescent bath of AA1050 melt (with $T_m = 657°\text{C}$, $k = 205\,\text{W/mK}$). The main purpose of these experiments was to validate and test the model.

Figure 4.14 shows the measured penetration depth for 90 measurements at the four feeding velocities $v = 6.4$, 9.6, 12.8, and 16.0 cm/s as well as five extra measurements at $v = 25.6$ and 38.4 cm/s.

In the rest of this section, we use dimensionless quantities for generality. The model was first fitted to the data (all 95 data points) to obtain $Bi = 0.0108$ and $Nu = 0.050$ ($\chi^2 = 352$, $\nu = 93$). It is interesting to note that by choosing a T_a of, say, 50°C instead, Bi increases with less than 2 % and Nu decreases with about 3 %. However, a reduction in T_m by 5°C, a small change, makes Bi and Nu both drop with about 10 %. This shows that the actual value of T_a is of minor importance while the melting point is far more significant. This is not surprising as the variable $(\theta_l - 1)$, which is an important variable in calculating Π, is very sensitive to changes in T_m.

Now, even at well-defined ambient temperature and melting point, the parameters Bi and Nu are subject to uncertainties. Figure 4.15 shows χ^2 as a function of these parameters. By use of *bootstrapping* (see Appendix E.2.2), we obtain an estimate of the uncertainty in the parameters: $Bi = 0.0103 \pm 0.0009$

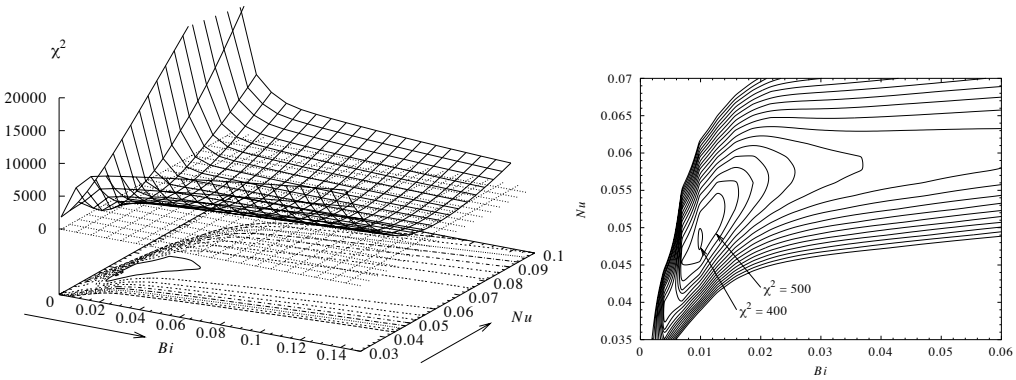

Figure 4.15: *Left:* χ^2 as a function of Bi and Nu with a contour plot in the base of the system. *Right:* a smaller area of the same contour plot

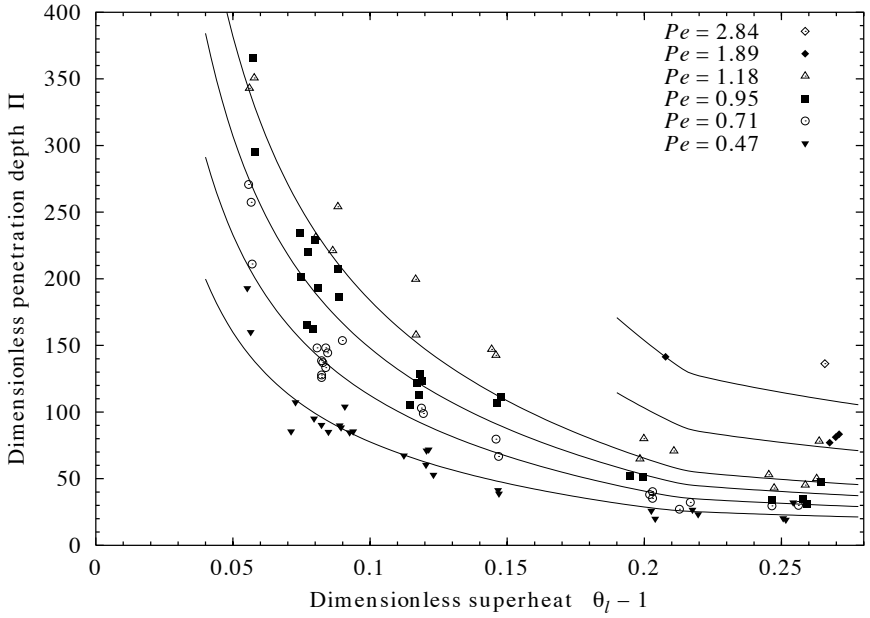

Figure 4.16: Measured penetration depth versus superheat at various feeding velocities v, represented by Pe, for the *quiescent-melt experiments*. The lines are the model prediction at fitted parameters $Bi = 0.0108$, $Nu = 0.050$.

and $Nu = 0.049 \pm 0.001$ for $n = 100$ repetitions, i.e. $s_{Bi}/Bi \simeq 10\,\%$ and $s_{Nu}/Nu \simeq 2.5\,\%$. The parameters differ slightly from the values obtained above, but within the uncertainties just presented. Figure 4.15 confirms this notion. The corresponding heat-transfer coefficients become $h_g = 3900 \pm 400\,\mathrm{W/m^2K}$ and $h_g = 18700 \pm 500\,\mathrm{W/m^2K}$.

Figure 4.16 shows the data and the model predictions for the six different velocities at the minimum of χ^2, $Bi = 0.0108$ and $Nu = 0.050$. Dimensionless quantities have been used.

In Section 2.10, we established a criterion for the shell formation: A shell should not be formed above a critical melt temperature given by $\theta_{l,\mathrm{crit}} = 1 + Bi/Nu$. The model realizes this as a break in the curves in Figure 4.16 at $\theta_{l,\mathrm{crit}} - 1 = Bi/Nu = 0.216$ ($T_{l,\mathrm{crit}} = 794°\mathrm{C}$) because the length of the shell abruptly becomes zero so that the slope of the curve is discontinuous at this point. It should be noted that the model cannot be expected to behave correctly above this critical temperature, partly because of the incorrect slope of the temperature at $\eta = 0$ when no shell is formed, and partly because a gas film must be present between the plate and the melt, lowering the thermal contact and thus the shell formation (see Section 5.4.1). This is not taken into account in the model.

4.4.2 Launder experiments

The launder experiments differ from the rest of the experiments because there is a new parameter, the melt-flow velocity V, which is plotted in Figure 3.6 on page 71 and listed for each experiment in Table F.2. For convenience, the flow velocities are divided into three groups $k = 1, 2, 3$ as listed in Table 4.2.

In Section 2.11.3, we derived a model for the variation of the average liquid heat-transfer coefficient h_l with the feeding velocity v and the melt-flow velocity V. This was based on the assumption that the end of the immersed plate was horizontal, i.e. that the penetration depth did not vary with the width of the plate.

However, the local liquid heat-transfer coefficient $h(z)$ (Equation (2.126)) is infinite at the point where the melt first gets in contact with the plate. Then it rapidly decreases as the melt passes over the plate and gets colder. In effect, the plate should penetrate shallowly upstream and deeper downstream. This was also the case. Figure 4.17 shows a typical example of the sloping end of a plate immersed into the launder with flowing melt.

A first-order approximation of the sloping end of the plate can be expressed as $P(z) = P_0 + \beta z$. Attempts were made to correlate the slope coefficient β with

Table 4.2: Groups of flow velocities. $\bar{V}$ is the mean for each group and $s_V^2 = \sum(V_k - \bar{V})^2/(N_k - 1)$ the estimated standard deviation.

Group k	V range [cm/s]	N_k	$\bar{V}$ [cm/s]	s_V [cm/s]
1	3.4–6.5	17	5.0	1.0
2	6.5–8.7	26	7.7	0.7
3	8.7–11.0	27	10.2	0.6

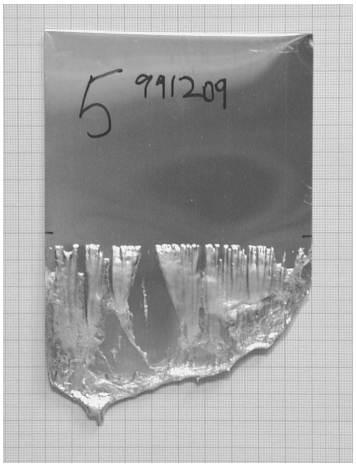

Figure 4.17: Photography of a typical plate end (no. 991209-05) from the launder experiments. The melt flowed from right to left.

the velocities v, V, and $V_{\text{eff}} = \sqrt{v^2 + V^2}$ by using the usual five measuments of P (see Section 3.7.1), but without success. The slope coefficient varied vastly. Thus, in the following, the average penetration depth is applied as usual.

Special to the launder experiments is also that the melt (AA6060 alloy) and the plates (AA1050) have different melting points. We can use the thermal conductivity of the AA1050 alloy ($k = 205\,\text{W/mK}$) since it is only used in the plate. But we use the melting point of both alloys, and Assumption 3 requires the same melting point both for the shell and the plate. We therefore choose the average temperature $T_m = 654°\text{C}$ in the following. The choice is discussed in Section 5.1.3.

The measured penetration depth for the total of 70 measurements is shown in Figure 4.18 separated into four plots according to feeding velocity. Fitting without distinguishing between the melt-flow velocities V gives $Bi = 0.012$ and $Nu = 0.055$ ($\chi^2 = 1272$, $\nu = 68$) and curve fits as in Figure 4.19. Bootstrapping adjusts the parameters to $Bi = 0.013 \pm 0.003$ and $Nu = 0.057 \pm 0.006$.

The parameters were also calculated for each group of flow velocities, and the values obtained are shown in Table 4.3. For high V, several sets of Bi and Nu can be used to get good fit of the model to the 27 measurement runs, as shown in Table 4.4. They were found by small variations in the guess values for the curve fitting. We take the set with the highest ratio between the heat-transfer coefficients as the most probable one, as will be discussed in Section 5.4.1. This ambiguity made the bootstrapping procedure fail, for the predicted mean value of Bi was not reproducible and its uncertainty was mostly more than 100 %. Nonetheless, a standard deviation for Nu could be found although it was large and thus of little interest.

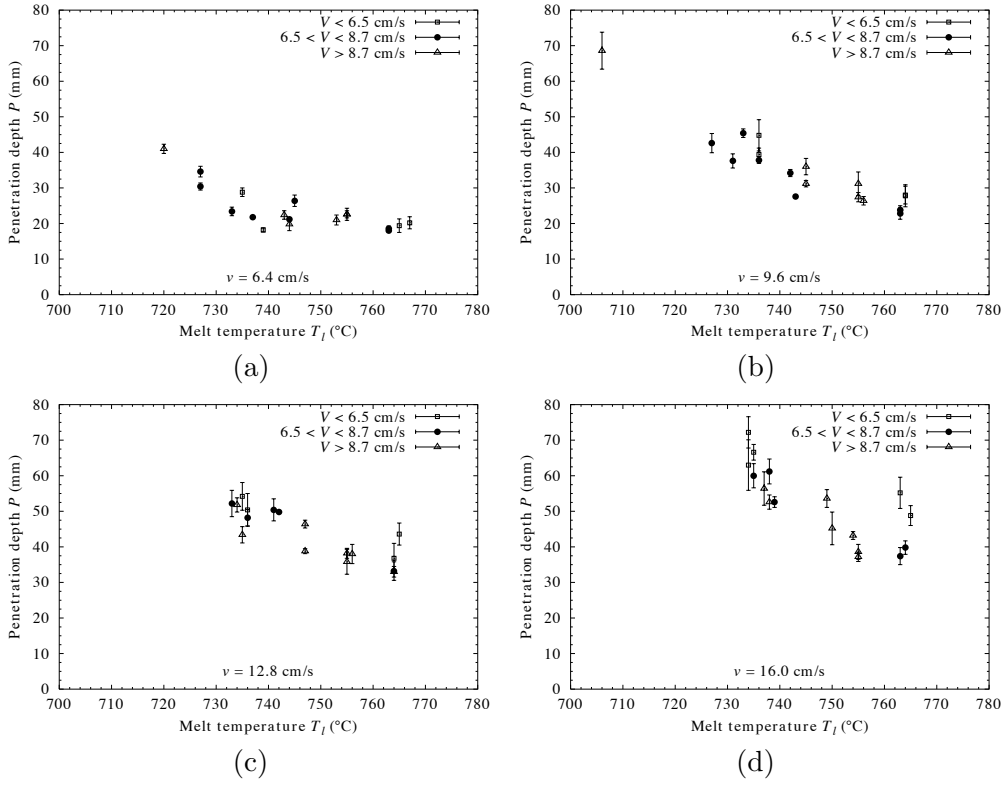

Figure 4.18: Measured penetration depth versus melt temperature for the three groups of melt-flow velocities for the *launder experiments* (AA1050). The feeding velocity is constant within each plot. The errorbars show the estimated standard deviation in each measurement.

Table 4.3: The parameters obtained by fitting and bootstrapping for each group of flow velocities. The χ^2 value refers to the normal fitting only.

Group	$\bar{V}$	ν_k	Bi		Nu		χ^2
k	[cm/s]		fitting	bootstrap	fitting	bootstrap	for fit
1	5.0	15	0.021	0.022 ± 0.004	0.064	0.064 ± 0.004	148
2	7.7	24	0.012	0.013 ± 0.004	0.055	0.057 ± 0.007	883
3	10.2	25	0.010	?	0.054	0.056 ± 0.010	154
All	(8.0)	68	0.012	0.013 ± 0.003	0.055	0.057 ± 0.006	1272

Table 4.4: Sets of parameters giving good fit for high V in order of decreasing h_g/h_l

Bi	Nu	χ^2	$h_g/h_l = Bi/Nu$
0.0101	**0.054**	**154**	**0.19**
0.0080	0.048	158	0.17
0.0068	0.044	151	0.15
0.0056	0.041	139	0.14

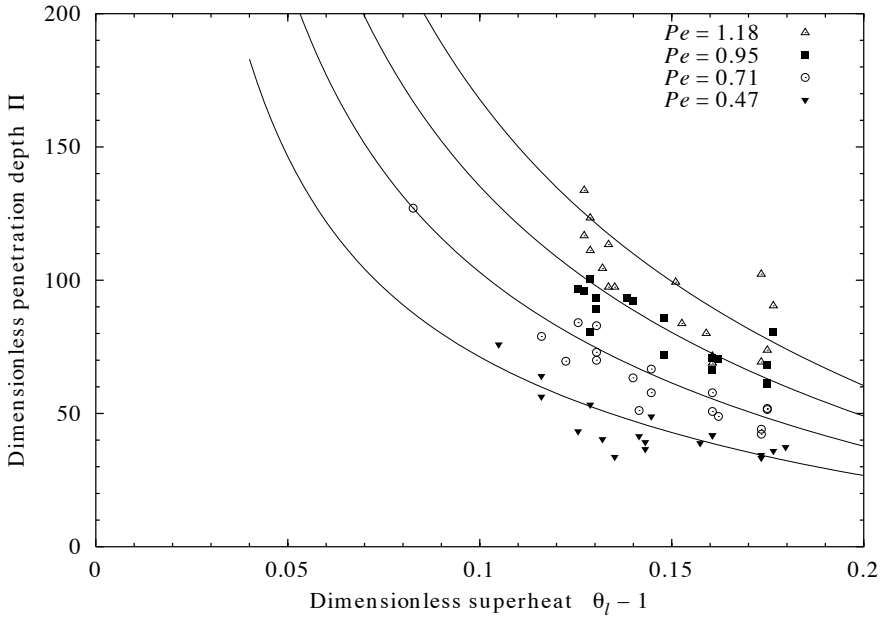

Figure 4.19: Measured penetration depth versus superheat at various feeding velocities v represented by Pe and all melt-flow velocities for the *launder experiments*. The lines are the model prediction at fitted parameters $Bi = 0.012$, $Nu = 0.055$.

4.4.3 No-lacquer experiments

In order to compare melting of lacquered plates with melting of plates without lacquer, a series of 37 feeding experiments were performed with plates of AA3105 without lacquer. They are plotted in Figure 4.20.

At the first glance, these data are well fitted with a simple linear function, but we know that the penetration depth necessarily will increase rapidly as the melt temperature approaches its melting point. Thus there must be another mechanism that makes the low-temperature penetration depths so small. We have chosen to omit the data below 700°C partly of this reason, partly because the other gave a very unstable solution. The discussion of this is deferred to Section 5.6. We use $T_m = 648$°C and $k = 166\,\mathrm{W/mK}$ and otherwise stick to the

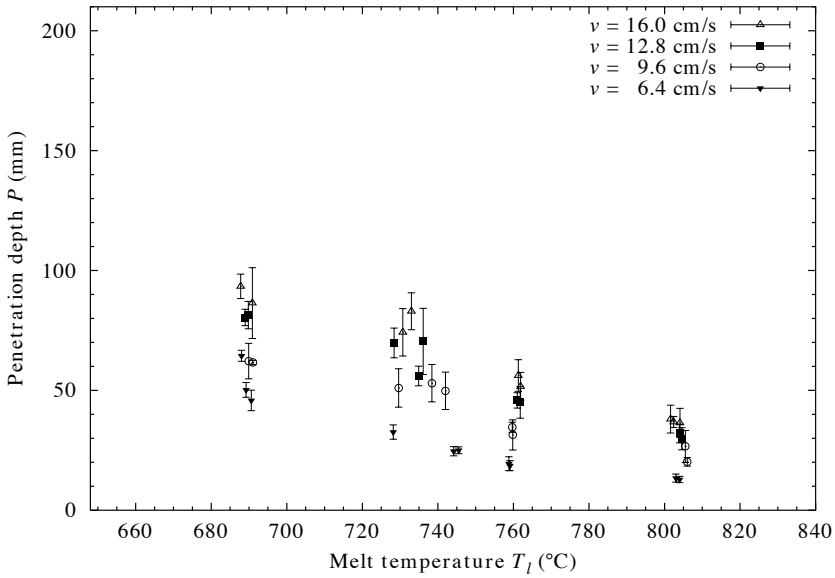

Figure 4.20: Penetration depth versus melt temperature at various feeding velocities for the *no-lacquer experiments* (AA3105). The errorbars show the estimated standard deviation in each measurement.

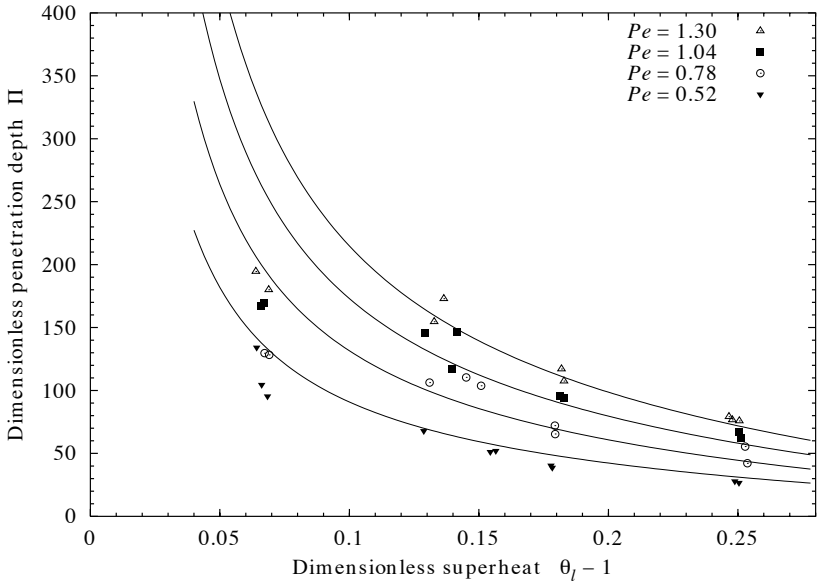

Figure 4.21: Measured penetration depth versus superheat at various feeding velocities v, represented by Pe, for the *no-lacquer experiments*. The lines represent the model prediction at fitted parameters $Bi = 0.016$, $Nu = 0.049$. The points below 700°C were excluded from the fitting.

properties of pure aluminium. Weighted least-squares fitting gives $Bi = 0.0159$ and $Nu = 0.049$ ($\chi^2 = 26.4$, $\nu = 26$), and bootstrapping gives $Bi = 0.016 \pm 0.002$ and $Nu = 0.049 \pm 0.002$.

4.4.4 Lacquer experiments

A number of 31 feeding experiments were performed with lacquered AA3105 plates, and the penetration depth is plotted in Figure 4.22. Half of the plates were fed at the lowest applied feeding velocity, 6.4 cm/s. From these, five runs were performed while an *argon atmosphere* was attempted established by squirting argon gas over the melt. This is indicated with a circle around the data points in the figure. Only four measurements were performed at the highest feeding velocity due to the large penetration depth, especially at low temperatures. Although no shell was formed on the plate surface, remains of melt could be found on the edges of the plate, thus making us able to measure the penetration depth in the usual way.

The feeding of lacquered plates produced flames licking up along the plate. Smoke rose from the penetration point and soot stuck to the plate, both above and below the melt surface. Bubbling was not observed. The experiments that

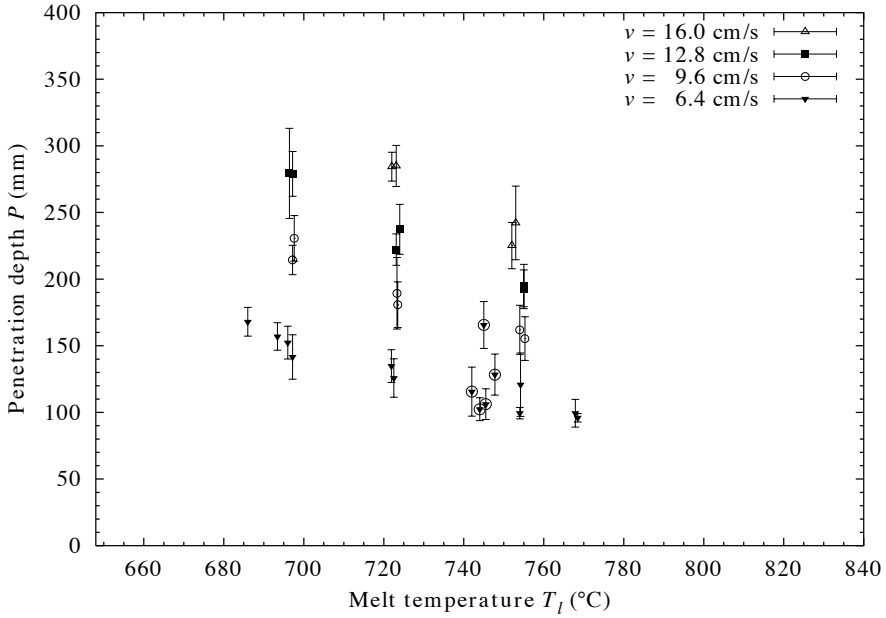

Figure 4.22: The penetration depth versus melt temperature at various feeding velocities for the *lacquer experiments*. The errorbars show the estimated standard deviation in each measurement. A circle around a point indicates use of argon.

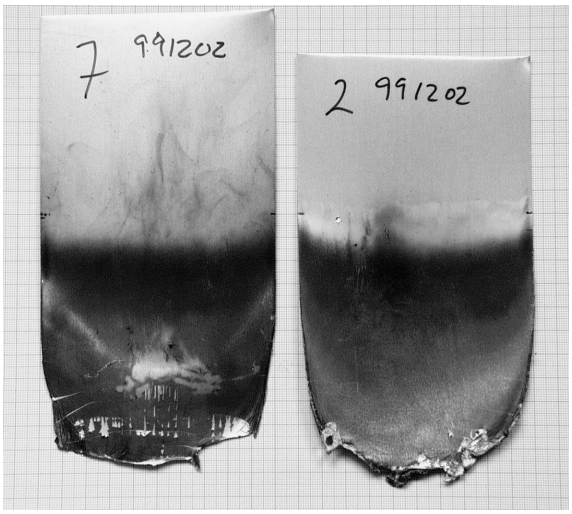

(air) (argon)

Figure 4.23: Lacquered plates fed in air and argon atmosphere

were performed with argon, produced much less flames and soot, and when the argon stream was turned directly towards the penetration point, it was possible to choke the flames completely, at least on this side of the plate. The difference in soot adsorption on the plate above the melt surface can be seen in Figure 4.23. But as can be seen from Figure 4.22, there was no significant deviation in the penetration depth caused by the use of argon. They are therefore treated together with the other data.

Furthermore, there was no shell formation on any of these plates, so Model 2 (Section 2.5) has been employed here. The same material properties as for the no-lacquer experiments are used, and fitting gives $Nu = 0.0075$. However, for consistency with the no-lacquer experiments, we omit the data below 700°C and obtain $Nu = 0.0070 \pm 0.0002$ ($\chi^2 = 63$, $\nu = 22$). The predicted penetration depth is plotted in Figure 4.24. Note that the Nusselt number expresses here the total heat-transfer coefficient h_t corresponding to the thermal resistance of the melt boundary layer *and* the layer of lacquer and entrained gas.

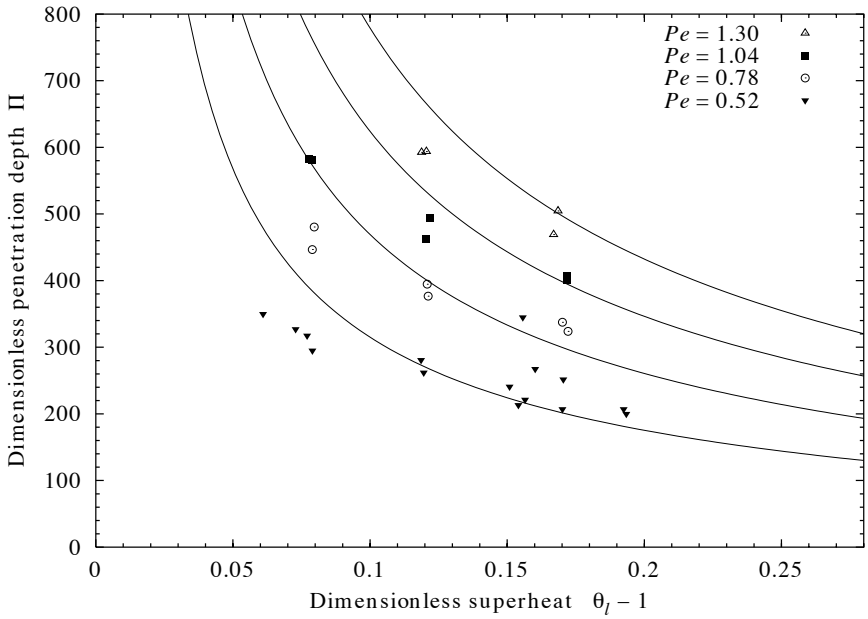

Figure 4.24: Measured penetration depth versus superheat at various feeding velocities v, represented by Pe, for the *lacquer experiments*. The lines represent the model prediction at fitted parameters $Nu = 0.0070$ (Model 2). The points below 700°C were excluded from the fitting.

4.4.5 Summary

The Biot and Nusselt numbers obtained from bootstrapping in the preceeding subsections are converted to heat-transfer coefficients and summarized in Table 4.5. Note that h_l is much more clearly determined than h_g and that no value could be given for h_g for the launder experiments with highest velocities due to large uncertainty and bad reproducibility.

Table 4.5: Summary of fitted heat-transfer coefficients for all experiment groups

Experiments	h_g [W/m^{2}K]	h_l [W/m^{2}K]
Quiescent melt	3900 ± 400	18700 ± 500
Launder, all V	4900 ± 1100	21600 ± 2300
low V	8400 ± 1500	24300 ± 1500
med. V	4900 ± 1500	21600 ± 2700
high V	?	21300 ± 3800
No-lacquer ($T > 700$°C)	5500 ± 700	16900 ± 700
Lacquer ($T > 700$°C)	$h_t = 2420 \pm 70$	

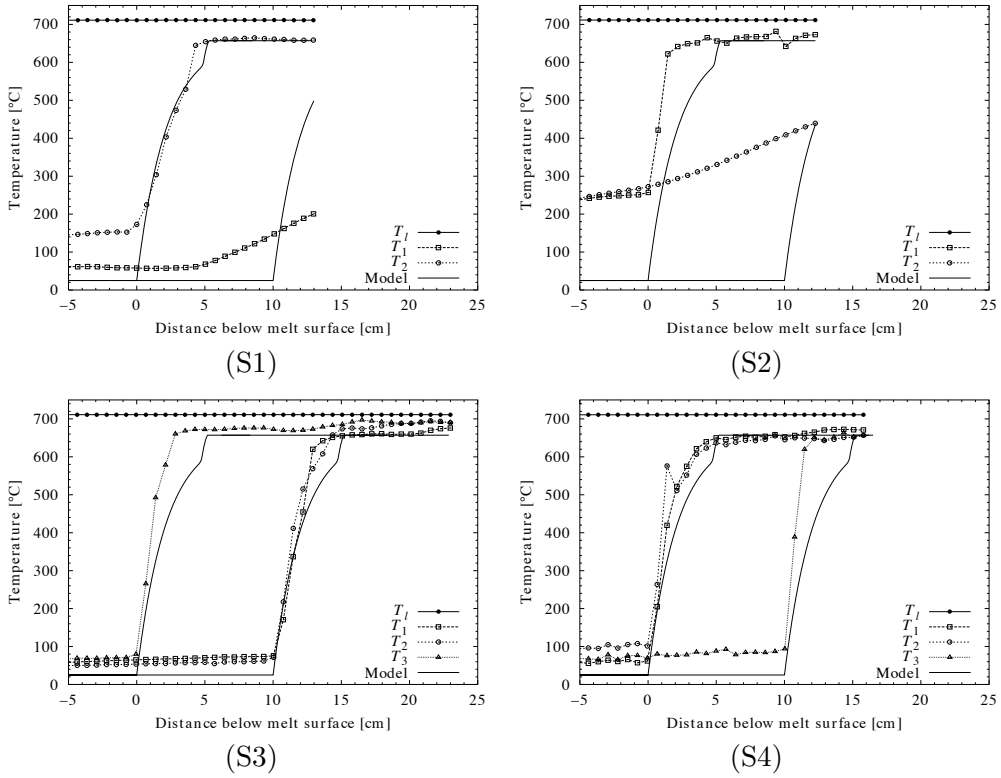

Figure 4.25: Measured and calculated temperature profiles for single plates with thermocouples attached to the plate surface.

4.5 Vertical temperature profile in plate

The temperature profile was attempted measured in two ways as described in Section 3.6, either by attaching the thermocouples on the surface of a single plate (denoted S1 through S4) or between two plates (denoted D1 through D3). Figures 4.25 and 4.26 show the temperature profiles measured until withdrawal in these two cases. The measurement conditions as well as the position of the thermocouples below the melt surface upon withdrawal are listed in Table 4.6. With these data plus the heat-transfer coefficients h_g and h_l found in Section 4.4.1, Model 1 was used to calculate the corresponding theoretical temperature profiles. They are included in the figures. The starting point of the model curves was adjusted by eye to the point where the first thermocouple penetrated the melt surface, and the other curves were merely placed according to the distance between the thermocouples attached to the plate.

The skill in performing the measurements improved with practice. A few problems occurred. The point weldings were not very strong, and a couple of ther-

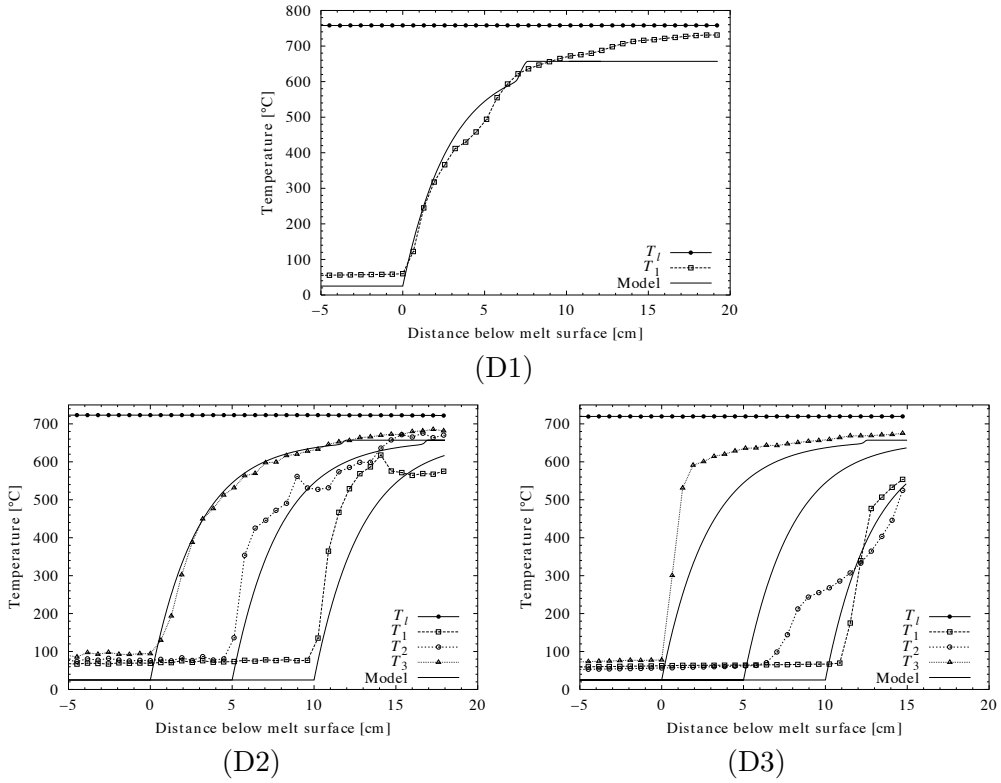

Figure 4.26: Measured and calculated temperature profiles for double plates with thermocouples attached between the two plates.

mocouples broke loose before the measurement and were removed because the point-welding equipment was not available. Another problem was that the wires got stuck in the feeding mechanism so that the measurement had to be interrupted. This resulted in preheating of the plate either because of direct contact with the melt or because of the heat radiation. Finally, a measurement was lost due to problems with the data logger.

In the two first measurements, S1 and S2, T_1 fell off during the feeding, and the experiment was momentarily stopped and then started again. Plate S3 bent somewhat during the feeding and was thus immersed a little askew, but it does not seem to have affected the result very much.

It is seen from S3 and S4 in the figure that the measured temperature increased quicker than expected from the model. This is probably because the thermocouple is in contact with the shell or the melt. The single-plate experiments were therefore not continued.

The double-plate experiments were much more difficult to prepare and perform

Table 4.6: The experimental conditions for the measurement of the temperature profile and the thermocouple position below the melt surface upon withdrawal.

Measurement	v	T_l	Thermocouple position [cm]		
type & no.	[cm/s]	[°C]	y_1	y_2	y_3
S1 (990713-05)	9.6	709	14 (front)	14 (back)	–
S2 (990713-04)	9.6	709	14 (front)	14 (back)	–
S3 (990713-03)	9.6	710	13 (front)	13 (back)	23 (back)
S4 (990714-01)	9.6	710	16 (front)	16 (back)	6 (back)
D1 (990917-01)	6.4	756	21	–	–
D2 (990920-02)	6.4	721	8	13	18
D3 (990920-03)	6.4	718	4	9	14

because the wires had to be between the two plates. The challenges were the same as with the single plates, and also here we had preheating. One wire (T_3) on D3 loosened and left a hole in the plate before the experiments and was attempted re-attached mechanically in the hole. Contact with the shell or melt seems to be the reason for its rapid heating. Nevertheless, the correspondence between the measurements and the theoretical curves was better in some cases for these experiments.

4.6 Thicker plates

The three plates with thickness $b = 1.50\,\text{mm}$ and the three double plates with thermocouples are the only measurements that were performed with plates thicker than about 0.5 mm. The measured penetration depths are shown in Figure 4.27 with the corresponding estimated standard deviation. Figure 4.28 contains the same points using dimensionless quantities as well as the penetration depth predicted by the model prediction (Model 1) with the heat-transfer coefficients obtained in Section 4.4.1. Notice that the penetration depth for $b = 1.5\,\text{mm}$ and $2 \times 0.54\,\text{mm} = 1.08\,\text{mm}$ at $6.4\,\text{cm/s}$ become almost equal in dimensionless quantities. The model predicts shorter penetration than was measured. This will be discussed in Section 5.7.

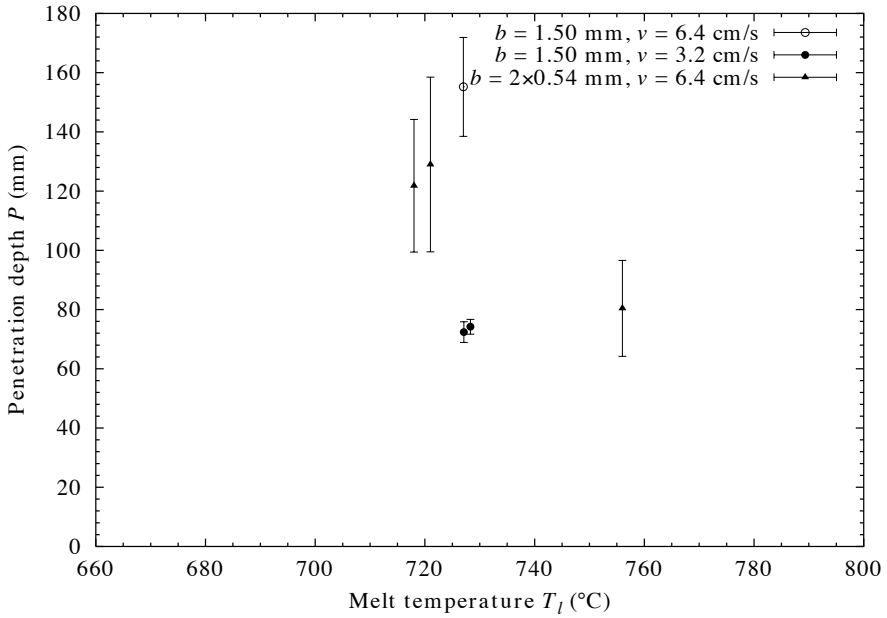

Figure 4.27: The penetration depth P versus melt temperature T_l for thicker plates ($b = 1.5\,\mathrm{mm}$) and for double thin plates with thermocouples between them.

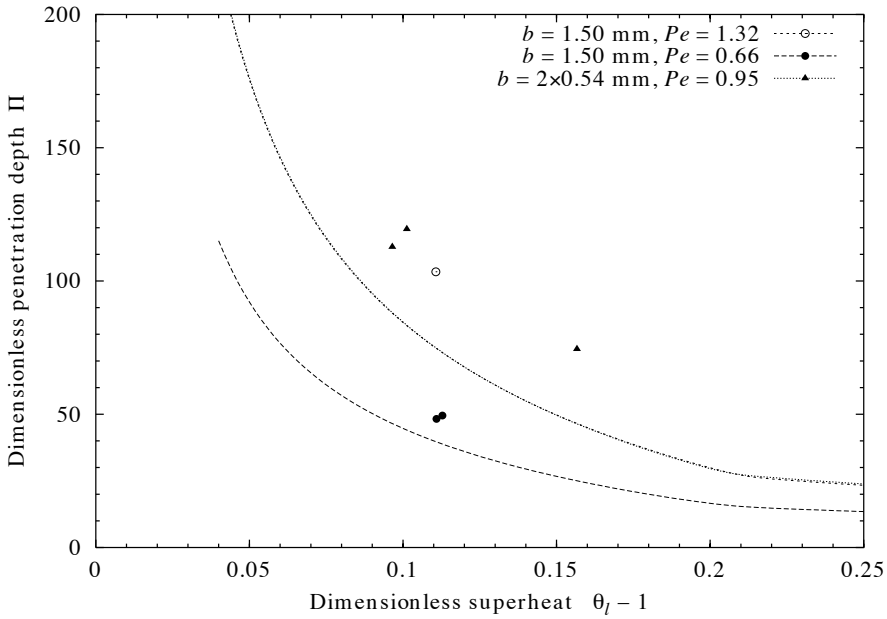

Figure 4.28: The penetration depth Π versus superheat $\theta_l - 1$ for thicker plates ($b = 1.5\,\mathrm{mm}$) and for double thin plates with thermocouple between them. Notice the overlap of the $Pe = 1.32$ and $Pe = 0.95$ lines.

Chapter 5

Discussion

This chapter is divided into two parts, one considering the assumptions made in the development of the model (Section 5.1), and the remaining sections comparing and discussing the mathematical model and the experimental results from different view points.

5.1 The validity of the model assumptions

It is necessary to evaluate the assumptions on which the mathematical model is based in order to compare the model and the experiments. The assumptions are discussed in the order that they appear in the model development.

5.1.1 Constant material properties

In the three mathematical models, only solid-state properties enter. They vary from room temperature to the melting point. The density ρ varies insignificantly: less than one percent from the mean density. However, the thermal conductivity k deviates up to six percent from its mean value, mainly decreasing with increasing temperature. The opposite is the case for the specific heat c, which increases monotonously with more than 30 % from room temperature to the melting point, a considerable variation. This can be seen in Table B.2.

More crucial is the fact that c and k enter the model equations as a part of the thermal diffusivity $\alpha = k/\rho c$ so that the effect of their opposite change with temperature is enhanced. It follows that the Péclet number $Pe = vb/\alpha$ is diminished at low temperatures and enhanced at high temperatures, and this affects the vertical temperature profile of the plate by contracting it at small

$\eta = y/b$ and expanding it at large η, as illustrated in Figure 5.1. This can be seen by inspecting the term $e^{-\lambda_2 \eta}$ in Equation (2.33), which dominates the temperature profile. With Bi small and $Pe \sim 1$, we get $\lambda_2 \approx 2Bi/Pe$. The exponential term then becomes $e^{-2\eta Bi/Pe}$. At small η, the temperature is low, and the reduction of Pe requires a proportional reduction of η in order to give the same temperature, thus a contraction at small η. Similarly, an increase of Pe at large η leads to an expansion further down in the melt. The use of average

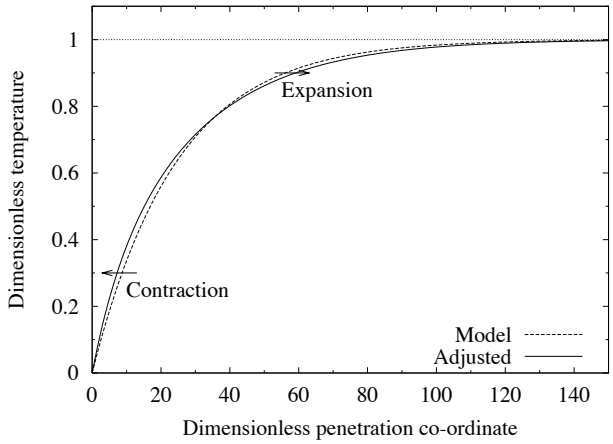

Figure 5.1: Adjustment of the temperature profile due when compensating for the temperature dependence of Pe. This example is for $v = 10\,\mathrm{cm/s}$ ($Pe \approx 0.7$) with $Bi = 0.015$ which are representative values.

values for c and k is consequently not so significant for the resulting penetration depth after all. This should justify Assumption 1 concerning constant material properties.

It should be mentioned that, above the melting point, only the viscosity changes significantly: it decreases about 20 % from 660 to 800°C. This affects the calculations of the liquid heat-transfer coefficient, but probably not more than the uncertainty of these calculations.

5.1.2 The effect of a melting range

Assumption 2 states that we have a well-defined melting point T_m. But although the melting point of pure aluminium is experimentally determined to the second decimal, aluminium of industrial interest is always alloyed. Even commercially pure aluminium (AA1050) is an alloy with a temperature interval in which it is more or less molten. This melting range is much larger for AA3105 (see Appendix B.2). The micrographs did not give much information about the effect of the melting range, so it will be discussed on a theoretical basis.

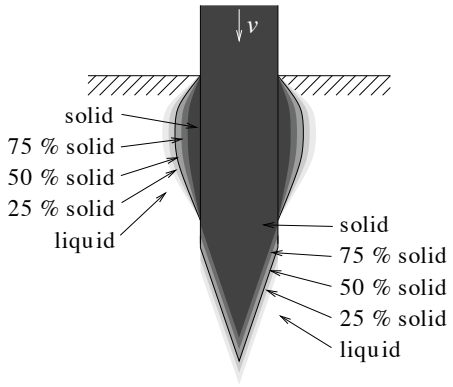

Figure 5.2: Illustration of the gradual change of state from solid to liquid. The solid line marks a solid fraction of 50 %.

When a melt is cooled and the temperature falls below the liquidus of that alloy, the first grains of solid appear. These grains have a different composition than the melt in accordance with the phase diagram. More and more melt solidifies as the temperature decreases, and if the solidification takes place at local equilibrium, the last melt disappears at the solidus. The area between liquid and solid is called the *mushy zone*. Rapid solidification depresses the temperature at which the final solidification occurs. Undercooling can also complicate the picture significantly. In any case, the latent heat of melting L is released gradually. And upon melting, the opposite process occurs.

In the current problem of melting by feeding a plate into a melt, we have two regions in which a phase change is taking place: solidification and melting in the shell region, and melting at the end of the plate. Thus, as long as there is a melting range, neither the shell nor the end of the plate will be exactly defined.

With our definition of T_m (see Section 3.4), the shell thickness is the distance from the plate to where the metal is half solid, half liquid. This is illustrated in Figure 5.2. At this hypothetical boundary, 50 % of the latent heat per unit mass is released. Inside this boundary, i.e. inside the shell, more than a half of the metal is solid whereas less than a half is solid outside. Now, if the total amount of liquid metal inside the boundary is equal to the total amount of solid metal outside the boundary in a given horizontal cross section, then the total latent heat released is the same as if the shell were completely solid and there were only liquid outside.

Similarly, the end of the plate is considered to be where the solid fraction is 50 %. Also here it is natural to believe that the liquid fraction above this boundary is about the same as the solid fraction below. Conclusively, Assumption 2 should be a reasonable approximation in combination with the applied definition of T_m.

However, it should be mentioned that the melting range also affects the mechanical strength of the metal. When the plate is withdrawn, it may snap off at some point along the wedge. This can affect the measured penetration depth as discussed in Section 5.6.

5.1.3 Equal melting point for plate and melt

For most of the experiments, the melt and the plate were both of the same alloy. In these cases, Assumption 3 of a common melting point for the plate and the melt is accommodated by the definition of the melting point presented in Section 3.4.

However, for the launder experiments, the melting point for the plate (657°C) is higher than that of the melt (651°C). In Section 4.4.2, we chose to use the average of these temperatures, 654°C, in order to have a single melting point. The argument for this choice is as follows.

According to the model, heat transfer from the melt to the shell is controlled by their temperature difference. If we increase the melting point of the *melt* towards that of the plate, the heat transfer is lowered and the shell becomes longer. At the same time, the heat transfer from the shell to the plate is increased so that the plate temperature becomes somewhat higher, but not enough to avoid that the penetration depth increases.

On the other hand, if the melting point of the *plate* is decreased towards that of the melt, nothing happens to Region A, but Region B becomes shorter as the melting point is reached earlier. Additionally, the wedge is shortened due to higher heat transfer from the melt. This means a decreased penetration depth.

It thus follows that the correct penetration depth is obtained at a common melting point somewhere between the two melting points and that a first approximation would be to use the average value.

5.1.4 Constant heat-transfer coefficients

The gap heat-transfer coefficient h_g gives the thermal resistance $1/h_g$ due to the gap between the plate and the shell. It was observed that, as the plate moves down into the melt, the shell tends to stick more tightly to the plate. This may be due to the variation in the hydro-static pressure in the melt along the shell. The resulting decrease in the gap thickness along the plate makes the local h_g increase downwards.

The opposite is the case with the local liquid heat-transfer coefficient h_l, which

will decrease downwards in the melt. This is due to the increase of the boundary-layer thickness, as illustrated in Figure 2.16 on page 64 and expressed by Equation (2.118), i.e.

$$h_l \propto y^{-\frac{1}{2}}. \tag{5.1}$$

Due to Assumption 4 the curve-fitted heat-transfer coefficients must be considered as mean values in the model. To some extent, the assumption can be justified in the same way as for the material properties (see Section 5.1.1), but Equation (5.1) implies that h_l is infinitely large at the penetration point ($y = 0$). Strictly, the criterion for shell formation should be applied with the conditions prevailing at the penetration point. Based on this, shell formation should never occur. This suggests that variation of h_l is more complicated than predicted by the boundary-layer theory. Furthermore, the boundary-layer theory implies that the mean h_l decreases with increasing penetration depth. This will be discussed in Section 5.2.

The discussion above casts some doubt upon the validity of the assumption in question. However, the significance of the variation of the mean heat-transfer coefficients is not known. Thus, since we depend on using constant heat-transfer coefficients in order to make an analytical model, this is an inevitable assumption. Its validity should be a subject in a later study.

5.1.5 The sensible heat of the melt

In the model, we did not take into account the sensible heat of the melt (see Section 2.4.2). We assumed that the melt was at the melting point T_m close to the shell (Assumption 5). This implied that q_{ly}, defined by Equation (2.14) and in Figure 2.4, did not contain T_l, but T_m. However, when the shell thickness increases, the thermal boundary layer is pushed out. Thus the same amount of melt that is solidified, must also be cooled from T_l to T_m. This implies a release of the sensible heat $c_l(T_l - T_m)$ of this melt as well. During melting of the shell, the opposite occurs.

But strictly, the local thermal boundary layer is probably thinner when the shell grows and thicker when it melts away. This is due to contraction of melt to solid metal and thus convection towards the shell during solidification and the corresponding expansion and convection away from the shell during melting. This also gives rise to variations of the liquid heat-transfer coefficient.

Mathematically, the sensible heat can simply be incorporated into the latent heat of melting, i.e. $L \rightarrow L + c(T_l - T_m)$ or $Sf \rightarrow Sf + (\theta_l - 1)$. The constant L thus becomes temperature dependent, and this complicates the shell equation

further. Furthermore, since the thickness of the thermal boundary layer varies along the plate, the model used and a model that includes the sensible heat of the melt would both be extremities between which the solution should lie.

To avoid the use of Assumption 5, which states that the said sensible heat is included in the liquid heat-transfer coefficient, a more elaborate study of what occurs in the melting/solidification region is necessary.

5.1.6 The same liquid heat-transfer coefficient in all regions

In Region A, the boundary between the shell and the melt should give little or no thermal resistance, and in any case it is easily included in the boundary-layer heat-transfer coefficient h_l^{A}. In Region B, where the shell has melted away, the gap heat-transfer coefficient h_g is not used in the model although there may remain an oxide film and possibly also a thin gas film. These resistances can in principle be included in the liquid boundary-layer heat-transfer coefficient h_l^{B} given by:

$$\frac{1}{h_l^{\mathrm{B}}} = \frac{1}{h_{\mathrm{ox}}} + \frac{1}{h_{\mathrm{gas}}} + \frac{1}{h_l^{\mathrm{A}}}. \tag{5.2}$$

The oxide layer is about 2–3 μm thick at room temperature (Wefers 1981), and with a thermal conductivity of about 30 W/mK (Weast 1979, p. D-56), the oxide layer has a heat-transfer coefficient of $h_{\mathrm{ox}} \sim 10^7$ W/m^{2}K. This is so much larger than h_l^{A} that it has no importance.

Micrographs and the fact that the shell sticks to the surface of the plate further down, indicate that there is no significant gas film where the shell melts away. Assumption 6 should thus be a fair assumption.

5.1.7 Constant shell temperature

Without Assumption 7 of a constant shell temperature, there would be a coupling between the temperature equations of the shell and the plate in Region A. Furthermore, the temperature in the shell would vary across its thickness, and the development of an analytical model would probably be impossible.

No attempt was made to measure the shell temperature since even the plate temperature proved to be very difficult to measure. However, in Section 1.5.4, we saw that Goudie and Argyropoulos (1995) measured the temperature in the shell around a cylinder immersed in a melt. The shell temperature was depressed about 15 % below the melting point in the very first seconds after immersion. The shell thickness was not reported, but it was probably larger than that experienced on the plates as their cylinder diameter was much larger than our plate thickness.

Thus Assumption 10 of horizontal isotherms in the plate should be relevant for the shell as well, in which case the shell should stay close to the melting point.

5.1.8 No heating of plate above melt surface

Assumption 8 states that the temperature of the plate at the penetration point $y = 0$ is T_a. This implies that there should be no heating of the plate above the melt surface. In Section 2.7.2, we found that heat conduction up through the plate above the melt surface gives some preheating depending on the feeding velocity. Heat radiation only made a negligible contribution to the preheating. The preheating can be treated as an upward shift of the temperature profile. This shift is small ($\Delta\eta = 1/Pe$, i.e. about a millimetre) and depends on the feeding velocity.

When measuring the penetration depth, we chose to set the penetration point to the assumed level of the melt surface and thus neglected the meniscus (see Section 5.3). However, the meniscus probably lowers the actual penetration point a few millimetres, thus shifting the temperature profile down and counteracting the effect of preheating.

Although Assumption 8 might not be completely justified, it simplifies the model considerably and introduces only a small error.

5.1.9 Steady state

In the experiments, the immersion time of the plates was at least six seconds for the lowest feeding velocity and more for higher velocities (see Section 3.5). In Section 2.8, a simple transient model was used to find an estimate for the transient period. A representative example indicated that the system obtains a steady state already during the time needed for the plate to move its penetration depth into the melt. As this takes a second or two, a steady state is reached long before the plate is withdrawn from the melt.

However, we did not consider the transient for the melt flow. The bulk melt will slowly start to move in the crucible, and it will take a long time to attain a steady state. However, the heat conductivity is large in an aluminium melt. The viscous boundary layer is thus so much thinner than the thermal boundary layer (see Section 2.11.1) that the slow change in melt circulation velocity probably is insignificant. We thus consider the steady-state assumption (Assumption 9) as a good approximation.

5.1.10 Horizontal isotherms in plate

All one-dimensional calculations were based on Assumption 10 saying that the heat conduction across the thickness of the plate is so high that there is no significant horizontal temperature difference inside the plate. The two-dimensional calculations in Section 2.9.2 show that the largest temperature difference between the centre and surface of the plate is close to the penetration point and for a plate thickness of $b = 0.5\,\text{mm}$ and feeding velocity of $v \approx 15\,\text{cm/s}$, it is only about 0.2 % of $(T_m - T_a)$, i.e. about 1°C. Even for five times thicker plates, the largest deviation is only one percent. The assumption of horizontal isotherms should therefore be quite acceptable.

5.1.11 Constant wedge temperature

Strictly, the wedge temperature cannot be constant since conduction of heat depends on a temperature gradient. However, as in the previous section, the horizontal temperature gradients are so small that Assumption 11 is nearly fulfilled. On the other hand, it could be discussed whether the wedge has the shape of a triangle because of the melting range, which makes the wedge break at some place as discussed in Section 5.1.2.

5.2 Melt flow and the liquid heat-transfer coefficient

In Section 2.11 we derived theoretical relations for the liquid heat-transfer coefficient h_l based on the boundary-layer theory. The approach requires laminar flow, and for a flat plate, transition to turbulence occurs around $Re_x = vx/\nu = 3\times10^5$ depending on the roughness of the surface and the literature source. Re_x increases with the distance x along the plate from the upstream edge of the plate and is at its maximum at the downstream end of the plate.

Converted to our system, and with a feeding velocity $v \sim 10\,\text{cm/s}$ and penetration depth $P \sim 10\,\text{cm}$, the largest Re_x becomes $Re_P = vP/\nu \sim 2 \times 10^4$. This confirms that we have laminar flow along the plate, so the approximation should be good. We will first consider the liquid heat-transfer coefficient when the plate is fed into a stagnant melt, when it is fed into a molten metal flowing along its surface.

5.2.1 Stagnant melt

From boundary-layer theory, it follows that the mean liquid heat-transfer coefficient for a plate that is fed into a stagnant melt is given by Equation (2.121):

$$h_l = \sqrt{\frac{4k_l^2 v}{\pi \alpha_l P}}. \tag{5.3}$$

This expression is not directly dependent on the melt temperature, but indirectly it is since P depends heavily on the melt temperature. Although its variation is damped by the square root, h_l varies from 18 000 to 32 000 $\mathrm{W/m^2K}$ for $v = 6.4\,\mathrm{cm/s}$ in the range 700 to 760°C. However, this is not a temperature phenomenon. The local heat-transfer coefficient is very large at the penetration point and decreases rapidly downwards. If the plate penetrates further down for some reason, the local heat-transfer coefficient will not change, but the mean one will decrease. The use of a mean h_l for all P is a weakness of the model resulting in giving an overestimate of P when P is small, and vice versa. This cannot be seen in the figures by comparing the curve fits and the experimental data because the fitting procedure will compensate for this.

However, we notice that the values of h_l predicted by the boundary-layer theory and the value obtained by curve fitting of the experimental data are of the same order of magnitude. Furthermore, the quiescent-melt experiments and the no-lacquer experiments are independent but still predict similar heat-transfer coefficients. Both points support the model.

5.2.2 Flowing melt

In the derivation of h_l for plates that are fed into a flowing melt, we got different expressions for V/v greater and less than B/P. However, it turns out that $V/v < B/P$ in all experiments performed. We can thus use Equation (2.125) exclusively:

$$h_l = \sqrt{\frac{4k_l^2 v}{\pi \alpha_l P}} \left(1 + \frac{VP}{3vB}\right), \tag{5.4}$$

where $B = 10\,\mathrm{cm}$ is the width of the plate. We can thus make an order-of magnitude estimate of the liquid heat-transfer coefficient h_l for a plate that is fed into a launder with flowing melt. With typical values $v = 10\,\mathrm{cm/s}$, $P = 5\,\mathrm{cm}$, and $V = 10\,\mathrm{cm/s}$, we get $h_l = 30\,000\,\mathrm{W/m^2K}$. As for the case of a stagnant melt, h_l varies with the melt temperature through P.

Table 4.5 shows that the values obtained from experiments seem to *decrease* with increasing melt velocity, contrary to expectations. However, the uncertainty in the values is so large that the decrease is hardly significant.

Finally, it is tempting to compare the liquid heat-transfer coefficient in stagnant and flowing melt. However, it varies considerably along the width of the plate in the latter case of melt flowing along the plate surface. This causes the plate end to slope as we saw in Figure 4.17 on page 97. The plate end will continue to slope as the width is increased, and the local penetration depth will increase downstream. Thus, the mean penetration depth will depend on the width of the plate, and a comparison with the stagnant-flow case is problematic.

5.3 Meniscus and shell start depth

In Section 1.6, we saw that a meniscus is formed at the intersection between a liquid and a solid surface. This is also what we observed when the aluminium plate was fed into the melt (Section 4.3.3). The video recordings did not offer much information about the formation of the meniscus, so an aluminium plate was moved manually up and down in the melt. The observations indicate that the meniscus dependents little on the surface tension and more on the oxide film. As a matter of fact, the melt surface "remembered" the last movement of the plate, that is, when the plate was pulled upwards and then kept at rest, the surface continued to curve upwards (about 5 mm), and vice versa.

A probable reason for this is the strength of the oxide skin and that the wettability of the melt on the plate changes due to the shell formation. When the plate is on its way down, the melt does not wet the plate because of the thin oxide layer on the plate and possibly also the oxide film on the melt. A shell forms at the point where the melt surface intersects or is sufficiently close to the plate surface. When the plate is stopped, the meniscus is probably kept turned downwards because the oxide film on the surface is connected to the top of the shell. Conversely, when the plate is pulled up, the part of the plate that has been immersed is covered with a shell, which is wetted by the melt. The meniscus turns upwards, and molten aluminium is pulled up with the shell. This will be discussed in Section 5.4.2.

Now, in Section 4.3.2, we saw that the shell starts further up on the side edges of the plate than on the plate surface. Furthermore, while we observed no significant meniscus on the edges of the plate during feeding, we note that the meniscus depth on the plate surface and the shell start depth are of the same magnitude: about 5 mm. It is natural to connect the two phenomena and assume that the shell starts at the point where the meniscus stops. No significant dependence on the feeding velocity or the melt temperature was found for the shell start depth and thus not for the meniscus depth either.

The existence of the meniscus introduces a source of error. When we applied

the experimental data to validate the model, we set $y = 0$ at the melt surface, as shown in Figure 2.2. This may lead to a systematic error in the penetration depth. However, the choice was made partly because the shell start depth was not obtainable for all plates, and partly because we can assume that this choice to some extent compensates that we neglected the heating of the plate above the melt surface (see Section 5.1.8).

5.4 Shell formation

5.4.1 Criterion for shell formation

Whether a shell was formed or not, the plate surface seemed untouched by the melt until some distance down into the melt, except for the thickening of the oxide layer. Sometimes it was even observed that the shell fell off during withdrawal. This suggests that where the meniscus ends, a thin *air film* continues down along the plate surface. Such an air film is a common phenomenon for solids or liquid jets penetrating into a liquid at sufficiently large velocity, and especially for nonwetting liquids (see Section 1.6). Thus, the melt does not wet the plate surface. The shell was found to attach to the plate further down, indicating that the air film vanishes at some distance below the melt surface when a shell is present. This should also be the case without shell formation. Otherwise, air would be entrained and cause bubble formation, which was not observed.

The mathematical criterion presented in Section 2.10 tells us whether the shell would grow or vanish once it is initiated: $q_g > q_l$ implies that it would grow. However, shell formation might not be initiated at all, depending on the thickness of the air film. The heat transfer across the air film can be expressed as $q_f = h_f(T_f - T_p)$, where the index f denotes *film*, and T_f is the temperature at the interface between the air film and the melt. If the air film is thick, then h_f is small, and the heat transfer from the bulk melt may be sufficient to avoid initiation of shell formation. Now, once a shell is formed, there is no reason to believe that the film thickness will change, so we may assume that $h_f = h_g$. Hence, our criterion for shell formation cannot only predict shell formation, but also predict that no shell should be formed. Because the air film should be formed in any case, the thermal resistance should be independent of shell formation, indicating that shell formation in itself is of minor importance for the melting rate of the plate.

The shell criterion gives a critical temperature $T_{l,\mathrm{crit}}$ given by $\theta_{l,\mathrm{crit}} = 1 + Bi/Nu$. Table 5.1 lists the heat-transfer ratio for all experiment groups. Its uncertainty

Table 5.1: The ratio of the heat-transfer coefficients for the quiescent-melt, launder, and no-lacquer (above 700°C) experiments

Experiments	Bi	Nu	Bi/Nu	$T_{l,\mathrm{crit}}$
Quiescent melt	0.010 ± 0.001	0.049 ± 0.001	0.22 ± 0.02	794 ± 13°C
Launder, all V	0.013 ± 0.003	0.057 ± 0.006	0.22 ± 0.06	791 ± 35°C
No-lacquer	0.016 ± 0.002	0.049 ± 0.002	0.33 ± 0.04	852 ± 27°C

is (Squires 1989, Tab. 4.1):

$$\Delta\left(\frac{Bi}{Nu}\right) = \frac{Bi}{Nu}\sqrt{\left(\frac{\Delta Bi}{Bi}\right)^2 + \left(\frac{\Delta Nu}{Nu}\right)^2}. \tag{5.5}$$

We now return to Section 4.3.1, where Figures 4.9–4.11 correlate shell formation on individual plates to the melt temperature. We ignore the open circles as they are ambiguous concerning shell formation, and set the filled circles (shell is formed) up against crosses and triangles (little or no shell). From the figures, the critical superheat $\theta_{l,\mathrm{crit}} - 1$ should be around 0.26 for the quiescent-melt experiments, around 0.17 for the launder experiments, and above 0.18 for the no-lacquer experiments as there were very few cases without shell. Although these observed values differ somewhat from those calculated above, the model predicts $\theta_{l,\mathrm{crit}}$ reasonably well.

This leads us to Section 4.4.2 where we had several good fits for the high-flow-velocity launder experiments, as seen in Table 4.4. They were obtained by small variations in the guestimate values used in the curve fitting. The ratio Bi/Nu was found to differ between the sets of possible parameters, i.e. the critical temperature varied. For this little group of experiments, there were no plates in the category "no shell", and three in "maybe no shell", at $\theta_l - 1 = 0.141$, 0.157, and 0.175. We thus expect that the critical superheat is around 0.17 or higher. This leaves two possibilities from which the highest Bi/Nu was chosen. χ^2 differed insignificantly. It should, however, be emphasized that the uncertainty is large, as the bootstrap method confirmed.

Before leaving this subject, it is necessary to comment the fact that a shell was often formed on one side only, or that the shell covered complementary spots on both sides of the plate (Section 4.3.1). We have not been able to find the reason for this, but we can outline a few possibilities: Although every effort was made to straighten the plate in the feeding mechanism, it is not likely that the plate penetrated the melt surface perfectly vertically. When a plate is fed a little askew, the air-film thickness may differ on the two sides of the plate and thus give rise to shell formation on one side and not on the other. Another possible reason is that once a shell is formed on one side, it may influence the situation

on the other side in some way. Furthermore, as we mentioned in Section 3.3, one side of the AA1050 plates was cleaner than the other side. The shell formation on the two sides seemed to differ in character, but no unambiguous correlation was found.

5.4.2 Shell thickness

We see from the micrographs in Section 4.1 that the thickness of the shell is of the same order of magnitude as the plate, i.e. $\xi_s \sim 1$. Figure 5.3 shows a calculated contour of a shell at typical values ($Bi = 0.01$, $Nu = 0.05$, $\theta_l = 1.1$, $Pe = 0.7$). Iteration of the equation for the shell growth, Equation (2.16), gives a maximum shell thickness of $\xi_s = 0.14$, which is about 10–20 % of that measured.

The main reason for this underestimate is probably that the melt wets the shell and thus sticks to the shell when the plate is pulled up. An estimate for the thickness of this layer of melt can be obtained from the viscous boundary-layer thickness $\delta \sim \sqrt{\nu y / v}$ (see Section 2.11.1). With withdrawal velocity $v \sim 50\,\mathrm{cm/s}$, we get $\delta \sim 0.2\,\mathrm{mm}$ a distance $y \sim 3\,\mathrm{cm}$ below the start of the shell. This melt solidifies in contact with the cold air and seems to be a part of the shell. In Figures 4.3 and 4.4 in Section 4.1, we see that the shell contains small grains (equiaxed dendrites) close to the outer surface while the rest of the shell consists of a columnar (oriented) dendritic structure (Fisher 1989, Fig. 4.18). While the plate is in the melt, there is a mix of solid and liquid aluminium (a mushy zone) gradually changing from completely solid close to the plate to completely liquid in the bulk melt. Oriented dendrites point out from the plate along the

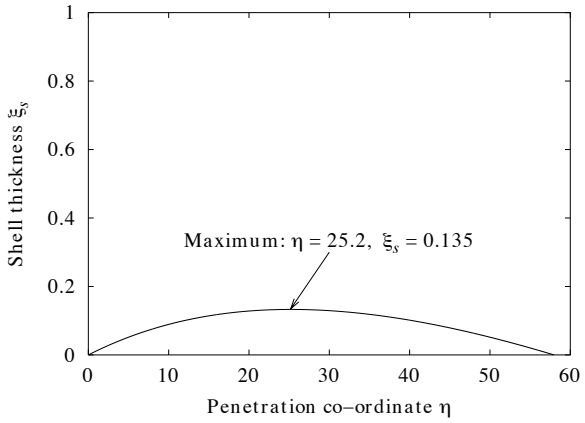

Figure 5.3: Shell thickness relative to the plate thickness along a plate melted at $\theta_l = 1.10$ (724°C) with $Bi = 0.01$, $Nu = 0.05$, and $Pe = 0.7$ and with the properties of pure aluminium.

large, positive temperature gradient. When the plate is withdrawn, the temperature gradient is reduced and becomes negative and small, resulting in growth of equiaxed dendrites and thus small grains, as observed. The layer of the shell consisting of small grains is most certainly formed due to solidification in air. Also parts of the columnar dendritic structure are probably solidified after withdrawal. This explains at least partly why the measured shell thickness is greater that the calculated. Furthermore, Assumption 7 of a constant shell temperature may also result in understimating the shell thickness.

5.5 The gap heat-transfer coefficient and lacquer

5.5.1 The gap heat-transfer coefficient

The heat-transfer coefficients h_g obtained for the gap between the shell and the plate in the present work varies from 3900 to 8500 $\mathrm{W/m^2K}$. This is in good agreement with values reported in the literature (see Sections 1.5.2 and 1.5.3). The most interesting values are those reported for aluminium: 2500 $\mathrm{W/m^2K}$ (Goudie and Argyropoulos 1995) and 4000 $\mathrm{W/m^2K}$ (Røhmen et al. 1995). The former is notably lower than our values, especially when taking into account that the heat transfer is enhanced due to thermal contraction of the shell around the expanding addition. Nevertheless, they are of the same order of magnitude.

The gap thickness can be estimated from h_g by assuming that it does not change and is filled with air. The thermal conductivity k_{air} of air varies from 26 to 68×10^{-3} W/mK in the temperature interval 300 to 1000 K (Weast 1979, p. F-13), seemingly independent of pressure. The mean is about 50×10^{-3} W/mK, and with a gap heat-transfer coefficient h_g of about 5000 $\mathrm{W/m^2K}$, this corresponds to a gap size of about $\delta = k_{\mathrm{air}}/h_g = 10\,\mu$m. Even if no shell is formed, there should be a gas film with the same thickness as indicated in Section 5.4.

5.5.2 The effect of lacquer

The lacquer increased the thermal resistance considerably. We obtained a total heat-transfer coefficient h_t of about 2400 $\mathrm{W/m^2K}$, i.e. about half that of the gap in the no-lacquer case. The thickness of the polyester lacquer is about 5 μm, and the thermal conductivity of cast polyester is about 0.17–0.20 W/mK (Perry and Green 1984, p. 23-54), so $h_{\mathrm{lacq}} \approx 40\,000$ W/mK. The total thermal resistance $1/h_t$ can be considered to consist of three terms:

$$\frac{1}{h_t} = \frac{1}{h_l} + \frac{1}{h_{\mathrm{lacq}}} + \frac{1}{h_f}, \tag{5.6}$$

where h_f is the unknown heat-transfer coefficient of a gas film between the plate or lacquer and the melt. We assume that h_l is the same as for the no-lacquer experiments, about 17 000 W/mK. This leaves $h_f \approx 3000$ W/mK, or a gas-film thickness of $\delta \approx 16\,\mu$m, about 50 % thicker than for the plates without lacquer. Gas formation due to combustion of lacquer in addition to the air film following the plate may be one reason for this.

Based on the above reasoning, the critical temperature can now be calculated by dividing h_f (neglecting h_{lacq}) by h_l: $\theta_{l,\text{crit}} \approx 1 + h_f/h_l = 1.18$, or $T_{l,\text{crit}} \approx 760°$C. However, the experiments showed no shell formation, so a much lower critical melt temperature was expected. This indicates that h_f is overestimated or h_l underestimated. Apart from decreasing h_f, the gas formation probably increases the convection in the boundary layer and thus increases h_l compared to the no-lacquer experiments.

5.6 Snap-off and uncertainties in penetration depth

The snap-off phenomenon was observed in Section 4.2, and in Section 5.1.2, the presence of a melting range was discussed. Thus, in the wedge region there will be a gradual transition from solid to molten metal downwards; the mushy zone. When the plate is withdrawn, viscous and inertia forces resist the fast movement and acceleration upwards. The mechanical strength of the mushy zone is limited, and at a certain point, the lower part of the plate snaps off and returns to the melt, as seen in Picture 8 in Figure 4.6. The snap-off point seemed to vary a little from measurement to measurement.

Apart from the mechanical strength of the mushy zone, oxide films may also influence the snap-off. Presence of air in the gap between the shell and the plate gives oxidation of the inner side of the shell as well as an increased thickness of the oxide layer on the plate surface due to the increased temperature of the plate. These oxide films follow down with the plate and disappear into the bulk melt as the plate melts away. When the plate is withdrawn, they envelope the wedge region and enhance its mechanical strength. This explains the droplet of melt that was observed at the end a number of plates as well as the fact that the lower part of the plate was soft and dangled a few seconds after withdrawal.

Thus, that the snap-off effect influences the penetration depth P. It seems to have played an important role for the experiments with AA3105 alloy, with and without lacquer. These experiments seemed to give a linear relation between P and the melt temperature T_l. Such a relation is unphysical since P should go to infinity when T_l approaches the melting point T_m. We suspect that the snap-off may be a cause for this linearity since the AA3105 alloy has poorer mechanical

strength close to the melting point than the AA1050 alloy due to its greater melting range. This may give rise to earlier snap-off for large than for small P during withdrawal. However, P is probably also affected by the thicker initial oxide layer on the plates due to anodization (eloxal) as well as differences in the mechanical strength of the oxide films due to the presence and oxidation of alloy elements.

Another source of error in the measurement of P may be the order of the experimental runs. They were mostly performed in series of eight runs, the first two at feeding velocity $v = 6.4\,\mathrm{cm/s}$, the next two at $9.6\,\mathrm{cm/s}$, and so on, all at approximately the same melt temperature T_l. If an unknown parameter that influences the measurement of P, changes slowly during a day of experiments, it could mistakenly be interpreted as an effect of the change in v or T_l. In practice, little could be done about the melt temperature since changing this between each run would mean hours of waiting. However, in retrospect, the eight runs in the same series should have been performed in random order to reduce the possible effect of an unknown parameter.

Finally, the estimated standard deviation of the penetration depth for each plate, $s_{P,i}$, was considered an underestimate of the uncertainty (Section 3.7.1). A better estimate for s_P may be obtained from Equation (3.5):

$$\chi^2(Bi, Nu) = \sum_{i=1}^{N} \left[\frac{\ln \Pi_i - \ln \Pi}{s_{\Pi,i}/\Pi} \right]^2. \tag{5.7}$$

Π is here a shorthand for $\Pi(\theta_{l,i}, Pe_i; Bi, Nu)$. The expected value of χ^2 for a moderately good fit is the number of degrees of freedom ν (see Appendix E). If we assume that our fit is moderately good, we should have $\chi^2 \approx \nu$. To achieve this, we adjust the standard deviation $s_{\Pi,i}$ by multiplying it by a constant γ, which is found by rearranging Equation (5.7):

$$\gamma^2 = \frac{1}{\nu} \sum_{i=1}^{N} \left[\frac{\ln \Pi_i - \ln \Pi}{s_{\Pi,i}/\Pi} \right]^2 = \frac{\chi^2}{\nu}. \tag{5.8}$$

γ is tabulated in Table 5.2 for all the experiments. The new estimate for the standard deviation is thus $\gamma s_{P,i}$.

5.7 Thick plates

Figure 4.28 in Section 4.6 shows that the model predicts shorter penetration depth than the experimental results indicate for thicker plates ($b = 1.50\,\mathrm{mm}$ and $2 \times 0.54\,\mathrm{mm}$). We assumed that we can use the same heat-transfer coefficients

Table 5.2: Summary of fitted *Bi* and *Nu* with the overall uncertainty factor γ for each experimental group

Experiments	*Bi*	*Nu*	χ^2	ν	γ
Quiescent melt	0.011	0.050	352	93	1.9
Launder, all V	0.012	0.055	1272	68	4.3
low V	0.021	0.064	148	15	3.1
med. V	0.012	0.055	883	24	6.1
high V	0.010	0.054	154	25	2.5
No-lacquer ($T_l > 700$°C)	0.016	0.049	26.4	26	1.0
Lacquer ($T_l > 700$°C)	—	0.0075	139	30	4.6

as for the thin plates of the same alloy since there is no indication that they should change with the thickness of the plate. Two possible explanations are that the increased thickness makes the isotherms in the plate less horizontal or the transient more important, or both.

In Section 2.9.2 we derived a relation for the deviation from horizontal isotherms, expresses as the maximum temperature difference between the centre and the surface of the plate, $\Delta\theta(\eta_{\max})$. Table 2.2 listed some values for this for different plate thicknesses and feeding velocities. It is clear that the temperature gradients across the thickness of the plate depend more on the plate thickness itself than the feeding velocity. Even for five times thicker plates, the largest temperature difference between the centre and the surface of the plate is only about 1 % of $T_m - T_a$ or 6°C. Since the values in the table are typical for the experiments in this work, the deviation from horizontal isotherms is insignificant and cannot account for the underestimated penetration depth.

Nor does the transient period seem to explain the discrepancy. Since the assumption of horizontal isotherms holds, we should be able to use the calculations of the transient period in Section 2.8 also for the thick plates. Figure 5.4 shows that a steady state is achieved after about $t = 1\,\text{s}$ ($\tau = \alpha t/b^2 = 35$) for plates triple thickness (1.50 mm). This is still not more than the time it takes to feed the plate its penetration depth into the melt, so a steady state should have been attained in the experiments.

However, the snap-off phenomenon is a possible cause for the longer penetration depth for the thicker plates. The viscous forces that resist the withdrawal of the plate depend on the surface, while force with which the plate is pulled up acts on the whole cross section of the plate. The thicker the plate, the larger the cross section, but the surface is approximately the same. It is thus probable that the snap-off occurs later for the thick plates, resulting in longer measured penetration depth. It could thus be discussed whether the measurements with

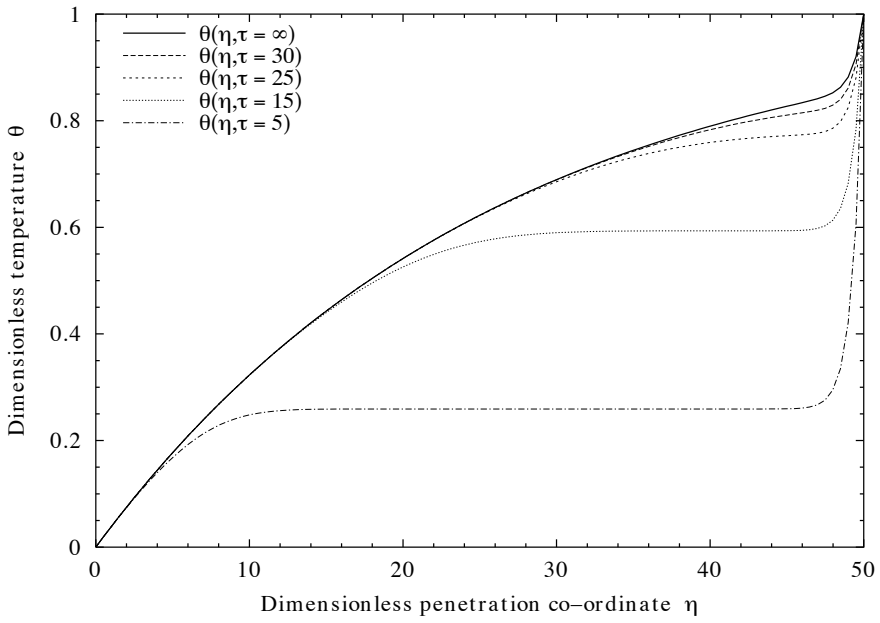

Figure 5.4: The transient temperature profile of an initially cold thick plate of thickness $3b$ immersed in a warm medium at same v and h_g as the thinner plate in Figure 2.11 page 55, i.e. $Pe = 1.5$ and $Bi = 0.03$.

the thicker plates represent the actual penetration depth better than those with thin plates. A study of the mechanical strength of the mushy zone may be a means to a better understanding of the snap-off mechanism and thereby the connection between the measured penetration depth and the depth that the plate penetrates.

5.8 The goodness of the main model

We have attained good agreement between the experiments and the developed model (Model 1), except when applied to the thicker plates and higher feeding velocities. In Sections 2.5 and 2.6, we developed two additional, simpler models describing a system without shell formation (Model 2) and one without a gap between the shell and the plate (Model 3). Figures 5.5 to 5.7 show the results of weighted fitting of each of the three models to experimental data. Only the quiescent-melt data are treated here. The fitting parameters obtained are listed in Table 5.3 together with χ^2 and the number of degrees of freedom ν for each model.

In the figures, we see that the two alternative models (Model 2 and 3), and in particular Model 2, tend to overestimate the penetration depth for high melt

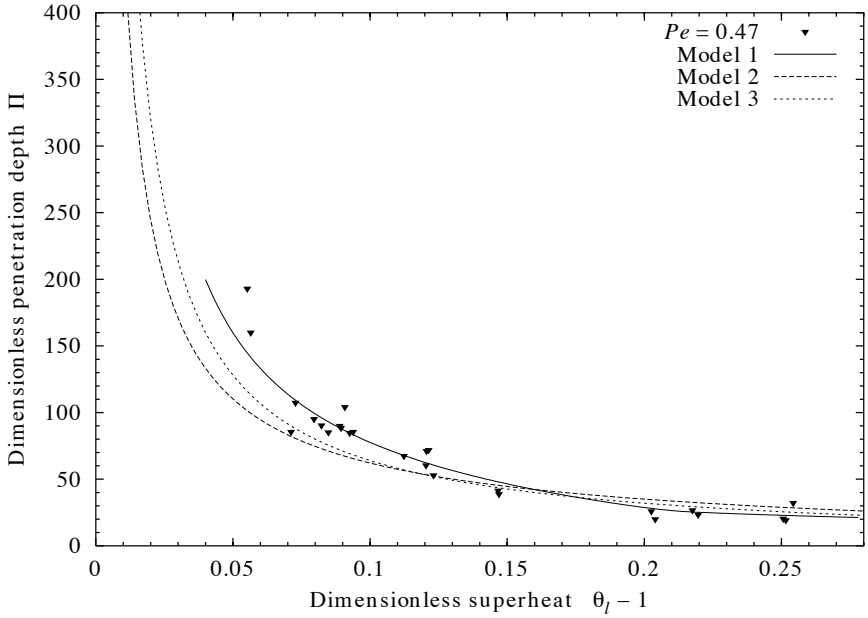

(a)

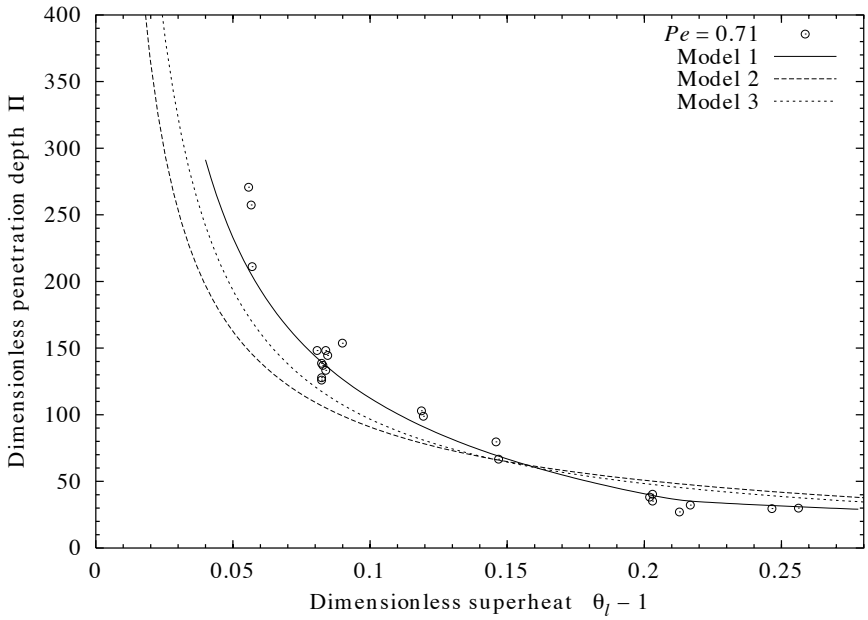

(b)

Figure 5.5: The measured penetration depth Π versus superheat $\theta_l - 1$ at $Pe = 0.47$ (a) and 0.71 (b) for the quiescent experiments. The lines are the predictions of the three models.

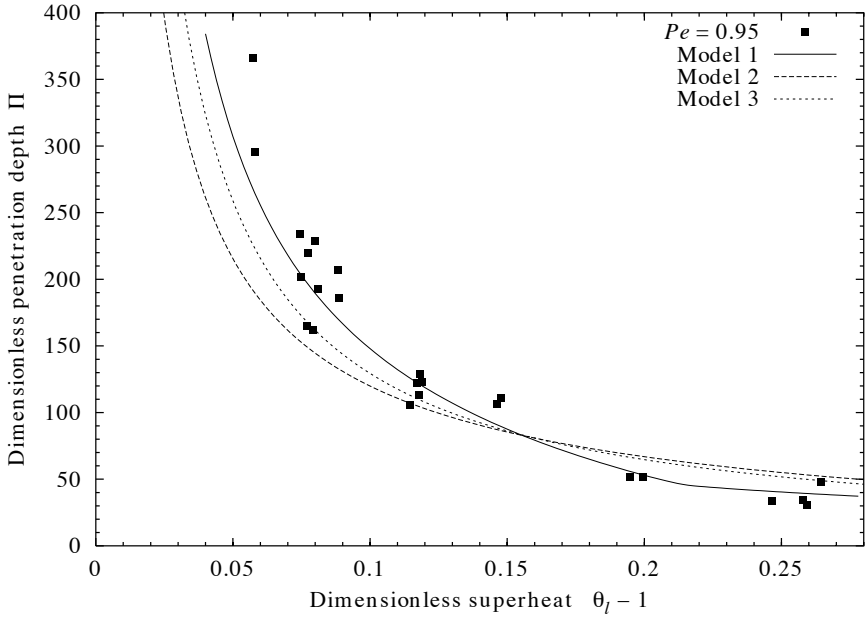

(a)

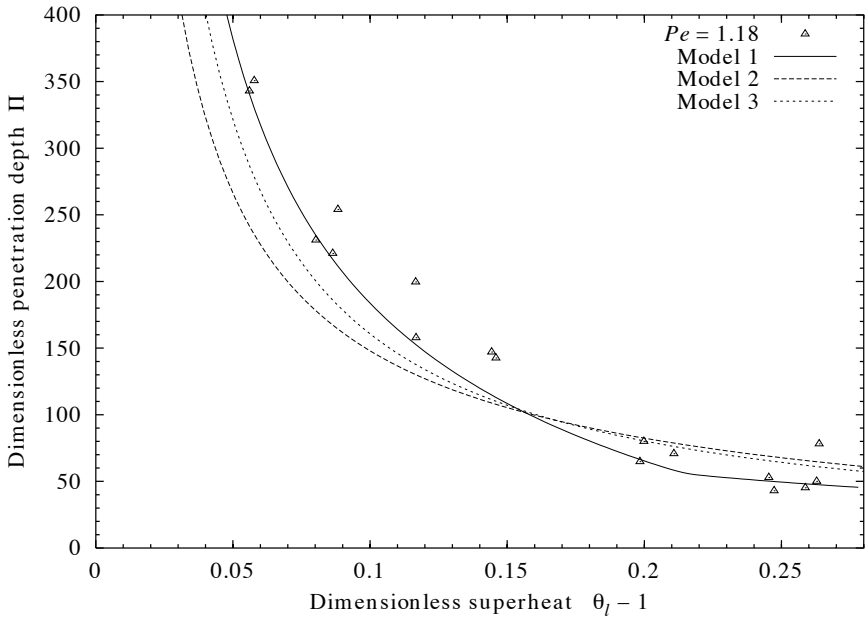

(b)

Figure 5.6: The measured penetration depth Π versus superheat $\theta_l - 1$ at $Pe = 0.95$ (a) and 1.18 (b) for the quiescent experiments. The lines are the predictions of the three models.

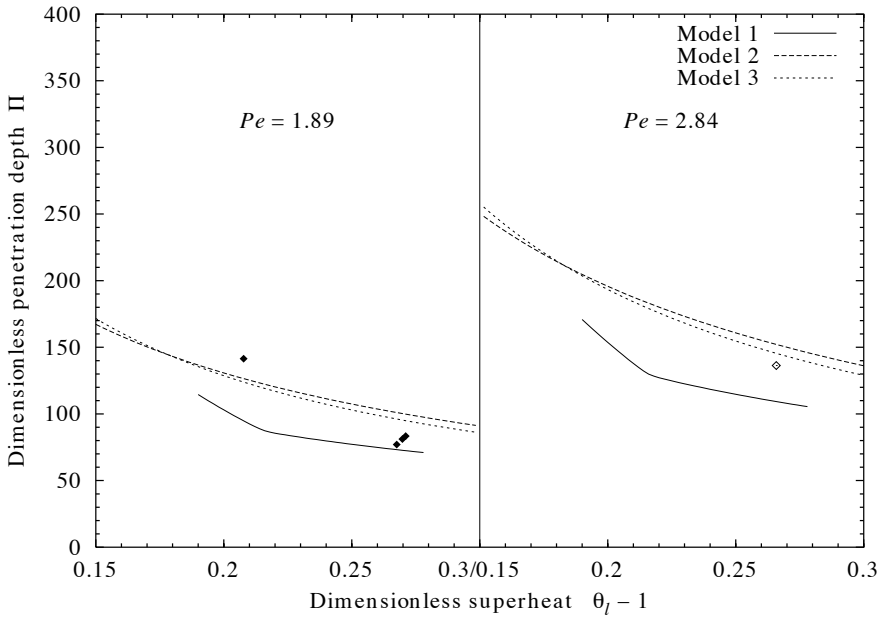

Figure 5.7: The measured penetration depth Π versus superheat $\theta_l - 1$ at $Pe = 1.89$ and 2.84 for the quiescent experiments. The lines are the predictions of the three models.

Table 5.3: The heat-transfer coefficients obtained for the quiescent-melt experiments when applying all three models. ν is the degrees of freedom and χ^2/ν expresses the goodness of the fit.

	h_g [W/m^{2}K]	h_l [W/m^{2}K]	χ^2	ν	χ^2/ν
Model 1*	3900 ± 400	18700 ± 500	353	93	3.8
Model 2	$h_t = 12900 \pm 400$		1814	94	19.3
Model 3	$h_t = 22400 \pm 400$		1024	94	10.9

* by means of bootstrapping

temperatures and underestimate it for low temperatures. This can be expressed qualitatively by studying the value of χ^2, which is the sum of squared deviations from the model prediction of the penetration depth. Quantitatively, we could test the goodness of the fits by using the χ^2-distribution, but due to the underestimation of the standard deviation in P, we get too large χ^2. However, by dividing χ^2 by the number of degrees of freedom ν, we get an expression for how much the experimental data in average deviate from each model prediction. χ^2/ν is listed for all three models in Table 5.3. Hence, Model 1 makes the best prediction and Model 2 the worst.

Now, neither Model 2 nor Model 3 treat the thermal resistance of the gas film or gap separately from the thermal resistance of the melt boundary layer, so it becomes included in a single heat-transfer coefficient h_t. Model 1, however,

considers the gap separately, and only in the shell region (through h_g) while the heat-transfer coefficient for the melt boundary layer, h_l, applies for the whole penetration depth of the plate. As Model 1 gives the best curve fit, followed by Model 3 and then Model 2, this is taken as proof for the necessity of employing two heat-transfer coefficients and the importance of including the gap between the shell and the plate.

For the lacquer experiments, Model 2 was employed. However, to improve this model for such plates without shell, the penetration depth of the air film should be studied.

Chapter 6

Conclusions and recommendations

6.1 Model and experiments

An analytical, one-dimensional, steady-state model has been developed for the melting of a thin metal plate that is fed into a melt. The model includes a shell that solidifies on the plate surface, and considers a gap between the shell and the plate. The gap introduces a thermal resistance $1/h_g$ in addition to the thermal resistance $1/h_l$ of the melt boundary layer. To the knowledge of the author, this system has not been studied for plates before.

An experimental apparatus was designed and constructed for feeding of a thin, continuous plate of aluminium from a coil into a stagnant bath of molten aluminium or into a launder with molten aluminium flowing along the surface of the plate. Experiments were performed to validate the model and to study the effect of lacquer and melt flow past the plate. Lacquer was found to prevent formation of a shell and gave a considerably lower melting rate. The launder experiments showed that the penetration depth of the plate would vary with the plate width because the heat-transfer coefficient varies in the flow direction along the width of the plate. Comparison with the stagnant-melt experiments was therefore difficult. No significant correlation between melt-flow velocity and melting rate was found.

The model was fitted to the experimental data by comparing the measured penetration depth of the plate to that calculated. The fitting parameters were the thermal resistances of the gap between the shell and plate, $1/h_g$, and of the thermal boundary layer of the melt, $1/h_l$. Reasonably good agreement with

calculations and literature values was achieved. The model underestimated the penetration depth for thicker plates, probably because of the weakening of the plate in the mushy zone. Thus, a thick plate snaps off further down during withdrawal than does a thin plate.

Introductory measurements of the temperature in the plate were performed, and a few temperature profiles were produced and compared to the model. The method needs improvement.

A temperature criterion was presented for whether a solidified shell is formed or not. The experiments showed qualitatively the predicted behaviour. The criterion implies that formation of shell can be prevented by preheating the plate or increasing the melt temperature, or by reducing the ratio h_g/h_l, for instance by increased convection in the melt or by the presence of lacquer or oil on the plate surface. Preheating the plate or increasing the melt temperature will increase the melting rate, but obviously, lacquer or oil will not. An air film with a thermal resistance similar to the gap is believed to form on the plate surface independently of whether a shell is formed or not. It is concluded that it is mainly this thermal resistance that reduces the melting rate, and not the shell itself.

Two additional models were developed, one which does not include a shell and the other disregarding the thermal resistance between the shell and the plate. Both models gave much poorer predictions of the penetration depth than the main model. This was taken as a confirmation of the existence of the gap between the plate and the melt.

6.2 Industrial implications

The motivation for the present work was the metal losses during remelting of aluminium scrap in the recycling industry. In Section 1.8, we suggested rolling the scrap to a strip and feeding it directly into a melt. The present model, developed for thin plates, is a first stage towards a comprehensive model describing the suggested system.

When automating such a scrap-feeding system, the model can probably be used to control the process if the material properties and heat-transfer coefficients are adapted to the strip to be charged and the degree of stirring of the melt in the charging well. The feeding velocity v could be optimized continuously depending on the process parameters to give the highest possible melting rate without driving the strip into the bottom of the well. The melting capacity can then be calculated by $\dot{m} = \rho v B b$ where ρ, B, and b are mean bulk density, width,

and thickness of the strip.

6.3 Recommendations for further work

The model should be tested further by improving the measurements of the temperature in the plate, and the shell temperature should be measured if at all possible. An experimental study of the extent and characteristics of the three regions of the main model should also be performed, with focus on the mushy zone where the plate snaps off during withdrawal.

In order to improve the model, it is likely that a varying shell temperature must be accepted, in which case a two-dimensional study becomes necessary and numerical simulations must then undoubtedly be employed. The same is the case if we want to describe the feeding and melting of plates much thicker than those used in this work or of strips of rolled scrap. The liquid heat-transfer coefficient should also be allowed to vary, and the snap-off mechanism should be included in the calculations. The present model can provide starting and reference values for such simulations.

Appendix A

Apparatus drawings

A.1 Water model

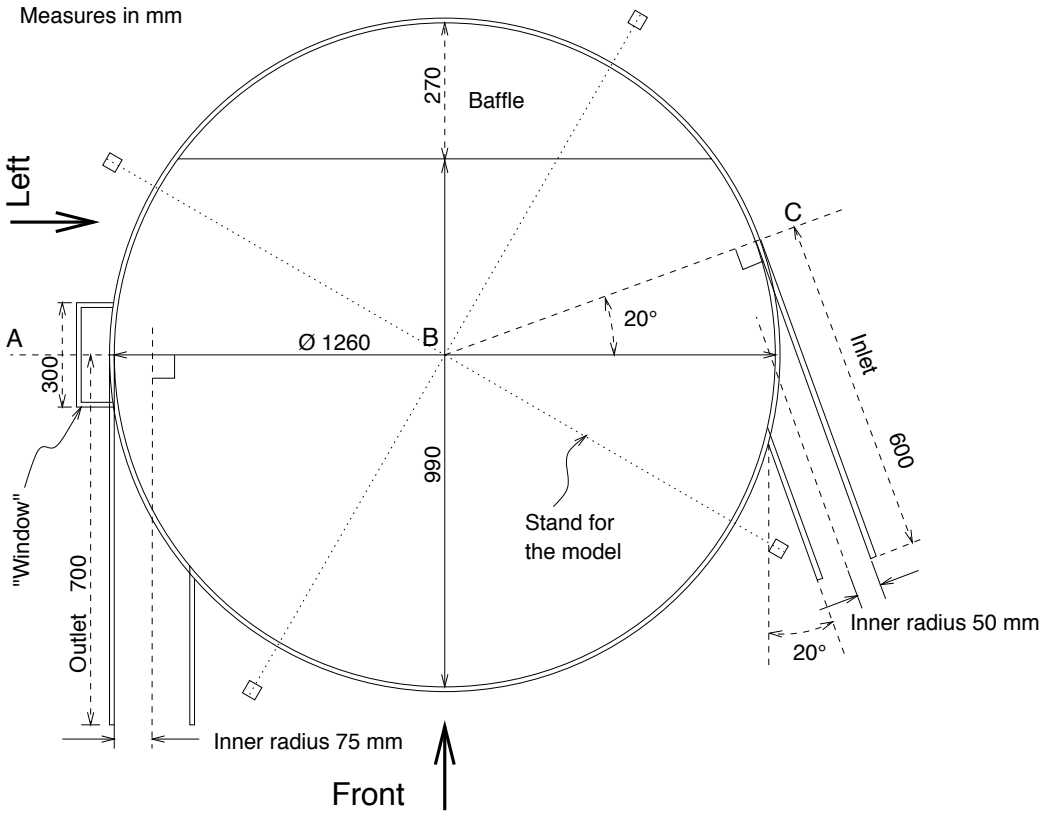

Figure A.1: Water model of vortex chamber seen from top. Vertical sections are shown in the following figures. The *window* is a pocket filled with water to avoid refraction of the light when looking into the chamber.

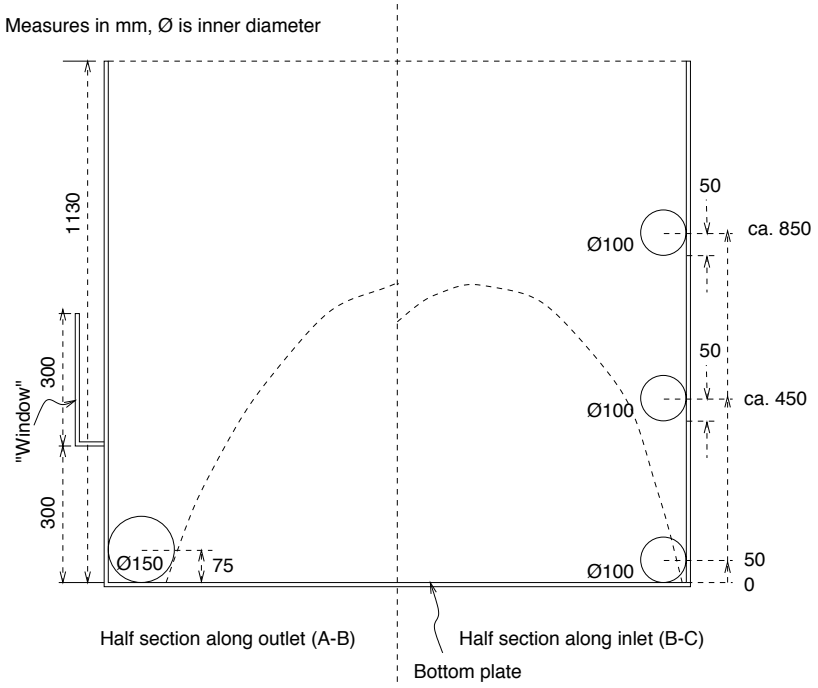

Figure A.2: Water model of vortex chamber seen from **Front**

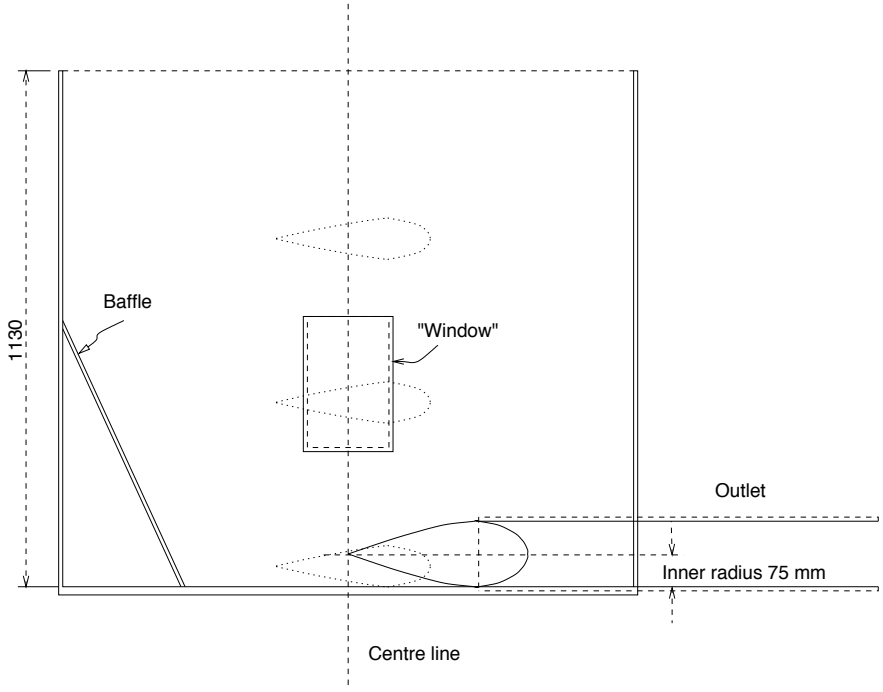

Figure A.3: Water model of vortex chamber seen from **Left**

A.2 Feeding apparatus

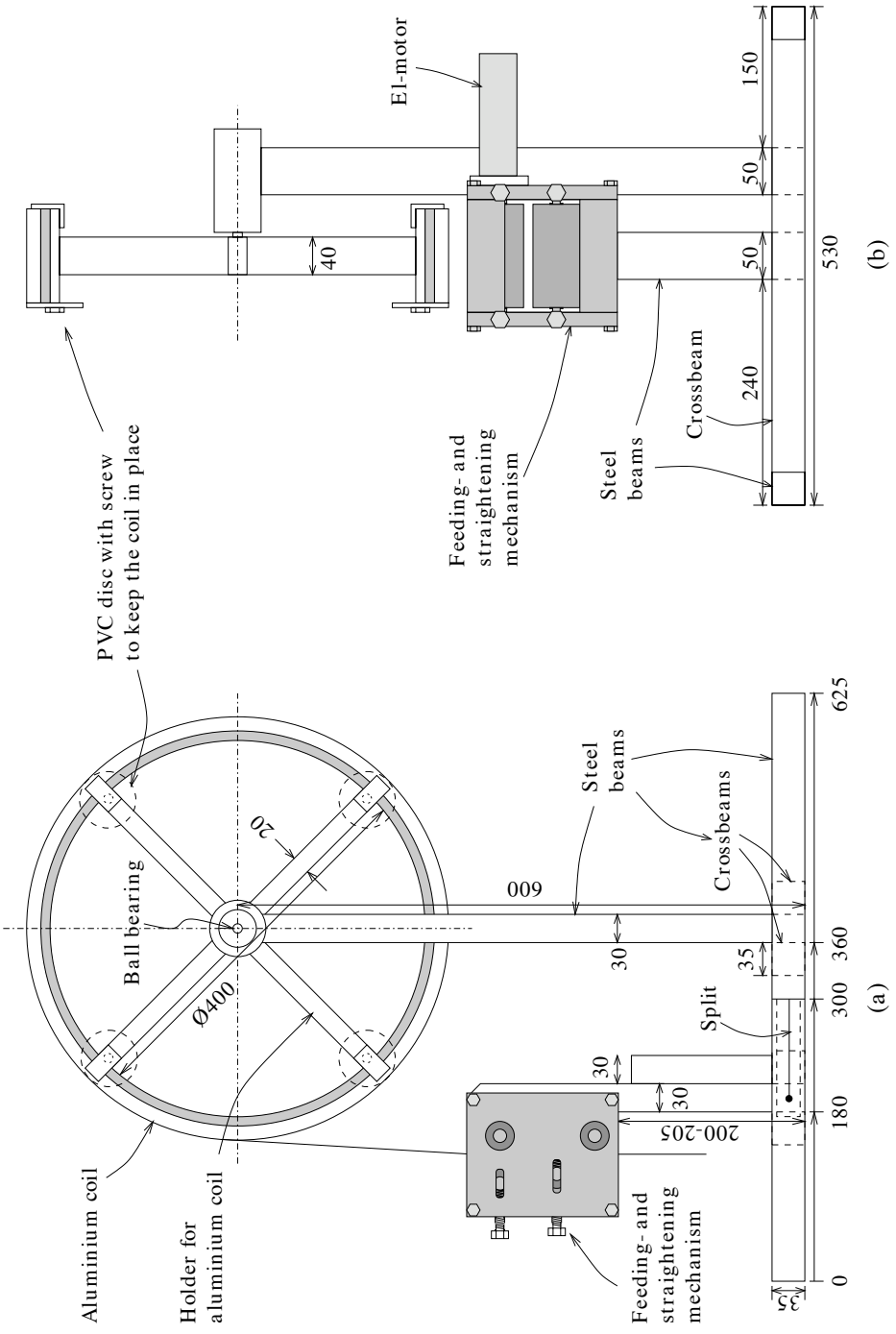

Figure A.4: Feeding apparatus from right (a) and front (b)

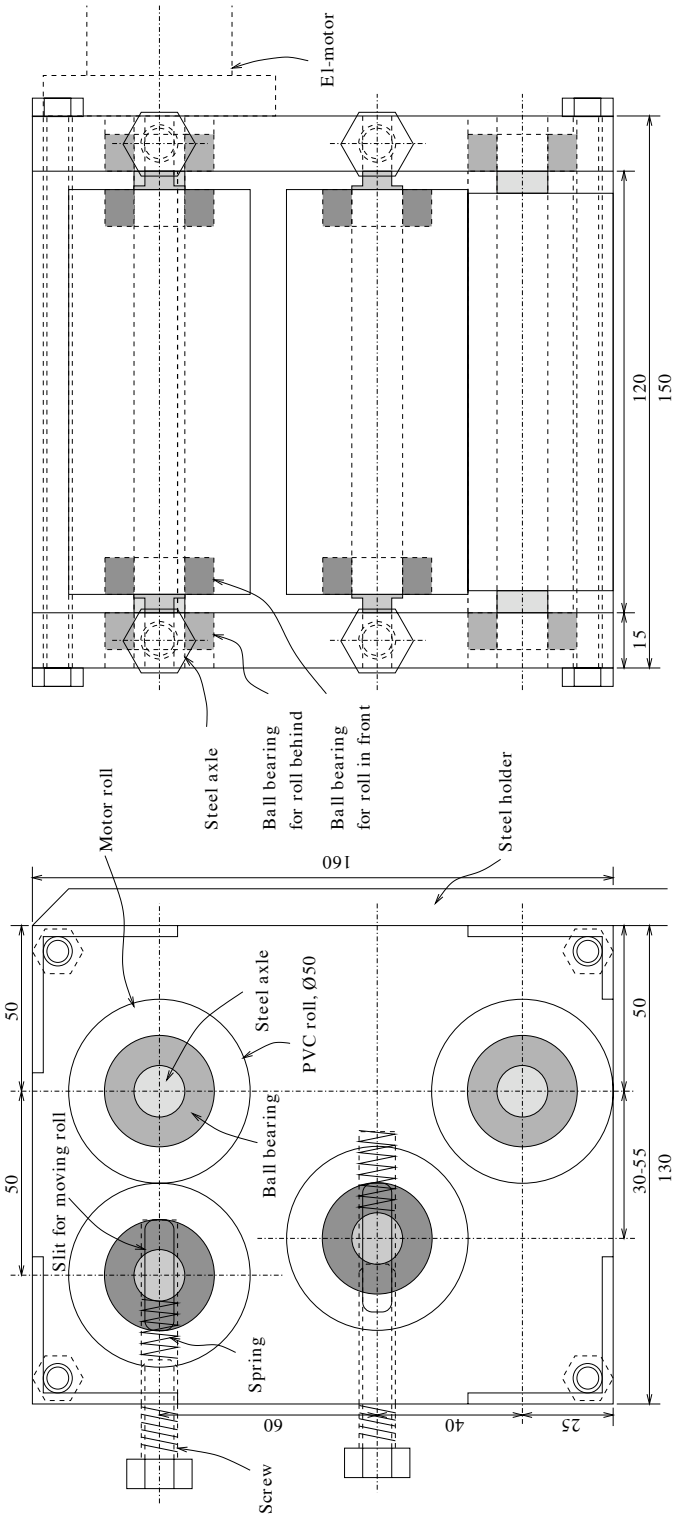

Figure A.5: Feeding and straightening mechanism from right (a) and front (b)

Appendix B

Material properties

B.1 Physical properties of pure aluminium

Table B.1 lists the material properties of pure aluminium, while Table B.2 tabulates values of the temperature-dependent properties. The values of the density, the specific heat, the viscosity, and the thermal conductivity are briefly discussed in Sections B.1.1 to B.1.4. Section B.2 compares the properties of pure aluminium to a few aluminium alloys. In this thesis, the properties of pure aluminium are used except for the thermal conductivity and the melting point, which vary with the alloy.

B.1.1 Density

The density of solid aluminium varies very little with the temperature. The expansion coefficient β is about $23.2 \times 10^{-6}\,\mathrm{K}^{-1}$ at room temperature ($T_a = 25°\mathrm{C}$) and $26.5 \times 10^{-6}\,\mathrm{K}^{-1}$ at 400°C (Knacke et al. 1991). Assuming a mean expansion coefficient of $26 \times 10^{-6}\,\mathrm{K}^{-1}$ from room temperature to the melting point T_m, we have the following relation for the density (in $\mathrm{kg/m^3}$):

$$\rho(T) = 2700 - 0.07(T - T_a), \qquad \text{for } T_a < T < T_m. \tag{B.1}$$

The average density in this temperature range thus becomes

$$\bar{\rho} = \frac{\rho(T_m) + \rho(T_a)}{2} = 2680\,\mathrm{kg/m^3}.$$

In the liquid state, the density of aluminium (in $\mathrm{kg/m^3}$) has the following temperature dependence (average of Knacke et al. 1991, Bolz and Tuve 1970, and

Table B.1: Some material properties of pure aluminium. Note that these values may differ from reference to reference. The quantities are averages in the intervals 25–660°C for the solid state and 660–800°C for the liquid state.

Mean solid property		Value (SI)	Reference
Density	ρ	$2680\,\mathrm{kg/m^3}$	Sec. B.1.1
Specific heat	c	$1048\,\mathrm{J/kg\,K}$	Sec. B.1.2
Thermal conductivity[a]	k	$229\,\mathrm{W/mK}$	Sec. B.1.4
Thermal diffusivity	α	$80 \times 10^{-6}\,\mathrm{m^2/s}$	$\alpha = k/\rho c$
Latent heat of melting	L	$397\,\mathrm{kJ/kg}$	Brandes and Brook (1992)
Mean liquid property		**Value (SI)**	**Reference**
Density	ρ_l	$2360\,\mathrm{kg/m^3}$	Sec. B.1.1
Specific heat	c_l	$1175\,\mathrm{J/kg\,K}$	Table B.2
Thermal conductivity	k_l	$93\,\mathrm{W/mK}$	Sec. B.1.4
Thermal diffusivity	α_l	$34 \times 10^{-6}\,\mathrm{m^2/s}$	$\alpha_l = k_l/\rho_l c_l$
Kinematic viscosity	ν	$0.50 \times 10^{-6}\,\mathrm{m^2/s}$	Sec. B.1.3

[a]Varies considerably with alloy. Use bold figures in Table B.4 instead.

Lide 1997):

$$\rho_l(T) = 2380 - 0.26(T - T_m), \qquad \text{for } T > T_m. \tag{B.2}$$

B.1.2 Specific heat

The specific heat (in J/kgK) of aluminium is approximately constant in the liquid state. In the solid state, it varies as follows with the temperature (in K; Knacke et al. 1991):

$$c(T) = 744 + 0.487T + 1.221 \times 10^6 T^{-2}. \tag{B.3}$$

The mean specific heat from $T_a = 298\,\mathrm{K}$ to $T_m = 933\,\mathrm{K}$ is

$$\bar{c} = \frac{1}{T_m - T_a} \int_{T_a}^{T_m} c(T)dT = 1048\,\mathrm{J/kgK}.$$

B.1.3 Viscosity

The ten experimental values of the viscosity (in kg/ms = Pas) of molten aluminium between 662 and 833°C from Lide (1990, p. 6-156) are well fitted by

$$\mu(T) = 1.37 \times 10^{-3} - 1.85 \times 10^{-6}(T - T_m). \tag{B.4}$$

However, they deviate by 10–15 % from the relation given in Brandes and Brook (1992, p. 14-7) (T in K):

$$\mu(T) = \mu_0 e^{E/RT} = 0.149 \times 10^{-3} e^{1985/T}. \tag{B.5}$$

Table B.2: The temperature variation of some material properties of pure aluminium. The horizontal line separates the solid and the liquid state.

Temperature		Density	Thermal cond.	Specific heat	Viscosity	
[K]	[°C]	ρ [kg/m^3][a]	k [W/mK][b]	c [J/kgK][c]	μ [mPas][d]	ν [μm^2/s][e]
273	0	–	236	–	–	–
298	25	2700	–	903	–	–
300	27	2700	237	904	–	–
350	77	2696	240	–	–	–
400	127	2693	240	946	–	–
500	227	2686	237	993	–	–
600	327	2679	232	1040	–	–
700	427	2672	226	1087	–	–
800	527	2665	220	1136	–	–
900	627	2658	213	1184	–	–
933	660	2655	(211)	1200	–	–
933	660	2380	(91)	1175	1.31	0.55
1000	727	2363	93	1175	1.18	0.50
1050	777	2350	–	1175	1.08	0.46
1100	827	2337	96	1175	0.98	0.42
1200	927	2311	99	1175	–	–

[a] See Section B.1.1
[b] Lide (1990). Values in parentheses are extrapolated from the data.
[c] Brandes and Brook (1992)
[d] See Section B.1.3
[e] Calculated using $\nu = \mu/\rho_l$. See Section B.1.3

We therefore make use of an intermediate relation for the viscosity:

$$\mu(T) = 1.31 \times 10^{-3} - 2.0 \times 10^{-6}(T - T_m). \tag{B.6}$$

Combined with Equation B.2, we get a relation for the kinematic viscosity (in m^2/s):

$$\nu(T) = \frac{\mu(T)}{\rho_l(T)} \approx 0.55 \times 10^{-6} - 0.80 \times 10^{-9}(T - T_m), \tag{B.7}$$

by using Taylor expansion of the fraction and neglecting the small higher-order terms.

The average viscosity from $T_a = 660$°C to $T_m = 800$°C is $\bar{\mu} = 1.2 \times 10^{-3}$ kg/ms, and the average kinematic viscosity becomes $\bar{\nu} = 0.5 \times 10^{-6}$ m^2/s.

Table B.3: Average measured composition of the aluminium alloys used in the experiments. (AA1050 is normally 99.5 % pure aluminium.) Below the line, three reported alloys (Lynch 1974) are added for comparison.

Alloy	Al (%)	Fe (%)	Mn (%)	Mg (%)	Si (%)	Zn (%)	Cu (%)
AA1050	99.4	0.44	0.01	–	0.07	–	–
AA3105	97.3	0.67	0.38	0.43	0.45	0.37	0.28
AA6060	98–99	0.24	0.02	0.41	0.35	–	–
AA1060	99.6	0.35	0.03	0.03	0.25	0.05	0.05
AA3003		0.7	1.0–1.5	–	0.6	0.10	0.20
AA3004		0.7	1.0–1.5	0.8–1.3	0.30	0.25	0.25

B.1.4 Thermal conductivity

The mean thermal conductivity is calculated from the values in Table B.2 by applying

$$\bar{k} = \frac{1}{T_2 - T_1} \int_{T_1}^{T_2} k(T)\, dT \approx \frac{1}{T_2 - T_1} \sum_{i=1}^{n-1} \frac{k_i + k_{i+1}}{2} (T_{i+1} - T_i). \tag{B.8}$$

where n is the number of values available in the temperature interval T_1 to T_2. For the solid state, $\bar{k} = 229\,\mathrm{W/mK}$, while in the liquid state we use the three lowest values only, and get $\bar{k}_l = 93\,\mathrm{W/mK}$.

B.2 Physical properties of aluminium alloys

In the work presented in this thesis, the commercially pure AA1050, the rolling alloy AA3105, and another rather pure alloy AA6060 were used. The actual content of elements was measured by spectrography and is shown in Table B.3. Note that AA1050 is normally 99.5 % pure aluminium, but the iron content increased a little (from below 0.4 % towards 0.5 %) during the experiments, probably due to the use of steel equipment. The AA3105 alloy seemed to lose magnesium. The melt was renewed every second experiment period of a couple of days. Average values are used in the table. Physical properties for three similar alloys were found in Lynch (1974) and their composition is shown below the line in the table. Some properties of these six alloys are listed in Table B.4.

All the values are subject to measurement uncertainties. And different handbooks present somewhat different values. We can assume that AA1050 and AA1060 do not differ very much from each other, so the differences in the specific heat and density with composition can be neglected. We will use the pure-aluminium values for these quantities. The thermal conductivity does however

Table B.4: Some properties of the alloys used in this thesis (calculated with Alstruc, see Section 3.4) and for three reference alloys AA1060, AA3003, and AA3004 (Lynch 1974).

Alloy	Density at 20°C [kg/m^3]	Melting range [°C]	Applied melting point[a] [°C]	Thermal conductivity at 20°C [W/mK][b]	Specific heat at 20°C [J/kg K]
AA1050	2700	650–659	**657**	220 (**205**)	900
AA3105	2720	633–653	**648**	160 (**166**)	890
AA6060	2700	637–655	**651**	200 (**197**)	900
AA1060	2710	646–657		220	920
AA3003	2740	643–654		190	920
AA3004	2710	629–652		160	920

[a]The temperature at which 50 % is solid, see Section 3.4
[b]Mean quantity in parentheses

vary significantly from alloy to alloy. So does the melting interval. We therefore use the values of the latter two quantities that are listed in boldface in Table B.2 instead of those for pure aluminium.

The viscosity μ was measured by Pedersen and Grande (1997) for additions of manganese and iron to pure aluminium. The temperature dependence was the same for all alloys, but the magnitude at, say, 660°C was higher for alloyed aluminium, as listed in Table B.5. This means that we should add some percent to the pure-aluminium value for the alloys in question.

Table B.5: Change in viscosity due to addition of manganese and iron at 660°C (slightly extrapolated values). For pure aluminium this was about 1.37 mPas.

Addition	Viscosity [mPas] for alloy	Increase in viscosity
1 wt% Mn	1.36	−0.7 %
3 wt% Mn	1.47	7 %
1 wt% Fe	1.54	12 %
1 wt% Fe, 1.5 wt% Mn	1.65	20 %

Appendix C

Mathematical details

C.1 Approximate equation for the shell growth

Instead of integrating the complicated shell-growth Equation (2.16) numerically, we can step back to the heat balance of a cross section of the shell, Equation (2.15), and assume that $(d\xi_s/d\eta)^2 \ll 1$. Then the square root vanishes, and we find a much simpler formula for the shell growth:

$$\frac{d\xi_s}{d\eta} = \frac{Bi\,(1-\theta_p(\eta)) - Nu\,(\theta_l - 1)}{Pe\,Sf}. \tag{C.1}$$

The constant A in Equation (2.33) is very small and its only significance is to provide a smooth temperature profile across $\eta = \Pi_\mathrm{A}$. Therefore we set $A = 0$ and substitute Equation (2.33) for θ_p in Equation (C.1) and integrate to obtain

$$\xi_s(\eta) = \frac{\dfrac{Bi}{\lambda_2}\left(1 - e^{-\lambda_2 \eta}\right) - Nu(\theta_l - 1)\eta}{Pe\,Sf}. \tag{C.2}$$

The first root of $\xi_s(\eta) = 0$ for $\eta > 0$ is Π_A, which can be found by rearranging the equation to

$$\eta_{i+1} = \frac{Bi}{Nu\lambda_2(\theta_l - 1)}\left(1 - e^{-\lambda_2 \eta_i}\right), \tag{C.3}$$

and iterating this until $|\eta_{i+1} - \eta_i| < \varepsilon$. A reasonable initial guess value is $\eta_0 = 100$, and $\varepsilon = 10^{-2}$ should be more than sufficient.

C.2 The coefficients of the two-dimensional steady-state solution

Equation (2.103) with $C_0 = 1$ is

$$\theta_i(\xi, \eta) = 1 - \sum_{i=0}^{\infty} C_i e^{-\lambda_i \eta} \cos \alpha_i \xi. \tag{C.4}$$

The coefficients C_i are found by applying boundary condition (2.95) and utilizing the orthogonality of the cosine function. Multiply

$$\sum_{i=1}^{\infty} C_i \cos \alpha_i \xi = 1$$

by $\cos \alpha_j \xi$ and integrate ξ from zero to $\frac{1}{2}$ to obtain

$$\sum_i C_i \int_0^{\frac{1}{2}} \cos \alpha_i \xi \, \cos \alpha_j \xi \, d\xi = \int_0^{\frac{1}{2}} \cos \alpha_j \xi \, d\xi. \tag{C.5}$$

Partial integration of the left-hand integral gives zero when $i \neq j$. When $i = j$, the integral of $\cos^2 \alpha_i \xi$ must be calculated. Thus

$$\int_0^{\frac{1}{2}} \cos \alpha_i \xi \, \cos \alpha_j \xi \, d\xi = \delta_{ij} \frac{1}{4} \left(1 + \frac{\sin \alpha_i}{\alpha_i} \right), \tag{C.6}$$

where δ_{ij} is unity when $i = j$ and zero otherwise. Substitute this into Equation (C.5) and calculate the right-hand integral. We get

$$\sum_i C_i \delta_{ij} \frac{1}{4} \left(1 + \frac{\sin \alpha_i}{\alpha_i} \right) = \frac{\sin \frac{\alpha_j}{2}}{\alpha_j}. \tag{C.7}$$

Only the terms with $i = j$ survive the sum on the left-hand side, and by rearranging the result we find the value of the constants C_i:

$$C_j = \frac{4 \sin \frac{\alpha_j}{2}}{\alpha_j + \sin \alpha_j}. \tag{C.8}$$

C.3 Inverse Laplace transformation

In Section 2.8, we used the Laplace transformation to transform the partial differential equation of the transient plate-feeding problem into an ordinary dif-

ferential equation. The problem was solved in the transformed system:

$$\begin{aligned}\tilde{\theta}(\eta,s) = \frac{2Bi}{s(2Bi+s)} + \frac{e^{-\frac{1}{2}Pe\,(\Pi_A-\eta)}\,\sinh[\eta\sqrt{C+s}]}{(2Bi+s)\,\sinh[\Pi_A\sqrt{C+s}]} \\ - \frac{2Bi\,e^{\frac{1}{2}Pe\,\eta}\,\sinh[(\Pi_A-\eta)\sqrt{C+s}]}{s(2Bi+s)\,\sinh[\Pi_A\sqrt{C+s}]}\end{aligned} \tag{C.9}$$

now rewritten with $C = Pe^2/4 + 2Bi$. This section contains the calculations to obtain the transient solution by means of the *inverse* Laplace transformation,

$$\theta = \frac{1}{2\pi i}\int_{\gamma-i\infty}^{\gamma+i\infty} \tilde{\theta}(\eta,s)e^{s\tau}\,ds = \frac{1}{2\pi i}\lim_{R\to\infty}\int_{L_R} \tilde{\theta}(\eta,s)e^{s\tau}\,ds. \tag{C.10}$$

The line segment L_R is drawn in Figure C.1 for finite R together with a semicircle C_R. Together they should enclose all poles s_k of $\tilde{\theta}$ in the s plane. The poles are singularities that occur because the denominator becomes zero while the numerator is different from zero. The two simplest poles are $s = 0$ and $s = -2Bi$, but $\sinh\left(\Pi_A\sqrt{C+s}\right) = 0$ gives an infinite number of poles as $i\sinh z = \sin iz$, so $\Pi_A\sqrt{C+s_k} = k\pi i$, or

$$s_k = -\frac{k^2\pi^2}{\Pi_A^2} - C, \qquad k = 1, 2, \ldots \tag{C.11}$$

Note that $k = 0$ does not give a pole, and that positive and negative k give the same poles. The inverse Laplace transformation, Equation (C.10), can be

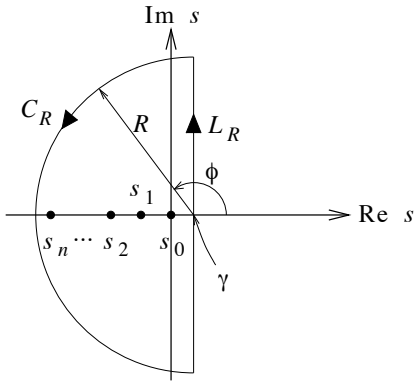

Figure C.1: The integration paths in the s plane

rewritten to

$$\begin{aligned}\theta(\eta,\tau) &= \frac{1}{2\pi i}\lim_{R\to\infty}\oint_{C_R+L_R}\tilde{\theta}(\eta,s)e^{s\tau}\,ds - \frac{1}{2\pi i}\lim_{R\to\infty}\int_{C_R}\tilde{\theta}(\eta,s)e^{s\tau}\,ds \\ &= \sum_{\text{all } s_k}\operatorname*{Res}_{s=s_k}\left[\tilde{\theta}(\eta,s)e^{s\tau}\right] - \frac{1}{2\pi i}\lim_{R\to\infty}\int_{C_R}\tilde{\theta}(\eta,s)e^{s\tau}\,ds.\end{aligned} \tag{C.12}$$

We have to evaluate the residues at the poles and the path integral along C_R as R approaches infinity. The residue of $\tilde{\theta}(\eta,s)e^{s\tau}$ at a pole s_k is obtained by the coefficient of the Laurent series that is of order s^{-1}. It can easily be calculated by the following formula (Kreyszig 1988, Sec. 15.1):

$$\operatorname*{Res}_{s=s_k}\left[\tilde{\theta}(\eta,s)e^{s\tau}\right] = \operatorname*{Res}_{s=s_k}\frac{p(s)}{q(s)} = \frac{p(s_k)}{q'(s_k)}, \tag{C.13}$$

where $q(s)$ should be set to the term in the denominator that causes the singularity for the pole in question. $p(s)$ is thus the rest of the expression. First separate the three terms in Equation (C.9) into three functions $\tilde{\theta}_1$, $\tilde{\theta}_2$, and $\tilde{\theta}_3$ so that $\tilde{\theta} = \tilde{\theta}_1 + \tilde{\theta}_2 + \tilde{\theta}_3$. In the following, we will process each pole or set of poles separately for the terms of $\tilde{\theta}$ involved with this pole.

For the pole $s = 0$, we set $q(s) = s$, i.e. $q'(s) = 1$, and calculate the residue for the terms in Equation (C.9) where we have this pole, that is $\tilde{\theta}_1$ and $\tilde{\theta}_3$. We get

$$\operatorname*{Res}_{s=0}\left[(\tilde{\theta}_1+\tilde{\theta}_3)e^{s\tau}\right] = 1 - \frac{\sinh[(\Pi_\mathrm{A}-\eta)\sqrt{C}]}{\sinh[\Pi_\mathrm{A}\sqrt{C}]}\,e^{\frac{1}{2}Pe\,\eta}. \tag{C.14}$$

For the pole $s = -2Bi$, $q(s) = 2Bi + s$, which yields $q'(s) = 1$ and residue

$$\begin{aligned}\operatorname*{Res}_{s=-2Bi}\left[(\tilde{\theta}_1+\tilde{\theta}_2+\tilde{\theta}_3)e^{s\tau}\right] &= e^{-2Bi\tau}\times \\ \times\left[-1 + \frac{\sinh[\frac{1}{2}Pe\,\eta]}{\sinh[\frac{1}{2}Pe\,\Pi_\mathrm{A}]}\,e^{-\frac{1}{2}Pe(\Pi_\mathrm{A}-\eta)} + \frac{\sinh[\frac{1}{2}Pe(\Pi_\mathrm{A}-\eta)]}{\sinh[\frac{1}{2}Pe\,\Pi_\mathrm{A}]}\,e^{\frac{1}{2}Pe\,\eta}\right].\end{aligned} \tag{C.15}$$

If we write out the hyperbolic sines as exponentials and simplify, everything cancels, and we simply get

$$\operatorname*{Res}_{s=-2Bi}\left[(\tilde{\theta}_1+\tilde{\theta}_2+\tilde{\theta}_3)e^{s\tau}\right] = 0. \tag{C.16}$$

The remaining poles, $s_k = -k^2\pi^2/\Pi_\mathrm{A}^2 - C$, are treated together as one set. We set $q(s) = \sinh[\Pi_\mathrm{A}\sqrt{C+s}]$, which gives us $q'(s) = \Pi_\mathrm{A}\cosh[\Pi_\mathrm{A}\sqrt{C+s}]/2\sqrt{C+s}$.

When we substitute s with s_k in the square root, we get

$$\sqrt{C+s_k} = \sqrt{C - \frac{k^2\pi^2}{\Pi_\mathrm{A}^2} - C} = i\sqrt{\frac{k^2\pi^2}{\Pi_\mathrm{A}^2}} = \frac{k\pi i}{\Pi_\mathrm{A}}.$$

We know that $\cosh iz = \cos z$ so that

$$q'(s) = \frac{\Pi_\mathrm{A}^2 \cos k\pi}{k\pi i}.$$

The relation $\sinh iz = i \sin z$ gives a similar effect on the numerator, and we use the relation $\sin(a-b) = \sin a \cos b - \cos a \sin b$ to convert $\sin\left(k\pi(\Pi_\mathrm{A} - \eta)/\Pi_\mathrm{A}\right)$ to $(-1)^{k-1}\sin(k\pi\eta/\Pi_\mathrm{A})$ in the last term. The residues thus become

$$\begin{aligned}\operatorname*{Res}_{s=s_k}\Big[(\tilde{\theta}_2 + \tilde{\theta}_3)e^{s\tau}\Big] = {} & \frac{2\pi\, e^{-\frac{1}{2}Pe(\Pi_\mathrm{A}-\eta)}}{\Pi_\mathrm{A}^2} \sum_{k=1}^{\infty} \frac{(-1)^k\, k \sin\frac{k\pi\eta}{\Pi_\mathrm{A}}}{\frac{k^2\pi^2}{\Pi_\mathrm{A}^2} + \frac{Pe^2}{4}}\, e^{-\left[\frac{k^2\pi^2}{\Pi_\mathrm{A}^2}+C\right]\tau} \\ & - \frac{4Bi\pi\, e^{\frac{1}{2}Pe\,\eta}}{\Pi_\mathrm{A}^2} \sum_{k=1}^{\infty} \frac{k \sin\frac{k\pi\eta}{\Pi_\mathrm{A}}}{\left[\frac{k^2\pi^2}{\Pi_\mathrm{A}^2} + \frac{Pe^2}{4}\right]\left[\frac{k^2\pi^2}{\Pi_\mathrm{A}^2} + C\right]}\, e^{-\left[\frac{k^2\pi^2}{\Pi_\mathrm{A}^2}+C\right]\tau}.\end{aligned} \tag{C.17}$$

Now that the residues are found, we must show that the integral along C_R in Equation (C.12) vanishes for $R \to \infty$. We use complex polar co-ordinates and set $s = \gamma + Re^{i\phi}$ for $\frac{\pi}{2} \le \phi \le \frac{3\pi}{2}$ and let $R \to \infty$. γ is the point where L_R intersects the horizontal axis to the right of the rightmost pole. Apart from this, its value is immaterial. The integral becomes

$$\lim_{R\to\infty} \int_{C_R} \tilde{\theta}(\eta, s)e^{s\tau}\, ds = ie^{\gamma\tau} \lim_{R\to\infty} \int_{\frac{\pi}{2}}^{\frac{3\pi}{2}} \left[\tilde{\theta}(\eta, \gamma + Re^{i\phi})e^{Re^{i\phi}\tau}\, Re^{i\phi}\right] d\phi, \tag{C.18}$$

and it approaches zero if the integrand does so when we go to the limit of R. First we realize that the real part $\mathrm{Re}(e^{i\phi}) < 0$ when $\frac{\pi}{2} < \phi < \frac{3\pi}{2}$ so that $e^{Re^{i\phi}} \to 0$ when $R \to \infty$. When $\phi = \frac{\pi}{2}$ or $\frac{3\pi}{2}$, $e^{Re^{i\phi}} = e^{iR}$ or e^{-iR}, which merely oscillates as R increases, and does not contribute to the disappearance of the integrand. Nor does $e^{i\phi}$ contribute. Thus we are interested in showing that $\tilde{\theta}(\eta, \gamma + Re^{i\phi})R \to 0$ for each of the three terms in Equation (C.9) at a time.

The first term, $\tilde{\theta}_1 R$, is easily shown to vanish as R goes to infinity:

$$\frac{2BiR}{s(2Bi+s)} = \frac{2Bi}{(\gamma + Re^{i\phi})(\frac{2Bi+\gamma}{R} + e^{i\phi})} \to \frac{2Bie^{-i\phi}}{(\gamma + Re^{i\phi})} \to 0. \tag{C.19}$$

Before considering the second term, let us examine the hyperbolic sine in the numerator:

$$\begin{aligned}\sinh[\eta\sqrt{C+s}] &= \sinh\left[\eta\sqrt{R\left(\tfrac{C+\gamma}{R}+e^{i\phi}\right)}\right] \\ &\to \sinh\left[R^{\frac{1}{2}}e^{i\frac{\phi}{2}}\eta\right] = e^{R^{\frac{1}{2}}e^{i\frac{\phi}{2}}\eta} - e^{-R^{\frac{1}{2}}e^{i\frac{\phi}{2}}\eta}.\end{aligned} \tag{C.20}$$

If now $\phi > \pi$, then $\mathrm{Re}(e^{i\frac{\phi}{2}}) > 0$, and the right-hand term vanishes while the other increases as $R \to 0$. Conversely, when $\phi < \pi$, the left-hand term vanishes. The same is the case for the hyperbolic sine in the denominator, and the fraction vanishes, here for the case that $\phi > \pi$:

$$\frac{\sinh[\eta\sqrt{C+s}]}{\sinh[\Pi_\mathrm{A}\sqrt{C+s}]} \to \frac{e^{R^{\frac{1}{2}}e^{i\frac{\phi}{2}}\eta} - e^{-R^{\frac{1}{2}}e^{i\frac{\phi}{2}}\eta}}{e^{R^{\frac{1}{2}}e^{i\frac{\phi}{2}}\Pi_\mathrm{A}} - e^{R^{\frac{1}{2}}e^{i\frac{\phi}{2}}\Pi_\mathrm{A}}} \to \frac{e^{R^{\frac{1}{2}}e^{i\frac{\phi}{2}}\eta}}{e^{R^{\frac{1}{2}}e^{i\frac{\phi}{2}}\Pi_\mathrm{A}}} = e^{-R^{\frac{1}{2}}e^{i\frac{\phi}{2}}(\Pi_\mathrm{A}-\eta)} \to 0. \tag{C.21}$$

When $\phi = \pi$, the fraction of hyperbolic sines merely oscillates and thus does not contribute to the vanishing of the second term $\tilde{\theta}_2 R$. The rest of this term does however vanish in the same way as the first term, independently of the fraction we just examined, so $\tilde{\theta}_2 R \to 0$ when $R \to \infty$.

The third term $\tilde{\theta}_3 R$ approaches zero in the similar way as the second, so no effort is used to show this in particular.

This means that, as $R \to \infty$,

$$\int_{C_R} \tilde{\theta}(\eta, s) e^{s\tau}\, ds \to 0 \tag{C.22}$$

The solution to the problem is thus given by the residues in Equations (C.14) and (C.17) only:

$$\begin{aligned}\theta(\eta,\tau) = 1 &- \frac{\sinh[(\Pi_\mathrm{A}-\eta)\sqrt{Pe^2/4+2Bi}]}{\sinh[\Pi_\mathrm{A}\sqrt{Pe^2/4+2Bi}]}\, e^{\frac{1}{2}Pe\,\eta} \\ &+ \frac{2\pi}{\Pi_\mathrm{A}^2}\sum_{k=1}^{\infty} \sin\tfrac{k\pi\eta}{\Pi_\mathrm{A}}\, e^{-\left[\frac{k^2\pi^2}{\Pi_\mathrm{A}^2}+\frac{Pe^2}{4}+2Bi\right]\tau} \times \\ &\times \left[\frac{(-1)^k\, k\, e^{-\frac{1}{2}Pe(\Pi_\mathrm{A}-\eta)}}{\frac{k^2\pi^2}{\Pi_\mathrm{A}^2}+\frac{Pe^2}{4}} - \frac{2Bi\, k\, e^{\frac{1}{2}Pe\,\eta}}{\left(\frac{k^2\pi^2}{\Pi_\mathrm{A}^2}+\frac{Pe^2}{4}\right)\left(\frac{k^2\pi^2}{\Pi_\mathrm{A}^2}+\frac{Pe^2}{4}+2Bi\right)}\right].\end{aligned} \tag{C.23}$$

Appendix D

Feeder control

Figure D.1 shows the control circuit for the electromotor that feeds the plate into the melt. The *up* potentiometer is turned to the absolute right in order to maximize the upward plate velocity, and the other, which has a number grading, is turned to the number giving the wanted feeding velocity, normally 50 (6.4 cm/s), 75, 100, and 125 (16.0 cm/s). Before a measurement run, the on/off switch is set to off and the up/down switch to down. The feeding is started by switching the on/off switch to *on*, and it is finished by switching to *up* for about a second before the on/off switch is switched to *off* again as the plate is drawn sufficiently up. The speed of the motor can be monitored by measuring the voltage of connection 15 (speed monitor) on the servo amplifier.

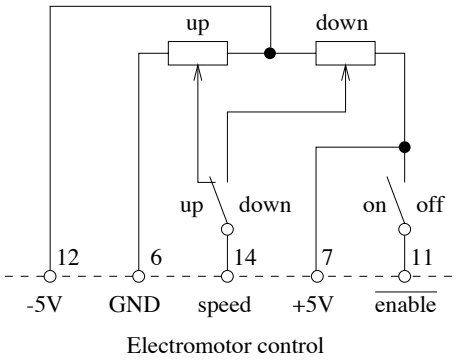

Figure D.1: The control circuit for the electromotor that feeds the plate into the melt

For readers who will be using the feeding apparatus, Figures D.2 and D.3 show the wire colours used between the electromotor with encoder and the servoamplifier in the current setup of the apparatus. Two shielded wires with six coloured

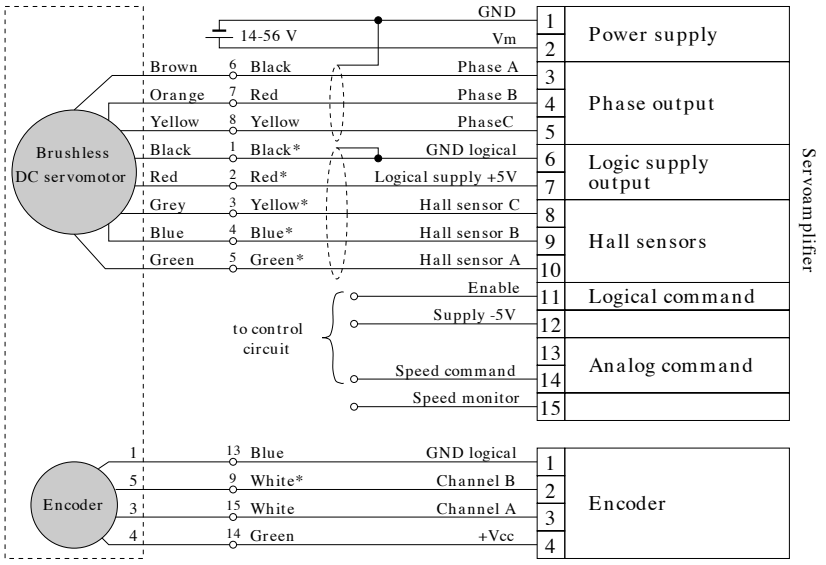

Figure D.2: The connection of the electromotor with encoder to the servoamplifier. The wires with asterisk (*) are shielded separately from those without and with different ground as partly indicated by the dashed ellipses.

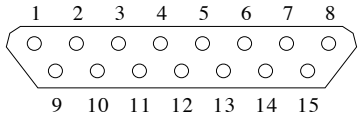

1	GND	Black*	**9**	Ch. B	White*
2	Vcc	Red*	**10**	NOC	—
3	Hall C	Yellow*	**11**	NOC	—
4	Hall B	Blue*	**12**	NOC	—
5	Hall A	Green*	**13**	GND	Black
6	Ph. A	Black	**14**	Vcc	Green
7	Ph. B	Red	**15**	Ch. A	White
8	Ph. C	Yellow			

Figure D.3: The wire side of the (female) plug connected to the servoamplifier. Wires with asterisk (*) are shieldes separately from those without.

conductors were used. The insulation of one of the wires is marked with a cross and its conductors are marked with asterisks (*) in the figures. This separation and shielding was recommended by the producer in order to avoid transferring noice from the phase conductors to the hall-sensor and logical-supply conductors. This is indicated in Figure D.2 by dashed ellipses with separate grounding. There was no recommendations concerning the conductors to the encoder, which controls the velocity of the motor, so these were included where there was space. This is not indicated in the figure to increase readability.

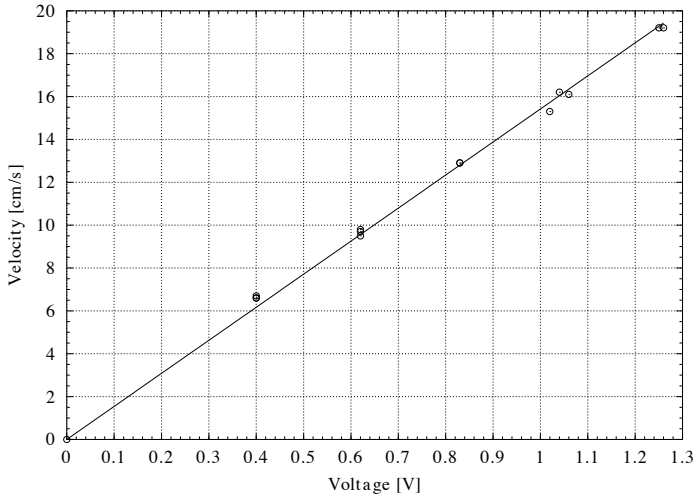

Figure D.4: Calibration curve between the voltage and the actual feeding velocity, $v = 15.4V$ in cm/s with an uncertainty of 0.6 %

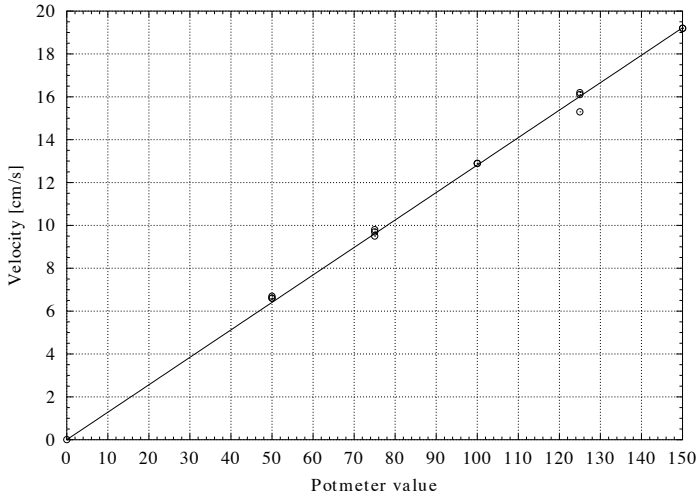

Figure D.5: Calibration curve between the setting of the potentiometer and the actual feeding velocity, $v = 0.128$Pot in cm/s with an uncertainty of 0.5 %.

The feeding velocity was calibrated by taking the time for a plate to move three metres through the feeder. The obtained relation between the voltage that is input to the servoamplifier (connection 14) and the actual feeding velocity is shown in Figure D.4. The potentiometer used for controlling the feeding velocity, has a number grading to make it possible to the set the potentiometer quite accurately. Through the curve in Figure D.5, its setting is easily translated to a feeding velocity.

Appendix E

Statistics of the experiments

When fitting a model to a set of data by means of a number of adjustable parameters, at least two things are important to remember. The first is that modelling is a matter of describing nature by mathematics, which makes it easier for us to predict nature, as stated in the preamble of Chapter 2. The other thing is that the curve-fitting is not finished when the parameters are found. The uncertainty in the parameters must be estimated, and a statistical measure of the goodness of the fit should be made. The latter is not included here as a simple and less robust method is used in Chapter 5. In the following, we more or less follow the approach in *Numerical Recipies in C* (Press et al. 1992, Ch. 15).

E.1 Weighted least-squares fit

In general, we have a number of random variables $X, Y, Z, \ldots$ that we can measure and assume to have a certain relationship. Let the dependent variable be $Y = y(\vec{X}; \vec{a})$ where $\vec{X} = (X, Z, \ldots)$, and $\vec{a} = (a_1, \ldots, a_M)$ is a vector of M adjustable parameters. Experiments will give a data set of N data points $(\vec{x}_i, y_i)$ where y_i are assumed to be *independent* and *identically distributed* with a mean η and a standard deviation σ at a given $\vec{x}$. The independent variables $X, Z, \ldots$ are assumed to have a negligible uncertainty so that $X = x$, $Z = z$ etc. To avoid confusion, we consequently let i count data points $(1, \ldots, N)$ and k and l count parameters $1, \ldots, M$.

We now want to adjust the parameters $\vec{a}$ to maximize the probability that the given data set could have occurred. This is taken to be mathematically equiva-

lent to *minimizing* χ^2 given by

$$\chi^2(\vec{a}) = \sum_{i=1}^{N} \left(\frac{y_i - y(\vec{x}_i; \vec{a})}{s_i} \right)^2 . \tag{E.1}$$

Minimizing χ^2 with two parameters may be compared to descending a mountain to find the lowest point in the terrain. It may imply following valleys downhill. The steepest way down is a useful approach, and a mathematical method for finding this way in M dimensions is described here.

For two points (i.e. sets of parameters) $\vec{a}$ and $\vec{a}'$ sufficiently close to each other, we can approximate $\chi^2(\vec{a})$ by its Taylor series around a point $\vec{a}' = \vec{a} - \Delta\vec{a}$:

$$\chi^2(\vec{a}) \approx \chi^2(\vec{a}') + \sum_k \frac{\partial \chi^2}{\partial a_k}\Big|_{\vec{a}'} \Delta a_k + \frac{1}{2} \sum_{k,l} \frac{\partial^2 \chi^2}{\partial a_k \partial a_l}\Big|_{\vec{a}'} \Delta a_k \Delta a_l. \tag{E.2}$$

We introduce the conventional definitions

$$\beta_k = -\frac{1}{2} \frac{\partial \chi^2}{\partial a_k}\Big|_{\vec{a}'} \quad \text{and} \quad \alpha_{kl} = \frac{1}{2} \frac{\partial^2 \chi^2}{\partial a_k \partial a_l}\Big|_{\vec{a}'}, \tag{E.3}$$

where $\vec{\vec{\alpha}}$ is the *curvature matrix*, and rewrite Equation (E.2) to

$$\chi^2(\vec{a}) \approx \chi^2(\vec{a}') - 2\vec{\beta} \cdot \Delta\vec{a} + \Delta\vec{a} \cdot \vec{\vec{\alpha}} \cdot \Delta\vec{a}. \tag{E.4}$$

The gradient of χ^2 in this point is thus

$$\nabla\chi^2(\vec{a}) = -2\vec{\beta} + 2\vec{\vec{\alpha}} \cdot \Delta\vec{a}, \tag{E.5}$$

where ∇ is the gradient operator with M components $\nabla_k = \partial/\partial a_k$. If we choose $\vec{a} = \vec{a}_{\min}$ to be the set of parameters minimizing χ^2 and $\vec{a}'$ the current trial parameters, then $\nabla\chi^2(\vec{a}) = 0$, and we get

$$\vec{a}_{\min} = \vec{a}' - \vec{\vec{\alpha}}^{-1} \cdot \vec{\beta}, \tag{E.6}$$

where $\vec{a}'$ is sufficiently close to $\vec{a}_{\min}$, i.e. within the area in which χ^2 is well approximated by the Taylor expansion of Equation (E.2). We can thus jump directly to the minimum by Equation (E.6). Further away, however, we should iterate towards the minimum by taking smaller steps along the steepest way down:

$$\vec{a}_{\text{next}} = \vec{a}' - (\text{const}) \nabla\chi^2|_{\vec{a}'}, = \vec{a}' + (\text{const})\vec{\beta}, \tag{E.7}$$

where the constant is small enough not to bring us up another hillside.

The Levenberg-Marquardt method elegantly reduces the two equations (E.6) and (E.7) into a single one in two steps (Press et al. 1992, Ch. 15): Dimensional

analysis suggests that the constant in Equation (E.7) is $1/\lambda\alpha_{kk}$, where λ is an adjustable constant whose inverse determines the size of the step. Thus, after some reorganization, the two equations can be expressed in terms of vector components as

$$\sum_l \alpha_{kl}\Delta a_l = \beta_k, \tag{E.8}$$

$$\lambda\alpha_{kk}\Delta a_k = \beta_k, \tag{E.9}$$

repectively, where $\Delta a_l = a_{l,\text{next}} - a'_l$ in accordance with the previous. The latter equation is employed far away from the minimum of χ^2 while the former is efficient when we get close to it.

Then, by redefining α_{kl} to

$$\alpha'_{kl} = \begin{cases} \alpha_{kl}(1+\lambda) & \text{for } k = l, \\ \alpha_{kl} & \text{for } k \neq l, \end{cases} \tag{E.10}$$

the two equations collapse into a single equation

$$\sum_l \alpha'_{kl}\Delta a_l = \beta_k, \tag{E.11}$$

which gives a smooth transition from Equation (E.9) at large λ to Equation (E.8) at small λ.

We define a tensor

$$\vec{\vec{C}}' = (\vec{\vec{\alpha}}')^{-1} = \frac{1}{\det \vec{\vec{\alpha}}'} \begin{pmatrix} \alpha'_{22} & -\alpha'_{12} \\ -\alpha'_{21} & \alpha'_{11} \end{pmatrix} \tag{E.12}$$

where $\det \vec{\vec{\alpha}}' = \alpha'_{11}\alpha'_{22} - \alpha'_{12}\alpha'_{21}$, and get the iteration formula of the Levenberg-Marquardt method:

$$a_{k,\text{next}} = a_k + \sum_{l=1}^{M} C'_{kl}\beta_l. \tag{E.13}$$

In practice a small number of λ, say 10^{-3}, is used. If Equation (E.13) results in a higher χ^2, then the step is too large (λ too small) so that λ must be increased (by a factor of 10 times, for instance), and a new calculation should be made. On the other hand, if χ^2 decreases due to the application of Equation (E.13), then λ can by decreased and we can proceed to the next iteration. The iteration can be halted when the change in χ^2 is less than $10^{-3}\chi^2$. χ^2 is χ^2-distributed with mean ν and standard deviation $\sigma_{\chi^2} = \sqrt{2\nu}$ where $\nu = N - M$ is the number of degrees of freedom. Further iteration is thus of no interest as $\sqrt{2\nu} \gg 10^{-3}\nu$.

Instead of calculating the second derivative of χ^2 in Equation (E.3) to get $\vec{\vec{\alpha}}$, we can substitute χ^2 by Equation (E.1) and then differentiate to obtain

$$\alpha_{kl} = \frac{1}{2}\frac{\partial^2\chi^2}{\partial a_k \partial a_l}\Big|_{\vec{a}'} = \sum_{i=1}^{N}\frac{1}{s_i^2}\left[\frac{\partial y(\vec{x}_i;\vec{a})}{\partial a_k}\frac{\partial y(\vec{x}_i;\vec{a})}{\partial a_l} - (y_i - y(\vec{x}_i;\vec{a}))\frac{\partial^2 y(\vec{x}_i;\vec{a})}{\partial a_k \partial a_l}\right]_{\vec{a}'}. \tag{E.14}$$

The factor $(y_i - y(\vec{x}_i;\vec{a}))$ is the residual, i.e. the deviation between the measured value y_i and the model prediction $y(\vec{x}_i;\vec{a})$. The residuals have random sign, and when they are summed up, they tend to cancel each other when the parameters are good, that is, when we are close to minimum χ^2. It is rather independent of the second derivative because it includes the measured value y_i. Hence, the rightmost term inside the brackets will be negligible compared to the leftmost term when close to minimum and summed up. Thus, the rightmost term will merely affect the iteration path towards minimum, and in some cases also destabilize the iteration (Press et al. 1992, Sec. 15.5). We therefore remove the term and approximate $\vec{\vec{\alpha}}$ with

$$\alpha_{kl} = \sum_{i=1}^{N}\frac{1}{s_i^2}\frac{\partial y(\vec{x}_i;\vec{a})}{\partial a_k}\frac{\partial y(\vec{x}_i;\vec{a})}{\partial a_l}. \tag{E.15}$$

E.2 Estimated error in the parameters

E.2.1 The covariance tensor

At minimum χ^2, let $\lambda = 0$ in $\vec{\vec{C}}'$ and get the estimated *covariance tensor* $\vec{\vec{C}} = \vec{\vec{\alpha}}^{-1}$ of the standard errors in the fitted parameters $\vec{a}$. Thus the diagonal elements $C_{kk} = s(a_k)^2$ and the other elements are covariances of combinations of the parameters.

E.2.2 Nonparametric bootstrapping

Another way to establish an estimate of the uncertainty in the parameters is *nonparametric bootstrapping*, which is a method that has grown popular with the development and availability of the computer resources and also accepted among statisticians. The idea is to use the obtained data set to produce new data sets. This is performed by randomly picking out N data from the original data set (sampling with replacement). The resulting data set is thus just as large as the original, but in average, $e^{-1} \sim 1/3$ of the data will be duplicated. The parameters are fitted to the new data in the same way as before, and a new set of parameters are obtained. This is repeated to gain a large number n of parameter sets $\vec{a}^j$ where $j = 1, \ldots, n$. Assuming that the bootstrap parameters

are normally distributed, the mean for each parameter is

$$\bar{a}_k = \sum_{j=1}^{n} \frac{a_k^j}{n} \tag{E.16}$$

and the bootstrap estimate of the standard deviation for each parameter is simply

$$s(a_k) = \sqrt{\sum_{j=1}^{n} \left(\frac{a_k^j - \bar{a}_k}{n-1} \right)^2} \tag{E.17}$$

for each parameter. In this thesis, we have used $n = 100$, which should be sufficient to establish a good estimate of the standard deviation for the parameters.

The method is described briefly in *Numerical Recipes* (Press et al. 1992, Sec. 15.6) and carefully discussed by Efron and Tibshirani (1986).

Appendix F

Experimental data

The following tables are divided into the four groups of experiments, quiescent-melt, launder, no-lacquer, and lacquer experiments. An additional table contains data for the thicker plates. T_l is the melt temperature, v the feeding velocity, V the melt-flow velocity, P the penetration depth, and s_P the standard deviation in P. The two columns δ_f and δ_b tell the distance from the top of the edge shell to the top of the surface shell on the front (f) and back (b) sides of the plate, respectively. An asterisk (*) is used where the shell had obviously fallen off and δ could not be measured, while parentheses around the number means that only about 10–50 % of the width of the plate was covered with shell. The *special* columns tell whether (X) or not (–) the plate was lacquered (Lq), had thermocouple (Th), was washed (Wa), whether it was skimmed before the experiment (Sk), and whether argon atmosphere was used (Ar).

Table F.1 Experimental data for the quiescent-melt experiments (AA1050, $b = 0.54$ mm)

Plate	T_l	v	V	P	s_P	δ_f	δ_b	Special				
no.	[°C]	[cm/s]	[cm/s]	[mm]	[mm]	[mm]	[mm]	Lq	Th	Wa	Sk	Ar
990520-06	708.3	12.8	–	104.2	6.6	5	5	–	–	–	–	–
990520-07	707.4	12.8	–	123.6	24.9	(4)	5	–	–	–	–	–
990520-08	705.7	12.8	–	89.2	2.8	*	5	–	–	–	–	–
990520-09	704.2	12.8	–	108.8	2.8	*	6	–	–	–	–	–
990520-10	703.0	6.4	–	58.0	6.6	3	7	–	–	–	–	–
990520-11	702.0	6.4	–	46.2	5.3	4	8	–	–	–	–	–
990521-01	716.3	6.4	–	46.2	3.6	4	6	–	–	–	X	–
990521-02	715.5	6.4	–	45.8	1.6	4	6	–	–	–	–	–
990521-03	713.2	6.4	–	48.6	2.9	4	6	–	–	–	X	–
990521-04	710.6	6.4	–	46.0	5.6	4	7	–	–	–	X	–
990521-05	709.0	6.4	–	48.8	2.8	4	7	–	–	–	X	–
990521-06	707.3	6.4	–	51.4	4.2	3	7	–	–	–	X	–
990521-07	707.1	12.8	–	87.6	3.6	*	7	–	–	–	X	–

Table F.1 (cont.) Quiescent-flow experiments

Plate	T_l	v	V	P	s_P	δ_f	δ_b	Special				
no.	[°C]	[cm/s]	[cm/s]	[mm]	[mm]	[mm]	[mm]	Lq	Th	Wa	Sk	Ar
990521-08	706.0	12.8	–	118.8	3.9	4	5	–	–	–	X	–
990521-09	704.0	12.8	–	126.4	12.0	*	5	–	–	–	X	–
990521-10	734.8	6.4	–	28.6	2.8	3	–	–	–	–	X	–
990521-11	733.1	6.4	–	32.6	4.6	5	7	–	–	–	–	–
990521-12	732.2	12.8	–	66.4	11.3	*	7	–	–	–	X	–
990521-13	731.4	12.8	–	61.0	4.6	(5)	6	–	–	–	X	–
990521-14	729.4	12.8	–	57.0	11.1	4	–	–	–	–	X	–
990521-15	728.0	6.4	–	36.4	4.7	5	(5)	–	–	–	–	–
990525-02	733.7	6.4	–	38.8	3.0	(4)	4	–	–	X	–	–
990525-03	733.2	6.4	–	38.4	3.2	(4)	5	–	–	X	X	–
990525-04	732.5	9.6	–	53.4	6.4	3	5	–	–	X	X	–
990525-05	732.0	9.6	–	55.6	5.5	5	5	–	–	X	X	–
990525-06	731.7	12.8	–	69.6	4.1	–	4	–	–	X	X	–
990525-07	731.0	12.8	–	65.8	4.6	*	7	–	–	X	X	–
990525-08	730.8	16.0	–	85.2	4.4	5	5	–	–	X	X	–
990525-09	730.7	16.0	–	107.8	8.3	–	6	–	–	X	–	–
990525-10	749.7	6.4	–	22.4	1.5	3	(5)	–	–	X	X	–
990525-11	749.9	6.4	–	21.0	1.2	3	(5)	–	–	X	X	–
990525-12	749.8	9.6	–	36.0	3.7	(5)	6	–	–	X	X	–
990525-13	749.2	9.6	–	43.0	8.0	4	6	–	–	X	X	–
990525-14	749.5	12.8	–	57.6	4.9	–	(3)	–	–	X	X	–
990525-15	750.3	12.8	–	60.0	6.4	5	5	–	–	X	X	–
990525-16	749.2	16.0	–	77.0	6.1	–	*	–	–	X	X	–
990525-17	748.2	16.0	–	79.4	9.4	*	3	–	–	X	X	–
990709-01	785.0	6.4	–	14.0	0.7	5	8	–	–	–	X	–
990709-02	785.9	6.4	–	10.8	0.8	2	4	–	–	–	X	–
990709-03	785.3	9.6	–	19.0	2.0	4	(5)	–	–	–	X	–
990709-04	784.6	9.6	–	20.6	2.1	4	(5)	–	–	–	X	–
990709-05	785.3	9.6	–	21.8	0.8	(4)	7	–	–	–	X	–
990709-06	780.0	12.8	–	28.0	1.4	5	–	–	–	–	X	–
990709-07	783.2	12.8	–	27.8	3.7	5	–	–	–	–	X	–
990709-08	783.3	16.0	–	43.2	6.1	5	(7)	–	–	–	X	–
990709-09	782.4	16.0	–	35.0	7.6	4	–	–	–	–	X	–
990712-01	692.7	6.4	–	86.4	8.4	(4)	6	–	–	–	X	–
990712-02	691.9	6.4	–	104.2	10.9	4	6	–	–	–	X	–
990712-03	692.2	9.6	–	146.2	17.4	5	6	–	–	–	X	–
990712-04	693.0	9.6	–	114.0	7.9	*	6	–	–	–	X	–
990712-05	692.8	9.6	–	139.0	12.2	5	6	–	–	–	X	–
990712-06	693.3	12.8	–	197.6	11.5	*	6	–	–	–	X	–
990712-07	693.6	12.8	–	159.6	8.5	5	5	–	–	–	X	–
990712-08	693.5	16.0	–	189.4	7.9	*	5	–	–	–	X	–
990712-09	692.4	16.0	–	185.2	4.1	5	6	–	–	–	X	–
990712-10	710.4	9.6	–	78.0	10.0	5	6	–	–	–	X	–
990712-11	709.3	9.6	–	74.0	5.8	5	5	–	–	–	X	–
990712-12	708.0	9.6	–	80.0	7.9	4	6	–	–	–	X	–

Table F.1 (cont.) Quiescent-flow experiments

Plate	T_l	v	V	P	s_P	δ_f	δ_b	Special				
no.	[°C]	[cm/s]	[cm/s]	[mm]	[mm]	[mm]	[mm]	Lq	Th	Wa	Sk	Ar
990712-13	707.7	16.0	–	124.8	11.1	*	5	–	–	–	X	–
990712-14	711.6	16.0	–	119.4	12.6	3	4	–	–	–	X	–
990712-15	712.7	12.8	–	111.8	16.1	5	5	–	–	–	X	–
990712-16	713.0	12.8	–	100.6	8.0	5	6	–	–	–	X	–
990712-17	713.5	6.4	–	47.8	4.5	5	6	–	–	–	X	–
990712-18	714.4	6.4	–	56.2	4.3	4	5	–	–	–	X	–
990712-19	713.8	9.6	–	83.0	9.6	*	(5)	–	–	–	X	–
990712-20	712.8	16.0	–	137.2	16.6	5	5	–	–	–	X	–
990714-01	709.0	9.6	–	74.8	8.3	–	–	–	X	–	X	–
990713-02	709.0	9.6	–	68.0	13.8	–	–	–	X	–	X	–
990713-03	709.0	9.6	–	69.0	5.6	–	–	–	X	–	X	–
990713-04	710.0	9.6	–	80.0	7.3	–	–	–	X	–	X	–
990713-05	710.0	9.6	–	72.0	4.2	–	–	–	X	–	X	–
990916-01	795.8	6.4	–	12.6	0.9	4	7	–	–	–	X	–
990916-02	794.5	6.4	–	14.4	1.3	4	7	–	–	–	X	–
990916-03	794.0	9.6	–	17.4	1.1	4	–	–	–	–	X	–
990916-04	791.5	9.6	–	14.6	1.1	4	8	–	–	–	X	–
990916-05	790.2	16.0	–	38.2	1.9	4	(7)	–	–	–	X	–
990916-06	788.3	25.6	–	76.4	5.1	–	(7)	–	–	–	X	–
990916-07	813.3	16.0	–	23.2	1.5	4	–	–	–	–	X	–
990916-08	812.1	16.0	–	28.6	3.9	(4)	6	–	–	–	X	–
990916-09	812.8	9.6	–	16.0	1.4	4	7	–	–	–	X	–
990916-10	812.8	12.8	–	18.2	1.9	3	–	–	–	–	X	–
990916-11	828.3	25.6	–	45.0	4.1	4	(7)	–	–	–	X	–
990916-12	827.5	25.6	–	43.8	4.3	(5)	(8)	–	–	–	X	–
990916-13	826.1	25.6	–	41.6	4.6	–	(5)	–	–	–	X	–
990916-14	825.0	38.4	–	73.6	9.2	–	(5)	–	–	–	X	–
990916-15	824.2	12.8	–	25.8	2.8	(4)	–	–	–	–	X	–
990916-16	823.7	16.0	–	42.2	6.1	(5)	–	–	–	–	X	–
990916-18	823.1	16.0	–	27.0	5.0	(4)	(7)	–	–	–	X	–
990916-19	820.5	16.0	–	24.4	3.2	5	–	–	–	–	X	–
990916-20	820.9	12.8	–	16.6	2.1	3	–	–	–	–	X	–
990916-21	820.0	12.8	–	18.6	2.3	3	–	–	–	–	X	–
990916-22	818.9	9.6	–	16.2	1.3	3	–	–	–	–	X	–
990916-23	817.7	6.4	–	17.4	3.0	3	(7)	–	–	–	X	–
990916-24	816.0	6.4	–	10.4	1.1	3	–	–	–	–	X	–
990916-25	815.4	6.4	–	11.0	0.7	4	–	–	–	–	X	–

Table F.2 Experimental data for the launder experiments (AA1050, $b = 0.54\,\text{mm}$)

Plate	T_l	v	V	P	s_P	δ_f	δ_b	Special				
no.	[°C]	[cm/s]	[cm/s]	[mm]	[mm]	[mm]	[mm]	Lq	Th	Wa	Sk	Ar
991208-01	767.0	6.4	4.5	20.2	1.7	–	–	–	–	–	X	–
991208-02	765.0	6.4	4.5	19.4	1.9	(4)	–	–	–	–	X	–

Table F.2 (cont.) Launder experiments

Plate	T_l	v	V	P	s_P	δ_f	δ_b	Special				
no.	[°C]	[cm/s]	[cm/s]	[mm]	[mm]	[mm]	[mm]	Lq	Th	Wa	Sk	Ar
991208-03	764.0	9.6	4.5	27.8	3.1	–	(5)	–	–	–	X	–
991208-04	764.0	9.6	4.5	28.0	2.5	5	(5)	–	–	–	X	–
991208-05	764.0	12.8	4.5	36.8	4.2	3	(3)	–	–	–	X	–
991208-06	765.0	12.8	4.5	43.6	3.1	(4)	3	–	–	–	X	–
991208-07	765.0	16.0	4.5	48.8	2.8	4	4	–	–	–	X	–
991208-08	763.0	16.0	4.5	55.2	4.4	5	(6)	–	–	–	X	–
991208-09	763.0	6.4	8.3	18.0	0.4	(4)	–	–	–	–	X	–
991208-10	763.0	6.4	8.3	18.6	0.7	–	5	–	–	–	X	–
991208-11	763.0	9.6	8.3	23.8	1.2	4	–	–	–	–	X	–
991208-12	763.0	9.6	8.3	22.8	1.6	(4)	(4)	–	–	–	X	–
991208-13	764.0	12.8	8.3	33.2	2.6	(5)	–	–	–	–	X	–
991208-14	764.0	12.8	9.7	33.0	1.5	(5)	(5)	–	–	–	X	–
991208-15	764.0	16.0	8.5	39.8	1.9	4	(4)	–	–	–	X	–
991208-16	763.0	16.0	8.5	37.4	2.4	3	(4)	–	–	–	X	–
991208-17	745.0	6.4	7.6	26.4	1.6	(5)	(6)	–	–	–	X	–
991208-18	744.0	6.4	7.6	21.2	0.4	4	–	–	–	–	X	–
991208-19	743.0	9.6	7.6	27.6	0.4	(4)	4	–	–	–	X	–
991208-20	742.0	9.6	7.6	34.2	1.0	–	4	–	–	–	X	–
991208-21	742.0	12.8	7.6	49.8	0.2	(5)	5	–	–	–	X	–
991208-22	741.0	12.8	7.6	50.4	3.1	4	4	–	–	–	X	–
991208-23	739.0	16.0	7.6	52.6	1.5	4	5	–	–	–	X	–
991208-24	738.0	16.0	7.6	61.2	3.5	4	4	–	–	–	X	–
991208-25	737.0	6.4	7.6	21.8	0.3	3	–	–	–	–	X	–
991208-26	736.0	9.6	7.6	37.8	0.9	5	(4)	–	–	–	X	–
991208-27	736.0	12.8	7.6	48.2	2.3	4	–	–	–	–	X	–
991208-28	735.0	16.0	7.6	60.0	3.4	5	3	–	–	–	X	–
991208-29	733.0	6.4	8.0	23.4	1.2	(5)	5	–	–	–	X	–
991208-30	733.0	9.6	6.7	45.4	1.2	(2)	3	–	–	–	X	–
991208-31	733.0	12.8	6.7	52.2	3.7	5	–	–	–	–	X	–
991208-32	735.0	16.0	5.7	66.6	2.2	5	5	–	–	–	X	–
991208-33	720.0	6.4	10.0	41.0	1.3	5	(5)	–	–	–	X	–
991208-34	706.0	9.6	11.0	68.6	5.2	8	3	–	–	–	X	–
991208-35	735.0	6.4	3.4	28.8	1.2	6	–	–	–	–	X	–
991208-36	739.0	6.4	6.1	18.2	0.6	4	–	–	–	–	X	–
991208-37	736.0	9.6	6.1	44.8	4.4	5	5	–	–	–	X	–
991208-38	736.0	9.6	5.6	39.4	1.8	4	–	–	–	–	X	–
991208-39	736.0	12.8	5.3	50.4	4.6	5	(5)	–	–	–	X	–
991208-40	735.0	12.8	5.3	54.2	3.9	5	(5)	–	–	–	X	–
991208-41	734.0	16.0	5.3	72.2	4.4	4	(5)	–	–	–	X	–
991208-42	734.0	16.0	5.3	63.0	7.1	5	(5)	–	–	–	X	–
991209-01	727.0	6.4	7.0	30.4	1.0	–	6	–	–	–	X	–
991209-02	727.0	6.4	7.0	34.6	1.5	4	6	–	–	–	X	–
991209-03	727.0	9.6	7.0	42.6	2.7	3	5	–	–	–	X	–
991209-04	731.0	9.6	7.0	37.6	2.0	4	–	–	–	–	X	–
991209-05	734.0	12.8	9.8	51.8	2.0	4	(4)	–	–	–	X	–

Table F.2 (cont.) Launder experiments

Plate	T_l	v	V	P	s_P	δ_f	δ_b	Special				
no.	[°C]	[cm/s]	[cm/s]	[mm]	[mm]	[mm]	[mm]	Lq	Th	Wa	Sk	Ar
991209-06	735.0	12.8	9.8	43.4	2.3	3	–	–	–	–	X	–
991209-07	737.0	16.0	9.8	56.4	4.7	(5)	5	–	–	–	X	–
991209-08	738.0	16.0	9.8	52.6	2.0	(3)	5	–	–	–	X	–
991209-09	743.0	6.4	9.8	22.4	1.2	(4)	(5)	–	–	–	X	–
991209-10	744.0	6.4	9.8	19.8	1.8	3	–	–	–	–	X	–
991209-11	745.0	9.6	9.8	31.2	0.9	(3)	5	–	–	–	X	–
991209-12	745.0	9.6	9.8	36.0	2.3	5	5	–	–	–	X	–
991209-13	747.0	12.8	9.8	38.8	0.7	4	–	–	–	–	X	–
991209-14	747.0	12.8	9.8	46.4	1.1	4	4	–	–	–	X	–
991209-15	749.0	16.0	9.8	53.6	2.5	5	6	–	–	–	X	–
991209-16	750.0	16.0	9.8	45.2	4.6	5	(4)	–	–	–	X	–
991209-17	753.0	6.4	9.8	21.0	1.4	(4)	(5)	–	–	–	X	–
991209-18	755.0	6.4	9.8	22.6	1.0	–	6	–	–	–	X	–
991209-19	755.0	9.6	9.8	27.4	1.3	4	–	–	–	–	X	–
991209-20	756.0	9.6	10.9	26.4	1.2	4	–	–	–	–	X	–
991209-21	756.0	12.8	10.9	38.0	2.7	4	–	–	–	–	X	–
991209-22	755.0	12.8	10.9	35.8	3.5	4	(4)	–	–	–	X	–
991209-23	755.0	16.0	10.9	38.6	2.1	3	3	–	–	–	X	–
991209-24	755.0	16.0	10.9	37.2	1.3	4	–	–	–	–	X	–
991209-25	755.0	6.4	10.9	22.6	1.7	5	8	–	–	–	X	–
991209-26	755.0	9.6	10.9	31.2	3.3	4	(4)	–	–	–	X	–
991209-27	755.0	12.8	10.9	38.2	1.4	3	3	–	–	–	X	–
991209-28	754.0	16.0	10.9	43.2	1.1	4	(4)	–	–	–	X	–

Table F.3 Experimental data for the no-lacquer experiments (AA3105, $b = 0.48\,\text{mm}$)

Plate	T_l	v	V	P	s_P	δ_f	δ_b	Special				
no.	[°C]	[cm/s]	[cm/s]	[mm]	[mm]	[mm]	[mm]	Lq	Th	Wa	Sk	Ar
991129-01	745.5	6.4	–	25.0	1.4	–	4	–	–	–	X	–
991129-02	744.2	6.4	–	24.6	1.9	–	4	–	–	–	X	–
991129-03	742.0	9.6	–	49.8	7.8	5	5	–	–	–	X	–
991129-04	738.4	9.6	–	53.0	7.8	5	5	–	–	–	X	–
991129-05	736.1	12.8	–	70.4	13.8	5	5	–	–	–	X	–
991129-06	734.9	12.8	–	56.0	4.1	4	(5)	–	–	–	X	–
991129-07	733.0	16.0	–	83.0	7.7	5	5	–	–	–	X	–
991129-08	730.7	16.0	–	74.2	9.9	5	4	–	–	–	X	–
991129-09	728.2	6.4	–	32.6	3.0	–	5	–	–	–	X	–
991129-10	729.6	9.6	–	51.0	8.0	4	4	–	–	–	X	–
991129-11	728.4	12.8	–	69.8	6.2	4	4	–	–	–	X	–
991130-01	688.0	6.4	–	64.4	2.3	(5)	–	–	–	–	X	–
991130-02	689.2	6.4	–	50.2	3.1	4	5	–	–	–	X	–
991130-03	690.6	6.4	–	45.8	4.3	5	4	–	–	–	X	–
991130-04	689.9	9.6	–	62.2	7.4	4	3	–	–	–	X	–
991130-05	689.8	12.8	–	81.4	5.7	4	4	–	–	–	X	–

Table F.3 (cont.) No-lacquer experiments

Plate	T_l	v	V	P	s_P	δ_f	δ_b	Special				
no.	[°C]	[cm/s]	[cm/s]	[mm]	[mm]	[mm]	[mm]	Lq	Th	Wa	Sk	Ar
991130-06	689.0	12.8	–	80.4	3.4	5	4	–	–	–	X	–
991130-07	691.0	9.6	–	61.6	0.9	4	3	–	–	–	X	–
991130-08	690.9	16.0	–	86.4	14.8	4	4	–	–	–	X	–
991130-09	687.8	16.0	–	93.4	5.1	4	4	–	–	–	X	–
991130-10	758.8	6.4	–	19.4	2.9	–	–	–	–	–	X	–
991130-11	759.1	6.4	–	18.6	2.1	–	4	–	–	–	X	–
991130-12	759.7	9.6	–	34.6	2.1	–	3	–	–	–	X	–
991130-13	759.8	9.6	–	31.4	6.3	–	4	–	–	–	X	–
991130-14	761.0	12.8	–	45.8	3.2	(4)	4	–	–	–	X	–
991130-15	761.8	12.8	–	45.0	6.6	(5)	(4)	–	–	–	X	–
991130-16	761.9	16.0	–	51.6	5.9	5	–	–	–	–	X	–
991130-17	761.3	16.0	–	56.2	6.6	–	5	–	–	–	X	–
991130-18	803.0	6.4	–	13.4	1.7	–	–	–	–	–	X	–
991130-19	804.0	6.4	–	12.8	1.3	–	–	–	–	–	X	–
991130-20	805.5	9.6	–	26.6	6.7	–	4	–	–	–	X	–
991130-21	806.0	9.6	–	20.2	1.8	–	4	–	–	–	X	–
991130-22	804.6	12.8	–	29.8	4.6	–	4	–	–	–	X	–
991130-23	804.0	12.8	–	32.0	3.9	(4)	3	–	–	–	X	–
991130-24	804.1	16.0	–	36.4	6.1	–	4	–	–	–	X	–
991130-25	802.4	16.0	–	36.8	2.3	–	4	–	–	–	X	–
991130-26	801.6	16.0	–	38.0	5.8	5	(5)	–	–	–	X	–

Table F.4 Experimental data for the lacquer experiments (AA3105, $b = 0.48\,\text{mm}$)

Plate	T_l	v	V	P	s_P	δ_f	δ_b	Special				
no.	[°C]	[cm/s]	[cm/s]	[mm]	[mm]	[mm]	[mm]	Lq	Th	Wa	Sk	Ar
991201-01	686.0	6.4	–	168.0	10.8	–	–	X	–	–	X	–
991201-02	693.4	6.4	–	157.0	10.3	–	–	X	–	–	X	–
991201-03	696.0	6.4	–	152.4	12.3	–	–	X	–	–	X	–
991201-04	697.2	6.4	–	141.6	16.7	–	–	X	–	–	X	–
991201-05	697.2	9.6	–	214.4	11.0	–	–	X	–	–	X	–
991201-06	697.6	9.6	–	230.6	17.1	–	–	X	–	–	X	–
991201-07	697.2	12.8	–	279.0	16.8	–	–	X	–	–	X	–
991201-08	696.4	12.8	–	279.4	33.8	–	–	X	–	–	X	–
991201-09	721.9	6.4	–	134.8	12.3	–	–	X	–	–	X	–
991201-10	722.5	6.4	–	125.8	14.4	–	–	X	–	–	X	–
991201-11	723.3	9.6	–	189.4	26.8	–	–	X	–	–	X	–
991201-12	723.5	9.6	–	180.8	17.1	–	–	X	–	–	X	–
991201-13	724.0	12.8	–	237.4	18.7	–	–	X	–	–	X	–
991201-15	723.1	12.8	–	222.2	11.8	–	–	X	–	–	X	–
991201-16	723.1	16.0	–	285.0	15.4	–	–	X	–	–	X	–
991201-17	722.0	16.0	–	284.4	10.8	–	–	X	–	–	X	–
991201-18	767.9	6.4	–	99.4	10.4	–	–	X	–	–	X	–
991201-19	768.5	6.4	–	96.0	3.2	–	–	X	–	–	X	–

Table F.4 (cont.) Lacquer experiments

Plate	T_l	v	V	P	s_P	δ_f	δ_b	Special				
no.	[°C]	[cm/s]	[cm/s]	[mm]	[mm]	[mm]	[mm]	Lq	Th	Wa	Sk	Ar
991202-01	742.0	6.4	–	115.6	18.4	–	–	X	–	–	X	X
991202-02	744.0	6.4	–	102.4	8.6	–	–	X	–	–	X	X
991202-03	745.0	6.4	–	165.6	17.6	–	–	X	–	–	X	X
991202-04	747.8	6.4	–	128.4	15.4	–	–	X	–	–	X	X
991202-05	745.5	6.4	–	106.2	11.5	–	–	X	–	–	X	X
991202-06	754.2	6.4	–	120.8	23.8	–	–	X	–	–	X	–
991202-07	754.0	6.4	–	99.4	4.3	–	–	X	–	–	X	–
991202-08	755.3	9.6	–	155.4	16.4	–	–	X	–	–	X	–
991202-09	754.0	9.6	–	162.0	18.4	–	–	X	–	–	X	–
991202-10	755.0	12.8	–	192.4	14.5	–	–	X	–	–	X	–
991202-11	755.0	12.8	–	195.2	15.9	–	–	X	–	–	X	–
991202-12	753.0	16.0	–	242.2	27.6	–	–	X	–	–	X	–
991202-13	752.0	16.0	–	225.2	17.4	–	–	X	–	–	X	–

Table F.5 Experimental data for the thick plates (AA1050, $b = 1.50\,\text{mm}$)

Plate	T_l	v	V	P	s_P	δ_f	δ_b	Special				
no.	[°C]	[cm/s]	[cm/s]	[mm]	[mm]	[mm]	[mm]	Lq	Th	Wa	Sk	Ar
990521-16	727.0	6.4	–	155.2	16.7	5	5	–	–	X	X	–
990521-17	727.1	3.2	–	72.4	3.5	5	5	–	–	X	X	–
990521-18	728.3	3.2	–	74.2	2.5	5	–	–	–	X	X	–

Table F.5 Experimental data for the double plate with thermocouples (AA1050, $b \sim 1.08\,\text{mm}$)

Plate	T_l	v	V	P	s_P	δ_f	δ_b	Special				
no.	[°C]	[cm/s]	[cm/s]	[mm]	[mm]	[mm]	[mm]	Lq	Th	Wa	Sk	Ar
990917-01	756.0	6.4	–	80.4	16.2	–	–	–	X	–	X	–
990920-02	721.0	6.4	–	129.0	29.5	–	–	–	X	–	X	–
990920-03	718.0	6.4	–	121.8	22.4	–	–	–	X	–	X	–

References

Adams, Jr., C. M. (1958). Thermal Consideration in Freezing. In *Liquid Metals and Solidification. 39th National Metal Congress and Exposition, Cleveland 1957*, pp. 187. Amer. Sos. for Metals. (Not obtained, ref. Sun 1970 or Robertson and Fascetta 1977).

Areaux, L. D. (1989). Metal chip furnace charge apparatus and method. US Patent no. 4,872,907.

Areaux, L. D. and R. J. Behnke (1992). Submerge Melt Technique for Aluminum Scrap. In *Light Metals 1992*, pp. 877–879. TMS.

Areauz, L. D. and R. H. Dudley (1987). Process and Apparatus for Introducing Metal Chips into a Molten Metal Bath thereof. US Patent no. 4,702,768.

Argyropoulos, S. A. and R. I. L. Guthrie (1979). The exothermic dissolution of 50 wt.% ferro-silicon in molten steel. *Canadian Metallurgical Quarterly*, **18**, pp. 267–281.

Bird, R. B., W. E. Stewart, and E. N. Lightfoot (1960). *Transport Phenomena*. John Wiley & Sons.

Bolz and Tuve (Eds.) (1970). *Handbook of Tables for Applied Engineering Science*. The Chemical Rubber Co.

Bouquerel, W. (1986). Original process to recover molten aluminium contained in dross after furnace cleaning. In *Yugoslav International Symposium on Aluminium, vol. II*, pp. 251–264.

Box, G. E. P., W. G. Hunter, and J. S. Hunter (1978). *Statistics for Experimenters*. John Wiley & Sons.

Brandes, E. A. and G. B. Brook (Eds.) (1992). *Smithells Metals Reference Book* (7 ed.). Butterworth-Heinemann Ltd.

Carslaw, H. S. and J. C. Jaeger (1959). *Conduction of Heat in Solids* (2 ed.). Oxford.

Cochran, C. N., D. L. Belitskus, and D. L. Kinosz (1977). Oxidation of Aluminium-Magnesium Melts in Air, Oxygen, Flue Gas, and Carbon Dioxide. *Metallurgical Transactions B*, **8**, pp. 323–332.

Crank, J. (1984). *Free and moving boundary problems*. Clarendon Press Oxford.

Dons, A. L. et al. (1999). The Alstruc Microstructure Solidification Model for Industrial Aluminium Alloys. *Metallurgical and Materials Transactions A*, **30**, pp. 2135–2146.

Drouet, M. G., M. Handfield, J. Meunier, and C. B. Laflamme (1994). Dross Treatment in a Rotary Arc Furnace with Graphite Electrodes. *JOM* no. 5, pp. 26–27.

Efron, B. and R. Tibshirani (1986). Bootstrap Methods for Standard Errors, Confidence Intervals, and Other Measures of Statistical Accuracy. *Statistical Science*, **1**, 1, pp. 54–77.

Ehrich, O., Y.-K. Chuang, and K. Schwerdtfeger (1978). The Melting of Metal Spheres Involving the Initially Frozen Shells with Different Material Porperties. *Int. J. Heat Mass Transfer*, **21**, pp. 341–349.

Ehrich, O., Y.-K. Chuang, and K. Schwerdtfeger (1979). The melting of sponge iron spheres in their own melt. *Arch. Eisenhüttenwesen*, **50**, pp. 329–334.

Ekström, H.-E. and O. Claesson (Eds.) (1983). *Aluminium* (1 ed.). Standardiseringskommissionen i Sverige. (In Swedish).

Engh, T. A. (1992). *Principles of metal refining*. Oxford University Press.

Farner, S. (1997). Resirkulering av aluminium ved HRM og oppfølging av G2 uke 41/1996. Restricted report STF24 F97546, SINTEF, Norway. (In Norwegian).

Farner, S. (1998). Dross Generation and Melting Rates of Direct Charging of Aluminium Swarf in Vortex Chamber. Restricted report STF24 F98645, SINTEF, Norway. (In Norwegian).

Farner, S., F. Frisvold, and T. A. Engh (2000). Remelting by continuous feeding of rolled scrap into melt. In *Light Metals 2000*, pp. 699–704. TMS.

Fisher, K. (1989). *Fundamentals of Solidification* (3 ed.). Trans Tech Publications.

Fox, M. H. and M. Nilmani (1993). Dross Minimisation — Its Relationship to Melting and Melt Handling Practice. In M. Nilmani (Ed.), *Aluminium Cast House Technology, Theory & Practice*, pp. 239–254. TMS.

Frisvold, F. and T. A. Engh (1997). Oxidation of Aluminium. A Literature Survey. Restricted report STF24 F97592, SINTEF, Norway.

Garcia, A. and M. Prates (1978). Mathematical Model for the Unidirectional Solidification of Metals: I. Cooled Molds. *Metallurgical Transactions B*, **9**, pp. 449–457.

Goudie, N. J. and S. A. Argyropoulos (1995). Technique for the Estimation of Thermal Resistance at Solid Metal Interfaces Formed During Solidification and Melting. *Canadian Metallurgical Quarterly*, **34**, 1, pp. 73–84.

Gourtsoyannis, L., H. Herein, and R. I. L. Guthrie (1974). Some Kinetic and Hydrodynamic Aspects of Making Aluminium and Ferro-Alloy Additions to Steel Baths. In *Physical Chemistry of Production or Use of Alloy Additives Proceedings*, pp. 45–67.

Gourtsoyannis, L. and F. Mucciardi (1982). The industrial application of an aluminum wire injector for ladle metallurgy. *CIM Bulletin*, **75**, 837, pp. 102–105.

Griffiths, W. D. (1999). The Heat-Transfer Coefficient during the Unidirectional Solidification of an Al–Si Alloy Casting. *Metallurgical and Materials Transactions B*, **30**, 3, pp. 473–482.

Guthrie, R. I. L. (1977). Addition Kinetics in Steelmaking. In *Electric Furnace Proceedings*, pp. 30–41.

Guthrie, R. I. L., R. Clift, and H. Henein (1975). Contacting Problems Associated with Aluminum and Ferro-Alloy Additions in Steelmaking-Hydrodynamic Aspects. *Metallurgical Transactions B*, **6**, pp. 321–329.

Guthrie, R. I. L. and L. Gourtsoyannis (1971). Melting rates of furnace or ladle additions in steelmaking. *Canadian Metallurgical Quarterly*, **10**, pp. 37–46.

Hald, N. E. (1995). *Aluminiumtap ved omsmelting og resirkulering av blankt og lakkert returmetall*. Diploma thesis, Dept. of Metallurgy, NTH, Norway. (In Norwegian).

Ho, K. and R. D. Pehlke (1985). Metal-Mold Interfacial Heat Transfer. *Metallurgical Transactions B*, **16**, pp. 585–594.

Hu, H. and S. A. Argyropoulos (1996). Mathematical modelling of solidification and melting: a review. *Modelling Simul. Mater. Sci. Eng.*, **4**, pp. 371–396.

Katyal, A. (1995). New electromagnetic pumping and stirring technology for metal melting. In *Cast Metals Development Ltd.–International Conference*.

Katyal, A., W. N. Brown, and R. Howitt (1994). Furnace with deflecting surface and method of charging metal solids. US Patent no. 5,350,440.

Kim, T.-G. and Z.-H. Lee (1997). Time-varying heat transfer coefficients between tube-shaped casting and metal mold. *Int. J. Heat Mass Transfer*, **40**, 15, pp. 3515–3525.

Knacke, O., O. Kubaschewski, and K. Hesselmann (Eds.) (1991). *Thermochemical Properties of Inorganic Substances* (2 ed.), Volume I. Springer-Verlag.

Kreyszig, E. (1988). *Advanced Engineering Mathematics* (6 ed.). John Wiley & Sons.

Kvithyld, A. Dr.ing. thesis, Dept. of Mater. Techn. and El.chem., NTNU, Norway. About decoating of aluminium, to be finished in 2002.

Lau, F., W. B. Lee, S. M. Xiong, and B. C. Liu (1998). A study of the interfacial heat transfer between an iron casting and a metallic mould. *Journal of Materials Processing Technology*, **79**, pp. 25–29.

Lide, D. R. (Ed.) (1990). *Handbook of Chemistry and Physics* (71 ed.). CRC Press.

Lide, D. R. (Ed.) (1997). *Handbook of Chemistry and Physics* (78 ed.). CRC Press.

Loulou, T., E. A. Artyukhin, and J. P. Bardon (1999). Estimation of thermal contract resistance during the first stages of metal solidification process: II—experimental setup and results. *Int. J. Heat Mass Transfer*, **42**, pp. 2129–2142.

Lynch, C. T. (Ed.) (1974). *Handbook of Materials Science*, Volume II. CRC Press.

Manfredi, O., W. Wuth, and I. Bohlinger (1997). Characterizing the Physical and Chemical Properties of Aluminum Dross. *JOM* no. 11, pp. 48–51.

Meyer, J. L. (1992). Electromagnetic Processes in Aluminium Casthouses and, Foundries: An Overview. In *Light Metals 1992*, pp. 1215–1231. TMS.

Mucciardi, F. A. (1980). *A Study of Light Alloy Addition Techniques in Steelmaking*. Ph.D. thesis, McGill University, Canada.

Neff, D. V. (1986). Optimizing Fluid Flow in an Aluminum Melting Furnace. In *Aluminum Industry Energy Conservation Workshop IX Papers*, pp. 227–248. Aluminum Association, Washington, DC, USA.

Neff, D. V. (1993a). Molten Aluminum in Motion. In M. Nilmani (Ed.), *Aluminium Cast House Technology, Theory & Practice*, pp. 197–211. TMS.

Neff, D. V. (1993b). Molten Metal Processing in Aluminum Recycling. In H. Henein and T. Oki (Eds.), *First International Conference on Processing Materials for Properties*, pp. 745–749. TMS.

Nishida, Y., W. Droste, and S. Engler (1986). The Air-Gap Formation Process at the Casting-Mold Interface and the Heat Transfer Mechanism through the Gap. *Metallurgical Transactions B*, **17**, pp. 833–844.

Øye, H. A. et al. (1999). Aluminum: Approaching the New Millennium. *JOM* no. 2, pp. 29–42.

Pedersen, S. and T. Grande (1997). Måling av viskositet av aluminium tilsatt 1–3 vekt% mangan eller jern. Unpublished work in Norwegian.

Perry, R. H. and D. W. Green (1984). *Perry's Chemical Engineers' Handbook* (6 ed.). McGraw-Hill.

Perry, R. T. (1966). *Fluid Mechanics of Entrainment through Liquid–Liquid and Liquid–Solid Junctures*. Ph.D. thesis, University of Minnesota.

Peterson, R. D. (1995). Issues in the Melting and Reclamation of Aluminum Scrap. *JOM* no. 2, pp. 27–29.

Pietsch, W. (1993). Briquetting of Aluminum Swarf for Recycling. In S. K. Das (Ed.), *Light Metals 1993*, pp. 1045–1051. TMS.

Prates, M. and H. Biloni (1972). Variables Affecting the Nature of the Chill Zone. *Metallurgical Transactions*, **3**, pp. 1501–1510.

Press, W. H. et al. (1992). *Numerical Recipes in C: The Art of Scientific Computing* (2 ed.). Cambridge University Press.

Reynolds, C. C. (1964). Thermal Behavior of Dies and Permanent Molds. *Trans. Amer. Foundrymen's Soc.*, **72**, pp. 342–347.

Røhmen, E. (1995). *Thermal Behaviour of a Spherical Addition to Molten Metals*. Dr.ing. thesis, Dept. of Metallurgy, NTH, Norway.

Røhmen, E. (1996). Oppvarming av ulakkerte plater i oksygenfri atmosfære. Restricted report STF24 F96625, SINTEF, Norway. (In Norwegian).

Røhmen, E., T. Bergstrøm, and T. A. Engh (1995). Thermal Behaviour of a Spherical Addition to Molten Metals. In Tuset, Tveit, and Page (Eds.), *INFACON 7*, pp. 683–695. FFF, Trondheim, Norway.

Robertson, S. R. and E. F. Fascetta (1977). An Analytical Technique for the Determination of the Thermal Contact Resistance Between a Solidifying Metal and Mold. *Metallurgical Transactions B*, **8**, pp. 619–624.

Rossel, H. (1990). Fundamental investigations about metal loss during remelting of extrusion and rolling fabrication scrap. In *Light Metals 1990*, pp. 721–729. TMS.

Roth, D. J. and A. R. Beevis (1995). Maximizing the aluminium recovered from your dross and elimination of any waste products in dross recycling. In *Light Metals 1995*, pp. 815. TMS.

Saavedra, A. F. (1993). Electromagnetic Stirrers–Their influence on Melter Operation and Dross Generation. In *Light Metals 1993*, pp. 739–743. TMS.

Sagen, M. (1996a). *Aluminiumtap ved omsmelting og resirkulering av returmetall*. Experimental work, Dept. of Metallurgy, NTNU, Norway. (In Norwegian).

Sagen, M. (1996b). *Endring i smelteovnsdrift ved installasjon av elektromagnetisk pumpe*. Diploma thesis, Dept. of Metallurgy, NTNU, Norway. (In Norwegian, Restricted).

Schlichting, H. (1979). *Boundary-Layer Theory* (7th ed.). McGraw-Hill.

Smith, L. (1986). Recovery of aluminium process scrap by coreless induction melting. In *Conference Proceedings Aluminium Technology*, pp. 753–762. Institute of Metals.

Squires, G. L. (1989). *Practical physics* (3 ed.). Cambridge University Press.

Sun, R. C. (1970). Simulation and Study of Surface Conductance for Heat Flow in the Early Stage of Casting. *AFS Cast Metals Res. J.*, **6**, pp. 105–110.

Szekely, J. and N. J. Themelis (1971). *Rate Phenomena in Process Metallurgy.* Wiley.

Tanaka, S. (1977). Deoxidation practice in continuous casting (aluminium-wire feeder system). *Ironmaking and Steelmaking* no. 6, pp. 350–354.

Taniguchi, S., M. Ohmi, and S. Ishiura (1983). A Hot Model Study on the Effect of Gas Injection upon the Melting Rate of Solid Sphere in a Liquid Bath. *Trans. Iron and Steel Inst. of Japan*, **23**, pp. 571–577.

Tanoue, T., Y. Umeda, H. Ichikawa, and T. Aoki (1973). Development of New Method of Aluminum Addition—Aluminum Bullets Shooting Method. *The Sumitomo Search* no. 9, pp. 74–78.

Weast, R. C. (Ed.) (1979). *Handbook of Chemistry and Physics* (60 ed.). CRC Press.

Wefers, K. (1981). Properties and characterization of surface oxides on aluminum alloys. *Aluminium*, **57**, pp. 722–726. Communication.

White, F. M. (1994). *Fluid Mechanics* (3 ed.). McGraw-Hill.

Zhang, L. and F. Oeters (1999). Mathematical modelling of alloy melting in steel melts. *steel research*, **70**, 4+5, pp. 128–134.

Index

air film, 119
AluCoat, *see* Hydro Aluminium
aluminium, 1–3
anodization, 73
argon atmosphere, 101
auger mechanism, 14

baffle, 24
beads, 26
Biot number (Bi), 37
bootstrapping, 94, 158
boundary layer, 61
bulk density, 10
bulk melt, 36

circular reference, *see* reference
closed-well chamber, 5
complementary shell, 88
contact angle, 23
covariance tensor, 157, 158
curvature matrix $\vec{\vec{\alpha}}$, 156
CWC, *see* closed-well chamber

droplike plate end, 85
dross, 6–10
    dry/wet, 7
dry-hearth furnace, 4

edge shell, 77
eloxal, 73

flotation furnace, 4
flow velocity, 70
Fourier's Law of Conduction, 17
free-boundary problems, 16

gap heat-transfer coefficient, 122

heat radiation, 47
heat-transfer coefficient
    calculated, flowing melt, 66
    calculated, stagnant melt, 64
    from boundary-layer theory, 63
    local, 63, 117
    of interface, 19
HRM, *see* Hydro Aluminium, Holmestrand Rolling Mill
Hydro Aluminium
    AluCoat, 73
    Holmestrand Rolling Mill, 5, 73
    Sunndal, 69

induction furnace, 4
inner side of plate, 73
Inverse Stefan number (Sf), 38

lacquer experiments, 73
Laplace transformation, 53
    inverse, 146
launder, 69
launder experiments, 96
light-gauge scrap, 4

main heating chamber, 5
meniscus, 23, 35, 92
metal losses, 7
MHC, *see* main heating chamber
moving-boundary problems, 16
mushy zone, 111

Newton's Law of Cooling, 17
no-lacquer experiments, 73

Nusselt number (Nu), 37
    from boundary-layer theory, 63

outer side of plate, 73

Péclet number (Pe), 37
penetration depth, 36
    illustration, 37
    uncertainties, 123
penetration point, 35
plasma furnace, 5
Prandtl number (Pr), 61
primary aluminium, 2
puddling device, 13

quiescent-melt experiments, 72, 94

recycled aluminium, 3
reference
    circular, *see* circular reference
Region A, 39
Region B, 39, 41
Reynolds number (Re), 64
rotary-barrel furnace, 5

secondary aluminium, 3
shell, 17, 36, 40
shell formation
    in pine of swarf, 29
shell start depth, 91
snap-off, 85, 86, 123
Stefan number, inverse (Sf), 38
Stefan problems, 16
stirring, 11
submersion time, 27
swarf, 8

thermal conductivity
    oxide layer, 114
transformation
    statistical, 80
transient period, 52

UBC, 4

uncertainties, 78
    material properties, 109
    penetration depth, 123

velocity
    melt flow, 70
vortex chamber, 6
vortexing, 13

wedge, 36
    region, 39, 42, 85
wet-hearth furnace, 5
window, 25
withdrawal of plate, 86